Computational Design and Screening of Functionalized Solid Support for Metal Ion and Isotope Separation Validated by Experiments

By
ASHISH KUMAR SINGHA DEB
CHEM01201404014

Bhabha Atomic Research Centre, Mumbai

A thesis submitted to the
Board of Studies in Chemical Sciences

In partial fulfillment of requirements
for the Degree of
DOCTOR OF PHILOSOPHY
of
HOMI BHABHA NATIONAL INSTITUTE

December, 2018

Homi Bhabha National Institute

Recommendations of the Viva Voce Committee

As members of the Viva Voce Committee, we certify that we have read the dissertation prepared by **Ashish Kumar Singha Deb** entitled **"Computational design and screening of functionalized solid support for metal ion and isotope separation validated by experiments"** and recommend that it may be accepted as fulfilling the thesis requirement for the award of Degree of Doctor of Philosophy.

Chairman – Prof. D. K. Maity		**Date:** 03/04/19
Guide / Convener – Prof. Sk. Musharaf Ali	Sk. M Ali	**Date:** 3/4/2019
Examiner – Prof. Jayant K. Singh	J Singh	**Date:** 3.4.2019
Member 1- Prof. A. K. Pandey	Pandey	**Date:** 3.4.2019
Member 2- Prof. S. Mukhopadhayay		**Date:** 3/4/19
Member 3- Prof. A. K. Ghosh		**Date:** 03/04/19

Final approval and acceptance of this thesis is contingent upon the candidate's submission of the final copies of the thesis to HBNI.

I/We hereby certify that I/we have read this thesis prepared under my/our direction and recommend that it may be accepted as fulfilling the thesis requirement.

Date: 08/04/2019

Place: HBNI, Mumbai

Sk. M Ali
(Dr. Sk. Musharaf Ali)

Guide

STATEMENT BY AUTHOR

This dissertation has been submitted in partial fulfillment of requirements for an advanced degree at Homi Bhabha National Institute (HBNI) and is deposited in the Library to be made available to borrowers under rules of the HBNI.

Brief quotations from this dissertation are allowable without special permission, provided that accurate acknowledgement of source is made. Requests for permission for extended quotation from or reproduction of this manuscript in whole or in part may be granted by the Competent Authority of HBNI when in his or her judgment the proposed use of the material is in the interests of scholarship. In all other instances, however, permission must be obtained from the author.

Ashish

Ashish Kumar Singha Deb

DECLARATION

I, hereby declare that the investigation presented in the thesis has been carried out by me. The work is original and has not been submitted earlier as a whole or in part for a degree / diploma at this or any other Institution / University.

Ashish Sdeb
Ashish Kumar Singha Deb

List of Publications arising from the thesis

Journal

1. Adsorptive removal of thorium from aqueous solution using diglycolamide functionalized multi-walled carbon nanotubes, **A.K. Singha Deb**, B.N. Mohanty, P. Ilaiyaraja, K. Sivasubramanian, B. Venkatraman, *J. Radoanal. Nucl. Chem.*, **2013**, 295,1161–1169
2. Nano Cavity Induced Isotope Separation of Zinc: Density Functional Theoretical Modeling, **A. K. Singha Deb**, Sk. M. Ali, K. T. Shenoy, and S. K. Ghosh, J. *Chem. Eng. Data*, **2014**, 59, 2472–2484.
3. Adsorption of Eu^{3+} and Am^{3+} ion towards hard donor-based diglycolamic acid-functionalised carbon nanotubes: density functional theory guided experimental verification, **A.K. Singha Deb**, Sk. M. Ali, K.T. Shenoy, S.K. Ghosh, *Molecular Simulation*, **2015**, 4, 490-503.
4. Diglycolamic acid functionalized CNT for preferential selection of Eu (III) over Am (III) ion: Density functional theoretical modelling validated by experiments, **A.K. Singha Deb**, A. Bhattacharyya, Sk. M. Ali, K.T. Shenoy, S.K. Ghosh, *Sep. Sci. Technol.*, **2015**, 50, 395–403.
5. Unanticipated favoured adsorption affinity of Th(IV) ions towards bidentate carboxylate functionalized carbon nanotubes (CNT–COOH) over tridentate diglycolamic acid functionalized CNT: density functional theoretical investigation, **A.K. Singha Deb**, Sk. M. Ali, K.T. Shenoy, *RSC Adv.* **2015**, 5, 80076–80088.
6. Sorption behaviour of Pu^{4+} and PuO_2^{2+} on Amidoamine functionalized carbon nanotubes: experimental and computational study, P. Kumar, A. Sengupta, **A.K. Singha Deb**, K. Dasgupta, Sk. M. Ali, *RSC Adv.,* **2016**, 6, 107011-107020.

7. Diglycolamic acid-functionalized multiwalled carbon nanotubes as a highly efficient sorbent for f-block elements: experimental and theoretical investigations, A. Sengupta, **A.K. Singha Deb**, K. Dasgupta, V. C. Adya, and Sk. M. Ali, *New J. Chem.*, **2017**, 41, 4531-4545.
8. Novel amidoamine functionalized multi-walled carbon nanotubes for removal of mercury(II) ions from wastewater: Combined experimental and density functional theoretical approach, **A.K. Singha Deb**, V. Dwivedi, K. Dasgupta, S.M. Ali, K.T. Shenoy, *Chem. Eng. J.*, **2017**, 313, 899–911.
9. Poly(amidoamine) dendrimer functionalized carbon nanotube for efficient sorption of trivalent f-elements: a comparison between 1st and 2nd generation, P. Kumar, A. Sengupta, **A.K. Singha Deb**, Sk. M. Ali, *ChemistrySelect*, **2017**, 2, 975–985.
10. Understanding the sorption behavior of Pu4+ on poly(amidoamine) dendrimer functionalized carbon nanotube: sorption equilibrium, mechanism, kinetics, radiolytic stability, and back-extraction studies, P. Kumar, A. Sengupta, **A.K. Singha Deb**, K. Dasgupta, Sk. M. Ali, *Radiochim. Acta*, **2017**, 105(9), 677–688.
11. Amidoamine functionalized task specific carbon nanotube for efficient sorption of penta and hexavalent neptunium: Experimental and Theoretical investigations, A. Sengupta, **A.K. Singha Deb**, P. Kumar, K. Dasgupta, Sk. M. Ali, *J. Environ. Chem. Eng*.**,** **2017**, 5, 3058-3064.
12. Carbon nano tubes functionalized with novel functional group amido-amine for sorption of actinides, **A.K. Singh Deb**, S. Pahan, K. Dasgupta, S. Panja, A.K. Debnath, P.S. Dhami, Sk. M. Ali, C.P. Kaushik, J.S. Yadav, *J. Hazard. Mater.*, **2018**, 345, 63–75.
13. Evaluation of 1st and 2nd generation of poly(amidoamine) dendrimers functionalized carbon nanotubes for the efficient removal of neptunium, A. Sengupta, **A.K. Singha Deb**, N.K. Gupta, P. Kumar, K. Dasgupta, Sk. M. Ali, *J. Radoanal. Nucl. Chem.*, **2018**, 315, 331-340.
14. Sulphur Ligand Functionalized Carbon Nanotubes for Removal of mercury from waste water – experimental and density functional theoretical study, **A.K. Singha**

Deb, N. Dhume, K. Dasgupta Sk. M. Ali, K. T. Shenoy, S. Mohan, *Sep. Sci. Technol.*, **2018**, DOI:10.1080/01496395.2018.1529044.

15. Improved Zn adsorption and isotope separation by dibenzo-18-crown-6 functionalized polymethacrylate Resin, **A.K. Singha Deb**, A. K. B. Bhosale, H. Jadhav, Sk. M. Ali, K. T. Shenoy, (*Communicated*)
16. Fixed-bed adsorption of zinc onto crown ether functionalized polymethacylate resin, **A.K. Singha Deb**, A. K. B. Bhosale, H. Jadhav, Sk. M. Ali, K. T. Shenoy, (*Communicated*)
17. Complexation of Eu(III) and Am(III) with 1st and 2nd generation of poly(amidoamine) dendrimer ffunctionalized carbon nanotube: A DFT study, **A.K. Singha Deb**, A. Sengupta, Sk.M. Ali, (*Communicated*)

Chapters in books and lectures notes

1. Computational Chemistry Assisted Design and Screening of Ligand-Solvent Systems for Metal Ion Separation; Sk. M. Ali, A. Boda, A. K. Singha Deb, P. Sahu, K. T. Shenoy, In, *Frontiers in Computational Chemistry*,Vol. 3, 2016, pp3-109; Eds, ZaheerUl-Haq and Jeffry D. Madura; Bentham Science Publishers, UAE.
2. Atomistic and Experimental Modeling for Adsorption of Metal Ions With Carbon Nanotubes in Aqueous Environment; Sk. M. Ali, A. Boda, A. K. Singha Deb, P. Sahu, In, *Aqueous Phase Adsorption Theory, Simulations and Experiments*, 2019, pp69-109; Eds, J. K. Singh and N. Verma; Taylor & Francis, CRC Press, Boca Raton.

Conferences

1. Diglycolamide functionalized CNT for preferential selection of Th (IV) over Sr (II) ion: Density functional theoretical investigation validated by experiments;

A.K. Singha Deb, A. Boda, Sk. M. Ali, K.T. Shenoy and S.K. Ghosh, DAE BRNS Symposium on Current Trends in Theoretical Chemistry,*CTTC*, **2013**.

2. Nano confinement induced isotope separation of Zinc: Density functional theoretical modelling; A.K. Singha Deb, Sk. M. Ali, K.T. Shenoy and S.K. Ghosh, DAE BRNS Symposium on Emerging Trends in Separation Science and Technology, *SESTEC*, **2014.**
3. Diglycolamic acid functionalized CNT for preferential selection of Eu (III) over Am (III) ion: Density functional theoretical modelling validated by experiments; A.K. Singha Deb, A. Bhattacharyya1 Sk. M. Ali, K.T. Shenoy, S.K. Ghosh; SECTEC-2014, DAE BRNS Symposium on Emerging Trends in Separation Science and Technology, *SESTEC*, **2014**
4. DFT Modeling on Functionalized Carbon Nanomaterials for Adsorptive Separation of Metal ion; A.K.Singha Deb, Sk. M. Ali, K.T. Shenoy, DAE-BRNS Theme meeting on Application of Molecular modeling in Separation Processes, *AMMSP*, **2015**.
5. Evaluation of Magnetic Carbon Nanotubes for Mercury(II) Removal from Water; A. K. Singha Deb, S. Vignesh, Sk. M. Ali, K. T. Shenoy, DAE-BRNS Emerging Trends in Separation Science and Technology, *SESTEC*, **2016**.
6. Separation of actinides by amidoamine functionalized carbon nanotubes; S. Pahan, A.K. Singha Deb, K. Dasgupta, Sk. M. Ali, K.T. Shenoy, J.G. Shah, K. Banerjee, DAE-BRNS Emerging Trends in Separation Science and Technology, *SESTEC*, **2016**.
7. Adsorption of Zn^{2+} ion by Benzo-15-Crown-5 ether anchored on polymethylacrylate resin: Batch adsorption and column chromatographic studies; S.K. Arora, A. Boda, A.K. Singha Deb, M. Jha, Sk. M. Ali, K.T. Shenoy, International Conference on Recent Advances in Analytical Sciences, *RAAS*, **2016**.
8. Magnetic Functionalized Carbon Nanotubes for Removal of Mercury(II) ions from Water, A. K. Singha Deb, V. Dwivedi, K. Dasgupta, Sk. M. Ali, K. T.

Shenoy, DAE-BRNS Interdisciplinary Symposium on Material Chemistry, *ISMC*, **2016.**

9. Sulphur Ligand Functionalized Carbon Nanotubes for Removal of mercury from waste water – batch to column study, A. K. Singha Deb, N. Dhume, K. Dasgupta Sk. M. Ali, K. T. Shenoy, S. Mohan, DAE BRNS Emerging Trends in Separation Science and Technology, *SESTEC*, **2018**.
10. Improved zinc adsorption and isotope separation by Crown Ether functionalized Resin, A. K. Singha Deb, A. K. B. Bhosale, H. Jadhav, A. Boda, Sk. M. Ali1, K. T. Shenoy, DAE-BRNS Interdisciplinary Symposium on Materials Chemistry, *ISMC*, **2018**.

Others

1. Removal of thorium from aqueous solution by adsorption using PAMAM dendron-functionalized styrene divinyl benzene, P. Ilaiyaraja, A. K. Singha Deb, K. Sivasubramanian, D. Ponraju, B. Venkatraman, *J. Radoanal. Nucl. Chem.*, **2013**, 297:59–69.
2. Adsorption of uranium from aqueous solution by PAMAM dendronfunctionalized styrene divinylbenzene, P. Ilaiyaraja, A. K. Singha Deb, K. Sivasubramanian, D. Ponraju, B. Venkatraman, *J. Hazard. Mat.***2013**, 250– 251: 155– 166.
3. Removal of cobalt from aqueous solution using xanthatefunctionalized dendrimer, P. Ilaiyaraja, A. K. Singha Deb, D. Ponraju, B. Venkatraman, *Desalin. Water Treat.* **2014**, 52: 438–445.
4. Conformational effect of dicyclo-hexano-18-crown-6 on isotopic fractionation of zinc: DFT approach, A. Boda, A.K. Singha Deb, Sk. M. Ali, K.T. Shenoy, S.K. Ghosh, *AIP Conference Proceedings* **2014**, 1591: 106-1067.
5. Dual mode of extraction for Cs^+ and Na^+ ions with dicyclohexano-18-crown-6 and bis(2-propyloxy)-calix[4]crown-6 in ionic liquids: density functional theoretical investigation, Sk. M. Ali, J. M. Joshi, A. K. Singha Deb, A. Boda, K. T. Shenoy, S. K. Ghosh *RSC Adv*. **2014**, 4: 22911-22925.

6. Removal of uranium and thorium from aqueous solution by ultrafiltration (UF) and PAMAM dendrimer assisted ultrafiltration (DAUF), P. Ilaiyaraja, A. K. Singha Deb, D. Ponraju, *J. Radioanal. Nucl. Chem.*, **2014**, 303: 441–450.
7. Xanthate functionalized pamam dendrimer chelating ligand for treatment of radioactive liquid wastes, P. Ilaiyaraja, A. K. Singha Deb, D. Ponraju, B. Venkatraman, *J. Environ. Chem. Eng*. **2015**, 3:1047-1054.
8. Change in the affinity of ethylene glycol methacrylate phosphate monomer and its polymer anchored on a graphene oxide platform toward uranium(vi) and plutonium(iv) ions,Sankararao Chappa, A. K. Singha Deb, Sk. M. Ali, A. K. Debnath, D. K. Aswal, Ashok K. Pandey, *J. Phys. Chem. B* **2016**, 120:2942-2950.
9. Molecular modeling guided isotope separation of gadolinium with strong cation exchange resin using displacement chromatography, A. Boda, S.K. Arora, A.K. Singha Deb, M. Jha, Sk. M. Ali, K.T. Shenoy, *Sep. Sci. Technol.* **2017**, 52(14), 2300–2307.
10. Elucidation of complexation of tetra and hexavalent actinides towards an amide ligand in polar and non-polar diluents: combined experimental and theoretical approach, A. Boda, A. K.Singha Deb, A. Sengupta, Sk. M. Ali, K.T. Shenoy, *Polyhedron* **2017**, 123: 234–242.
11. Surface Engineering of PAMAM-SDB Chelating Resin withDiglycolamic Acid (DGA) Functional Group for Efficient Sorption ofU(VI) and Th(IV) from Aqueous Medium, P. Ilaiyarajaa, A.K. Singha Deb, D. Ponraju, Sk. M. Ali, B. Venkatraman, *J. Hazard. Mater.* **2017**, 328, 1–11.
12. Molecular engineering of functionalized crown ether resins for the isotopic enrichment of gadolinium: from computer to column chromatography, A. Boda, A. K. Singha Deb, Sk. M. Ali, K. T. Shenoy and S. Mohan, *Mol. Syst. Des. Eng.*, 2017, 2, 640–652.
13. Unusual extraction of trivalent f-cations using diglycolamide dendrimers in a room temperature ionic liquid: extraction, spectroscopic and DFT studies, S. A. Ansari, P. K. Mohapatra, A. Leoncini, Sk. M. Ali, A. K. Singha Deb, J. Huskens and W. Verboom, *Dalton Trans.*, **2017**, 46, 16541–16550.

14. Interfacial Behavior of Cs$^+$, K$^+$, Na$^+$, and Rb$^+$ Extraction in the Presence of Dibenzo-18-Crown-6 from the Nitrobenzene−Water Biphasic System: Experimental, Quantum Chemical, and Molecular Dynamic Studies, R. Biswas, P. Ghosh,T. Banerjee, Sk. M. Ali,and A. K. Singha Deb, ACS Omega 2018, 3, 1663−1674.
15. Tailoring of carbon nanotubes for the adsorption of heavy metal ions: molecular dynamics and experimental investigations, P. Sahu, A. K. Singha Deb, Sk. M. Ali, K. T. Shenoy, S Mohan, Mol.Syst.Des.Eng., 2018, 3, 917-929.

Ashish SDeb

Ashish Kumar Singha Deb

Dedicated to…..

……..My Parents……..

ACKNOWLEDGEMENTS

First of all, I would like to express my deepest appreciation and sense of gratitude to my mentor and guide Prof. Sk. Musharaf Ali for introducing me to present area of research. The present thesis work would not have been possible without his endless support, valuable guidance and constant encouragement. His contagious enthusiasm and uninterrupted motivation has driven me to carry out timely submission of this dissertation. His patience, friendly support, and immense knowledge helped me throughout the time of my research.

Next, I would like to acknowledge and express my deepest appreciation to my Doctoral Committee Chariman Prof. Dilip Kumar Maity, and members Prof. Ashok Kumar Pandey, Prof. Sulekha Mukhopadhyay, and Prof. Asim Kumar Ghosh for their valuable time to time evaluation of the research work, and suggestions which helped me in improving the quality of my research work.

I wish to express my sincere gratitude to Shri K. T. Shenoy, Head, Chemical Engineering Division for allowing me to presue my PhD work programme and his keen interest in my work. I am delighted to thank Shri Sandip K Ghosh (Ex. Director, ChEG), Shri., Dr. (Smt.) S. B. Roy (Ex. Associate Director, ChEG) and Dr.(Smt.) Sadhana Mohan (Associate Director, ChEG) for their help during my Ph. D work.

I am particularly grateful for the assistance given my friend and batch mate Dr. Anil Boda and Dr. Arijit Sengupta during all steps of the work.

I am extremely grateful to Dr. K. Dasgupta, Dr. S. Panja, and Mr. S. Pahan for their fruitful collaboration and suggestions during my PhD work.

I would also like to extend my deepest gratitude to my seniors Dr. Raghunath Choudhury Dr. Siddartha Kolay and Shri Arya Das for their support in various aspects during my PhD work.

I am extremely grateful to Mr. J. N. Sharma, Mr. P. Khan, Mr. P. Singha Roy, Dr. D. Mondal, Mr. N. Gughe, Dr. S. Majumdar and Dr. B. Paul for their help in material characterization.

I would like to thank my colleague and laboratory mates Smt. S.K. Arora, Dr. J. M Joshi, Smt. P. Sahu, Smt. S Govalkar, Ms. Rani V Singh, Ms. M. Jha, Shri P. V. Kadale and Ms. A. Mokel for their valuable support during the Ph. D work. I take this opportunity to thank my colleagues Dr. K. K. Singh, Mr. N. Sen, Mr. M. Darekar, Mr. S. Sarkar, Mr. A. P. Kulkarni, R. K. Jha, A. Kumar, M. Pradhan and divisional staffs of ChED.

I have greatly benefitted from prject trainees Ms. V. Dwivedi, Mr. Vignesh S., Ms. S. Choudhary, Ms. M. Jain, Ms. N. Dhume, Mr. A. Krishnan, Mr. H. Bhosale and Mr. A. Yadav in course of my PhD work. I sincerely acknowledge and thank each of them.

I would like to offer my special thanks to Dr. D. Ponraju, Dr. P. Ilaiyaraja, Dr. K. Sivasubranian, Dr. R. Venkatraman, Mr. H. Krishnan, Mr. B.N. Mahanty, Mr. S. Joshi, Smt. Y. Ramini, Dr. N. Sivraman, and Dr. Brahmananda Rao of IGCAR, Kalpakkam for their help and encouragement.

I gracefully acknowledge the contributions of all the teachers in my school, college, university and BARC training school who have played a pivotal role in my life.

The list of friends can be huge, however, I would like to name few of them, Sandip, Sabyaachi, Sumana, Amrita, Soumitra, Nanda, Sutanuva, Sanat, Santu, Soumyajyoti, Hirak, Sourav, Sanat Karmakar, Locky, Mithun, Kandarpa, Tushar, Abhijit, Soumen and Rahul for their help and wishes.

I wish to express my sincere gratitude to my beloved mother, father, sisters, brothers, sister-in-laws, brother-in-laws, nephews, nieces, and all other family members for their unflagging love and support throughout my life. This achievement is simply impossible without them.

I humbly owe my sincere thanks to the almighty God, without His blessing and love I could do nothing.

At last but not least, I would like to express my sincere thanks to everybody who have helped me in various ways during the course of this thesis work and I have forgotten to mention.

Asihsh Kumar Singha Deb

CONTENTS

SYNOPSIS

Title: Computational design and screening of functionalized solid support for metal ion and isotope separation validated by experiments

Separation of various metal ions and isotopes of several elements are of immense importance in the development of nuclear science and technology. The three-stage Indian nuclear energy program is based on a closed fuel cycle, where the spent fuel of one stage is reprocessed to produce fuel for the next stage [1].The nuclear fuel cycle comprises of processes and operations needed to manufacture nuclear fuel starting from mining and milling of uranium ore, its irradiation in nuclear power reactors and storage, reprocessing, recycling or disposal [2]. Liquid stream generated in each step contains different kinds of metal ions whose separation followed by utilization and disposal is essential for the nuclear fuel cycle. These streams are mostly termed as radioactive liquid waste due to presence of radionuclide. These radioactive waste are loosely categorized into three classes, namely: high-level (HLLW), intermediate level (ILLW) and low-level (LLLW), based on the radioactivity levels. HLLW has been generally accepted as the liquid effluent from the first cycle of fuel reprocessing (PUREX, Plutonium Uranium Recovery by EXtraction) operation. The effluent contains over 99.9% of the non-gaseous fission products, unrecovered plutonium and the higher actinides (Np, Pu, Am, Cm). Thorium-based fuel cycle does not produce Pu and minor actinides, An like Np, Am and Cm but is associated with other radionuclide such as ^{231}Pa, ^{229}Th and ^{230}U [3]. The ILLW and LLLW vary considerably with respect to transuranic and fission product content. ILLW can arise from many sources, such as: spills, off-gas scrubber solutions, cask and plant decontamination solutions, plant solvent washes, chemical decladding solutions, raffinate from U-Pu purification cycles and some laboratory wastes etc. Examples of LLLW are evaporator and concentrator condensates, laundry wastes and possible radionuclide leakage into cooling water or process steam [4].

Apart from radioactive waste, nuclear and several non-nuclear industry also release mercury in waste water [5, 6]. Among various treatment processes, adsorption using sorbents has emerged as one of the most popular methods since proper design of the adsorbents and adsorption process will produce high-quality treated effluents. Adsorption is believed to be simple, efficient, effective and economical techniques in the treatment of waste water of different origin due to availability of several classes of adsorbent materials. Activated carbon, zeolites, clay, polymeric materials, silica, metal oxides and biomaterials are frequently used for the removal of metal ions in waste water treatment [7]. The surface area of adsorbents play an important role for the extent of adsorption and key separation parameters as it is directly related to its porosity which enables large internal surface constituted by pore walls. Engineered activated carbons and oxidic adsorbents have been extensively utilized for removal of contaminants from aqueous medium [8]. The hydroxyl groups of oxidic adsorbent, carboxyl, carboxylic anhydrides, lactone/lactol groups and phenolic hydroxyl of activated carbon are responsible for strong adsorption.

With advent of nanotechnology, the research and development on engineered nanomaterials for waste water treatment are in full surge [9]. Nanomaterials intrinsically possesses highly porous and large surface area due to their small shape and size, thus potentially has adsorbent properties. Among various nanoadsorbents, carbon nanotubes (CNTs) are extensively studied due to their unique properties. CNTs, which were first discovered by Ijiima in 1991 [10], are seamless cylindrical structure of hexagonal honeycomb lattice of sp^2 hybridized carbon atoms. Depending on the numbers of concentric tubes, CNTs take form as single-walled (SWCNT), double-walled (DWCNT) and multi-walled (MWCNT). A wide spectrum of metal ions and organic compounds has been studied as the target pollutants on CNTs. Highly porous and hollow structures, large surface area, low density, high mechanical, thermal and chemical stabilities are the properties which makes them better adsorbent. The high stabilities of CNT structures would be very useful solid support for treatment of radioactive liquid waste stream where separation has been carried out in radiation and chemically stringent environment. The main driving forces for uptake of metal ions and organics by CNT are π–π, cation-π and electrostatic interaction [11]. Thus pristine CNTs (p-CNT) can adsorp metal ions, however, removal efficiency and selectivity for separation of metal ions and radionuclide are rather low. The surface chemistry of CNTs is an important factor affecting the adsorption characteristics. Upon oxidation, various oxygenous functional groups like carboxylic acid (-COOH) and phenolic hydroxyl (-OH) can be covalently linked with sp^2 carbon of CNT, which are utilized for functionalization on the surface following solid phase organic synthetic (SPOS) methodologies. Different metal ions have preferential/selective complexation towards a specific ligands arising from the nature of cations and type of binding sites (O, N, S) in the ligands. Owing to this, several functional group/ligand functionalized CNTs have been studied for the adsorption of metal ions from aqueous solution [12].

Development of new adsorbents by experiments alone is a very time consuming and costly affairs. Computational chemistry is used to screen a molecular system prior to synthesis in the laboratory. Density Functional Theory (DFT) is a computational method that derives properties of the molecule by exploiting electron density. Binding of metals ions with ligands and ligand functionalized CNTs can also be modeled using DFT. The studies on complexation of various metals ions with different types of functional groups/ligands have been established to understand the binding selectivity [13, 14]. DFT calculation on the complexation of metal ions with functionalized CNTs to design and screen a novel nanoadsorbents and then experimental verification of the calculated results and vice versa is rarely practiced.

Separation of zinc isotopes is important in nuclear science mainly due to the use of ^{64}Zn-depleted Zn in the primary coolant of nuclear power plant to reduce the formation of radioactive cobalt ^{60}Co, which is a radiation hazard [15]. Different crown ethers are evaluated to be useful for Zn isotope separation which on functionalization with polymeric resin showed higher isotope separation factor in multistage operation than solvent extraction [16, 17]. DFT calculation can be used to screen a particular crown ether for desired isotope separation and to design suitable crown ether functionalized resin, which can be validated by solid-liquid separation experiments.

The objective of this thesis is to design suitable ligand functionalized CNTs and polymeric solid support for metal ion (Th, U, Np, Pu, Am, Cm, and Hg) and isotope (Zn) separation after selecting proper ligand and solid support from literature using DFT calculations, preparation of the adsorbents and experimental adsorption studies. Preparation of a particular ligand functionalized solid support, its experimental adsorption studies and then DFT calculations on the system to corroborate the observed data have also been followed. Finally, the fixed-bed column separation experiments have been performed to check its applicability for scaling up. The thesis consists of seven chapters elaborating the work done on the above theme.

Chapter 1: Introduction

The first chapter deals with the fundamental knowledge on nuclear fuel cycle and waste containing radionuclide. The origin of Hg containing waste water and its treatment are discussed. The importance of separation of radionuclide and Hg and the role of adsorption processes are emphasized. The need of Zn isotope separation is briefed. Requirement of functionalized solid support like, CNTs for adsorptive separation of radionuclide and Hg, and polymeric resin for Zn isotope separation are addressed. Process of functionalization of CNTs and polymeric resins are described. Brief discourse on DFT method used for modeling molecular system are given. Finally, the scope of present work is presented along with the overview of relevant literatures.

Chapter 2: Experimental and Theoretical Methodologies

This chapter describes the materials, equipments and instruments used in the experimental studies. The synthesis route of functionalized CNTs and polymethacylate (PMA) resins are depicted. The characterizations of prepared materials and experimental procedure for batch adsorption studies are also discussed. The theory for kinetic, isotherm and thermodynamic modeling of experimental data and governing equations are discussed. The fundamental of fixed-bed column separation along with analysis of breakthrough and desorption curve are described. The computational methodology for the structure, binding and interaction energies are presented. The theoretical calculation of complexation energies between metal ion-functionalized CNTs and isotope separation factors in zinc-crown ether functionalized solid support are discussed.

Chapter 3: Carboxylic and diglycolamic Acid functionalized Carbon Nanotubes

In this chapter, -COOH and diglycolamic acid (DGA) functionalized CNTs are evaluated for the adsorption of Th(IV) ions. The B3LYP functional and TZVP basis set in conjunction with COnductor like Screening MOdel (COSMO) solvation approach have been used to predict the free energy of adsorption for Th^{4+} ions with p-CNT, oxidized (CNT–COOH) and DGA functionalized CNTs (CNT–DGA). Experimentally observed values of adsorption capacities of Th^{4+} by CNTs indicate that CNT–COOH has the strongest binding with Th^{4+}, whereas p-CNT has the lowest; CNT–DGA shows less adsorption than CNT–COOH [18].

DFT calculations are carried out on the structure, bonding, energetic and thermodynamics for the complexation/extraction of Eu^{3+}/Am^{3+} ions with CNT–DGA. The free energy of extraction (ΔG_{ext}) for Eu^{3+} was found to be higher than that of Am^{3+} ion using the Born–Haber thermodynamic cycle in conjunction with COSMO. Further, MWCNT-DGA was prepared and distribution constant for metal ions determined by adsorption revealed that Eu^{3+} is preferentially extracted over Am^{3+} ion and same selectivity trend was reported in liquid-liquid extraction [19].

MWCNT-DGA are also demonstrated to be a highly efficient for Am^{3+}, Pu^{4+} and PuO_2^{2+} ions with following trend of distribution coefficient, K_d : $Am^{3+} > Pu^{4+} > PuO_2^{2+}$. The sorption energy calculated from the Dubinin–Radhuskevich isotherm revealed that interaction between MWCNT-DGA and An is chemisorption. Suitable stripping agents were identified for the back-extraction of the actinides. The sorbent was also found to have good radiolytic stability. DFT revealed a tridentate coordination mode of the DGA moiety towards Pu^{4+}/Am^{3+} and a bidentate coordination towards PuO_2^{2+}. The binding energy of sorption with DGA-CNT of Pu^{4+} was higher than that of PuO_2^{2+}, whereas for Am^{3+} it was higher than for PuO_2^{2+} but less than for Pu^{4+} [20].

Chapter 4: Amidoamine and Ploy(amidoamine) functionalized Carbon Nanotubes

Amidoamine functionalized MWCNTs (CNT-AA) are evaluated for the sorption of U(VI), Am(III) & Eu(III) from aqueous medium. Both UO_2^{2+} and Eu^{3+} followed Langmuir sorption model with maximum sorption capacity of 20.66 and 16.10 mg g^{-1} respectively. This has been explained by DFT calculations which show that more negative free energy of U(VI) compared to Am(III)/Eu(III) and stronger U-MWCNT-AA complex is responsible for higher sorption capacity of U(VI) compared to Am(III)/Eu(III) [21].

CNT-AA are used for efficient and selective solid phase separation of Pu(IV) and Pu(VI). The sorption proceeded through monolayer coverage of MWCNT-AA with capacities of 91.2 mg g^{-1} and 89.4 mg g^{-1} for Pu^{4+} and PuO_2^{2+}, respectively following a Langmuir isotherm. The DFT study reveals that the metal ion is deca-coordinated in the case of Pu^{4+} and octacoordinated in PuO_2^{2+}. The calculated ΔG_{ext} was found to be almost three times higher for Pu^{4+} than PuO_2^{2+}, which thus confirms the experimentally observed higher sorption of Pu^{4+} compared to PuO_2^{2+} [22]. Similarly, DFT calculation and experimental studies on the sorption of NpO^{2+} and NpO_2^{2+} by CNT-AA revealed the same result that hexavalent Np is more selective than pentavalent [23].

Batch adsorption and fixed-bed column separation of Hg(II) ions from aqueous medium by CNT-AA are investigated. The adsorbent showed superior selectivity with high adsorption capacity towards mercury as compared to other metal ions. DFT calculations establish the bi-dentate mode of complexation and correlate the experimental selectivity [24].

In addition, the 1st and 2nd generation of poly(amidoamine) functionalized MWCNTs (CNT-PAMAM) were evaluated for the adsorption of Pu(IV) [25], Am(III) [26], and Np(V) [27] separately. The 2nd generation CNT-PAMAM showed superior adsorption than the 1st generation one. The sorption equilibrium, mechanism, kinetics, radiolytic stability, and back-extraction studies are performed. The unique binding pattern of CNT-PAMAM was elucidated by DFT.

Chapter 5: Sulphur Ligand Functionalized Carbon Nanotubes

This chapter deals with the adsorption of Hg(II) by newly prepared thiol(SH) and dithiocarbamate (DTC) functionalized MWCNT, owing to the strong interaction of mercury with sulphur. The maximum adsorption capacity of CNT-DTC was found to be 3.5 times higher than that of CNT-SH at the optimum pH of 6. The kinetics and equilibrium data revealed that the adsorption of Hg^{2+} follow pseudo-second order and Langmuir isotherm model, respectively. DFT calculations show CNT-DTC displays greater adsorption than CNT-SH as observed in the experiments. Feasibility of continuous separation of Hg^{2+} is successfully tested by demonstrating a small scale fixed bed column filled with CNT-DTC.

Chapter 6: Crown Ether Functionalized Resin

In this chapter, DFT results for the isotopic fraction of zinc in the nano cavity of crown ethers and crown ethers anchored on polymeric resin are discussed. The isotope separation factor of various isotope pairs are calculated from reduced partition function ratio. Benzo-18-crown-6 (B18C6) and benzo-15-crown-5 (B15C5) showed higher isotope separation factor for zinc [28]. Further, DB18C6 and B15C5 functionalized PMA resins were prepared and evaluated for Zinc adsorption and isotope separation. Separation of Zn in a fixed-bed column using PMA-DB18C6 is carried out with various column parameters. Breakthrough and elution curves are analyzed with available model and scaling up of the column separation is assessed.

Chapter 7: Summary and Future Scope

The summary and discussions on the future scope of the work reported in the thesis are presented in this chapter. It summarizes the important results obtained on: i) Synthesis and characterization of functionalized CNTs, ii) Theoretical and experimental results on the separation of radionuclide from aqueous medium using prepared functionalized CNTs, iii) Studies on the mercury ion removal using nitrogen and sulphur ligand functionalized CNTs, iv) DFT calculations on zinc isotope separation by crown ethers functionalized resins, and v) Static and dynamic studies for zinc adsorption and isotope separation using crown ether functionalized PMA resins. In future scope, the applicability of the functionalized CNTs for radioactive and waste streams treatment for the removal/pre-concentration emphasized. Discussion is also made on the large scale preparation of crown ether functionalized PMA resin and chromatographic zinc isotope separation with long column to obtain enriched/depleted isotopic zinc compounds.

References

1. S. Banerjee, H.P. Gupta, Progress in Nuclear Energy, **2017**, 101, 4-18.
2. Spent Fuel Reprocessing Options. IAEA TECDOC Series. **2008**, IAEA-TECDOC-1587, Vienna.
3. Thorium fuel cycle — Potentialbenefits and challenges, TECDOC Series. **2005**, IAEA-TECDOC-1450, Vienna.
4. W. L. Lennemann, Radioactive Waste Management, IAEA Bulletin, **1976**, 18(5/6), 40-47.
5. T. E. Widner,S. R. Ripple, J. E. Buddenbaum, Health Phys. **1996**, 71(4), 457-469.
6. Air quality guidelines for Europe, 2nd edition, World Health Organization, **2000**.
7. G. Crini, Prog. Polym. Sci. **2005**, 30, 38–70.
8. E. Worch, AdsorptionTechnology in WaterTreatmentFundamentals, Processes, and Modeling, Germany, De Gruyter, **2012**.
9. M.M. Khin, A.S. Nair,V.J. Babu, R. Murugana, S. Ramakrishna, Energy Environ. Sci., **2012**, 5, 8075.
10. Iijima, Nature, 1991, 354, 56-58.
11. S.W. Kim, T. Kim, Y. S. Kim, H. S. Choi, H. J. Lim,S. J. Yang, C. R. Park, Carbon **2012**, 50, 3-33.
12. Ihsanullah, A. Abbas, A. M. Al-Amer, T. Laoui, M. J. Al-Marri,M. S. Nasser, M. Khraisheh, M. A. Atieh, Sep. Purif. Technol. **2016**, 157, 141–161
13. L. Rulisek, Z. Havlas, J. Phys. Chem. A**2002**,106,3855-3866.
14. Z. Kolarik, Chem. Rev.**2008**,108,4208–4252.
15. H. Hosokawa, M. Nagase, J. Nucl. Sc.Technol. **2004**, 41, 682−689.

16. K.Nishizawa, K. Nakamura, T. Yamamoto, T. Masuda, Solv.Extr. Ion Exch. **1993**, 11, 389−394.
17. X. Ding, M. Nomura, T. Suzuki, Y. Sugiyama,T. Kaneshiki, Y. Fujii, J. Chromatogr. A, **2006**, 1113, 182–185.
18. A.K. Singha Deb, Sk. M. Ali, K.T. Shenoy, RSC Adv. **2015**, 5, 80076–80088.
19. A. K. Singha Deb, Sk. M. Ali, K.T. Shenoy, S.K. Ghosh, Molecular Simulation, **2015**, 4, 490-503.
20. A. Sengupta, A.K. Singha Deb, K. Dasgupta, V. C. Adya, S.M. Ali, New J. Chem., **2017**, 41, 4531-4545.
21. A.K. Singh Deb, S. Pahanb, K. Dasgupta, S. Panja, A.K. Debnath, P.S. Dhami, Sk. M. Ali, C.P. Kaushik, J.S. Yadav, , J. Hazard. Mater. **2018**, 345, 63–75.
22. P. Kumar, A. Sengupta, A.K. Singha Deb, K. Dasgupta, Sk. M. Ali, RSC Adv., **2016**, 6, 107011-107020.
23. A. Sengupta, A.K. Singha Deb, P. Kumar, K. Dasgupta, Sk. M. Ali, J. Environ. Chem. Eng. **2017**, 5(3), 3058-3064.
24. A.K. Singha Deb, V. Dwivedi, K. Dasgupta, Sk .M. Ali, K.T. Shenoy, Chem. Eng. J. **2017**, 313, 899–911.
25. P. Kumar, A. Sengupta, A.K. Singha Deb, K. Dasgupta, Sk. M. Ali, Radiochim. Acta **2017,** 105(9): 677–688.
26. P. Kumar, A. Sengupta, A.K. Singha Deb, and Sk. M. Ali, Chemistry Select **2017**, 2, 975 –985.
27. A. Sengupta, A.K. Singha Deb, N.K. Gupta, P. Kumar, K. Dasgupta, Sk. M. Ali, J. Radioanal. Nucl. Chem. **2018**, 315, 331-340.
28. A. K. Singha Deb, Sk. M. Ali, K. T. Shenoy, and S. K. Ghosh, J. Chem. Eng. Data, **2014**, 59, 2472–2484.

LIST OF FIGURES

LIST OF TABLES

1 Introduction

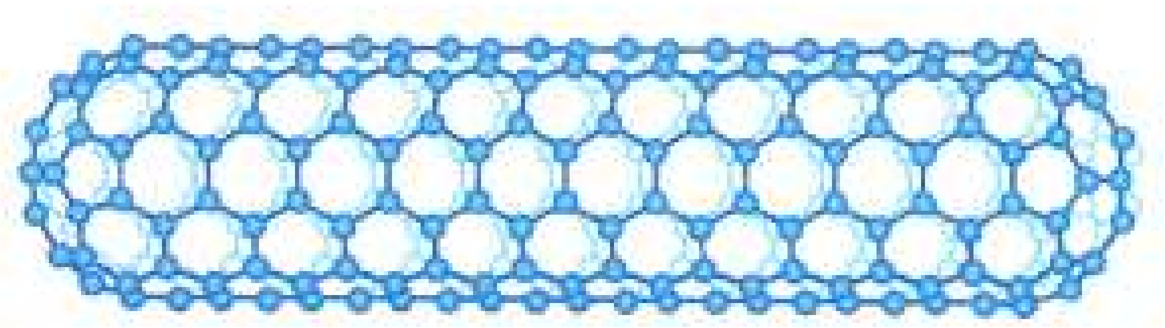

1.1 Indian Nuclear Energy Program

India has opted for a unique three stage nuclear power program suiting its small uranium and large thorium reserves in the country[1]. The first stage utilizes the limited natural uranium resources for power generation in Pressurized Heavy Water Reactors (PHWRs) as well as for conversion of uranium to plutonium. Second stage employ the plutonium and depleted uranium produced in the first cycle as fuel to harness power and to enhance the fissile inventory necessary by converting fertile ^{232}Th to fissile ^{233}U in the blanket of the reactor for launching the third stage thorium based power reactors, where natural Th and ^{233}U will act as fuel[2]. A schematic of the programme is shown in **Figure 1.1**. The first stage composed of 18 PHWRs in operation and many under construction and planning stages. Besides, two Boiling Water Reactors (BWRs) and two Water-Water Energetic Reactor (WWER or VVER) reactors are operational for power generation. Thus first stage has reached a state of commercial maturity. The second stage is well underway with a Fast Breeder Test Reactor (FBTR) operational since 1985 and a 500MWe Prototype Fast Breeder Reactor (PFBR) in final stages of construction. An Advanced Heavy Water Reactor (AHWR) based on thorium fuel is being developed to provide impetus for development of thorium based technologies for the 3rd stage and to demonstrate industrial-scale use of thorium [3].

1.2 Nuclear Fuel Cycle

The nuclear fuel cycle starts with uranium exploration and ends with disposal of materials used and generated during the whole cycle. It may be broadly defined as the set of processes and operations needed to manufacture nuclear fuel, its irradiation in nuclear power reactors and storage, reprocessing, recycling or disposal. There are two fuel cycle options: 'open' (or once-through) fuel cycle (without reuse of nuclear materials) and 'closed' fuel cycle (with reuse of nuclear materials extracted from irradiated fuel [4]. Both the options require robust and safe waste management technologies. India has opined for 'closed' option due to its limited uranium resources. In a closed nuclear fuel cycle the unburnt and bred fuel are recycled, recovered and reused as fuel in reactor. Closed fuel cycle pursued in India by the pioneers envisaging sustainable source of power through nuclear energy.

1.3 Spent Fuel, Reprocessing and Radioactive waste

The fuel discharged from a nuclear reactor after its utilization, called spent fuel, contains unburnt uranium, fissile plutonium, fission products, activation products and transuranic actinides. A standard PWR spent fuel contains ~45% of the Periodic Table elements as shown in **Figure 1.2**[2].

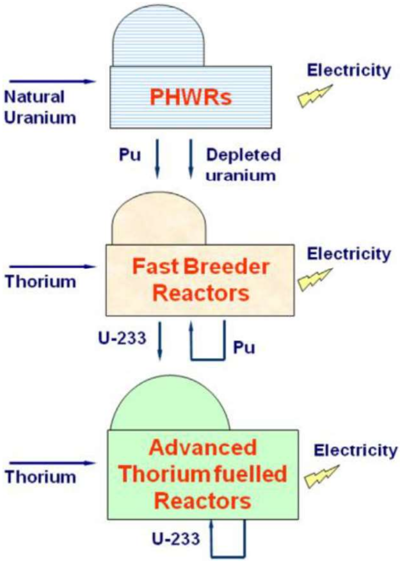

Figure 1.1 Schematic of the three stage Indian Nuclear Energy Programme [3]

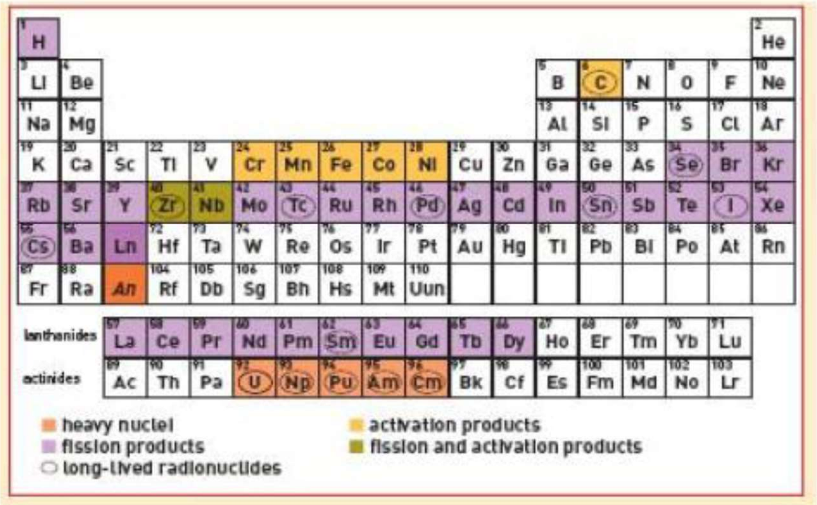

Figure 1.2 The typical elements contained in a standard PWR spent nuclear fuel [2]

Reprocessing is the process of separating uranium and plutonium from the fission products, activation products and transuranic actinides in the spent fuel. PUREX (Plutonium Uranium Redox Extraction) process is being used worldwide in the reprocessing of spent fuel employing tributyl phosphate (TBP) extractant in hydrocarbon. After decladding, the spent fuel is dissolved in nitric acid medium. U and Pu then separated together from the rest of the spent fuel solution by solvent extraction process using TBP extractant. In the proceeding steps, U and Pu are separated from each other by redox reaction and converted to respective oxides after purification by ion-exchange resin[5]. In the THOREX (thorium uranium extraction) process, the same TBP extractant are used to separate U and Th from the irradiated thorium fuel from the fission products and other transthorium actinides followed by uranium and thorium product into their respective oxides[6]. The raffinate of the PUREX and THOREX process contain intensely radioactive fission products, activation products, minor actinides, and small amounts of other actinides. The short and medium lived fission products and long lived transuranic actinides are the cause of radiotoxicity as well as high decay heat power of the raffinate[7], and known as radioactive waste. The radiotoxicity of the spent fuel requires several thousand years to reduce its toxicity to natural level (**Figure 1.3**)[8]. Spent Fuel reprocessing and partitioning & transmutation (P&T) are the two important strategies to remove the radionuclide from the total waste and reduce the time required for the waste to reach an acceptable activity level[9].

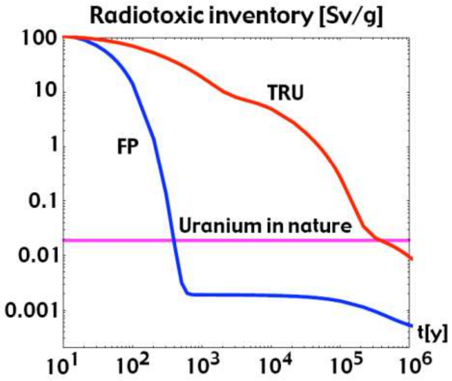

Figure 1.3 Radiotoxicity decay of fission products (FP) and transuranic actinides with time [8]

Radioactive waste stream are also generated in the other steps of nuclear fuel cycle. Before reprocessing, the main steps of the cycle are uranium mining and milling, conversion of uranium oxide to uranium hexafluoride and back, enrichment, fuel fabrication, reactor operation, and spent fuel storage[10]. The effluent of each of these steps is normally contaminated with radionuclides. In mining and milling, this waste is created from the production of uranium. It contains low concentrations of uranium and its daughter products, e.g. thorium, radium and radon. In refining, enrichment and fuel fabrication step, waste may result from trapping materials from off-gas systems, lightly contaminated trash, and residues from recycle or recovery operations. It generally contains uranium and, in the case of mixed oxide fuel, also plutonium. The origin of waste from reactor operations/power generation resulted from treatment of cooling water and storage ponds, equipment decontamination, and routine facility maintenance. Reactor waste is mainly contaminated with fission products and activation products. Radioactive waste generated from routine operations of reactors includes contaminated clothing, floor sweepings, paper and concrete[11]. Radioactive waste streams are also generated from research, and medical and industrial use of radioisotopes. The research activities include research involving reactors and fuel cycle facilities, radioisotope production and application, and the use of radioisotopes as tracers or for the irradiation of materials. Research, trade, industry, medicine and agriculture extensively use sealed radioactive sources. Radioactive sources are applied in several industries including the calibration of measuring devices, materials testing, irradiation/ sterilization of products, and level and density measurements. In medicine, radioisotopes are mostly used for diagnosis, and therapy of diseases and irradiation of blood. Military and defense programmes involving nuclear material are also responsible for production of radioactive waste effluents[12]. Depending on the amount of radionuclide present, radioactive liquid waste streams are commonly classified as exempt waste, low-level waste, LLW (Radioactivity content: 37–3.7×10^6 Becquerel per Litre, Bq/L), intermediate-level waste, ILW (3.7×10^6–3.7×10^{11} Bq/L) and high-level waste, HLLW (above3.7×10^{11} Bq/L)[13].

1.4 Water/Waste Water Containing Heavy metal, Mercury

Like nuclear industry, other industries also discharge effluent containing various non-radioactive toxic substances. Heavy metals such as cadmium, mercury, lead and arsenic, are the most hazardous among the toxic materials and rank among the priority metals that are of public health significance[14]. Industrial use of the heavy metals has enhances the contamination chances in the waste water effluent. In this regard, mercury has an extensive application in various industrial processes which leads to the mercury contamination in the effluent. All these processes involve emissions/release of mercury in atmosphere, soil and aquatic environment. Aquatic contamination of mercury will only be addressed here.

Industrial production of chlorine and alkalis, such as sodium hydroxide was started with chlor-alkali process, where liquid mercury cathode electrolysis of saline solutions of alkali metals, e.g. NaCl produces alkali metal amalgams which on hydrolysis decomposed to alkali metal hydroxides and anode electrolysis converts chloride to chlorine gas[15]. Industrial production of chlorine increased from 2.0 metric tons in 1950 to over 15 metric tons in 2010. Out of that quantity, over 7 metric tons of chlorine were produced via mercury cathode electrolysis of sodium chloride[16]. Although mercury circuits and electrolysis cells are sealed and encapsulated, mercury emissions still observed to air and waste water. The main sources of mercury contamination in the waste water from a chlor-alkali plant are presented in **Table 1.1**[17]. A study based in India suggests that about 0.23 kg of mercury is lost per tonne of caustic soda produced in Chlor-alkali process[18]. While many countries have stopped using the mercury cell process because of environmental and health hazards, mercury use in chlor-alkali industry is still very prevalent in India. The Government of India has banned the commissioning of new mercury cell based chlor-alkali plants since 1991 and mandatory rule has been made for new chlor-alkali plants based on modern membrane cell technology only[19].

Table 1.1 Emission sources of mercury in waste water of a chlor-alkali plant [17]

Sources of mercury release	Mercury emission factors g/tonne of annual chlorine capacity		
	Min	**Max**	**Median**
the process waste water: brine purge, (back)washing water from brine purification, condensate and wash liquor from treatment of chlorine and hydrogen, condensate from caustic concentration units, brine leakage, ion-exchange eluate from process water treatment the wash water from the cell cleaning operations: inlet and outlet boxes the rinsing water from the electrolysis hall: cleaning of the floors, tanks, pipes and dismantled apparatus the rinsing water from maintenance areas outside the electrolysis hall, if they are cleaned with water with run-off water	>DL	1.65	0.02

A similar electrolytic process like chlor-alkali, is used in the lithium enrichment plants in many countries. A lithium-mercury amalgam is prepared by electrolysis of natural lithium solution using liquid mercury cathode. Upon agitation, the rare ^{6}Li isotope concentrate in the amalgam phase and the more common ^{7}Li isotope migrate to the lithium solution. Cascading of the flow of amalgam and lithium solution leads to desired enrichment of ^{6}Li[20]. Like in chlor-alkali industry, mercury cell process for the lithium enrichment also discharges mercury to land, water and air.

Many medical and industrial instruments for measurement and control operation use mercury. All types of thermometers such as clinical, laboratory and meteorological ones, as well as blood pressure monitors (sphygmomanometers) and barometers are the best examples. It will take time to replace mercury in this industry. Apart from thermometers, mercury is also widely used in the health sectors, e.g., dentistry, pathology. On an average India manufacture 10 to 12 million clinical and laboratory thermometers as well as blood pressure monitors (sphygmomanometers) in a year, consuming about 15 tonnes of mercury annually. Breakage and disposal of these instrument leads to release of mercury in the environment[21].

Mercury has been used globally in electrical apparatus manufacturing industry especially in the production of electrical switches, lamps (fluorescent lamps, mercury vapour lamps), and batteries. Recovery of mercury from the broken appliances and the direct disposal of these apparatus can release mercury in the environment.

Many organo-mercury compounds, e.g, ethyl mercury phosphate, phenyl methyl acetate, are being used in fungicide industry. Although India and most of the countries have banned the use of these fungicides because they get accumulated into the plants through treated seeds, huge stockpile of the organo-mercury fungicide are available and some of the compounds are also in use[22]. Apart from accumulation in plants, mercury directly enters into the aquatic environment and in the food chain of human and animals.

Sources of aerial emission of mercury are also very common in modern times. Mercury is released in the atmosphere from the burning fossil fuels such as coal oil refining, cement production, mining, smelting, and production of iron and non-ferrous metals. These industrial processes do not use mercury, but large amount of mercury gets released in the air and is further accumulated, as mercury remains persistent in the environment. About

59.29 tonnes per annum mercury immobilized from coal-fired thermal power plants alone[23].

Natural sources of mercury emission and release are well known which include volcanic eruptions, geothermal activities, and weathering of rock containing mercury. Overall, total global Hg emissions to the atmosphere range from 6500 to 8200 tonnes/yr, of which 4600 to 5300 tonnes/yr are from natural processes and sources[24].

Movement of the emission of elemental mercury, Hg(0) in air as well as release of inorganic/organic mercury, Hg(II) in water/waste water and land from natural an anthropogenic means, can be clearly understood from the estimates of the fluxes and pools of mercury at the earth's surface as shown in **Figure 1.4**[25].

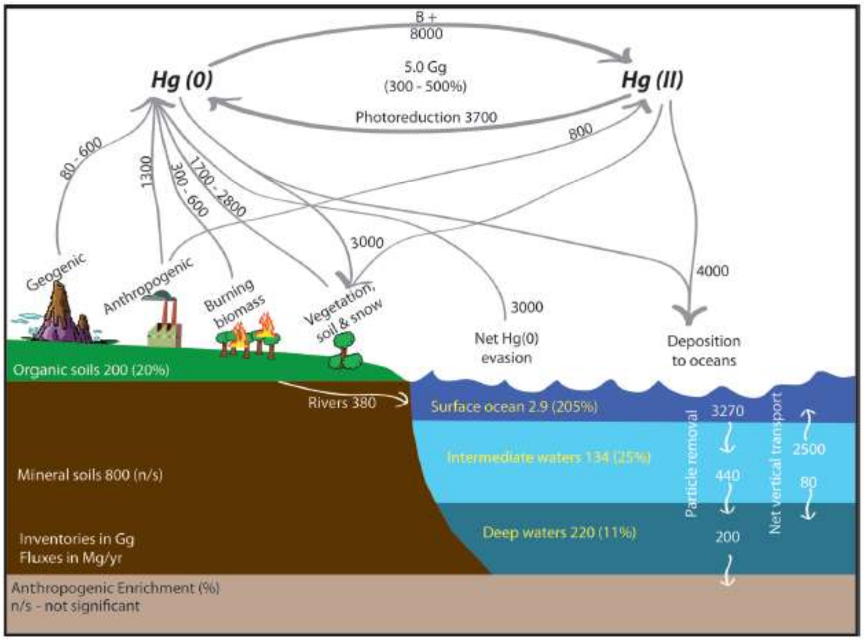

Figure 1.4 Current estimates of the fluxes and pools of mercury at the earth's surface, (Mg = Megagram (Tonne)) [25]

1.5 Need of waste water Treatment

The long term hazard of radioactive waste is associated with actinides, (U, Pu, Np, Pu, Am and Cm), while the short and long term risks are due to the mobility of fission products in the geosphere and the possibility of their entering the biosphere. Radiotoxicity of these radionuclides refers to the adverse biological effects on humans from radioactive material in radioactive waste stream. Three different kinds of rays, known as alpha, beta and gamma rays are associated with radiotoxicity. The alpha rays are particles (nuclei of helium atoms) carrying a positive charge, beta rays particles have negative charge (streams of electrons) and gamma rays are charge less electromagnetic radiation with shorter wavelengths than any X-rays. These 'rays' can penetrate living tissues for short distances and affect the tissue cells[26]. Hence, the treatment for radioactive waste either through direct surveillance disposal, reprocessing or partitioning and transmutation (P&T) are being pursued worldwide. Reprocessing removes and reuse the fissile U and Pu content, whereas P&T programme envisages the removal of the transuranic actinides and fission products from the radioactive waste and their transmutation into stable or shorter lived isotopes through nuclear reaction. Radiotoxicity of the radioactive waste can be reduced to the natural radioactivity level from 250000 years to 250 years with suitable P&T strategy (**Figure 1.5**)[9].

Due to their extreme solubility in the aquatic environments, heavy metals [27] can be absorbed in living organisms. Thus they enter the food chain and large concentrations of mercury may accumulate in the human and animal body. The flow of mercury from waste sources though bioaccumulation to human and animal body is evident from the **Figure**

1.6 [19]. Once the metal is ingested beyond the permitted concentration, they can cause serious health disorders. The mercury vapour can develop harmful effects on the nervous, digestive and immune systems, lungs and kidneys causing fatal consequences upon inhalation. The mercury salts are corrosive to the skin, eyes gastrointestinal tract, and kidney if ingested[28]. Humans may be exposed directly by eating contaminated fish. Transplacental exposure may dangerously affect the fetal brain causing neurological disorder. Neurological symptoms include mental retardation, seizures, vision and hearing loss, delayed development, language disorders and memory loss[29]. Minamata disease is a neurological syndrome caused by severe mercury poisoning. The disease, first discovered in Japan in 1956, was caused by the release of organo-mercury in the industrial wastewater from the Chisso Corporation's chemical factory. Bioaccumulation of this

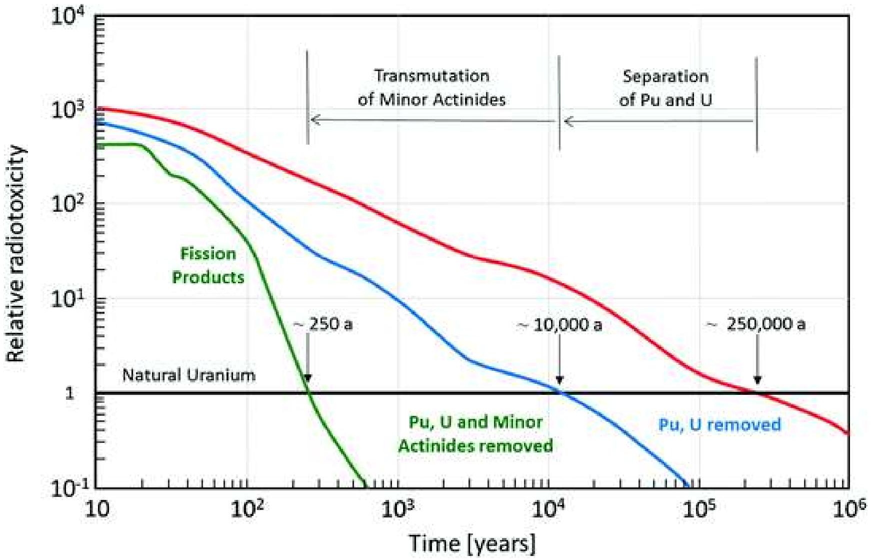

Figure 1.5 Radiotoxicity ingestion through P&T strategy [27]

highly toxic mercury compound in shellfish and fish in Minamata Bay and the Shiranui Sea, which when eaten by the local populace leads to mercury poisoning[30].

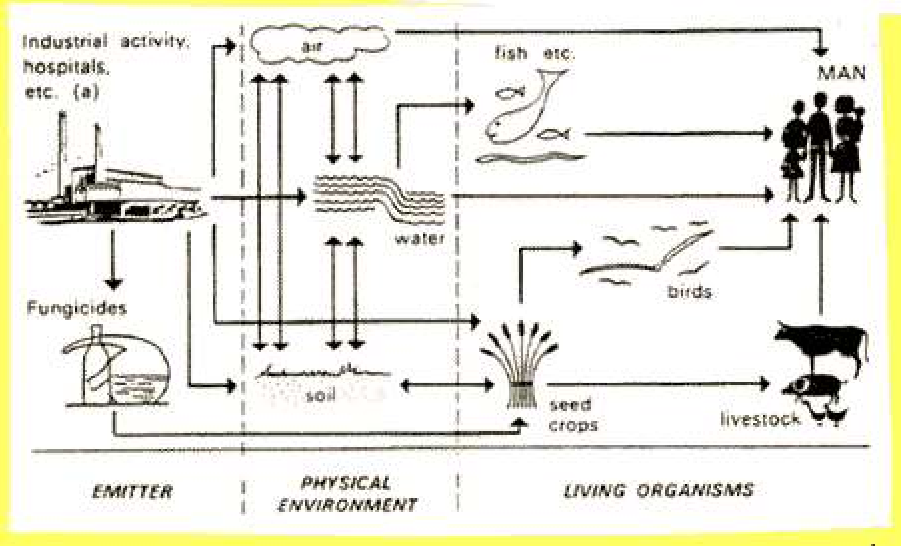

Figure 1.6 Flow of mercury within the biosphere [19]

1.6 Radioactive/Waste Water Treatment

The essential need to reduce the release of radioactive and other toxic substances into the environment requires constant improvement/upgrading of processes and technologies for treatment and conditioning of liquid waste streams. Several established processes, such as solvent extraction, filtration, precipitation, sorption, ion exchange, evaporation and membrane separation, are applied to meet the requirements for the discharge of treated effluents and the conditioning of the waste concentrates for disposal/storage. The Main features and limitation of these treatment processes are shown in **Table 1.2**. Developments of new and improved materials

Table 1.2 Features and limitation of different aqueous liquid treatment options [30].

Technology	Features	Limitations
Precipitations	• Suitable for large volumes and high salt content waste • Easy non-expensive operations	• Low decontamination factor (DF) • Efficiency depends on solid-liquid separation steps
Ion-exchange	• Good chemical, thermal and radiation stability • Large choice of products ensuring high selectivity	• Affected by high salt content • Blockage problem • Regeneration and recycling sometime difficult to employ
Evaporation	• DF > 104 – 106 • Well established technology • High volume reduction factor • Suitable for variety of radionuclides	• Process limitations (scaling, foaming, corrosion, volatility of certain radionuclides) • High operation & capital cost
Reverse Osmosis	• Removes dissolved salts • DF 102 – 103 • Economical • Established for large scale operation	• High pressure system, limited by osmotic pressure • Non-back washable, subject to fouling
Ultrafiltration	• Separation of dissolved salts from particulate and colloid solution • Good chemical and radiation stability for inorganic membranes	• Fouling • Organic membranes subject to radiation damage
Microfiltration	• High recovery (99%) • Low fouling when air back-wash	• Sensitive to impurities in waste stream
Solvent Extraction	• Selectivity enabled removals, recovery or recycle of actinides	• Generate aqueous and organic secondary waste

are under consideration worldwide. Combination of the processes and their serial and parallel application are being attempted to reach the final objective of improved decontamination, waste volume reduction, minimum/zero generation of secondary waste, simple and easy conditioning and disposal of waste, safety, and overall cost effectiveness in the treatment[31].

Use of adsorbents with other treatment methods, such as solvent extraction, precipitation or membrane separation, is a logical development of radioactive liquid waste treatment. Adsorption coupled with membrane filtration can provide efficient removal of both dissolved and suspended contaminants even in a colloidal form[31]. Due to the low cost and simple operation compared to the complex operation and maintenance coupled with high cost of the processes such as reverse osmosis and ultrafiltration, precipitation, and solvent extraction, adsorption processes are considered as one of the best potential strategy for removal of radionuclide and metals from aqueous solutions[32, 33].

1.7 Adsorption Processes for waste water treatment

Adsorption processes are widely used in radioactive as well as non-radioactive waste water treatment for the removal of radionuclide[31, 32], and heavy metals[33]. Generally, this waste effluent contains solute in low concentrations and the uses of solvent extraction or solvent-based membrane processes lose their advantage, since the loss of solvent in the aqueous phase through solubility or entrainment is greater than the amount of solute recovered. **Figure 1.7** illustrates the applicability of different separation technologies in appropriate concentration ranges[34].

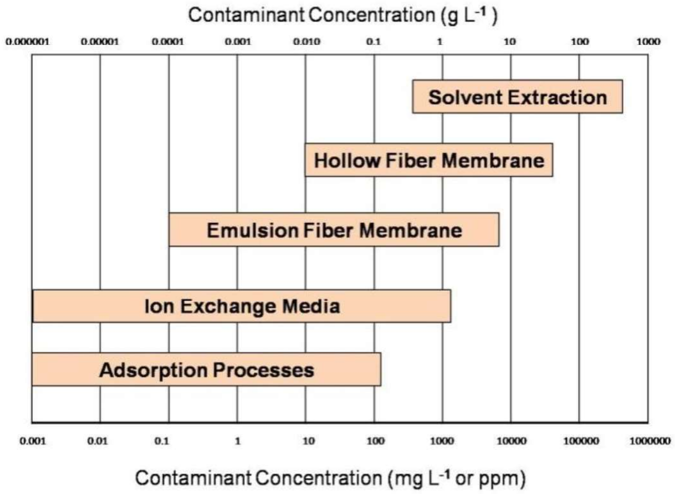

Figure 1.7 Solute concentration rangesfor separation technologies (Developed from Ref. 34)

Adsorption treatment method has several advantages: i) easy use, ii) flexibility, iii) versatile design, iv) low-energy requirements, and v) cost-effectiveness. Overall, the applicability of adsorption processes depends on several factors: i) adsorbent type, ii) fluid properties iii) pollutants to be removed, iv) operating conditions, v) process conFigureuration, vi) regeneration, and vii) waste disposal.

Two types of adsorption systems can be employed for the treatment process: batch and continuous. Batch systems are used to determine adsorption parameters such as capacities, rates, optimum acidity or pH, desorption, effect of presence of other materials, and thermodynamic parameters including the analysis of the adsorbate(s)-adsorbent interactions. On the other hand, fixed-bed columns are suitable for treatment in large-scale applications where significant volumes of fluids can be treated in short period of time. Adsorption experiments in packed bed columns are required to estimate useful parameters for scale-up such as the breakthrough and saturation times, adsorbent bed adsorption capacity, and other mass transfer parameters. The adsorption conditions of dynamic column systems have lower residence time than the equilibrium time achieved in batch systems. Therefore, the removal effectiveness of continuous processes is lower than that obtained for batch processes[35].

Adsorption occurs whenever a solid surface is exposed to gas or liquid and is defined as the enrichment of a materials or increase in the concentration of the fluid in the vicinity of an interface. Under certain conditions, there is an appreciable enhancement in the concentration of a particular substance on the interface of a particular solid surface. The substance that concentrates on the surface of the solid support is termed as adsorbate and the solid support is called adsorbent. The overall extent of the adsorption processes is dependent mainly on: i) external and internal surface area, ii) porosity, iii) density, and iv) surface chemistry characteristics of the adsorbents. An efficient adsorbent should possess low density, high porosity and large surface area. Depending on the type of adsorbate and adsorbent, surface chemistry greatly influence the adsorbate/adsorbent interaction[36]. Depending on the interaction or affinity between the adsorbate –adsorbent, adsorption are classified into two categories: i) when the force of attraction are due to weak van der Waals type of interaction, it is called physical adsorption or physisorption, and ii) when the attraction comes from chemical force or due to the formation of chemical bond, it is called chemical adsorption or chemisorptions. Physical Adsorption occurs with formation of multilayer of adsorbate on the solid support with low enthalpy of adsorption (ΔH_{ads}), whereas formation of monolayer of adsorbate on adsorbent with high ΔH_{ads} is characteristic of chemical adsorption. The differences of the two type of adsorption are shown in **Figure 1.8**. Most important types of adsorbents frequently used for the removal of metal ions and organic substance from water/waste water are: i) activated carbon, ii) oxidic materials, iii) synthetic zeolites, iv) polymeric materials, and v) biological materials or natural and low-cost materials.

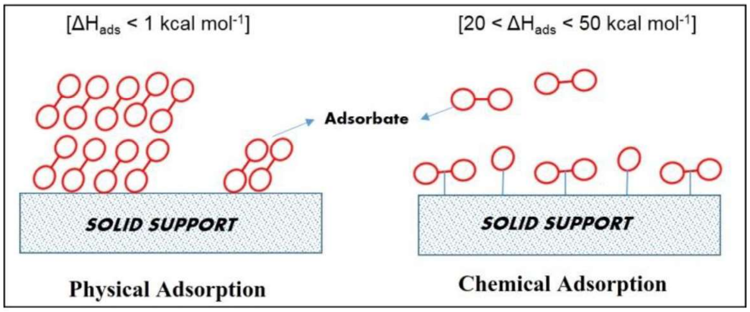

Figure 1.8 Two types of adsorption

Natural and low-cost adsorbents can be classified into three categories: i) natural materials (wood, coal, peat, chitin, chitosan, natural zeolite, clay), ii) agricultural waste/by-products (straw, sawdust, shells/hulls/stonesfrom fruits and nuts, corncob waste, sunflower stalks), and iii) industrial waste/by-products (fly ash, bagasse, bagasse pith, bagasse fly ash, palm oil ash, shale oil ash, red mud) [36].

1.8 Adsorbents for radionuclide (actinides) and heavy metal [27] separation

Removal of radionuclide and mercury from water/waste water has been practiced with different kinds of adsorbents. A brief discussion on the nature of the adsorbents and its performance are carried out.

1.8.1 Activated Carbon

Activated carbon (AC) is the universal adsorbent used from long time and still prevails as the main commercial product for water/waste water treatment. Activated carbons can be produced from different carbon-containing raw materials (wood, charcoal, coal, fruit shell etc.) and by different activation processes. AC possesses graphitic structure with oxygenous function groups like, carboxyl, phenolic hydroxide, carboxylic anhydrides, lactone and lactol groups with surface area ranging from some hundred m^2/g to more than thousand m^2/g. In nuclear technology, it is mainly used for the adsorption of radioactive gases such as radon, iodine[37]. Commercial AC[38-41] as well as AC prepared from various agricultural, industrial and forestry wastes, such as apricot shell[42], grinded used tire[43], rice straw [44], charcoal [45], oliver stone [46], and coconut shells [47], were used for U(VI) and Th(IV) adsorption from aqueous solution. Adsorption capacity of U(VI) showed to be higher than that of Th(IV). Uranyl cations and its cationic hydrolyzed species, UO_2^{2+}, $[(UO_2)_2(OH)_2]^{2+}$ dimer, $[(UO_2)_3(OH)_5]^+$ trimer, were reported to be exchanged with the proton of carboxyl functional groups on the surface of activated carbon. AC was used for >98% removal of Pu after pH adjustment at 8.3 from laboratory waste [48].

AC has also been used for Hg removal for years by the researchers. AC prepared from various carbon sources showed significant adsorption capacity for Hg(II) from aqueous medium[49]. On either impregnated with sulphur species (sulpherization) or modified with sulpfur-containing functional group, ACs exhibited higher Hg adsorption capacities. Besides the sulfur-containing functional groups, various other functional groups such as -NH_2, -$NHCOCH_3$,-Br, -Cl, -I, -C=N, -OH, have also been introduced onto the surface of ACs resulting improved Hg(II) adsorption compared to unmodified AC. More electron-donating halogen modified ACs showed better sorption[50].

1.8.2 Oxidic materials

All the oxidic adsorbents exhibit large number of surface hydroxyl (-OH) groups which participate in the adsorption process and also used for chemical modification of the e surface. The presence of polar basic surface on the surface makes them good adsorbents for ionic compound. The sorption of metal cation is associated with exchange of bound H ion on the oxide surface asdescribed by the following scheme.

$$M^{n+} + x[\equiv R - OH] = M[\equiv R - O]_x^{(n-x)+} + xH^+ \tag{1.1}$$

where M is the metal ion, x is the number of moles in oxidic group, and $[\equiv R - OH]$ and $[\equiv R - O]$ are the oxidic surface sites. As the protonation and deprotonation of the acidic –OH group play a crucial role in the binding of ions, adsorption by oxidic adsorbents are strongly dependent on pH of the aqueous medium. Iron and manganese oxides are capable of capturing alpha emitting radionuclide ofu, Pu, Am and Cm from ground water along with Rn and Ra radionuclide[51, 52]. Laboratory synthesized iron hydroxide, goethite (α-FeOOH) and oxides, hematite (α-Fe2O3) and magnetite (Fe3O4) are studied for the removal of Th^{4+}[53], UO_2^{2+}[54, 55], PuO^{2+}[56, 57] from aqueous solution showing a strong pH dependence sorption. Adsorption of alpha-emitters radionuclide U, Th, Pu, Am on manganese dioxide were studied for their determination and revealed that the method can be applied for U measurement whereas may not be reliable to estimate other Th, Pu and Am [58, 59]. Alumina showed 99.5% removal of Am and Pu from aqueous acidic solutions and results provide evidences for the synergic sorption mechanism of americium–ligand cationic complexes onto the alumina below pH 7, whereas anionic complexes of Am at higher pH are not sorbed[60-62]. Surface complexation of Hg(II) on iron oxides and silica was established from experimental and modeling studies[63]. Owing to the high affinity of the sulfur containing functional groups for Hg(II), the iron oxide and silica modified with dithiocarbamate, 2-mercaptobenzothiazole and phenylthiourea group, were developed as a new adsorbent for removal of Hg(II) with faster and efficient adsorption compared to bare oxides [64-69].

1.8.3 Zeolites

Zeolites[70] possess porous structure characterized by windows and caves of defined sizes for their particular tetrahedral pore framework leading to large surface area, strong capability of ions exchange and adsorption. A number of studies were carried out for adsorptive separation of radionuclide, mainly mono and divalent fission products [71-73], U[74, 75] and Th[76, 77], whereas very little literature is available for the study on adsorption of TRU actinides. The adsorptive behavior of Am by zeolites is evaluated using batch as well as fixed bed mode to investigate its migration in the repository conditions[78]. These inorganic materials possess high exchange capacity, possible selectivity and specificity, good resistant to radiation [79]. Different varieties of zeolites were used for Hg(II) removal, and β-zeolite has shown to posses higher adsorption capacity[80]. Composite of iron oxide and zeolite clusters showed adsorption selectivity toward Hg(II)[81]. The adsorption mechanism by zeolites mostly based on ion exchange reaction of metal ions with the exchanging cation in the micropores and adsorption of hydroxides on their surfaces.

1.8.4 Polymeric materials

Polymeric materials, also referred to as adsorbent resins, are porous solids with considerable surface areas and distinctive adsorption capacities and produced by copolymerization of styrene, or acrylic acid esters, with divinyl benzene as a cross-linking agent. The pore size and surface area can be tailored by controlling the degree of cross-linking. The solid matrix of the polymeric chain contains ion exchangeable cationic or anionic functional (ionogenic) groups with mobile ions, which may be exchanged with ions of the same charge dissolved in the surrounding liquid media. **Figure 1.9** shows the typical structure of cation and anion exchange styrene-divinyl benzene resin. Based on the type of the functional group, ion exchange adsorbent resins can be divided into four types: strong acidic, strong basic, weak acidic and weak basic. In **Table 1.3** different functional groups on the commercial resins and their negative logarithm of the dissociation constant (pK) are presented.

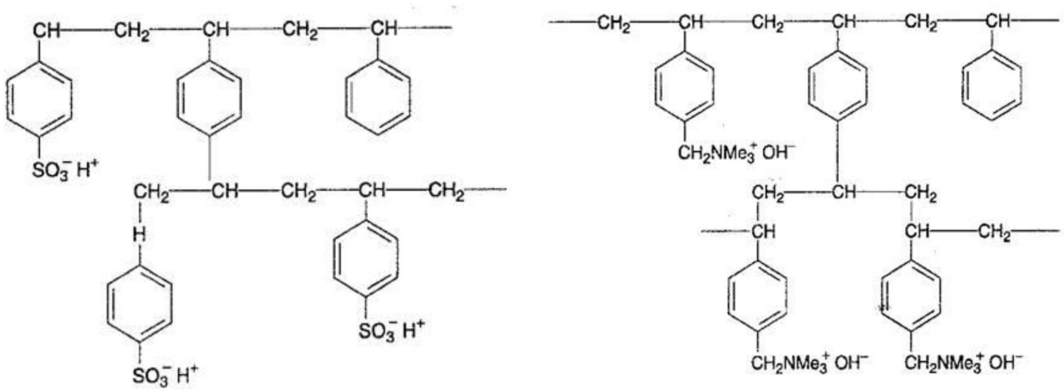

Figure 1.9 Structures of polymeric resins

Table 1.3 Most common functional groups of polymeric resin with pK values

Cation Exchangers		**Anion Exchangers**	
Functional Group	**pK**	**Functional Group**	**pK**
$-SO_3H$ (strong acidic)	1-2	ΞN (strong basic)	1-2
$-PO_3H_2$	2-5	=N	4-6
-COOH	4-6	=NH	6-8
-OH (weak acidic)	9-10	$-NH_2$ (weak basic)	8-10

The use of ion exchange resins in water/ wastewater treatments was well developed by the time this technique was first applied in the nuclear industry. Since then much progress has been made in improving the technology, and ion exchange methods have been widely used to remove soluble radionuclide from liquid waste[79]. Ion exchange resins were extensively applied for the separation and purification of radionuclide from nuclear process and waste solutions[82]. Both cation and anion exchange processes were employed for separation and purification of Pu from PUREX solutions. Pu(IV) is preferentially sorbed on anion resin as $Pu(NO_3)_6^{2-}$ in the presence of 7-8 M HNO_3 and eluted by dilute nitric acid[83]. Similarly, recovery and purification of U was also carried out by sorbing uranyl sulphato anionic complexes in anion exchange resin. Np(IV) has also been separated from U, Pu and other metal ions by adsorption on anion exchangers in 6 M nitric acid solution containing ferrous sulfamate reducing agent to maintain Pu(III) and Np(IV) [84]. Cation exchange combined with other separation techniques was used for the separation and purification of Am and heavier actinides[85]. Parallel to the wide applicability, resins also have few limitations, like, poor thermal stability, degradation of ion exchange properties under high radiation field, generation of large amount of solid radioactive waste. Studies on removal of mercury from water/water by simple cation and anion exchange resins[86] are scare as heavy metal [27] selective chelating resins are available commercially.

Ion exchange resins containing chelating ligands covalently binded to the polymer matrix with same bead form and polymer matrix as usual resins[87] are known as chelating resin. As chelating groups, various ligands, which have nitrogen (N), oxygen (O), and/or sulfur (S) donor atoms, are attached on the matrix. Thiol group containing chelating resin (Duolite GT-73, SH-ePMO) shows very high mercury adsorption compared to ion exchange resin[88, 89]. A variety of commercial chelating resins)such as Duolite ES-466, Dowex A-l, Nisso Alm-525 Diaion CR-l 0 Amberlite IRC-718 Unicellex UR-10, Sirorez-Cu, Sumichelate Q-l 0) shows very high selectivity for Hg(II) removal from waste water [90]. Further, novel mercury selective chelating resins (viz., amidoxime, aminopyridine chelating resin with magnetic properties) have been prepared and adsorption behavior was studied[91, 92] .

1.8.5 Biological Materials

The kinds of materials of biological origin that have been investigated for biosorbent preparation include microbial biomass (bacteria, archaea, cyanobacteria, filamentous fungi and yeasts, microalgae), seaweeds (macroalgae), industrial wastes (fermentation and food wastes, activated and anaerobic sludges, etc.), agri-cultural wastes (fruit/vegetable wastes, rice straw, wheat bran, sugar beet pulp, soybean hulls, etc.), natural residues (plant resi-dues, sawdust, tree barks, weeds, sphagnum peat moss) and other materials (chitosan, cellulose, etc.)[93]. Biosorption process can effectively be used to sequester the metal ions from dilute solutions, therefore it is an ideal candidate for the treatment of high volume and low concentration complex wastewaters[94]. A large number of biosorbents types have been studied for their metal binding capability under various conditions. Eight different microbial biomass studied by M. Tsezos and B. Volesky showed 1 – 180 mg/g adsorption capacity for U and Th, which is higher than that of extensively used activated carbon and resin[95]. Biosorption of actinides by hen egg-shell membrane from dilute solution has been complied and showed very high accumulation of U and Th[96]. The mechanism of the radionuclide binding on the biosorbents were also established using advanced analytical instrumentation which indicates that the binding of radionuclide by the bacterial biomass takes place through displacement of cellular potassium / calcium and strong involvement of cellular phosphate, carboxyl and amide groups. Thus overall binding mechanism in uranium and thorium sequestration by this bacterium is based on a combined ion-exchange–complexation–microprecipitation[97-99]. For the development of low cost, strong affinity, eco friendly and high adsorption capacity efficient adsorbents for mercury removal from waste water, several biomass materials such as bamboo strips[100], bamboo charcoal [101], starch[102],cellulose[103], lignin[104], Lemna[105], kenaf fibers [106], cork stoppers [107] were investigated. Low cost agricultural by-products based biosorbents such as rice husk [108, 109], rice straw[110], wheat straw [111], banana stem[112], almond shell [113], buckwheat hulls[114], barley husk[115], mandarin peel[116], mulberry twig chars[117], adulsa leaves[118] are extremely efficient in removal of Hg(II) ions. Rice hasks have been successfully used for mercury ion decontamination from 500 ppb in a river water[109].

1.8.6 New generation nanoadsorbents

With the progress of research and development in nanoscience and technology, nanomaterials are being applied in various fields such as electronics, medicine, fuel cells, batteries, food, sensors etc. Water and waste water treatment has also not been omitted from fetching opportunities of nanotechnology. Different kinds of nano sized materials are being prepared and evaluated for removal of wide range of metal ions from aqueous medium. These nanoscale particles from organic or inorganic materials have proven themselves as excellent adsorbents due to their unique features. The most important characteristics which made them ideal adsorbents are small size, high porosity, catalytic potential, high reactivity, large surface area, and large number of active sites for interaction with different contaminants. The properties lead to high adsorption capacities by increasing the surface area, free active valences, and surface energies of nanomaterials. These adsorbents are now called as nanoadsorbents or new generation adsorbents [119, 120]. Metal oxide nanomaterials and carbon based nanomaterials are two types of nanoadsorbents studied.

Nanosized ferric oxides, manganese oxides, aluminum oxides, titanium oxides, magnesium oxides, manganese oxides and cerium oxides, are emerging as the promising nanoadsorbent for removal of pollutants from aqueous systems. Use of Nanosized metal oxides (NMOs) in wastewater treatment for removal of heavy metals and radionuclide are reviewed in literature and environmental clean-up technologies have been proposed[121-125]. In recent times, carbon-based nanomaterials: nanoporous activated carbon, fullerene, graphene, graphene oxides (GO), and carbon nanotubes (CNTs), have been probed as superior adsorbents for the removal of inorganic metal ions[126, 127]. Among the new generation nanoadsorbents, CNTs have been most extensively studied for the removal of metal ions due to their unique adsorbents properties. It will not be an exaggeration to say that use of nanotechnology in environmental remediation has emerged as an interesting field of study after promising results from CNTs in this area. The structure and properties which makes CNT as prominent adsorbents are discussed here.

1.9 Carbon nanotubes

Carbon nanotubes are one of the allotropes of carbon with nanometer-sized diameter and micrometer-sized length (where the length to diameter ratio exceeds 1000). The structure of CNT comprise of enrolled cylindrical graphitic sheet (called graphene) rolled up into a seamless cylinder with diameter of the order of a nanometer. Graphene is a layer of sp^2 bonded carbon atoms arranged in a hexagonal honeycomb lattice and can be seen simply as one atomic layer of graphite. **Figure 1.10** depicts the structures of CNTs as well as another rolled graphene form of carbon, fullerene. Depending on the numbers of graphene sheets rolled in the formation, CNTs

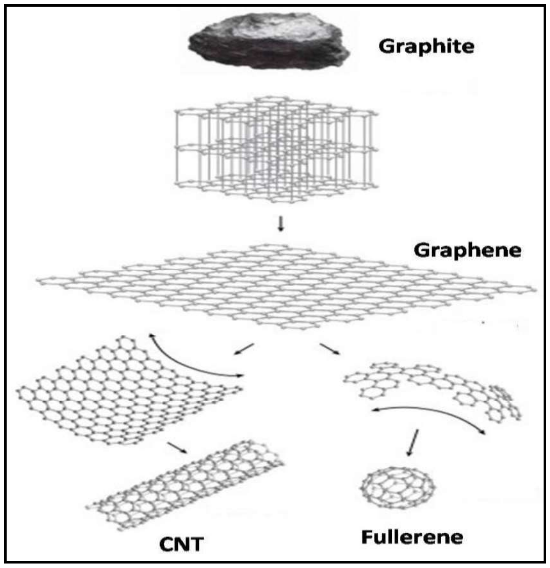

Figure 1.10 Rolling of one layer graphite, graphene into fullerene and CNT

are divided mainly in two categories, single-walled CNTs (SWCNTs) and multi-walled CNTs (MWCNTs) (**Figure 1.11**). They are generally made of a sidewall and two end caps: sidewall is made of benzene rings and end caps are half-fullerene balls. Due to this sp^2 hybridized carbon-carbon bond delocalized throughout the hexagonal honeycomb lattice, CNTs posses amazing rigid and tough properties, such as exceptionally high elastic properties, large elastic strain, and fracture strain sustaining capability [128]. CNTs are the strongest fibers known. The Young's Modulus of SWNT is around 1TPa, which is 5 times greater than steel (200 GPa) while the density is only 1.2~1.4 g/cm^{3}[129]. This means that materials

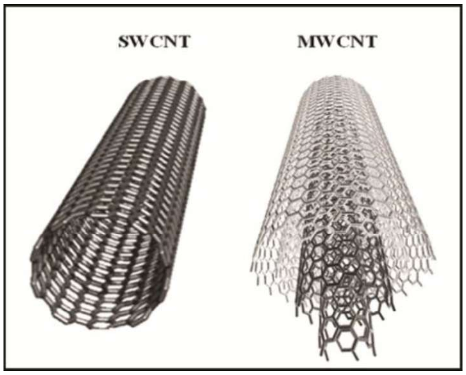

Figure 1.11 Structure of SWCNT and MWCNTs

made of nanotubes are lighter and more durable[130]. Beside their well-known extra-high mechanical properties, SWNTs offer either metallic or semiconductor characteristics based on the chiral structure. They possess superior thermal and electrical properties [131]. The rigid structure of CNTs imparts high thermal and chemical stability on their structure [132, 133]. Adsorption properties of CNTs arises due to their highly porous and hollow structures, large surface area, low density, high mechanical, thermal and chemical stabilities. Geometrically, CNTs bundles have four different spaces which act as adsorption sites for binding of substrate as shown in **Figure 1.12**. The grooves present on the periphery of a nanotubes bundle and the exterior surface of the outer most nanotubes, where two adjacent parallel tubes meet.

Exposed surface site or outside surface site is highly accessible for the adsorbate (external surface adsorption) and found on the curved surface of individual nanotubes on the outside of the nanotube bundles. Interstitial channels are easily accessible for the adsorbate species and found in the interior space of the bundle between individual nanotubes. Internal sites are found within the hollow structure of tubes and available only when ends of the tube are open. Adsorptive removal of metal ions, e.g. Pb, Ni, Co, Zn, Cu, Cd, Cr, Mn, Fe, Ag, Sr, Cs etc. by MWCNTs and oxidized-MWCNTs have been widely studied and literature reviews are available. MWCNTs and oxidized-MWCNTs have also been used for adsorption of radionuclide owing to their radiation stability which include U, Th, Pu, Am, Cs and Eu. However, the removal efficiency, selectivity and sensitivity of the raw or oxidized-MWCNTs for separation of metal ions and radionuclide remain quite limited.

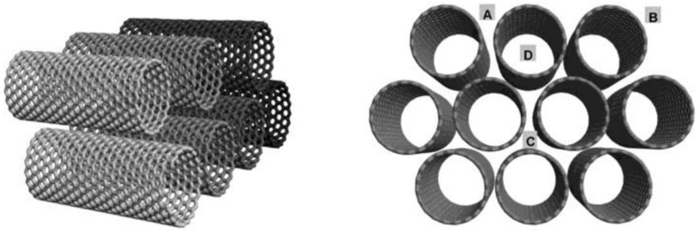

Figure 1.12 Different adsorption sites in bundle of CNTs: A. Grooves of bundles B. External Surface C. Interstitial Channels. Sites C and D comprise the internal porous volume of the bundle, whereas sites A and B are both located on the external surface of the bun

CNTs functionalized with some organic ligands are expected to be more selective than untreated and oxidized-CNTs if we choose the organic ligands which is selective towards specific metal ions or radionuclide.

1.10 Functionalized Solid Support

Functionalization is the process of adding new functions, features, capabilities, or properties to a material by changing the surface chemistry of the material. It is performed by attaching molecules/ligand (functional groups, extractants, receptor) or nanoparticles to the surface of a material, sometimes with a chemical bond but sometimes just through adsorption. Functionalization of the surface of solid support materials for its improved adsorption properties has now been followed in diverse application. Due to high chemical stability, i.e., the lack of solubility and the difficult manipulation in any solvents (as-produced CNT are insoluble in all organic solvents and aqueous solutions, they can be dispersed in some solvents by sonication, but precipitation immediately occurs when this process is interrupted), surface modification of CNT solid supports has concise paths. The main approaches for the modification of these quasi one-dimensional structures can be grouped into four categories: (a) the covalent attachment of chemical groups through reactions onto the π-conjugated skeleton of CNT; (b) the noncovalent adsorption or wrapping of various functional molecules; and (c) the endohedral filling of their inner empty cavity, and (d) the exohedral or external decoration with inorganic materials. **Figure 1.13** explains these functionalization processes. Covalent attachments of the ligands on the CNT surface are preferred for its application in adsorptive separation of metal ions from water and waste water as major advantage of this route is that a covalent bond is much more stable than other methods such as non-covalent modification.

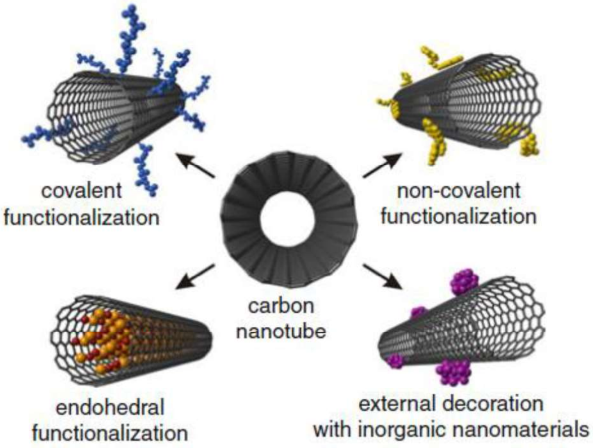

Figure 1.13 Schematic representation of different categories for the functionalization of carbon nanotubes

1.11 Zinc isotope separation and functionalized solid support

Apart from metal ion and radionuclide, separation of isotopes plays a vital role the nuclear industry. Isotope separation of Zn is important mainly through two aspects. Naturally occurring zinc contains five stable isotopes with natural abundances of 48.63% (^{64}Zn), 27.90% (^{66}Zn), 4.10% (^{67}Zn), 18.75% (^{68}Zn) and 0.62% (^{70}Zn). ^{67}Zn and ^{68}Zn are used as a target materials during (p, n) nuclear transmutation reaction for the production of nuclear medicinally important radioisotope ^{67}Ga ($t_{1/2}$ = 61.8 h, E_γ =185 keV) which is widely used for diagnosis for tumour localization[134, 135]. ^{67}Zn, ^{68}Zn and ^{70}Zn can all be used for the production of the radionuclide ^{67}Cu which have diagnostic and therapeutic application in cancer treatment[136, 137]. ^{66}Zn has been proposed as an alternative target for the production of diagnostically potential ^{64}Cu radioisotopes[138]. Secondly, ^{64}Zn-depleted zinc is used in the primary coolant of nuclear power plant to reduce the formation of radioactive cobalt isotope, ^{60}Co ($t_{1/2}$ = 5.27 y, E_γ =1170 and 1330 keV), presence of which leads to radiation threat to the working personal[139]. During the course of operation, thin corrosion oxide film develops in the coolant circuit of nuclear power reactor and ^{60}Co is one of the components of these films[140]. Zn present in the coolant piping would competes with Co for sites in those films and thus suppresses the buildup of ^{60}Co. Additionally, addition of Zn in the form of oxide or acetate prevents stress corrosion cracking in the structural material of the piping of the primary coolant[141]. ^{64}Zn-depleted zinc is used since this most abundant isotope generates highly radioactive ^{65}Zn [$t_{1/2}$ = 244.4 days, E_γ =1116 keV] in the reactor environment.

Separations of zinc isotopes by liquid-liquid extraction using crown ethers[142] have been reported[143, 144]. Isotope effects in the complex formation of zinc with various crown ethers have been investigated[143]. Stereochemical effect on the isotope separation of zinc by liquid-liquid extraction with crown ether has been recently studied[145]. Crown ether has shown promise for isotope separation albeit small separation factor which can be exploited in chromatography mode. The solid support of the chromatography column has be functionalized with crown ethers to avail the potential of these ligands in zinc isotope separation application.

1.12 Computational protocol for designing functionalized solid support

Along with experimental studies, lot of effort is being put for the understanding of the structure, bonding and thermodynamics of metal ions with varieties of ligands and ligand functionalized solid supports using quantum chemical calculations. In this regard, Cao et al.[146] and Batista et al.[147] have reported the preferential selectivity of Am^{3+}/Cm^{3+} ion over Eu^{3+} ion towards dithiophosphonic acid based ligands using Density functional theory (DFT). Similarly, Bhattacharyya et al.[148] studied the selectivity of dithiophosphinate for Am^{3+} over Eu^{3+} using DFT. Wang et al.[149] has recently reported the complexation interaction of Am^{3+} and Eu^{3+} with n-octyl(phenyl)-N,N-diisobutyl-methylcarbamoyl phosphine oxide (CMPO) and its derivative using DFT. Density functional theory investigations of the trivalent lanthanide and actinide extraction complexes with different derivatives of diglycolamides have been studied[150] . The binding strength of the carboxylic acid group (-COOH) with different divalent metal ions by computational method revealed the experimental selectivity[151].

Designing novel materials through functionalization of carbon nanotubes for application in nuclear waste management solely using DFT calculation was investigated with the complexation of uranyl ion with CNT solid support functionalized with carboxylate functionalized SWCNTs [152]. The adsorption of mercury in elemental and ionic form on different surfaces such as CuO[153] , Fe_2O_3 [154] were investigated DFT studies.

Theoretical Investigation of Isotope Fractionation of Zinc using Aqua, Chloride, and Macrocyclic ligands[155-157] has laid the foundation in the searching of suitable functionalized solid support for zinc isotope separation.

Understanding and designing new molecular systems will gain remarkable control of chemical selectivity during nuclear waste and industrial waste water processing. For designing new ligands or improving the existing ones, understanding the accurate nature of ion-ligand interactions together with the structural parameters, binding energies, conformational features of the ligands and solvent effect would be very helpful. In this regard, computational chemistry provides useful insights and rationalization of large class of molecules.

There is a wide variety of computational methods starting from semi-empirical to ab-initio, each having its own merits and demerits in terms of cost, time and accuracy for a particular application[158]. Semiempirical methods can be useful for initial screening of the molecular system of interest[159]. Among ab initio methods, though HF is considered to be the cheapest it has some serious limitation due to inability to handle the electron correlation[160]. The MP_n [161] and CCSD[162] methods are quite accurate but heavily expensive and hence can be restricted to small molecular system. However, density functional theory (DFT)[163] based methods, which earlier was considered to be ab initio has partly lost its ab initio credential due to large number of parameterization of the exchange-correlation functional but still is the work horse for large molecular system.

There is a wide variety of DFT functional one can select for a specific interest of application. Similarly, the size of the basis set can be chosen depending on the molecular properties to be evaluated. Clearly, there is a tradeoff between the functional and size of the basis set depending on the molecular size and chemical properties. In case of heavy elements the scalar relativistic effective core potentials[164] were used to take care of relativistic effect. All the quantum calculations were conducted in the gas phase. Since, most of the problems in the chemistry deal with liquid phase, it is important to treat the solute-solvent interactions in quantum chemical calculations. The explicit treatment of solvent by placing large number of solvent molecules around solute requires electronic relaxation as well as geometry relaxation of complete solute-solvent system. So this approach is impractical. Continuum solvation models replace the solvent with continuum which describes the electro static behaviour of the solvent. Unlike other continuum solvation models, conductor like screening model[165] (COSMO) uses scaled-conductor approximation to derive the polarization charges of the continuum, caused by the polarity of the solute. The computational chemistry is growing rapidly with the continuing development of methodologies, computer power, robust algorithms, and the availability of software[166]

1.13 Scope of the Thesis

The objective of this thesis is to design suitable ligand functionalized CNTs and polymeric solid support for metal ion (Th, U, Np, Pu, Am, Cm, and Hg) and isotope (Zn) separation after selecting proper ligand and solid support from literature using DFT calculations, preparation of the adsorbents and experimental adsorption studies. Preparation of a particular ligand functionalized solid support, its experimental adsorption studies and then DFT calculations on the system to corroborate the observed data have also been followed. Finally, the fixed-bed column separation experiments have been performed to check its applicability for scaling up. The complete approach for the design and screening of functionalized solid support for metal ion and isotope separation can be summarized in **Figure 1.14**.

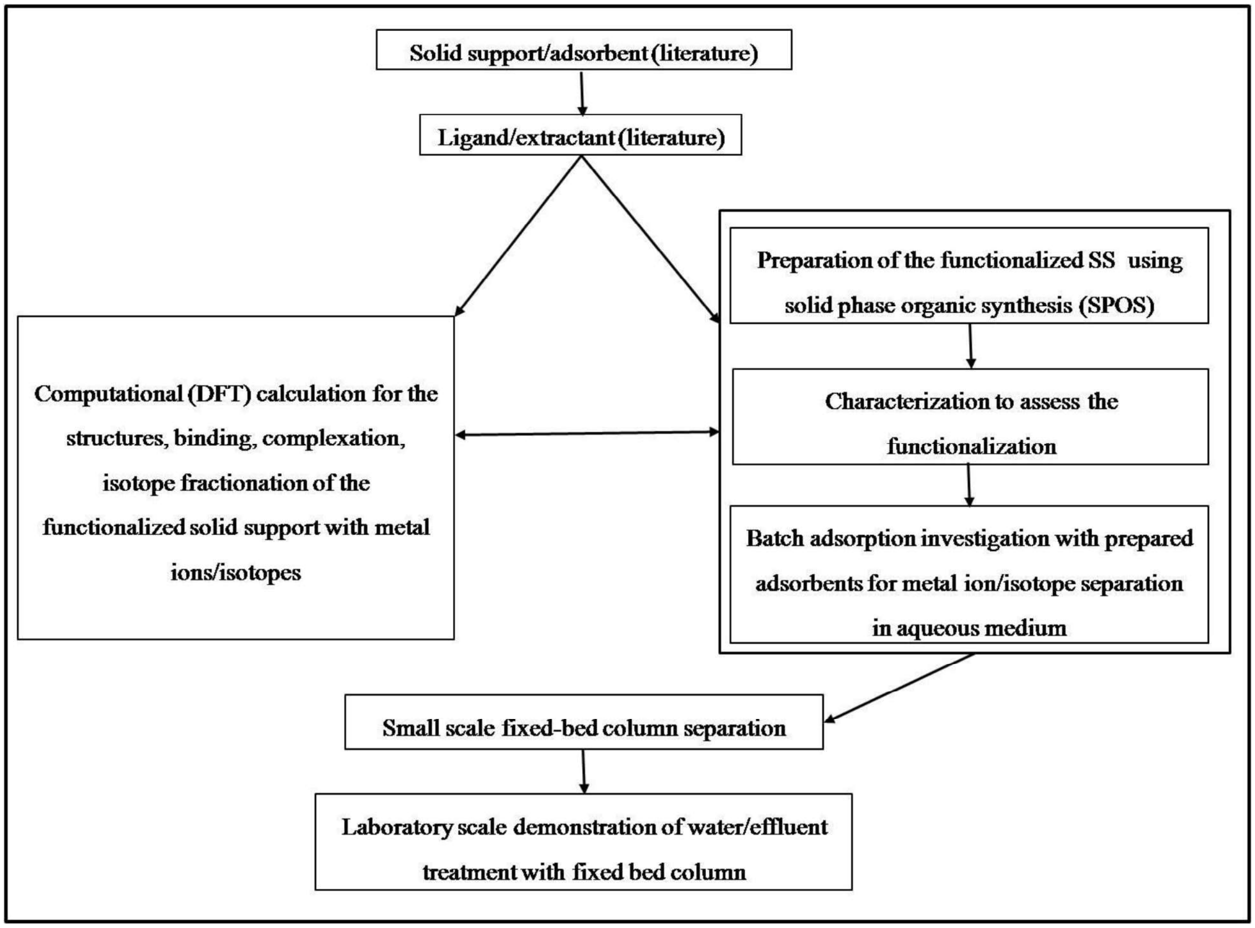

Figure 1.14 Present approach for the design and screening of functionalized solid support for metal ion and isotope separation

The succeeding chapters of this thesis comprise the work done under the above theme as:

Chapter 2: Experimental and Theoretical Methodologies

This chapter describes the materials, equipments and instruments used in the experimental studies. The synthesis route of functionalized CNTs and polymethacylate (PMA) resins are depicted. The characterizations of prepared materials and experimental procedure for batch adsorption studies are also discussed. The theory for kinetic, isotherm and thermodynamic modeling of experimental data and governing equations are discussed. The fundamental of fixed-bed column separation along with analysis of breakthrough and desorption curve are described. The computational methodology for the structure, binding and interaction energies are presented. The theoretical calculation of complexation energies between metal ion-functionalized CNTs and isotope separation factors in zinc-crown ether functionalized solid support are discussed.

Chapter 3: Carboxylic and diglycolamic Acid functionalized Carbon Nanotubes

In this chapter, -COOH and diglycolamic acid [124] functionalized CNTs are evaluated for the adsorption of Th(IV) ions. The B3LYP functional and TZVP basis set in conjunction with COSMO) solvation approach have been used to predict the free energy of adsorption for Th^{4+} ions with p-CNT, oxidized (CNT–COOH) and DGA functionalized CNTs (CNT–DGA). Experimentally observed values of adsorption capacities of Th^{4+} by CNTs indicate that CNT–COOH has the strongest binding with Th^{4+}, whereas p-CNT has the lowest; CNT–DGA shows less adsorption than CNT–COOH[167].

DFT calculations are carried out on the structure, bonding, energetic and thermodynamics for the complexation/extraction of Eu^{3+}/Am^{3+} ions with CNT–DGA. The free energy of extraction (ΔG_{ext}) for Eu^{3+} was found to be higher than that of Am^{3+} ion using the Born–Haber thermodynamic cycle in conjunction with COSMO. Further, CNT-DGA was prepared and distribution constant for metal ions determined by adsorption revealed that Eu^{3+} is preferentially extracted over Am^{3+} ion and same selectivity trend was reported in liquid-liquid extraction[168].

CNT-DGA are also demonstrated to be a highly efficient for Am^{3+}, Pu^{4+} and PuO_2^{2+} ions with following trend of distribution coefficient, K_d : $Am^{3+} > Pu^{4+} > PuO_2^{2+}$. The sorption energy calculated from the Dubinin–Radhuskevich isotherm revealed that interaction between CNT-DGA and An is chemisorption. Suitable stripping agents were identified for the back-extraction of the actinides. The sorbent was also found to have good radiolytic stability. DFT revealed a tridentate coordination mode of the DGA moiety towards Pu^{4+}/Am^{3+} and a bidentate coordination towards PuO_2^{2+}. The binding energy of sorption with DGA-CNT of Pu^{4+} was higher than that of PuO_2^{2+}, whereas for Am^{3+} it was higher than for PuO_2^{2+} but less than for Pu^{4+}[169].

Chapter 4: Amidoamine and Ploy(Amidoamine) functionalized Carbon Nanotubes

Amidoamine functionalized CNTs (CNT-AA) are evaluated for the sorption of U(VI), Am(III) & Eu(III) from aqueous medium. Both UO_2^{2+} and Eu^{3+} followed Langmuir sorption model with maximum sorption capacity of 20.66 and 16.10 mg g^{-1} respectively. This has been explained by DFT calculations which show that more negative free energy of U(VI) compared to Am(III)/Eu(III) and stronger U-CNT-AA complex is responsible for higher sorption capacity of U(VI) compared to Am(III)/Eu(III)[170].

CNT-AA are used for efficient and selective solid phase separation of Pu(IV) and Pu(VI). The sorption proceeded through monolayer coverage of CNT-AA with capacities of 91.2 mg g^{-1} and 89.4 mg g^{-1} for Pu^{4+} and PuO_2^{2+}, respectively following a Langmuir isotherm. The DFT study reveals that the metal ion is deca-coordinated in the case of Pu^{4+} and octacoordinated in PuO_2^{2+}. The calculated ΔG_{ext} was found to be almost three times higher for Pu^{4+} than PuO_2^{2+}, which thus confirms the experimentally observed higher sorption of Pu^{4+} compared to PuO_2^{2+} [171]. Similarly, DFT calculation and experimental studies on the sorption of NpO^{2+} and NpO_2^{2+} by CNT-AA revealed the same result that hexavalent Np is more selective than pentavalent [172].

Batch adsorption and fixed-bed column separation of Hg(II) ions from aqueous medium by CNT-AA are investigated. The adsorbent showed superior selectivity with high adsorption capacity towards mercury as compared to other metal ions. DFT calculations establish the bi-dentate mode of complexation and correlate the experimental selectivity [173].

In addition, the 1st and 2nd generation of poly(amidoamine) functionalized CNTs (CNT-PAMAM) were evaluated for the adsorption of Pu(IV) [174], Am(III) [175], and Np(V) [176] separately. The 2nd generation CNT-PAMAM showed superior adsorption than the 1st generation one. The sorption equilibrium, mechanism, kinetics, radiolytic stability, and back-extraction studies are performed. The unique binding pattern of CNT-PAMAM was elucidated by DFT.

Chapter 5: Sulphur Ligand Functionalized Carbon Nanotubes

This chapter deals with the adsorption of Hg(II) by newly prepared thiol (SH) and dithiocarbamate (DTC) functionalized CNT, owing to the strong interaction of mercury with sulphur. The maximum adsorption capacity of CNT-DTC was found to be 3.5 times higher than that of CNT-SH at the optimum pH of 6. The kinetics and equilibrium data revealed that the adsorption of Hg^{2+} follow pseudo-second order and Langmuir isotherm model, respectively. DFT calculations show CNT-DTC displays greater adsorption than CNT-SH as observed in the experiments. Feasibility of continuous separation of Hg^{2+} is successfully tested by demonstrating a small scale fixed bed column filled with CNT-DTC[177].

Chapter 6: Crown Ether Functionalized Resin

In this chapter, DFT results for the isotopic fraction of zinc in the nano cavity of crown ethers and crown ethers anchored on polymeric resin are discussed. The isotope separation factors of various isotope pairs are calculated from reduced partition function ratio. Benzo-18-crown-6 (B18C6) and benzo-15-crown-5 (B15C5) showed higher isotope separation factor for zinc[178]. Further, DB18C6 and B15C5 functionalized PMA resins were prepared and evaluated for Zinc adsorption and isotope separation. Separation of Zn in a fixed-bed column using PMA-DB18C6 is carried out with various column parameters. Breakthrough and elution curves are analyzed with available model and scaling up of the column separation is assessed.

Chapter 7: Summary and Future Scope

The summary and discussions on the future scope of the work reported in the thesis are presented in this chapter. It summarizes the important results obtained on: i) Synthesis and characterization of functionalized CNTs, ii) Theoretical and experimental results on the separation of radionuclide from aqueous medium using prepared functionalized CNTs, iii) Studies on the mercury ion removal using nitrogen and sulphur ligand functionalized CNTs, iv) DFT calculations on zinc isotope separation by crown ethers functionalized resins, and v) Static and dynamic studies for zinc adsorption and isotope separation using crown ether functionalized PMA resins. In future scope, the applicability of the functionalized CNTs for radioactive and waste streams treatment for the removal/pre-concentration emphasized. Discussion is also made on the large scale preparation of crown ether functionalized PMA resin and chromatographic zinc isotope separation with long column to obtain enriched/depleted isotopic zinc compounds.

2 Chapter 2: Experimental and Theoretical Methodologies

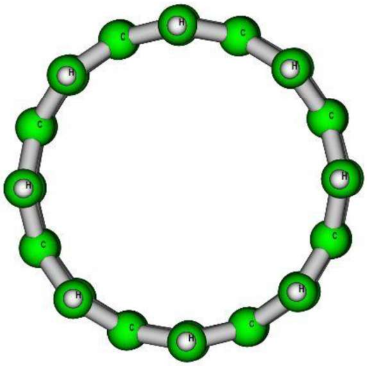

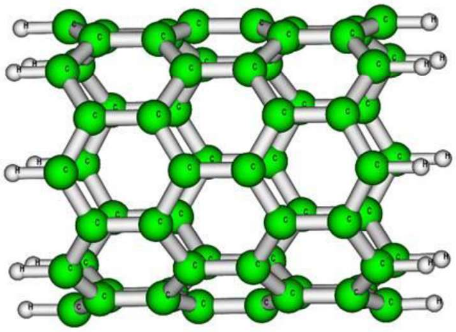

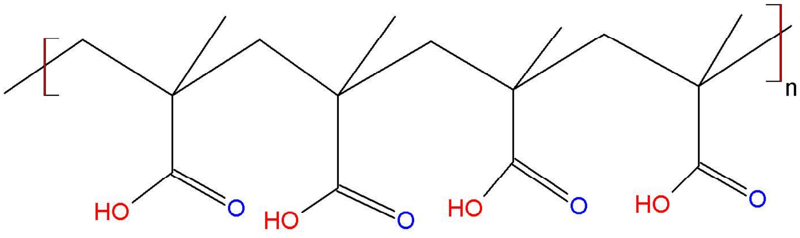

2.1 Introduction

Multi-walled carbon nanotubes were functionalized with different ligands following chemical covalent synthetic processes. Commercially available polymeric resin was grafted with crown ethers using solid phase organic synthesis[179, 180] model. The procedures of these solid phase organic synthesis and related characterization using various state-of-the-art analytical techniques were discussed. The experimental methods employed for adsorptive separation of metal ions from aqueous solution with varying process parameters such as pH, acidity, concentration, temperature, radiation, presence of other ions, stripping agent, and adsorption-desoprtion cycles, were discoursed. The theoretical methods and models used to simulate the experimental kinetic, equilibrium and temperature dependant data are briefed. The experimental procedure utilized to generate dynamic adsorption information from indigenously prepared functionalized solid support filled fixed-bed column study and calculation of characteristic parameters for metal ion and isotope separation involve in the breakthrough and elution profile are described. This is followed by a brief treatise on DFT theoretical methods employed for evaluation of electronic structure, bonding, interaction of metal and isotopes with ligand and ligand functionalized adsorbents using computational program, Turbomole[181] on workstation is provided. The calculation of metal ion complexation energies and thermodynamic parameters from the computational data is described. Finally, the theory behind the calculation of isotope separation factor from DFT theory is reported.

2.2 Materials

2.2.1 Chemicals and Reagent

Concentrated nitric acid, sulfuric acid, hydrochloric acid, sodium hydroxide, magnesium sulphate, chloroform, acetic acid, methanol, ethanol, oxalic acid, sodium carbonate, zinc chloride, zinc sulphate and acetone were purchased from local suppliers. Ethylenediamine (EDA), thionyl chloride ($SOCl_2$), Tetrahydrofuran (THF), diglycolic anhydride, triethylamine (TEA), dimethyl formamide (DMF), N,N'-Dicyclohexylcarbodiimide (DCC), 4-Dimethylaminopyridine (DMAP), Dimethylformamide(DMF), methylacrylate(MA), carbon disulphide (CS_2), methylacrylate, benzo-15C5 (B15C5), dibenzo-18-crown-6 (DB18C6) are purchased from S D Fine Chemicals Pvt. Ltd. Thiourea, cysteamine hydrochloride, 1-Ethyl-3-(3-dimethylaminopropyl)carbodiimide (EDCl) and N-hydroxysuccinamide (NHS) were purchased from Spectrochem Pvt. Ltd. Mercury Chloride ($HgCl_2$), titriplex III (Na_2EDTA), Pd/C (10%), diglycolic anhydride and 1-hydroxybenzotriazole (HOBt) were bought from Sigma Aldrich. All chemical were of analytical grade and used without any further purification.

2.2.2 Solutions

1000 mg/L stock mercury solution of Hg^{2+} and Zn^{2+} were prepared by dissolving required amount of $HgCl_2$ and $ZnSO_4$, respectively in acidified de-ionized water. Solutions of some metal ions were prepared from ICP standard of 1000mg/L concentration. ^{241}Am, ^{239}Pu, ^{239}Np and other radionuclides from lab stock were used as tracers. Working standards were prepared by progressive dilution of stock solution.

2.3 Analytical Equipment and Techniques

2.3.1 Equipment

Millipore (Direct Q) water purification system, Millipore water (resistivity 18.2 MΩ cm) was used in all experiments. KS 4000i control-incubator shaker (IKA make) was used for equilibration studies. Echo Testr pH2 (Eutech make) pH meter was used for pH adjustment. Millipore vacuum filtration unit with 0.22 lm Millipore membrane filter was used for filtration. Refrigerated centrifuge (REMI Model No. C-24 BL) and Laboratory centrifuge (Remi R-8C DX) were used for separation of CNTs from aqueous/organic solution. Vacuum oven (SEMCO make) and Ultrasonic bath (Life-care make EN 50US) were employed during experiment.

2.3.2 Techniques

2.3.2.1 **Fourier Transform Infra-Red Spectroscopy (FT-IR)**

FTIR spectra were recorded in between 500 cm^{-1} and 4000 cm^{-1} with 16 cm^{-1} resolution using ABB-MB3000 FTIR instrument. Samples are mixed well with sprectrapure KBr powder in 1:100 to 1:200 mass ratio in a mortar using pestle. This mixture is used for making 15mm diameter disc which were mounted in the sample location of FTIR machine and spectra are recorded.

2.3.2.2 **Element (CHNS) Analyzer**

CHN content in the synthesized materials was measured using an Elementar (Germany)Vario Micro Cube elemental analyser.

2.3.2.3 X-ray Photoelectron Spectroscopy (XPS)

X-ray photoelectron spectroscopy (XPS) measurements of selected samples were carried out using Mg-Kα (1253.6 eV) source and DESA-150 electron analyzer (Staib Instruments, Germany) to study the functionalization process of the MWCNTs. The spectrometer binding energy scale was calibrated with Au- $4f_{7/2}$ photo peak at a binding energy of 83.95 eV. The spectrum was recorded as the intensity (number of counts per second) versus binding energy (BE).

2.3.2.4 Thermogravimetric Analysis (TGA)

Thermogravimetry-Differential Thermal Analysis (TG-DTA) of the prepared product and reactants were carried out by TG-DTA instruments (Make: Netzsch, Model: STA 449 Jupiter F3) under nitrogen gas flow.

2.3.2.5 Nuclear Magnetic Resonance Spectroscopy (NMR)

^{1}H and ^{13}C-NMR, (BrukerAvance 500) spectroscopy was used to monitor the nitration and amination of benzo-crown ethers.

2.3.2.6 Scanning Electron Microscope-Energy Dispersive Spectrometry (SEM-EDS)

Surface morphology, porous structure and particle size of the prepared MWCNTs and resins were studied by using scanning electron microscope (Camscan MV2300CT/100). Energy dispersive spectroscopy (EDS, Oxford X-Max 80) was used for chemical analysis of the samples.

2.3.2.7 Dynamic Light Scattering (DLS)

DLS technique using Malvern Zetasizer Instrument (Nano-ZS 4800, UK) was employed to determine the mean size of the synthesized MWCNTs.

2.3.2.8 X-ray Diffraction (XRD)

Inel Equinox 3000 PXRD machine was used for analyzing X-ray diffraction pattern of the product. X-ray photoelectron spectroscopy (XPS) measurements of functionalized MWCNTs was carried out using Mg-Kα (1253.6 eV) source and DESA-150 electron analyzer (Staib Instruments, Germany).

2.3.2.9 Raman Spectroscopy

The spontaneous Raman spectra of the MWCNT and functionalized MWCNTs were recorded using a STR-300 micro-Raman spectrometer (SEKI Technotron, Japan) at room temperature. The samples were excited at 532 nm (power ~20 mW at the sample spot, DPSS) using a 10 × objective lens (Olympus). The scattered light was collected by the same objective lens and a fiber-coupled 300 mm spectrograph (Acton series SP 2300i, 1200 g mm^{-1}) and detected by a thermo-electric cooled (-75^0C) charge-coupled device (CCD).

2.3.2.10 Transmission Electron Microscope (TEM)

For better surface nature, defects and nature of CNTs, TEM of selected samples were conducted in TEM-model JEOL 2000FX, 200 kV.

2.3.2.11 **Luminescence**

PL emission and excitation spectra were recorded on an Edinburgh F-900 Fluorescence Spectrometer in the 200–750 nm region with a Xe lamp as an excitation source, M-300 monochromators, and a Peltier cooled photomultiplier tube as detector. The acquisition and analysis of the data were carried out by F-900 software supplied by Edinburgh Analytical Instruments, UK.

2.3.2.12 **Inductively Coupled Plasma-Optical Emission Spectroscopy (ICP-OES)**

ICP-OES (Horiba Scientific, model Jobin Yvon Ultima) was used for the measurement of elemental concentration throughout the PhD work. It is based on the measure of emission intensity of given analyte after excitation and ionization by the plasma. **Table 2.1** shows the elements analyzed and emission lines used for the analysis.

Table 2.1 Emission lines used for analysing concentration of metals in ICP-OES

Metal	Emission Line (nm)	Metal	Emission Line (nm)
Hg	194.164	Cu	324.754
Fe	259.94	Zn	202.551
K	766.49	Na	588.995
Li	670.784	Ni	231.604
Mg	280.27	Pb	283.306
Ca	33.366	Si	251.611

2.3.2.13 **Multi Collector-Inductively Coupled Plasma Mass Spectrometry (MC-ICP-OES)**

The isotopic analysis of zinc isotope was performed in MC-ICP-MS at the Department of Geology and Geophysics, Indian Institute of Technology, Kharagpur.

2.4 Synthetic Routes

2.4.1 Functionalization of carbon nanotube

2.4.1.1 **Multi-walled Carbon Nanotubes (MWCNTs)**

The MWCNTs used in this work are supplied by Dr. Kinshuk Dasgupta, MMD, BARC. Catalytic CVD method was used to synthesize MWCNTs using a fluidized bed at 800°C. Acetylene carbon precursor and ferrocene catalyst were utilized. The experimental setup and procedure have been reported in studied literature[182].As produced MWCNTs were subjected to hydrochloric acid treatment to remove catalyst particles followed by heating at 400°C in air to remove amorphous carbon. MWCNTs having purity greater than 98.5%, outside diameter (OD) 15-25 nm, inside diameter (ID) 5-8 nm, length ~200 μm, and specific surface area (SSA) more than 150 m^2/g, were obtained by this method.

2.4.1.2 **Carboxylic acid functionalized MWCNTs (MWCNT-COOH)**

1 g purified MWCNTs were added to 200 mL of 3:1 (v/v) mixture of concentrated sulfuric and nitric acid. This mixture was sonicated in an ultrasonic bath for 5 hours at 60^0C. The black suspension was then cooled, filtered and washed with distilled water until the pH of the filtrate became neutral. The filtered product was dried at 100^0C under vacuum overnight.

2.4.1.3 **Acylated MWCNTs (MWCNT-COCl)**

About 400 mg of above MWCNT-COOH was sonicated with 60 mL of $SOCl_2$ for 30 minutes at room temperature. This suspension was refluxed under magnetic stirring at room temperature for 48 hours. The acylated MWCNTs were separated by centrifuging at

5000 rpm for 20 minutes. The supernatant solution was decanted and the residue was washed with anhydrous THF for five times to remove the excess $SOCl_2$. The product, MWCNT-COCl was dried in the vacuum oven for overnight at room temperature.

2.4.1.4 Amidoamine functionalized MWCNTs (MWCNT-AA) from MWCNT-COCl

About 300 mg of MWCNT-COCl was sonicated with 100 mL of DMF for 30 minutes. About 80 mL of EDA were added and refluxed under magnetic stirring at 367 K for 24 hours. After cooling to room temperature, the MWCNT-AA was separated by centrifuging at 5000 rpm for 20 minutes and the supernatant solution was discarded. The residue was washed with acetone five to six times to remove excess EDA and dried in the vacuum oven at room temperature for overnight.

2.4.1.5 Amidoamine functionalized MWCNTs (MWCNT-AA) from MWCNT-COOH

500mg of MWCNT-COOH was dispersed in 30mL EDA solution by sonicating for 30 minutes at room temperature, following which the suspension was stirred for 30 minutes at 300 rpm. 70mg DCC was slowly added to the suspension, after which it was refluxed for 48 hours at a controlled temperature of 90^{o}C. The mixture was then transferred in an oak ridge centrifuge tube with ethanol, and centrifuged at 5000 rpm for 15 minutes. It was then allowed to stand for a few minutes. The supernatant solution was removed and the black residue obtained was washed three times with ethanol. Each time the colorless supernatant solution was decanted. Finally, the product was transferred to a glass petri-dish using methanol, and kept overnight for drying at 80^{o}C in a vacuum oven. The dried product thus obtained (MWCNT-AA) was collected aside and weighed.

2.4.1.6 **Diglycolamic acid functionalized MWCNTs (MWCNT-DGA)**

About 200 mg of MWCNT-AA were dispersed in 100 mL of THF and 2 ml of TEA and the resulting mixture was sonicated for 2 hours at room temperature. About 2.4 g of DGA was added and refluxed under magnetic stirring for another 24 hours at 353 K. The suspension was cooled to room temperature and centrifuged at 5000 rpm for 30 minutes. The supernatant solution was discarded and the residue was washed with acetone five to six times by repetitive centrifugation. Finally, the product, MWCNT-DGA was transferred to a glass petri-dish using acetone, and kept overnight for drying at 80^{o}C in a vacuum oven.

2.4.1.7 **Thiol functionalized MWCNTs (MWCNT-SH)**

2g of MWCNT-COOH was dispersed in 670ml ethanol by sonication at 50^{0}C. After 1 hour, 0.8g of EDC was added to the solution. After another hour of continuous sonication, 0.5g of NHS was added to the mixture. 1.137g of cysteamine hydrochloride was added after further 2 hours of sonication. The solution was then refluxed at 60^{0}C for 48 hours. CNT-SH was centrifuged and washed with ethanol, water and methanol and then dried for 18 hours in a vacuum dryer.

2.4.1.8 **Dithiocarbamate functionalized MWCNTs (MWCNT-DTC)**

2g of CNT-AA was added to 400ml of 1% NaOH solution in a 1000ml round bottom flask. The

Solution was sonicated for 2 hours and stirred using a magnetic stirrer for 30 minutes to obtain uniform dispersion.20ml of ethanol and carbon disulphide were added slowly using a dropping funnel. The solution was stirred for 72 hours. After stirring, the solution was centrifuged and washed with water, acetone and methanol. The CNT-DTC was dried for 18 hours in a vacuum drier at 80^0C.

Figure 2.1 depicts the reaction scheme of the above reactions.

Figure 2.1 Reaction routes followed for making various functionalized MWCNTs

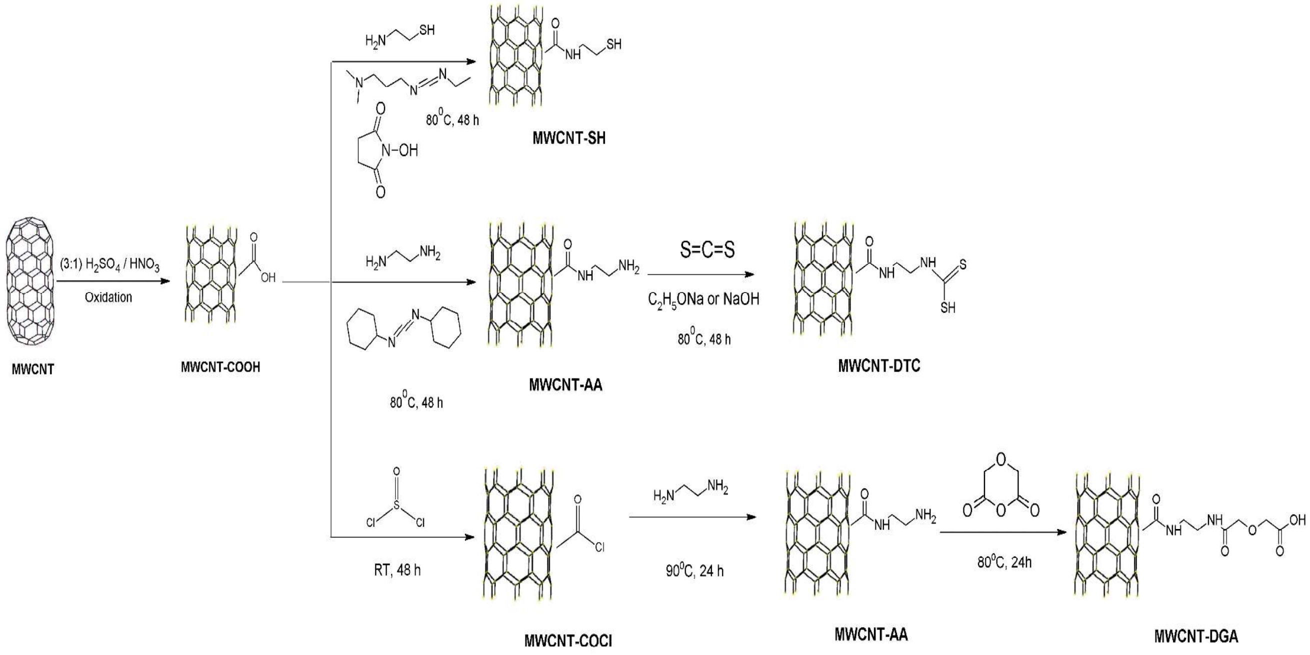

2.4.1.9 Poly(Amioamine), PAMAM dendrimers functionalized MWCNTs (MWCNT-PAMAM)

Amioamine MWCNT was first prepared from MWCNT-COOH following section 3.1.5, with little modification in the reagents for better functionalization. Coupling amidation reaction between carboxylic acid group of MWCNT-COOH and amine of EDA in presence of DCC activating agent and DMAP coupling additive agent was used. Brief reaction procedure: 100mg of MWCNT-COOH was dispersed in 150mL DMF. Then to this mixture 0.26 g of DCC, 0.0196 g of DMAP and 5 ml EDA were added. The reaction mixture was stirred for 24 h at room temperature. The black suspension reaction mixture was transferred to centrifuge tube with ethanol and centrifuged at 5000 rpm for 15 minutes. The residue was washed with ethanol three times and was transferred to a glass Petri dish with methanol and dried at 80^0C in a vacuum oven for overnight.

Growth of poly(Amioamine), PAMAM dendrimer up to generation five on the MWCNT (MWCNT-PAMAM$_{Gx\ (x=0.5,\ 1,\ 1.5,\ 2,\ .....5)}$)

Stepwise growth of PAMAM dendrimer on the surface of CNTs was already reported in few literatures [24]. The same method with little modifications has been followed to grow PAMAM dendrimer of generation 1 to 5 on MWCNT.

2.4.1.9.1 Preparation of MWCNT-PAMAMG$_{0.5}$

Ester terminated half generation PAMAM dendrimers grown by Michael addition reaction between the amine donor of the MWCNT-AA and methylacrylate in methanol medium. The brief procedure is mentioned. 50mL methylacrylate in 100ml methanol was added to a 500 three-necked round-bottom flask. As prepared MWCNT-AA initiator in 50mL methanol was carefully dropped into methylacrylate solution within 20min, with continuously stirring. This solution was placed in an ultrasonic bath for 2 h at 50^oC, and the mixture was stirred for another 24h. After cooling the product suspended in the reaction mixture were separated by centrifugation with repetitive washing with methanol. To ensure that no ungrafted polymer or free reagents were present in the product, the solid was dispersed in methanol, filtered and washed with methanol till no more smell of methylacyrlate. The product was dried overnight at 70^0C under vacuum to MWCNT-$PAMAM_{G0.5}$.

2.4.1.9.2 Preparation of MWCNT-$PAMAM_{G1}$

Amine terminated full generation of PAMAM was prepared by amidation reaction between ester terminated PAMAM of the surface of the CNTs and amine groups of EDA. Brief reaction method: MWCNT-$PAMAM_{G0.5}$ in 80 ml methanol was added to a 500mL three-necked round-bottom flask. These solutions were placed in an ultrasonic bath for 15 min. After dispersion 80 ml solution of 1:1 methanol/ethylenediamine were dropped into it. These solutions were placed in an ultrasonic bath again for 5 h at 50^oC, and the mixture were stirred for another 24 h at 50^oC. The solid obtained were separated by centrifugation and washed three times with methanol and dried in vacuum oven at 80^oC to give a generation 1.0 dendrimer modified MWCNT.

2.4.1.9.3 Preparation of MWCNT-$PAMAM_{G1.5}$

This half generation product was synthesized from MWCNT-$PAMAM_{G1}$by procedure mentioned in Sec 2.4.1.9.1.

2.4.1.9.4 Preparation of MWCNT-$PAMAM_{G2}$

This full generation product was synthesized by amidation of ester groups of MWCNT-$PAMAM_{G1.5}$ and EDA following procedure described on Sec 2.4.1.9.2.

2.4.1.9.5 Preparation of MWCNT-PAMAM$_{G5}$

Repetitive Michael addition reaction (Sec 2.4.1.9.1) followed by amidation (Sec 2.4.1.9.2) of the MWCNT-PAMAMG$_2$ gives rise to fifth generation PAMAM dendrimer functionalized MWCNT (MWCNT-PAMAMG$_5$).

The overall reaction process of dendrimer functionalization is shown in was shown in

Figure 2.2

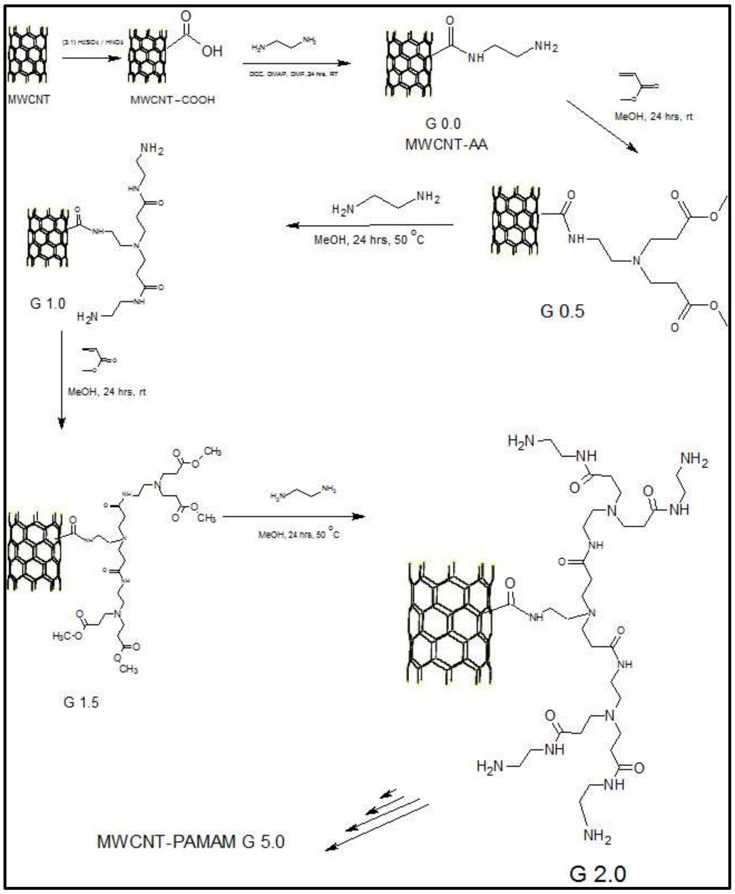

Figure 2.2 PAMAM dendrimer functionalization of MWCNTs up to generation five

The MWCNT-PAMAMG_5 would take a structure of tree branch like depicted in **Figure 2.3**.

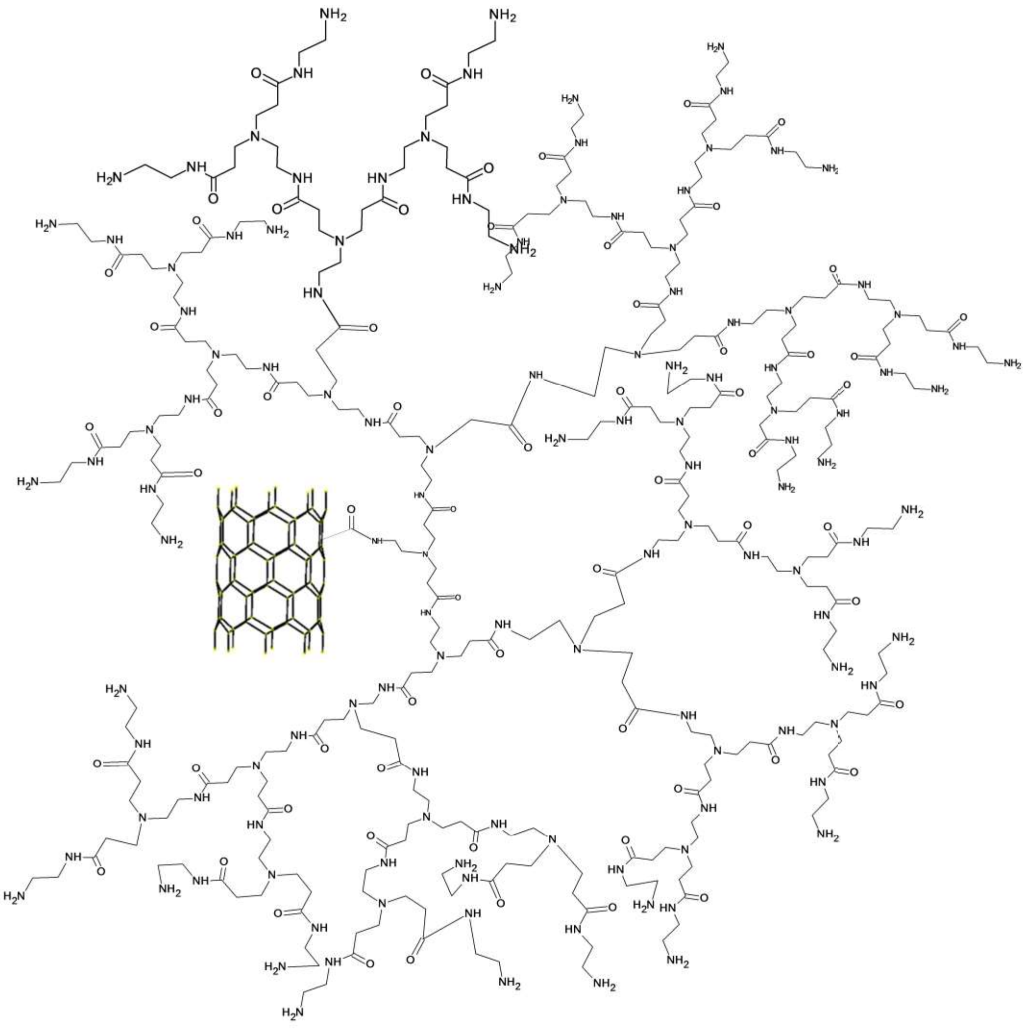

Figure 2.3 Schematic structure of MWCNT-PAMAM$_{G5}$

2.4.2 Functionalization of resin with crown ethers

Nitration and amination of DB18C6 and B15C5 fit carried out as described in literature[183, 184] with slight modification. Coupling of carboxyl group of PMA resin and amine group of amino crown ether [185, 186] is then carried out. A brief procedure is given below.

2.4.2.1 **4,4'-dinitrodibenzo-18-crown-6 (DNDB18C6) and 4'-nitrobezo-15-crown-5 (NB15C5)**

2.4.2.1.1 Nitration of DiBenzo-18-Crown-6 (DB18C6)

DB18C6 (10 g) was dissolved in 200 mL of chloroform. After mixing 150 mL of glacial acetic acid, nitrating mixture (7 mL of concentrated nitric acid in 20 mL of glacial acetic acid) was added drop wise into the mixture under stirring. The stirring was continued for next 24 hours at room temperature. The resulting brown colour reaction mixture was washed with aqueous sodium carbonate until neutral to litmus. Then the organic layer was separated and the aqueous layer was extracted twice with fresh chloroform. The combined organic layers were dried over anhydrous $MgS0_4$ and distilled off the chloroform. The brownish yellow residue of 4, 4′-DiNitroDiBenzo-18-Crown-6 (DNDB18C6) was dried under vacuum at 50°C for overnight. The pure product was obtained after the recrystallisation from hot ethanol. m.p. 203-205°C. Yield 84%. IR (KBr): 1345 and 1520 cm^{-1} ($-NO_2$) 1614, 1519, 1513 (benzene rings); 1229 (C C); 1131, 1031 (C-O); UV-Vis Spectra (hot ethanol): λmax (nm) = 298 and 338.

2.4.2.1.2 Nitration of Benzo-15-Crown- (B15C5)

5g of monobenzo-15-crown-5 was dissolved in mixture of 70ml chloroform and 60ml acetic acid, 17ml of nitric acid (70%) was added drop-wise over a 30 min time period. The mixture was left for stirring for 24 hours. The mixture was then neutralized with aqueous Na_2CO_3 and chloroform layer was separated. The aqueous layer was extracted with $CHCl_3$ 2-3 times so as to ensure maximum extraction. The combined chloroform extracts were dried over $MgSO_4$.The $CHCl_3$ was distilled in vacuum distillation unit at about 50^0C; a yellow-coloured solid crude NB15C5 product was obtained. m.p. 70^oC. Yield 75%. IR(KBr): 3090, 2945, 2870, 1587, 1520, 1450, 1338, 1280, 1137, 1090, 1048, 950, 925, 875, 806, 745, 650 cm^{-1}. 1H NMR (500 MHz, TMS): 3.756 (m, 16 $–CH_2$-), 6.866-7.911 (m, 3 ArH).

2.4.2.2 **4,4'-diaminodibenzo-18-crown-6 (DADB18C6) and 4'-aminobezo-15-crown-5 (AB15C5)**

2.4.2.2.1 Amination of DiNitroDiBenzo-18-Crown-6 (DNDB18C6)

DNDB18C6 (10 g) was dissolved in 400mL of boiling ethanol. To the solution, 1.2 g of 10% Pd/C catalyst was added and then solution of 60 mL of hydrazine hydrate was, cautiously, added dropwise. The reaction mixture was refluxed for 7 h and then filtered hot; the diamino derivative (white cotton like) precipitated by cooling/long standing. The white solid product was obtained by filtration. The pure product (for characterization) was obtained after the recrystallisation from ethanol. m.p. $178-182^oC$. Yield 45%. IR (KBr, cm^{-1}): 3423, 3356 [187]; 1614, 1519, 1513 (benzene rings); 1229 (C C); 1131, 1031 (C O).

2.4.2.2.2 Amination of NitroBenzo-15-Crown-5 (NB15C5)

The crude NB15C5 was dissolved in 100ml of ethanol at boiling point of ethanol. The whole clear solution was transferred to a 3-neck RBF placed over an oil bath with magnetic stirrer. Temperature of oil bath maintain such that ethanol nearly at boiling. Condenser was added to the RBF; water flow to the condenser started. Then 0.5 g of Pd/C (10%) was added to the reaction mixture slowly. 25 mL of hydrazine hydrate was added very slowly with very small portions from the side neck of the RBF through a funnel so that it touches the mixture on the wall of the RBF. The mixture was refluxed for minimum 7 hours. The resulting reaction mixture was immediately filtered in hot condition through Whatman 541 filter paper; black residue was washed three times with hot ethanol; funnel should not be disturbed, so as to stop black residue to come to the filtrate. Again the mixture was mixed with water and extracted with chloroform. The chloroform layer was dried over $MgSO_4$ and $CHCl_3$ was distilled off. Brown color oil of AB15C5 formed which solidified upon standing. Yield 65%. IR (KBr): 3336, 3220, 2876, 2361, 1617, 1510, 1457, 1350, 1300, 1225, 1123, 1190, 943, 980, 847, 650 cm^{-1}. 1H NMR (500 MHz, TMS): 3.451 (m, 16 $–CH_2$-), 5.340 (s, broad, 2H, NH_2), 6.193-6.264 (ds, 1H, H_b), 6.706-6.726 9dd, 1H, H_c), 7.266 (s, 1H, H_a).

2.4.2.3 **Crown ether grafting on polymethylacrylate (PMA) resin**

Crown ether grafted PMA resin was synthesized by amidation coupling reaction between carboxyl of PMA resin and amine of crown ethers in presence of coupling agent DCC/DMAP or EDCl/HOBt in DMF solvent.

2.4.2.3.1 B15C5 functionalized PMA resin (PMA-B15C5)

25 g of DADB18C6 dissolved in DMF was added in 50 g of dry white PMA resin (-COOH content: 9.6mmol/g) swelled in DMF. The mixture was either slowly stirred using magnetic stirrer or shaken in a orbital shaker. 20 g of DCC activating agent followed by

3.2 g of DMAP additive agent (of EDCl/HOBt) were added. After 10 min, the 300 ml solution of DADB15C5 in DMF is poured slowly into the reaction flask under magnetically stirring or shaking condition. The mixture was stirred gently for another 24 hours or shaken in orbital shaker for 120 hours. The grafted resin was filtered and washed with copious amount DMF, water and methanol till the supernatant become colorless. The light brown colored DADB18C6 was dried in vacuum oven at 80°C for overnight.

2.4.2.3.2 DB18C6 functionalized PMA resin (PMA-DB18C6)

Similar process as the preceding section was followed to make brown colored PMA-B15C5 from PMA resin and AB15C5.

The whole reaction scheme of the crown ether functionalization is depicted in **Figure 2.4** and **2.5**.

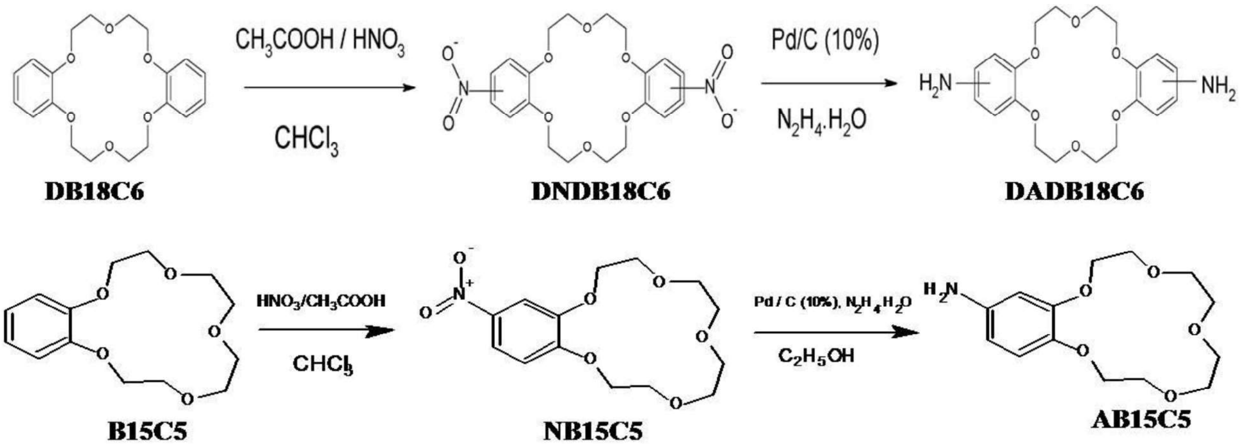

Figure 2.4 Preparation of amino crown ethers from crown ethers

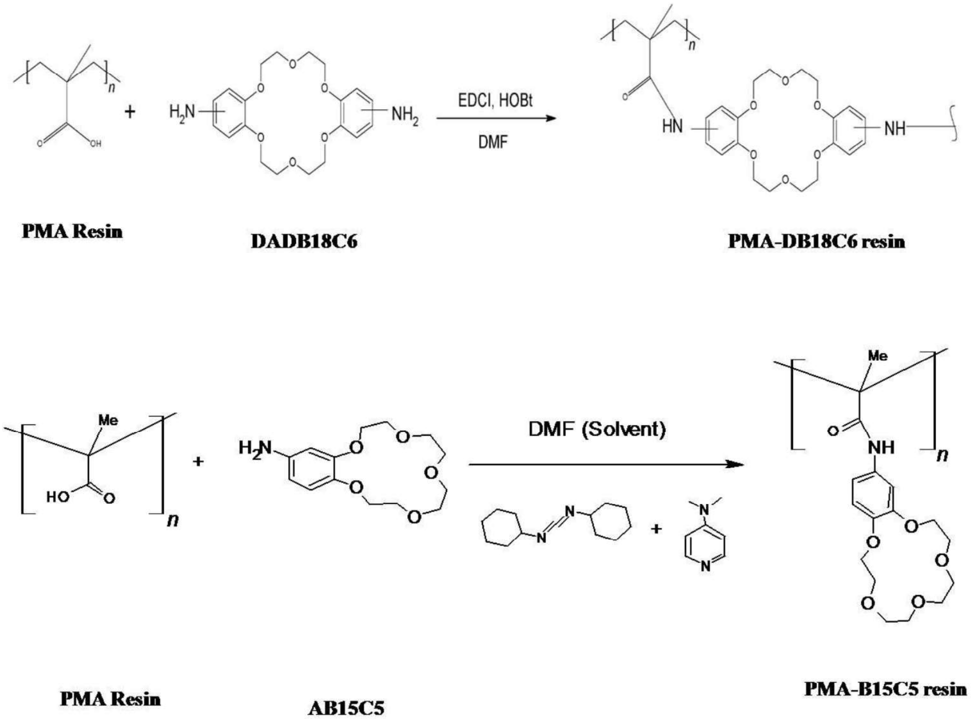

Figure 2.5 Coupling reactions to prepare DB18C6 and B15C5 functionalized PMA resin

2.5 Characterization

2.5.1 Characterization of functionalization on MWCNTs

2.5.1.1 Element (CHNS) Analysis

Table 2.2 shows the elemental composition of synthesized materials and their intermediates. It can be observed that MWCNT-SH and MWCNT-DTC contain some amount of Sulphur while the other materials contain no sulphur. More amount of sulphur in MWCNT-DTC is because the structure of dithiocarbamate contains more sulphur compared to thiol.

The growth of PAMAM dendrimer upto generation 5 can be clearly seen from the gradual increase in the oxygen and nitrogen content with increase in generation numbers in the elemental analysis of CNT-PAMAM samples (**Table 2.3**).

Table 2.2 Elemental composition of functionalized MWCNTs

	Elemental Composition				
	C (wt%)	H(wt%)	O(%)	N(wt%)	O(wt%)
CNT-COOH	91.92	0.69	0.17	0	7.21
CNT-SH	86.48	1.19	1.06	0.53	10.74
CNT-AA	88.0	2.89	2.95	0	6.16
CNT-DTC	83.7	1.67	4.06	0.91	9.67

Table 2.3 Elemental composition of MWCNTs functionalized with PAMAM dendrimer upto generation 5

	C (wt%)	H(wt%)	O(%)	N(wt%)
CNT-PAMAMG1	88.00	2.89	6.16	2.95
CNT-PAMAMG2	88.74	2.08	6.06	3.12
CNT-PAMAMG3	86.32	2.42	7.63	3.63
CNT-PAMAMG4	85.14	2.44	8.49	3.93
CNT-PAMAMG5	83.16	2.81	9.49	4.54

2.5.1.2 FTIR Spectra analysis

Stepwise Chemical modification of MWCNTs to diglycolamic acid functionalized MWCNTs were monitored by analyzing the FT-IR spectra of end product at each step. FT-IR spectrum of MWCNTs (as received), MWCNT-COOH and MWCNT-DGA are shown in **Figure 2.6(a)-(c)**. Infrared spectra of MWCNTs (as-received) are featureless (Figure 2.6 a). In Figure 1(b), the peaks at 2800-3050 cm^{-1} region are characteristic of C-H stretches and the broad shoulder band at 3100-3600 cm^{-1} region is characteristic of acid O-H stretches. The dominant peak at 1638 cm^{-1} can be clearly assigned to the hydrogen bonded carboxylic acid and 1448 cm^{-1} peak can be due to O-H in plane bending of carboxylic acid. In the FT-IR spectrum of MWCNT-DGA (Figure 2.6c) the broad peak at 3425 cm^{-1} can be assigned to the N-H stretching mode of the amide moiety. The peak at 1742 cm^{-1} can be due to C=O stretch of acid and the peak at 1610 cm^{-1} can be C=O stretch in amide moiety. Bands at 1414 and 1310 cm^{-1} can be identified as the C-N stretching. Peaks at 1125 and 1060 cm^{-1} are due to C-O-C stretching mode of diglycolamic acid group.

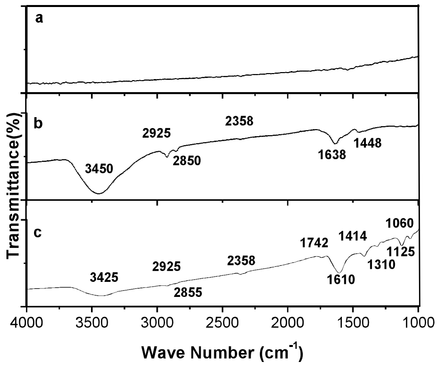

Figure 2.6 FT-IR Spectra of (a) MWCNTs (as received), (b) carboxylated MWCNTs and (c) DGA functionalized MWCNTs

The FT-IR spectrums of CNT-COOH, CNT-AA, and CNT-SH, CNT-DTC are recorded and the characteristic bond vibrational frequencies of all the compounds with their interpretation are shown in **Table 2.4**. The presence of peaks at 3445 and 1650 cm^{-1} are related to the stretching vibrations of v(OH) and v(C=O) of the carboxyl groups (COOH), respectively. Symmetric and asymmetric methylene stretching bands at 2935 and 2891 cm^{-1}, respectively, are observed to be present in the MWCNTs-COOH. It is assumed that defective sites on the sidewall of MWCNTs contain these groups. These characteristic peaks are presents for all the CNTs. The peak at 3420 cm^{-1}overlapping with the stretching vibration of v(-OH) in the MWCNTs-NH$_2$ is due to the –NH$_2$ stretching of the amine group that confirms the successful engulfing of the amine to carboxyl groups. The vibrational peak for C-S at 650-700 cm^{-1} along with amidic peak around 1642 cm^{-1} in the spectrum of MWCNT-SH suggest the attachment of –SH group through the amidic linkage with carboxyl of MWCNT-COOH and amine of cysteamine. The FT-IR spectra of MWCNT-DTC showed the appearance of new peaks at 1020cm^{-1} and 1250 cm^{-1}, which are representatives of the v(C=S) vibration and v(N-C=S) vibration of dithiocarbamate group. The peak at 3420cm^{-1} is due to the N-H stretching vibration of the amine group. The data verified that thedithiocarbamate groups were successfully introduced to MWCNTs. As shown in **Table 2.5**, the growth of PMAMAM dendrimers on the MWCNT surface was monitored the appearance of carbonyl ester vibration peak (1700 cm^{-1}) in the half generations ($\text{CNT-PAMAM}_{\text{Gx},\ [x=0.5,\ 1.5,\ 2.5,\ 3.5,\ 4.5]}$) and amide carbonyl peak (1640 cm^{-1}) in the full generations ($\text{CNT-PAMAM}_{\text{Gx},\ \{x=1,\ 2,\ 3,\ 4,\ 5\}}$) with enhanced peak intensities in the higher generations.

Table 2.4 Characteristic FTIR peaks of the functionalized CNTs

Compound	**Characteristic Peak (cm^{-1})**	**Interpretation**
MWCNT-COOH	3445	O-H stretching of carboxyl
	2935, 2891	Aliphatic C-H stretching
	1650	C=O stretching of carboxyl
MWCNT-NH_2	3420	N-H of stretching of amine and amide
	2935, 2891	Aliphatic C-H stretching
	1743, 1640	C=O stretch of acid, amide
	1540, 1520	-NH bending, C=C stretching
MWCNT-SH	2935, 2891	Aliphatic C-H stretching
	1642	C=O stretching of amide
	650-700	C-S stretching
MWCNT-DTC	2935, 2891	Aliphatic C-H stretching
	1642	C=O stretching of amide
	650-700	C-S stretching
	1020, 1250	C=S, N-C-S stretching

Table 2.5 Characteristic FTIR peaks of CNT-PAMAM dendrimers

Sample	IR pear (cm^{-1})	Interpretation
MWCNT-COOH	1700	C=O str. acid
MWCNT-$PAMAM_{GX.5}$	1725	C=O str. ester
MWCNT-$PAMAM_{GX.0}$	1640	C=O str. amide

2.5.1.3 **XRD Analysis**

X-ray diffraction was carried out to investigate alteration in the crystalline structure of the CVD prepared MWCNTs upon the functionalization with DGA groups. **Figure 2.7** compares the XRD patterns for the MWCNTs and DGA-CNT. Generally, it is evident from the patterns that the MWCNTs, and DGA-CNT exhibit two peaks; one at 26.2° (0 0 2 plane) and the other at 44.2° (1 0 0 plane), corresponding to an inter-planar space of 3.4 Å and 2.0 Å, respectively[188]. These are characteristic peaks of MWCNTs[189]. Thus functionalization of the MWCNTs with DGA groups did not alter the crystallographic character of the MWCNTs as it possessed only two prominent peaks, although the XRD pattern of DGA-CNT was also characterized by a new small peak at 27.6^0which could be due to the high degree of functionalization on the surface of the MWCNTs. This clearly indicates that even after the functionalization there is no change in the cylindrical wall structure as raw MWCNTs and inter planner spacing. Again, X-ray diffraction was carried out to investigate the crystalline structure of the functinalized CNTs and its Hg bonded form after adsorption study. **Figure 2.8** compares the XRD patterns for the CNT-SH and Hg adsorbed CNT-SH. Generally, it is evident from the patterns that the MWCNTs, and CNT exhibit two peaks; one at 26.2° (0 0 2 plane) and the other at 44.2° (1 0 0 plane), corresponding to an inter-planar space of 3.4 Å and 2.0 Å, respectively.

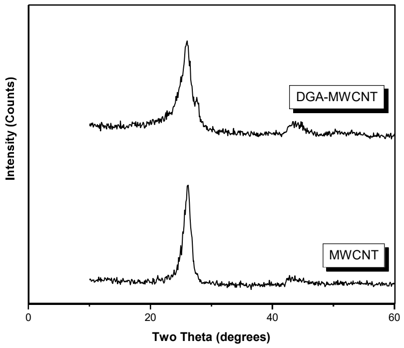

Figure 2.7 XRD pattern of MWCNTs and DGA-functionalized MWCNTs

These are characteristic peaks of MWCNTs. Thus functionalization of the MWCNTs with SH groups did not alter the crystallographic character of the MWCNTs as it possessed only two prominent peaks, although it has also small peak at 27.6^0 which could be due to the high degree of functionalization on the surface of the MWCNTs. The Hg adsorbed XRD pattern (red colour) is characterized by five evident extra peaks at 30.25, 34.68, 40.33, 45.10, and 58.16 degree, which are standard peaks of Hg-S, Hg compound. Thus XRD analysis confirms the nanotubes structures and covalent complexation of the mercury ion on the CNT surface.

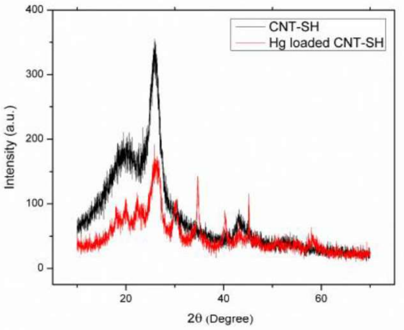

Figure 2.8 XRD pattern of CNT-SH and mercury ion adsorbed CNT-SH

2.5.1.4 SEM – EDS Analysis

Figure 2.9 depicts the SEM image of MWCNTs (as-received) and DGA-functionalized-MWCNTs. It is observed that the tubular structure of multi-walled carbon nanotubes is well retained after functionalization.

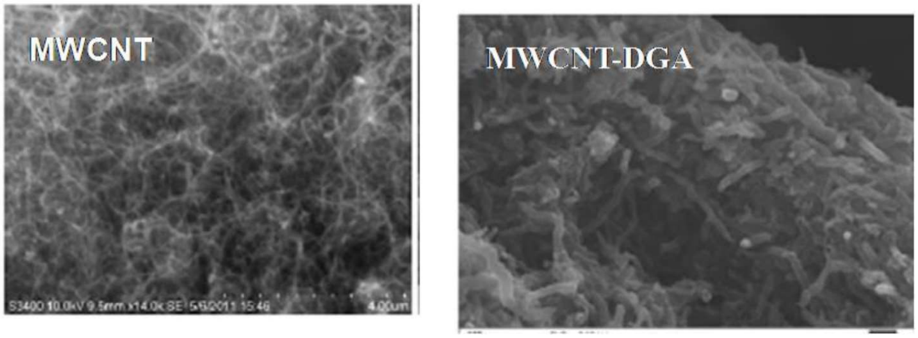

Figure 2.9 SEM image of MWCNTs and Diglycolamide functionalized MWCNTs

The agglomerated tubes of MWCNTs are vividly seen in the low resolution SEM image of MWCNT-SH and MWCNT-DTC in **Figure 2.10** (a) and (b), respectively. The presence of Sulphur and oxygen element due to the attachment of the thiol and DTC group on the surface of CNT can be attributed from the corresponding peaks in the EDS spectrum.

2.5.1.5 TEM imaging

The surface morphological structure of the prepared DGA-CNT was studied using TEM imaging. **Figure 2.11** shows representative images at low magnifications and high resolutions. It is clear from the images that the tubular structures are multiwall in nature with outer diameter 10-30 nm and 10-15 numbers of walls with hollow core of CNT. The patches in the images may be attributes to the chemical functionalization on the surface of the CNT. High resolution TEM image reveals that the walls are well aligned and the distance between the walls is about 3.4 Å.

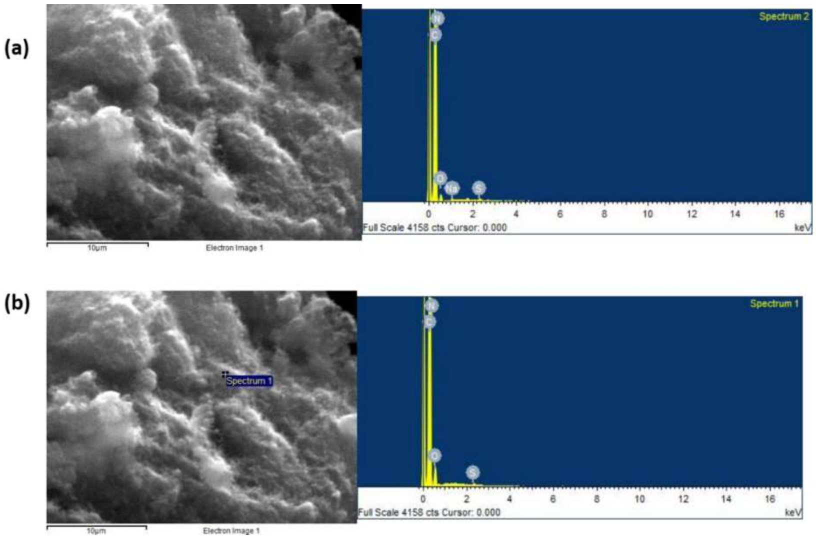

Figure 2.10 SEM image and EDS spectrum of (a) MWCNT-SH, and (b) MWCNT-DTC

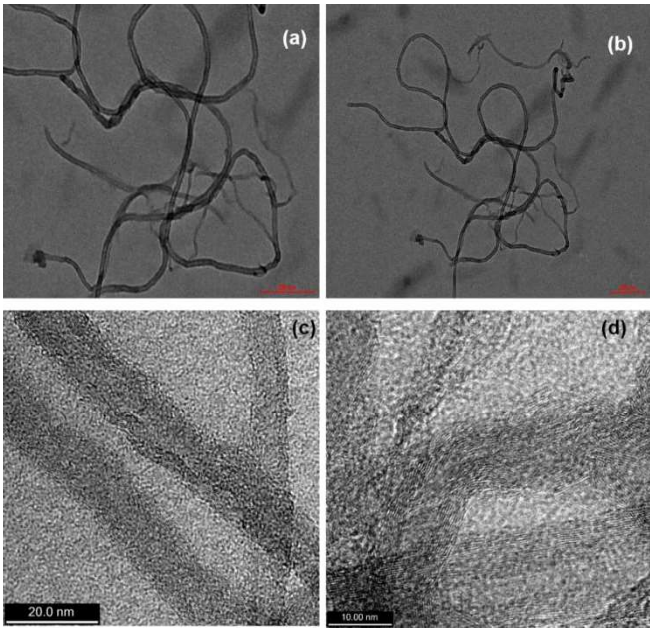

Figure 2.11 TEM Micrographs of prepared DGA-CNTs: (a), (b) low magnification, and (c), (d) high resolution

2.5.1.6 **Raman Spectroscopy**

The functionalized MWCNT's were characterized by Raman Spectroscopy which is a powerful tool for characterizing functional groups. The Raman spectrum is shown in **Figure 2.12** There are two types of peaks observed in Raman spectra of CNTs, G lines (tangential mode peaks) and D lines (attributed to defects and disorder induced peaks). The G lines generally appear at 1560-1580 cm^{-1} and D lines are observed at 1338-1340 cm^{-1} for MWCNT, MWCNT-COOH and MWCNT-AA[189]. The (I_D/I_G) ratio changes from MWCNT to MWCNT-COOH and MWCNT-AA indicating a partial destruction in the conjugation structure of the MWCNTs due to functionalization[190]. Significant differences in the tangential vibration mode (TM) can also be observed in the in the MWCNT functionalized with COOH and $CONHCH_2CH_2NH_2$ group. The TM peak was found to shift downwards from MWCNT to MWCNT-AA sample (from 1579 cm^{-1} to 1569 cm^{-1}). The softening in the TM can be interpreted in terms of valence electron transfer from the electron donor, the $–NH_2$ group into the π* band of carbon.

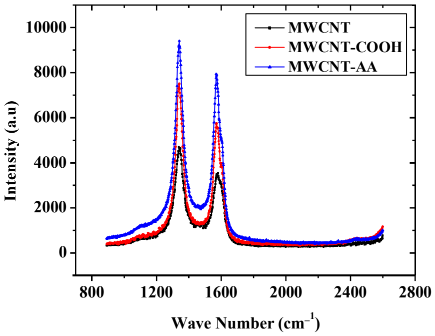

Figure 2.12 Raman spectra of the functionalized and un-functionalized MWCNT

2.5.1.7 **XPS spectroscopy**

The C-1s XPS core-level spectrum of the MWCNT-COOH and MWCNT-AA are given in **Figure 2.13**A and **2.14**A respectively, where curve fitting and deconvolution of the spectrum yields two and three separated spectra with different BE values for C atoms residing in various chemical environments for MWCNT-COOH and MWCNT-AA respectively. The intense component peak of the deconvoluted C-1s spectrum appeared at the lowest BE of 284.8 eV (FWHM: 1.44 eV) is ascribed to the non-oxygenated ring C of C – C or C – H. The broader and less intense peak appearing at BE of 286.1 eV (FWHM: 2.31 eV) refers to the C of O=C – OH functional groups for the MWCNT-COOH. The deconvoluated C1s spectra of MWCNT-AA (**Figure 2.14**A) shows a presence of another carbon with different chemical environment and is ascribed to the C-N of the amido-amine functional group thus indicating clearly the presence of amino group in MWCNT-AA. The deconvoluated O1s XPS spectra (**Figure 2.13**B and **2.14**B) of the more surface specific element O (the O1s photoelectron kinetic energies are lower than those of the C1sand so the sampling depth of O1s is smaller) reveal that the oxygen in MWCNT-COOH and MWCNT-AA exists in a single electronic state. The existence of N1s XPS spectra (**Figure 2.14**C) in MWCNT-AA and the absence of the same in MWCNT-COOH prove the existence of ‘N’ bearing functional groups in the MWCNT-AA.

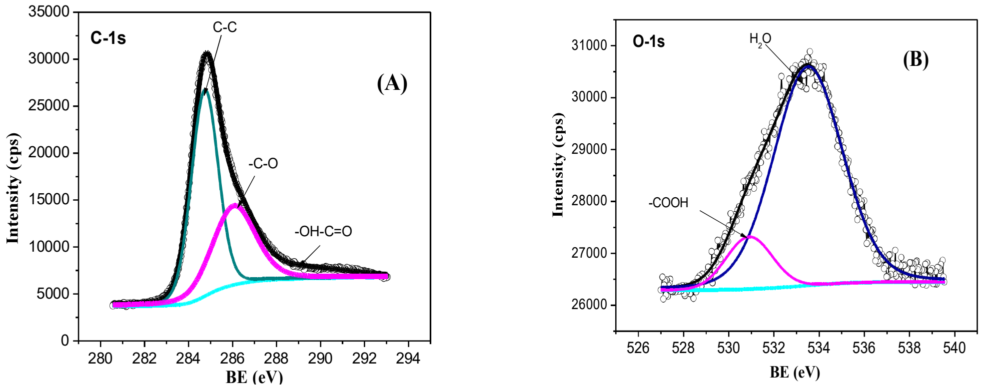

Figure 2.13 High resolution XPS core level spectra, (A) C-1s and (B) O-1s of the MWCNT-COOH (line with bullets: experimental data; solid line: curve fit for the experimental data)

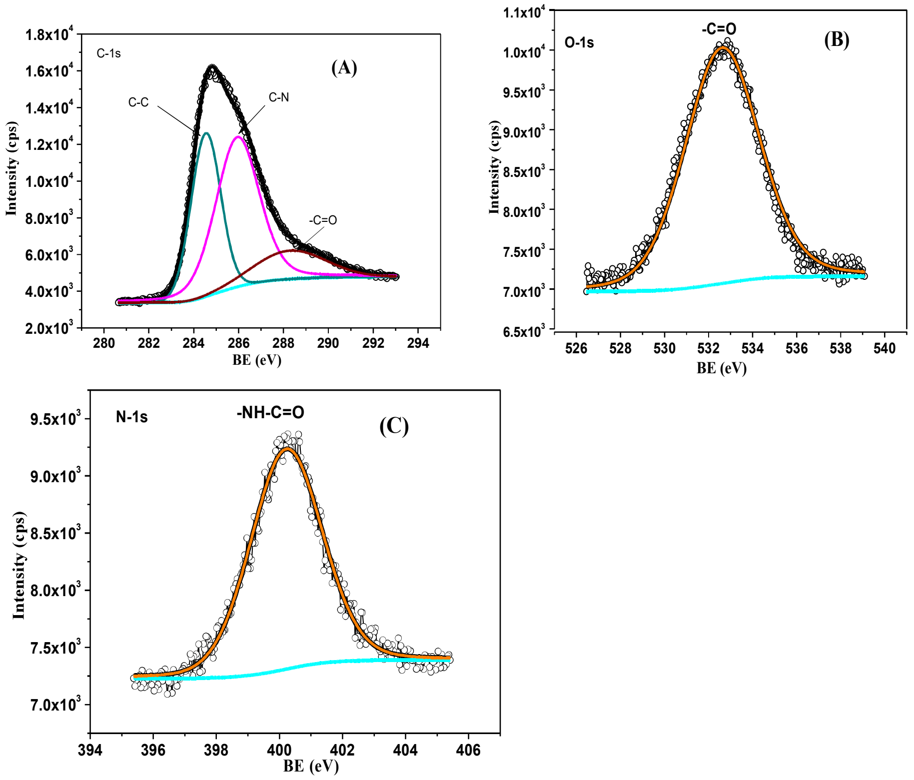

Figure 2.14 High resolution XPS core level spectra, (A) C-1s and (B) O-1s (C) N-1s of the MWCNT-AA material (line with bullets: experimental data; solid line: curvefit of the experimental data).

2.5.1.8 **TGA analysis**

Figure 2.15 shows the TG-DTA curves for MWCNT-AA. The sample was heated from 30^{o}C to 1500^{o}C at 20^{o}C/min in a nitrogen atmosphere. The TG curve shows that 20% weight loss occurred till 1400^{0}C. In inert atmosphere MWCNTs have been found to be stable up to 1300^{0}C. Decomposition after this temperature is [133] observed in the endothermic peak of the DTA curve of **Figure 2.15**. Thus, the initial exothermic peak in the DTA curve and weight loss in the TG curve may be attributed to the decomposition of the amidoamine functionality anchored on the surface of the MWCNTs.

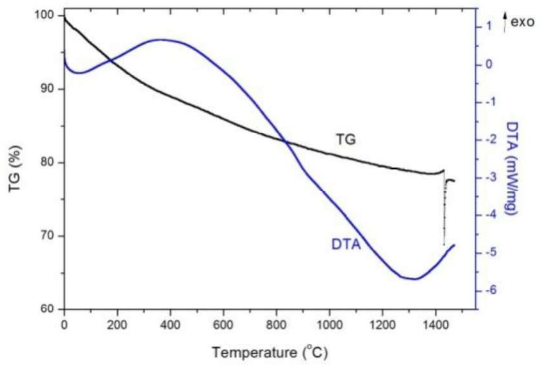

Figure 2.15 TGA-DTA curves for MWCNT-AA

2.5.1.9 **DLS Study**

Though DLS is mainly used to estimate the hydrodynamic radius of spherical shaped particles, it has also been used to give the particle size distribution of CNTs. **Figure 2.16** shows the distribution of particle size of the dispersion of MWCNT-AA in water medium as measured by the DLS instrument. The aqueous suspension of MWCNT-AA shows a mean size of 33- 42 nm which may be attributed to the lower degree of agglomeration in the polar solvents resulting from the presence of amidoamine functionality on the surface of MWCNTs. This leads to the hydrodynamic size being just 10-20 nm larger than the outer diameter of the nanotube.

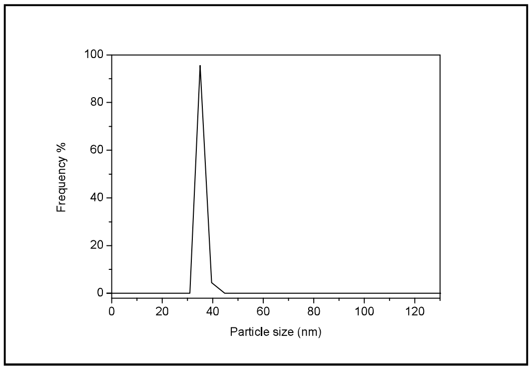

Figure 2.16 DLS size distribution curve of MWCNT-AA

2.5.2 Characterization of functionalization on PMA resins

2.5.2.1 **FTIR spectroscopy**

The characteristic peaks for the nitration of B15C5 and amination of NB15C5 are interpreted in the synthesis section. **Figure 2.17** shows the FTIR spectra of B15C5, NB15C5, and AB15C5.

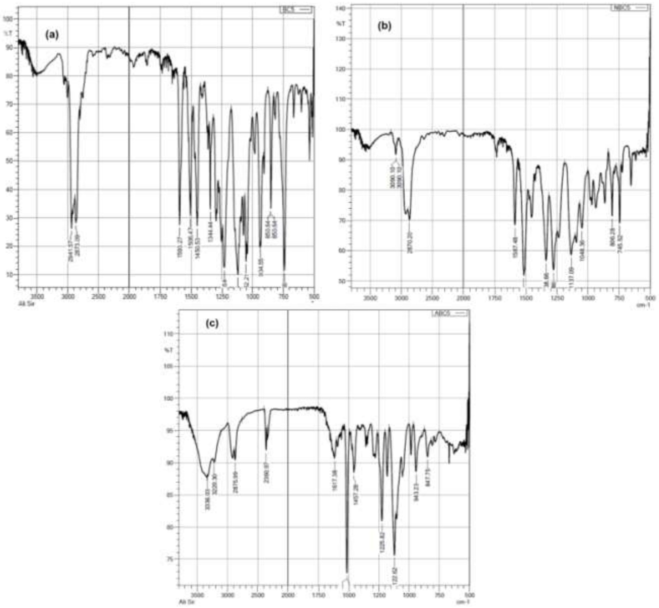

Figure 2.17 FTIR spectra of (a) B15C5, (b) NB15C5, and (c) AB15C5

FTIR spectra of PMA resin and PMA-B15C5 are showed in **Figure 12.18**. The appearance of amide (CO-NH) bond vibration (1620-1660 cm^{-1}) along with the carboxyl peak (1715 cm^{-1}) of PMA polymeric backbone indicates the bonding of –COOH of PMA and –NH$_2$ of AB15C5.

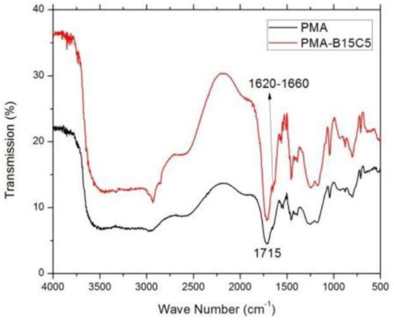

Figure 2.18 FTIR spectra of PMA and PMA-B15C5

2.5.2.2 **NMR spectroscopy**

The characteristic 1H NMR chemical shifts for the nitration of B15C5 and amination of NB15C5 are mentioned and interpreted in the synthesis section. **Figure 2.19** shows the ^{1}H NMR spectra of B15C5, NB15C5, and AB15C5.

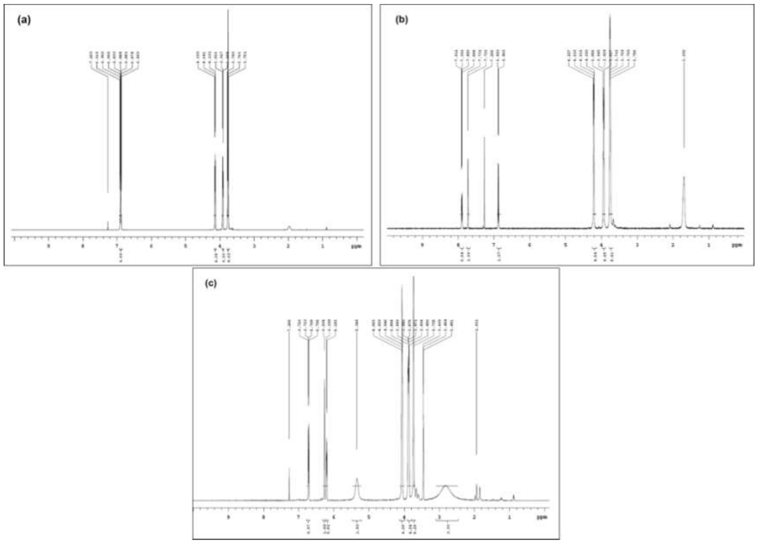

Figure 2.19 ^{1}H NMR spectra of (a) B15C5, (b) NB15C5, and (c) AB15C5

2.5.2.3 **TGA analysis**

The overlay TGA curves of PMA and PMA-B15C5 are shown in **Figure 2.20**. The little lower thermal stability of PMA-B15C5 throughout the temperature range can be attributed to the surface modification due to functionalization reaction. The higher weight loss at 370^0C indicates the detachment of B18C5 crown ether from the PMA surface prior to the decomposition of the polymeric network.

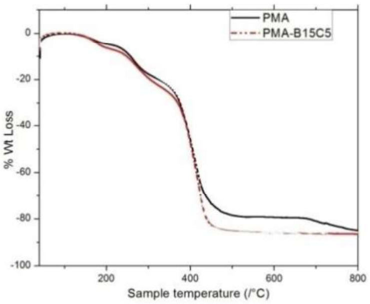

Figure 2.20 TGA curves of PMA and PMA-B15C5

2.5.2.4 **SEM microcopy**

The surface morphology of PMA and PMA-B15C5 resin are studied by SEM microscopy. As can be seen from the **Figure 2.21** functionalization has resulted in roughness in the surface of the resin beads. The porous structure inside the beads has also modified indicating more porous nature after reaction.

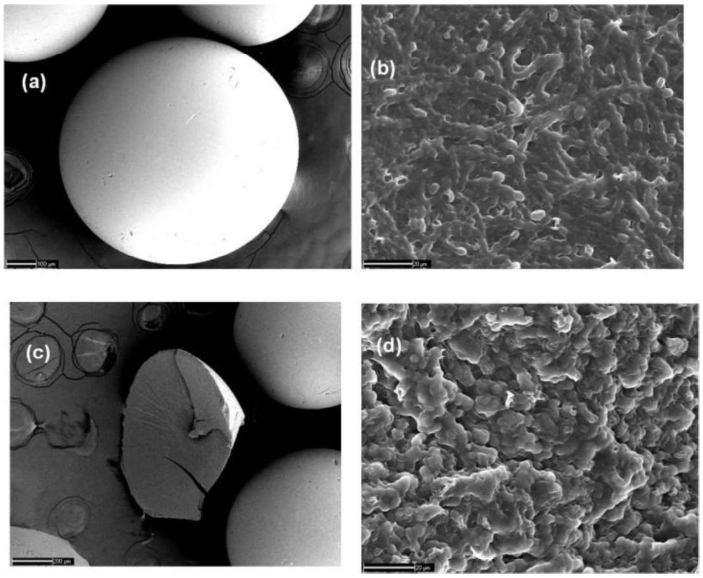

Figure 2.21 SEM images of PMA (a - b) and PMA-B15C5 (c – d) in lower (200µm) and higher (20µm) magnification

2.6 Experimental Adsorption Studies

2.6.1 Batch adsorption studies

Batch solid-liquid separation studies were carried out at room temperature. A fixed amount of adsorbent (5 – 25mg for MWCNTs and 50 – 250mg for PMA resin) and a fixed volume of suitable concentration of metal ions in a 50 mL screw capped glass vials or polypylene tubes were shaken mechanically for equilibration using an orbital shaker at room temperature for 2 - 4 hours. Dilute HNO_3 and NaOH were added to maintain desired pH. Separation of the metal loaded adsorbent was done by allowing the solution to settle down followed by centrifugation. Immediate analysis of the remaining transparent solution was done using ICP-OES. Experiments were performed by duplicate and average values were considered for the calculation.

The extraction profiles for radionuclide metal ions (Am^{3+}, UO_2^{2+}, Pu^{4+}, PuO_2^{2+}, NpO_2^{+}, and NpO_2^{2+}) were established using suitable amount of functionalized MWCNTs and was allowed to equilibrate for two hours with the aqueous phase containing radionuclide tracer (^{241}Am, ^{233}U, ^{239}Pu, and ^{239}Np) in specified oxidation states with acidity range 0.01 M - 6 M HNO_3 or pH range. It was then centrifuged for complete phase separation followed by the estimation of radiocuclide by radiometric analysis using liquid scintillation counting. All experimental data were the averages of duplicate or triplicate experiments. The relative errors of the data were about ±5%.

The amount of metal ion adsorbed (mg/g) at time't' and at equilibrium was calculated from the following equations, respectively:

$$q_t = (C_0 - C_t) \times \frac{V}{m} \tag{2.1}$$

$$q_e = (C_0 - C_e) \times \frac{V}{m} \tag{2.2}$$

Where C_o, C_t and C_e are thorium concentrations at initial, time't' and equilibrium (mg L^{-1}) respectively, V is the volume of the solution (L) and m is the mass of DGA-MWCNTs (g).

The adsorption of thorium was expressed in terms of distribution coefficient ($K_{d,}$ mLg^{-1}) and adsorption percentage (%), which were obtained from the following equations:

$$K_d = \frac{C_o - C_e}{C_e} \times \frac{V}{m} \tag{2.3}$$

$$\%Ads = \frac{C_o - C_e}{C_o} \times 100 \tag{2.4}$$

Where V, volume of the solution, should be expressed in mL.

2.6.1.1 **Effect of pH and acidity on adsorption**

Initial pH or acidity of the feed solution is an important factor which must be taken into account during adsorption studies. Therefore, experiments were carried out to investigate the effect of pH or acidity on the adsorption to find out the optimum pH at which separation experiments can be conducted. In order to evaluate the adsorption properties, solutions of fixed metal ion solution were prepared having pH between 2 to 10 or acidity between 0.01 to 6M HNO_3 respectively, and the experimental procedure described above was followed.

2.6.1.2 **Effect of contact time on adsorption and Adsorption Kinetics**

Adsorption kinetics, which describes the solute adsorption rate, is an important characteristic in evaluating the efficiency of adsorption. It is studied in order to understand the nature of the adsorbent surface along with the timeline of the entire process. Suitable amount of the adsorbent was added to a fixed volume of suitable concentration of metal ion solution having required pH or acidity. The solution was placed on the shaker for 4 hours at a controlled temperature of 30^oC, and Small volume of samples were withdrawn at time intervals of between 1 - 240 minutes and analyzed for metal ion concentration.

To get into more insight of sorption, the kinetics data were also fitted into different models for sorption kinetics: Lagergren first order or pseudo first order, pseudo second order and intra-particle diffusion model. The intra-particle diffusion model was also used to break the entire adsorption process into three parts in order to explain the steps followed during the adsorption process. Both the linear and non-linear forms as shown in **Table 2.6** of these models are used for fitting[191] .

Table 2.6 Basic and liner forms of adsorption kinetic model used for fitting

Model	**Basic form**	**Linear form**
Pseudo first order	$q_t = q_e(1 - e^{-k_1 t})$	$\ln(q_e - q_t) = \ln q_e - k_1 t$
Pseudo second order	$q_t = \frac{k_2 q_e^2 t}{1 + k_2 q_e t}$	$\frac{t}{q_t} = \frac{1}{k_2 q_e^2} + \frac{1}{q_e} t$
intra-particle diffusion	$q_t = k_i t^{0.5} + c$	$q_t = k_i t^{0.5} + c$

Where k_1 (min^{-1}), k_2 ($g\ mg^{-1}\ min^{-1}$) and k_i ($mg\ g^{-1}\ min^{-1/2}$) are the rate constant of the pseudo-first-order, pseudo-second-order and intraparticle diffusion model respectively. The parameters in these models can be determined by either by non-liner fitting using qt vs t plot or linear fitting using plots of $\ln(q_e\text{-}q_t)$ vs. t, (t/q_t) vs. t, q_t vs. lnt and q_t vs. $t^{0.5}$ respectively.

The pseudo first order rate equation of Lagergren has been widely applied to describe the kinetic process of liquid–solid phase adsorption[192]. If the concentration of one relative reactant remains constant as it remains in great excess, its concentration can be absorbed at the expressed constant rate, obtaining the pseudo first order reaction constant, because in fact, it depends on the same concentration of only one of the two reactants. The name physisorption was given for the model since the rate-limiting step in this kind of mechanism is diffusion and not dependent on the concentrations of both reactant (physical exchange)[193]. In pseudo second order model, the chemical reaction seems significant in the rate-controlling step and chemical reaction kinetics provide the best correlation of the experimental data and the adsorption's mechanism is chemically rate controlling and because of this it is called chemisorption[194]. The intra-particle diffusion model has been used to describe the sorption process occurring on a porous sorbent. A process is diffusion-controlled if its rate depends on the rate at which the components diffuse towards each other[195].

2.6.1.3 **Effect of initial metal ion concentration on adsorption and Adsorption isotherm**

Adsorption isotherm models represent the equilibrium relationship by explaining the mechanism of interaction between the adsorbate and adsorbent. An adsorption isotherm is an important curve describing the phenomenon governing the retention (or release) or mobility of a substance from the aqueous porous media or aquatic environments to a solid-phase at a constant temperature and pH[196]. Adsorption equilibrium is established when an adsorbate containing phase has been contacted with the adsorbent for sufficient time, with its adsorbate concentration in the bulk solution is in a dynamic balance with the interface concentration[197, 198]. Typically, the mathematical correlation, which constitutes an important role towards the modeling analysis, operational design and applicable practice of the adsorption systems, is usually depicted by graphically expressing the solid-phase against its residual concentration[199]. They are therefore indispensable for optimizing the adsorption pathway, modifying the surface properties of the adsorbent to enhance its capacity and also to design effective adsorption systems[200].

The isotherm data were then correlated with two parameter equilibrium isotherm models (Langmuir, Freundlich, Temkin and Dubinin-Radushkevich) as well as three parameter models (Redlich-Peterson, Sips and Toth) models. The governing equations of the models and parameters in the model are described in **Table 2.7**

Table 2.7 Description of the equilibrium isotherm models used

Parameters	Model	Basic form	Linear form
2	Langmuir	$q_e = \frac{q_m b C_e}{1+bC_e}$	$\frac{C_e}{q_e} = \frac{1}{q_m b} + \frac{C_e}{q_m}$
2	Freundlich	$q_e = K_F C_e^{1/n}$	$\ln q_e = \ln K_F + \frac{1}{n}\ln C_e$
2	Temkin	$q_e = B_t \ln(A_T C_e)$	$q_e = B_T \ln A_T + B_T \ln C_e$ $B_T = \frac{RT}{b}$
2	Dubinin-Radushkevich	$q_e = q_o e^{-B_{DR}\varepsilon^2}$ $\varepsilon = RT\ln(1+\frac{1}{C_e})$ $E_a = \frac{1}{\sqrt{2B_{DR}}}$	$\ln q_e = \ln q_0 - K_{DR}\varepsilon^2$
3	Redlich Peterson	$q_e = \frac{K_{RP}C_e}{1+a_{RP}C_e^{g}}$	$\ln(K_{RP}\frac{C_e}{q_e} - 1) = g\ln C_e + \ln a_{RP}$
3	Toth	$q_e = \frac{K_{th}C_e}{(a_T + C_e)^{1/t}}$	$\ln\frac{q_e}{K_{th}} = \ln C_e - \frac{1}{t}\ln(a_{th}C_e)$
3	Sips	$q_e = \frac{K_s C_e^{b_s}}{1+a_s C_e^{b_s}}$	$b_s \ln C_e = -\ln\frac{K_s}{q_e} + \ln a_s$

The description of each parameters are shown in **Table 2.8**

Table 2.8 Isotherm parameters' description

q_m	-	maximum monolayer coverage capacities (mg/g)
b	-	Langmuir isotherm constant (L/mg)
K_F	-	Freundlich isotherm constant (mg/g) (L/g)^n

n - adsorption intensity
B_t - Tempkin isotherm constant
K_T - Tempkin isotherm equilibrium binding constant(L/g)
q_o - theoretical isotherm saturation capacity (mg/g)
B_{DR} - Dubinin–Radushkevich isotherm constant(mol^2/kJ^2)
Ea - Energy of adsoption (kJ/mol)
K_{RP} - Redlich–Peterson isotherm constant (L/g)
a_{RP} - Redlich–Peterson isotherm constant $(L/mg)^g$
g - Redlich–Peterson isotherm exponent
K_{th} - Toth isotherm constant (mg/g)
a_{th} - Toth isotherm constant (L/mg)
t - Toth isotherm constant
K_s - Sips isotherm model constant (L/g)
A_s - Sips isotherm model constant (L/mg)
b_s - Sips isotherm model exponent

Langmuir isotherm explains monolayer formation in between adsorbate and adsorbent on the surface of adsorbent. The Langmuir isotherm is based on the following assumptions: (1) All the sorption sites on adsorbent are equivalent and it should have finite no of site; (2) Each active site can adsorb only one molecule of adsorbate; (3) There is no transmigration of adsorbate on the surface i.e. adsorbate molecule doesn’t interact with each other.

Freundlich isotherm is taking account of the heterogeneous surface of adsorption. It describes the relation between adsorbate concentration on the surface to the adsorbate concentration in liquid. This isotherm can be applied to multilayer adsorption and are not restricted to monolayer, with non-uniform distribution of adsorption.

The Tempkin isotherm model is based on the fact that the heat of adsorption of all molecules in the layer decreases linearly (not with a logarithmic nature) with a uniform distribution of binding energies.

Dubinin–Radushkevich isotherm is generally applied to express the adsorption mechanism with a Gaussian energy distribution onto a heterogeneous surface. This model was initially created for the adsorption of subcritical vapors onto micropore solids following a pore filling mechanism. D-R isotherm is good for the high solute activities, in intermediate range of concentrations. It is generally used for distinguishing the physical and chemical adsorption of metal ions, with its mean free energy, E per molecule of adsorbate.

Redlich–Peterson isotherm is a hybrid isotherm blending both Langmuir and Freundlich isotherms, adding three parameters into an empirical equation. The R-P equation has a linear dependence on concentration in the numerator and an exponential function in the denominator to express adsorption equilibria over a wide concentration range, that can be applied both for homogeneous or heterogeneous systems. In the limit, it approaches Freundlich isotherm model at high concentration (as the exponent g tends to zero) and is in accordance with the low concentration limit of the ideal Langmuir condition (as the values are all close to one).

Sips isotherm is also a combination of Langmuir and Freundlich isotherms deduced for predicting the heterogeneous adsorption systems and avoiding the limitation of the rising adsorbate concentration associated with Freundlich isotherm model. At low adsorbate concentrations, it reduces to Freundlich isotherm; while at high concentrations, it predicts a monolayer adsorption capacity characteristic of the Langmuir isotherm.

Toth isotherm model , is another empirical equation developed to improve Langmuir isotherm fittings (experimental data), and useful in describing heterogeneous adsorption systems, which satisfying both low and high-end boundary of the concentration.

2.6.1.4 **Effect of temperature on adsorption and adsorption thermodynamics**

The thermodynamic parameters such as change in standard free energy (ΔG^o), enthalpy (ΔH^o) and entropy (ΔS^o) for metal ion adsorption to MWCNTs or PMA resins can be obtained from the temperature dependent data. These parameters can be use to evaluate the orientation and feasibility of the physiochemical adsorptive reaction and can provide strong information regarding the inherent energy in the adsorbate-adsorbent interaction, structural changes due to adsorption, and also the mechanism involved in the process. The adsorption studies were carried out at different temperatures (40 to 80°C) with fixed metal ion concentration and amount of adsorbent at specific pH or acidity. The equilibration shaking was conducted at a particular temperature which kept constant during the shaking to separation of aliquot for metal analysis. These thermodynamic parameters were determined by using following equations[201].

$$K_0 = \frac{C_{solid}}{C_{liquid}} \qquad (2.5)$$

$$\Delta G^0 = RT \ln K_0 \qquad (2.6)$$

$$\ln K_0 = \frac{\Delta S^o}{R} - \frac{\Delta H^o}{RT} \qquad (2.7)$$

Here Ko is the equilibrium constant, C_{solid} is the solid phase concentration at equilibrium (mg L^{-1}), C_{liquid} is the liquid phase concentration at equilibrium (mg L^{-1}), T is the temperature in Kelvin and R is the gas constant (8.314×10^{-3} kJ $mol^{-1}K^{-1}$). The ΔH° (kJ mol^{-1}) and ΔS° (kJ $mol^{-1}K^{-1}$) values obtained from the slope and intercept of Van't Hoff where $\ln K_0$ is plotted against 1/T according to the equation 2.7.

2.6.1.5 **Desorption Studies**

Desorption of adsorbate from the adsorbent is essential to make it renewable in practice. Inorganic acid soliution or complexing agent like oxalic acid, Na_2CO_3, EDTA, thiourea were used for desorption of metal-loaded functionalized MWCNT or PMA resins. These stripping agent solutions were added to fixed amount of metal-loaded sorbent to perform desorption. The samples were placed on the shaker for 3 hours, following which analysis was performed using suitable techniques. % desorption was calculated in each case as:

$$\%Desorption = \frac{\text{Amount of metal ion released in supernatant}}{\text{Amount of metal ion adsorbed}} \times 100 \qquad (2.8)$$

2.6.1.6 **Regeneration Studies**

In order to be used at an industrial scale, an adsorbent should possess the ability to be regenerated, so that it can be used multiple times, thereby reducing the cost of the process and reducing waste, while also allowing easy desorption of loaded material from its surface, in order to recycle/store it by enabling its easy separation from other compounds. Metal-loaded functionalized MWCNT was desorbed and regenerated and thus several 6 cycles were performed. Adsorption was allowed for 3 hours, followed by desorption with stripping agent solution. Analysis with of the metal ions with suitable techniques was done at both, adsorption and desorption stage. The functionalized MWCNT was then washed multiple times with Millipore water and methanol, followed by drying under vacuum conditions. The dried and regenerated sample was then added to an equivalent amount of metal ion solution and further cycles of adsorption and desorption were thus carried out.

2.6.1.7 **Selectivity Study**

Any adsorbent should be selective in order to efficiently remove the specific adsorbate from wastewater. The adsorption of the desired metal ion from a mixture of other metal ions is thus an imperative study. For radionuclide extraction, the selectivity studies were conducted from simulated radioactive liquid waste solution whose composition are given in the concerned sections. The major source of mercury is industrial (e.g. chlor-alkali plant) waste water [202], and a typical cationic composition of it is depicted in **Table 2.9**. In order to test the selectivity and applicability of synthesized f-MWCNTs in industries, binary selectivity studies for Hg were performed using binary solution (individual metal ion concentration of 50 mg/L) with Cd, Mg, Si, Ca, Li and Na.

Table 2.9 Typical cationic composition of chloralkali waste water

Metal ion	**Concentration (mg/L)**	**Metal ion**	**Concentration (mg/L)**
Hg^{2+}	17.6	Ca^{2+}	41.2
Pb^{2+}	2.7	Na^{+}	280.8
Cd^{2+}	0.5	NH_4^{+}	20.7

2.6.1.8 **Radiolytic stability of f-MWCNTs**

The best sorbents for actinides are those which retain its efficiency even after high radiation energy deposition without any radiolytic degradation. So it is necessary to check radiolytic stability of new sorbent materials being used because during the processing of radioactive waste solution, the sorbent is expected to be in continuous interaction with high energy particle like alpha, beta and gamma. Due to high energy deposition there would be breaking of weker bonds in the sorbent materials which lead to different radiolytic products. Consequently, the sorption characteristics including efficiency may decrease. To observe the radiolytic stability, the f-MWCNTs was exposed to different amount of gamma irradiation exposure upto 1500 kGy. With the irradiated MWCNT materials, the sorption experiments were carried out following above procedure keeping metal concentration and adsorbate dose constant.

2.6.2 Fixed bed column adsorption studies

Batch adsorption studies provide indispensable information about the equilibrium characteristics, adsorption kinetics and thermodynamics, whereas column studies provide scale-up data required to design an adsorption column by providing breakthrough curves which govern the life span of a fixed adsorbent column[203]. In a batch reactor, very low residual concentrations can only be achieved if the adsorbent dose is very high. On the other hand, if a fixed-bed column study is carried out, the adsorbate can be completely removed until breakthrough is attained. Again, the solid-liquid extraction envisaged for zinc isotope separation must be carried out in continuous column chromatographic mode to achieve a reasonable isotope separation factor. In view of this, preset study tests mercury removal in a fixed-bed column made of MWCNT and MWCNT-AA, and Zn adsorption by PMA and PMA-DB18C6 in column chromatographic mode.

A glass column (ID -1cm, L - 25cm) was filled with 0.37 g of the MWCNT or MWCNT-AA on ceramic support. The bed height of the adsorbent was 5cm. First, 200 mL of distilled water having pH6 was delivered down flowto the column by using a peristaltic pump (Miclins Peristaltic Pump PP 20 EX model) at a flow rate of 0.7mL min^{-1}. The column study setup has been shown in **Figure 2.22** .Hg(II) solution (500 mg/L) was then passed through the column at the same flow rate till exhaustion of the column was attained. 5mL samples were collected during the entire duration and analyzed using ICP-OES. The desorption studies using 0.05M EDTA solution was carried out after mercury solution from the column was washed.

Figure 2.22 Small scale fixed bed column separation set up for Hg2+ removal by MWCNT-AA

The continuous zinc adsorption studies were conducted in a glass plastic-coated column with an internal diameter of 1.5 cm and length of 30 cm. A known quantity of PMA or DB18C6-PMA was placed in the adsorbent column to yield the desired adsorbent bed height of (3, 6, 10 cm). A solution of zinc sulphate of specific concentrations (70, 250, 500ppm) was then passed through the adsorbent bed using a peristaltic pump at the desired flow rates (0.5, 2, 4.5 mL/min). The fixed-bed column set up used is shown in **Figure 2.23**. Sampling of column effluent was done at specified time intervals in order to evaluate the parameters like breakthrough point, saturation point and the profile of (adsorption) breakthrough curve. The concentration of Zn (II) ions was determined by analysing the column effluent by ICP-OES. The operation of the adsorber was stopped when the adsorbent bed got saturated. The desorption/elution curves were obtained by passing the 1 M sulphuric acid throughout the loaded column using the same flow rate held for the adsorption. The adsorption-desorption cycles were conducted at different bed heights, initial concentrations and flow rates of the influent solutions. The modeling of the breakthrough curves was done for the determination of the parameters for the scale up process.

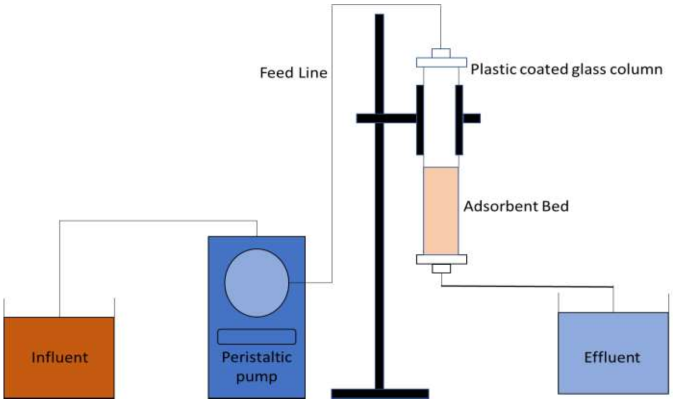

Figure 2.23 Extraction chromatography set up for Zn adsorption and isotope separation by PMA-DB18C6

Breakthrough curves (as shown in **Figure 2.24**[204]) are graphically represented in terms of normalized concentration, which is calculated as the ratio between outlet concentration (Co) and the inlet or feed concentration (Ci). The breakthrough time t_b and the exhaustion time t_e are defined as the time taken to reach Co/Ci= 0.05 and Co/Ce=0.95 respectively[205].

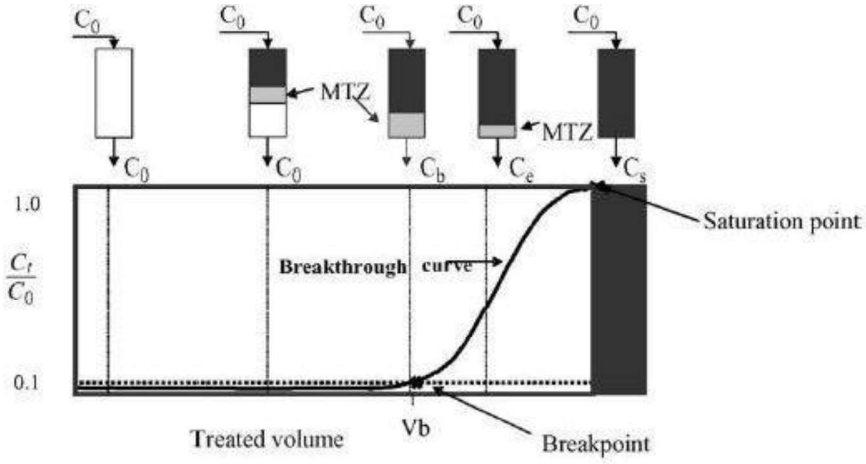

Figure 2.24 Typical breakthrough curves showing the movement of mass transfer zone

The total quantity of adsorbate adsorbed (Q_{tot}) for a given feed concentration and flow rate is the area under the curve where Co-Ci is plotted against V and is given as:

$$Q_t = \int_0^{v_T} (Co - Ci)dV \qquad (2.9)$$

Q_t can also be calculated by

$$Q_t = F_V C_0 \int_0^t \left(1 - \frac{C_t}{C_o}\right) dt \qquad (2.10)$$

where V_T is the volume of effluent collected at t_e, F_v is the feed solution volumetric flow rate (mL min^{-1} or m^3 h^{-1}). The adsorbent bed adsorption capacity (ABAC) can thus be calculated using equation 2.11

$$ABAC, Q_e = \frac{Q_{tot}}{M} \qquad (2.11)$$

where M is the mass of the adsorbent present in the fixed bed column. Equilibrium takes place in a broad zone of the adsorbent bed called the mass transfer zone (MTZ) which is characterized by concentrations and loading profiles. The height of the mass transfer zone (h_z)[19]can be calculated as

$$h_z = L\frac{t_e - t_b}{t_e} \tag{2.12}$$

where L is the bed height.

The empty bed contact time (or bed service time) is the time in which the adsorbent bed is in contact with the adsorbate feed solution. It is an important parameter in the design of a continuous adsorber and is often expressed in terms of the empty bed contact time (EBCT). It affects the volume to breakthrough and the shape of breakthrough curve. EBCT at different experimental conditions was determined from the following equation

$$\text{Empty bed contact time; } EBCT(\text{min}) = \frac{V_b}{F_v} \tag{2.13}$$

The performance of fixed-bed was further evaluated in terms of the adsorbent usage rate, Ur (g/L) which is defined as the weight of adsorbent saturated per litre of adsorbate solution treated. The Ur is given by Eq.

$$\text{Adsorbent usage rate, } U_r = \frac{m_a}{V_s} \tag{2.14}$$

where m_a is the mass of adsorbent in the adsorber (g), V_s is the volume of adsorbate feed solution treated at breakthrough (L).

2.6.3 Calculations for isotope separation from Column Chromatography

MC-ICP-MS provides the ratio of two pair of isotopes ($^{i}Zn/^{64}Zn$; i=66, 67, 68, 70) for batch and column solid-liquid extraction of Zn by PMA and PMA-DB18C6 resins. The enrichment factor was calculated as:

$$\beta = \left(\frac{^{i}Zn}{^{64}Zn}\right)_{sample} \Bigg/ \left(\frac{^{i}Zn}{^{64}Zn}\right)_{original} \qquad (2.33)$$

β values larger than 1.000 mean that the heavier isotope of zinc is preferentially enriched in the eluted samples.

In the present work, the total zinc isotopic fractionation was analytically studied at the breakthrough and elution samples collected by fraction during fixed-bed column chromatography run. Single-stage isotope separation factor, α, is defined in the equation 2.34 as the ratio $[^{H}Zn]/[^{64}Zn]$:

$$\alpha = \left(\frac{^{H}Zn}{^{64}Zn}\right)_{\text{Resin}} \Bigg/ \left(\frac{^{H}Zn}{^{64}Zn}\right)_{Solution} = 1 + \varepsilon \qquad (2.24)$$

where ^{H}Zn denotes heavy zinc ^{66}Zn, ^{68}Zn, or ^{70}Zn. $([^{H}Zn]/[^{64}Zn])_{\text{Resin}}$ and $([^{H}Zn]/[^{64}Zn])_{\text{solution}}$ are ratios for the resin and for the aqueous phase, respectively. Separation factor indicates the deviation of the isotopic abundance ratios between two different phases at equilibrium. ε in the equation denotes the separation coefficient. The value of the separation coefficient can be evaluated from the isotopic enrichment curves of the breakthrough line according to equation 2.25 which was developed by Spedding et al.[206] and by Kakihana[207].

$$\varepsilon = \frac{\sum q_i |R_i - R_0|}{Q_{tot} R_0 |1 - R_0|} \qquad (2.25)$$

where q_i is the amount of zinc in each fraction sample, Q_{tot} is the total amount of adsorbed zinc on the resin, R_i is the isotopic percentage of ^{H}Zn, and the subscripts i and o denote the fraction number and the original sample, respectively.

2.7 Computational protocol

2.7.1 Density Functional Theory

The central thought of DFT is to substitute the much problematical N-electron wave function and the allied Schrodinger equation with the simple electron density ρ (r). The well known Thomas-Fermi model is a quantum statistical model which assumes that the electrons are uniformly distributed over the six-dimensional phase space.

The overall energy expression for the molecular system in terms of electron density can be written by combining the kinetic energy term of Thomas and Fermi (1927) and the Exchange correlation energy term of Dirac (1930) as[163]

$$E_{TF}[\rho] = C_F \int \rho^{5/3}(\vec{r})d\vec{r} - Z\int \frac{\rho(\vec{r})}{r}d\vec{r} + \frac{1}{2}\iint \frac{\rho(\vec{r}_1)\rho(\vec{r}_2)}{r_{12}}d\vec{r}_1 d\vec{r}_2 + C_X \int \rho^{4/3}(\vec{r})d\vec{r} \qquad (2.26)$$

A huge effort was devoted to improve the Thomas-Fermi model with limited success in terms of predictability and accuracy of bonding . Finally, the essential breakthrough in density based theory was achieved by Hohenberg and Kohn (H-K) in 1964[208].

For any molecular system, the electron density is a function of only three spatial coordinates (for a given set of nuclear positions). The essence of the first H-K theorem is that the ground state energy of an N-electron system is a unique functional of its ground state electron density ρ(r) under an external potential v(r) .

$$\rho(\mathbf{r}_1) = N \int |\Psi(\vec{x}_1, \vec{x}_2, ..., \vec{x}_N; \vec{R}_1, ..., \vec{R}_{Nn})|^2 \, d\sigma_1 d\vec{x}_2 .. d\vec{x}_N \qquad (2.27)$$

The integral of the density over all space equals N. The total energy can be expressed as

$$E[\rho] = T[\rho] + V_{ee}[\rho] + \int \rho(\vec{r})V(\vec{r})d\vec{r} \qquad (2.28)$$

In 1965, Kohn and Sham[209] (KS) formulated an indirect way of calculating the kinetic energy functional which makes the DFT method as an efficient and powerful means for carrying out rigorous calculations. The KS method relies on the consideration of fictitious reference systems of non-interacting electrons that is constructed to have the same electron density as the system of interest. These electrons must move in a complex potential that takes into account the actual forms of electron correlation and the difference between the kinetic energy functional of the reference system and the real system.

The reference system of fictitious non-interacting particles has a rigorous solution in terms of single electron wave functions, or molecular orbitals known as the Kohn-Sham orbitals. Thus, we can express the kinetic energy exactly for the reference system as the sum of the expectation value of the Laplacian for each "electron".

$$T_S[\rho_S] = -\frac{1}{2}\sum_{j=1}^{N} < \chi_j \,|\, \nabla_j^2 \,|\, \chi_j > \tag{2.29}$$

Provided that the density of the real system, $\rho = \rho_S = \sum_{j=1}^{N}\sum_{\sigma} |\chi_j(\vec{r},\sigma)|^2$. Then, the energy functional of the real system is expressed as:

$$E[\rho] = T_S[\rho] + J[\rho] + V_{nn}[\rho] + Exc[\rho] \tag{2.30}$$

Where all the unknown terms are composed into the Exchange Correlation energy,

$$E_{xc}[\rho] = T[\rho] - T_S[\rho] + E_{ee}[\rho] - J[\rho] \tag{2.31}$$

The above expression for the Exchange-Correlation energy includes the error in the kinetic energy, the correlation effects, and also the correction for the self –interaction of the electron that has been incorporated in the classical Coulomb integral J.

The main challenge in implementing DFT is to uncover a good guess to the exchange-correlation energy functional $E_{xc}[\rho]$. There are various approximations to calculate $E_{xc}[\rho]$, such as Local Density Approximation [35], Local Spin density Approximation (LSDA), Generalized Gradient Approximation (GGA) and many other hybrid functional.

Since, most of the reactions occur in the liquid phase, it is important to take care of the solute-solvent interactions in calculations. The explicit treatment of solvent by inserting large number of solvent molecules around solute requires both electronic as well as geometry relaxation of the solute-solvent system, which is unworkable. The electrostatic behaviour of the solvent is accounted through continuum solvation models. The conductor like screening model [210] (COSMO) derives the polarization charges of the continuum, caused by the polarity of the solute by adopting scaled-conductor approximation. The essence of the model is that If the solvent behves like an ideal conductor the electric potential on the cavity surface must disappear. The charge q* on the surface segments can be computed from the distribution of the electric charge in the molecule using quantum chemistry. The charge q in a solvent of dielectric constant, ε is lowered by a factor $f(\varepsilon)$ as:

$$q=f(\varepsilon)q^* \qquad (2.32)$$

$$f(\varepsilon)=(\varepsilon-1)/(\varepsilon+x) \qquad (2.22)$$

Here, the value of x lies between 0-2. The interaction energy between the solvent and the solute molecule can be calculated from the determined solvent charges q and the charge distribution of the molecule.

The realization of the COSMO model are carried out by the following steps[201].

1. First, a cavity Γ separating the solute volume from the embedding dielectric continuum is constructed for a given solute geometry and is described as a set of m surface segments, with positions, t_I and areas, s_i.
2. The dielectric polarization of the continuum is represented by a set, $q = \{q_1,\ldots,q_m\}$, of apparent surface charges on the m segments. These are computed by a set of linear equations, $Aq + BQ=0$, from the charge distribution Q of the solute, where Q may be just a set of point charges or, usually, obtained from the nuclear charges and electron density of the solute. The linear operators, A and B depend on the used boundary condition.
3. The calculated total energy gain of the system due to the polarization of the continuum is then obtained using $qE_{tot} =0.5\Phi q$, where $\Phi = \{\Phi_1, \ldots,\Phi_m\}$ is the solute electrostatic potential on cavity Γ.
4. In the quantum electronic structure calculations, the screening charges q are resubstituted into the next SCF step as external charges, which generates a chnaged electron density and requires the recurrence of step 2 leading to self-consistency between the solute electron density and the polarization charges.

2.7.2 Structural and Bonding analysis

The coordination number of metal ion in the aqueous phase is very important for the design of ligand. If the metal ions experience a similar coordination environment in the extractant phase, the transfer will be facilitated with minimum energy barrier. In order to achieve an efficient extraction, the coordination of the ligand should satisfy the coordination of metal ion in the aqueous feed phase. The charge transfers from the ligand to metal ion during the complexation process can be monitored by orbital occupancy, charge on the atom, and HOMO-LUMO energies.

DFT has an extra-ordinary potential for calculating global and local indices that describe the inherent reactivity of chemical species quantitatively and is thus very useful to describe the host (crown ether) guest (metal ion) type interaction. Chemical systems are generally characterized by its electronic chemical potential, μ and absolute hardness, η and are defined as

$$-\mu = (I+A)/2 = \chi \qquad \eta = (I-A)/2 \qquad (2.23)$$

where I is the ionization potential and A is the electron affinity. Here, χ is called the absolute electronegativity. According to Koopmans' theorem, I and A can be obtained as

$$I = -E_{HOMO} \qquad A = -E_{LUMO} \qquad (2.24)$$

If donor acceptor system is brought together, electrons will flow from that of lower χ to that of higher χ, until the chemical potentials become equal. The amount of charge transfer, ΔN can be calculated by applying the following formula

$$\Delta N = (\chi_M - \chi_L) / \{2(\eta_M + \eta_L)\} \qquad (2.25)$$

Here, M stands for metal ion, which acts as Lewis acid i.e. acceptor and L stands for crown ether, which acts as Lewis base i.e. donor.

A higher value of E_{HOMO} indicates a tendency of the molecule to donate electrons to appropriate acceptor molecule of low empty molecular orbital energy. On the other hand, the energy of the lowest unoccupied molecular orbital indicates the ability of the molecule to accept electrons. Larger values of the energy difference, $\Delta E = E_{LUMO} -$

E_{HOMO}, provide low reactivity to a chemical species and lower values of the energy difference indicates higher reactivity.

Another important criterion in metal ligand complexation is the fitting of the ion within appropriate cavity of the ligand when macrocyclic supramolecular ring based molecules are used as ligands. The size of the bare and hydrated metal ions markedly influences the coordination behaviour of chelating or macrocyclic ligands. The orientation of the donor atom centres of the ligand, the shape and size of the ligand have pronounced effect on the complexation. Thus, the coordination of ligand and metal ion, orientation of metal in the ligand, charge on the metal, HOMO-LUMO energies are addressed by evaluating the structural parameters from the molecular modeling studies.

2.7.3 Complexation thermodynamics of Metal by functionalized solid support

The complexation ability of f-CNTs or other ligand with metal ions can be evaluated from the gas phase binding energy (BE). The BE (ΔE) of the metal ion (M^{3+}) and CNTs (L) complexation reaction,

$$M^{n+} + L = M^{n+}L \tag{2.26}$$

is defined by the following general relation,

$$\Delta E = E_{M^{n+}-CNT} - (E_{M^{n+}} + E_{CNT}) \tag{2.27}$$

where, $E_{M^{4+}-CNT}$, $E_{M^{n+}}$ and E_{CNT} refer to the energy of M^{n+}-CNT complex, M^{n+} ion and the free CNT system respectively.

The thermal correction to the electronic energy (E_{el}), enthalpy (H) and free energy (G) of the optimized structures has been performed to predict the thermodynamic parameters[211]. The thermal and zero point energy corrected binding energy is

$$\Delta U = U_{M^{n+}-CNT} - (U_{M^{n+}} + U_{CNT}) \qquad (2.28)$$

where , $U_{M^{n+}-CNT}$, $U_{M^{n+}}$ and U_{CNT} represent the internal energy of the M^{n+} -CNT complex, M^{n+} ion and the free CNT system respectively.

The binding enthalpy (ΔH) and binding free energy (ΔG) for the metal ion-CNT complexation reaction in Equation 2.23 are calculated using the following standard thermodynamic relations

$$\Delta H = \Delta U + \Delta nRT. \qquad (2.29)$$

$$\Delta G = \Delta H - T\Delta S. \qquad (2.30)$$

Where ΔS was calculated from the following equation

$$\Delta S = S_{M^{n+}-CNT} - (S_{M^{n+}} + S_{CNT}) \qquad (2.31)$$

The entropy of individual reactant or product is simulated from the partition function (Q) values by the computation program following statistical thermodynamics[212]. Neglecting the effect of rotational-vibrational coupling, anharmonicity, and centrifugal distorsion, the absolute entropy of an arbitrary molecule are given by the standard formulas of statistical mechanics as sum of translational, rotational and vibrational contributions.

$$S^0 = S^0_{tr} + S^0_{rot} + S^0_{vib} \qquad (2.32)$$

The translational, rotational and vibrational entropies are calculated using their relation with Q. The relation used for entropy calculation is shown here.

$$S = k_B \ln Q + k_B T \left(\frac{\partial \ln Q}{\partial T} \right)_{N,V} \qquad (2.33)$$

Where k_B, T, N, and V represent Boltzman constant, temperature, number of moles, and volume, respectively. The Q has been computed from equation 2.33 considering all molecular energies (translational, rotational, and vibrational) where i runs over all possible energy states of the system having energy Ei.

$$Q = \sum_i e^{\frac{-E_i}{k_B T}} \tag{2.34}$$

One of the key properties to be calculated in the metal ion-ligand complexation is the free energy of extraction (ΔG_{ext}). The metal ion-ligand complexation reaction is modeled using two schemes. In the Scheme-1, the metal ion (such as Th^{4+}) and the nitrate ion is considered to be separately hydrated species as follows:

$$Th^{4+}_{(aq)} + 4NO^{-}_{3(aq)} + CNT_{(aq)} \xrightarrow{\Delta G_{ext}} \left[CNT - Th(NO_3)_4\right]_{(aq)} \tag{2.35}$$

In Scheme-2, the metal cation and nitrate anion is considered to be in the ion pair forms as frequently used by few groups by citing the presence of high HNO_3 concentration[41].

$$Th(NO_3)_4(H_2O)_{2(aq)} + CNT_{(aq)} \xrightarrow{\Delta G_{ext}} \left[CNT - Th(NO_3)_4\right]_{(aq)} + 2H_2O \tag{2.36}$$

We have further performed single point energy calculation using optimized structures obtained from the BP86 functional with hybrid B3LYP functional as it includes the non-local HF contribution. Hybrid DFT was found to be superior to GGA functional for thermochemistry of actinides as reported earlier.[150] Relativistic effects, which are mandatory to include for heavy elements such as lanthanides and actinides, were accounted for by relativistic pseudopotentials, similar to previous studies.[213]

Most of the metal ion extraction takes place from the aqueous solution phase aided by ligand. Hence, the consideration of solvent effect on the complexation of the ligand moiety with metal ion in the QM calculation is thus indispensable. COSMO is an improved solvation model, where the polarization charges of the solute is calculated in a continuum solvent using scaled conducting boundary condition and has been used successfully for the free energy calculation in solution containing the first solvation shell[214]. Further, there is very little effect on the solvation energy using the optimized geometry at the solvent phase[215-218]. Hence, the aqueous solvent effect was inducted by performing single point energy calculation using the optimized geometry obtained from BP86 level of theory employing COSMO solvation model as implemented in TURBOMOLE quantum chemistry package.

The MOLDEN graphical program[219] was used for the visualization of various molecular geometry and structural parameters. Orbital population analysis was performed using natural population analysis (NPA)[220].

The free energy of extraction (ΔG_{ext}) is the most important parameter as it can be used as yardstick for the comparative selectivity in the metal ion-ligand complexation. Here a 1:2 (M:L) stoichiometric metal ion-ligand complexation reaction is considred for discussing as follows:

$$M_{(aq)} + nNO^{-}_{3(aq)} + 2L_{(org)} \xrightarrow{\Delta G_{ext}} [ML_2(NO_3)_n\,]_{(org)} \tag{2.37}$$

where, L corresponds to ligand. The change in Gibbs free energy of extraction, ΔG_{ext}, in equation 2.37 can be obtained by the Born-Haber thermodynamic cycle shown in **Figure 2.25**, in terms of the free energy change in gas phase, $\Delta G_{(gas)}$, and the solvation free energies of the products and reactants, $\Delta\Delta G_{(sol)}$. The overall complexation reaction is characterized by the free energy of extraction, ΔG_{ext} as

$$\Delta G_{ext} = \Delta G_{gas} + \Delta\Delta G_{(sol)} \tag{2.38}$$

$$\Delta G_{gas} = G_{ML_2(NO_3)_{n(gas)}} - (G_{M(gas)} + nG_{NO_3(gas)} + 2G_{L(gas)}) \tag{2.39}$$

$$\Delta\Delta G_{(sol)} = \Delta G_{ML_2(NO_3)_{n(org)}} - (\Delta G_{M(aq)} + n\Delta G_{NO_3(aq)} + 2\Delta G_{L(org)}) \tag{2.40}$$

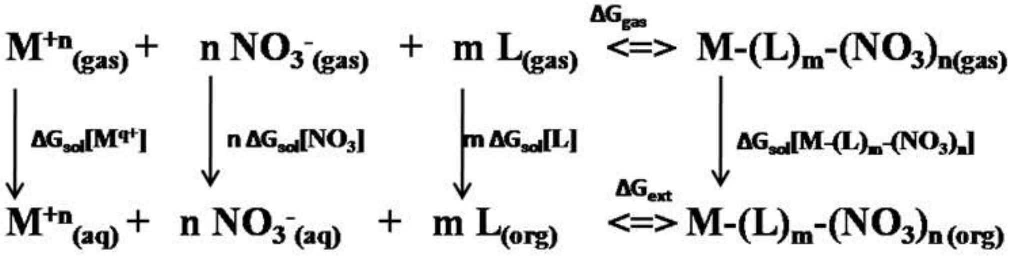

Figure 2.25 Thermodynamic cycle (Born-Haber) for the evaluation of free energy of extraction

2.7.4 Calculations of isotope separation factor by DFT calculation

The zinc isotopic exchange for heavy (M) and lighter isotope (m) between two solvent phases (water and water immiscible) is written as

$${}^{m}Zn^{2+}{}_{(sol)} + {}^{M}Zn^{2+}{}_{(compl)} \leftrightarrow {}^{m}Zn^{2+}{}_{(compl)} + {}^{M}Zn^{2+}{}_{(sol)} \tag{2.41}$$

The separation factor α for the above exchange reaction is given by

$$\alpha = \frac{\left(f^{r}_{Zn^{2+}}\right)_{sol}}{\left(f^{r}_{Zn^{2+}}\right)_{compl}} \tag{2.42}$$

Where "sol "means solvated by solvent and "compl" means complexed by the ligand. The reduced partition function ratio (RPFR), f^r, [221] of two isotopes with masses M (heavier) and m (lighter) is expressed as follows:

$$f^{r} = \frac{z_{vib,{}^{M}Zn^{2+}} \prod \frac{h\nu_{i,{}^{M}Zn^{2+}}}{k_B T}}{z_{vib,{}^{m}Zn^{2+}} \prod \frac{h\nu_{i,{}^{m}Zn^{2+}}}{k_B T}} \tag{2.43}$$

Here, Z_{vib} $^{M}Zn^{2+}$ is the vibrational partition function of molecular species with $^{M}Zn^{2+}$ isotope and ν_i is the harmonic frequency. k_B and h are the Boltzmann and Planck constant respectively and T is the temperature. The main input required for the evaluation of RPFR is the harmonic vibrational frequency which is evaluated from hessian calculation of the respective Zn^{2+} ion complexes.

It is important to emphasize that the isotope effect as represented by f^r or any other isotope separation by an isotopic exchange reaction must be a quantum effect. Thus separation factor (equation 2.42) of the istope exchange reaction (equation 2.41) can be evaluated from the vibrational frequencies of the participating molecules. In terms of f^r, some simple and practical relations can be derived to understand the direction and magnitude of the isotope separation. At higher temperature f^r will be close to 1 and hence α also will be unity. The values of f^r are nearly always larger than 1, since vibrational frequencies of heavier isotope molecules are smaller than those of the lighter isotope.

Larger the relative mass difference between the isotopes, larger will be the difference in f^r, and hence larger α would be expected. A very useful rule of thumb is: the heavier isotopes enriches in that isotopic molecule which has larger f^r, in other words, the heavious accumulates where the binding is stronger.

2.7.5 Molecular Dynamics Simulation Methodology

In order to study the condensed phase solvent effects on the Gibbs free nergy of Zinc ion, MD simulations were conducted. All simulations were carried out using the GROMACS simulation package. The system consists of 216 solvent molecules (water, ethanol, acetone and dimethyl ether) and one solute molecule (Zn^{2+} ion) in a cubic box with periodic boundary conditions employing the minimum image convention in the NPT ensemble with T = 298 K and P = 1 atm. The interaction parameters for ethanol, acetone and dimethyl ether were taken from the OPLS force field. The simple point charge (SPC) potential was used for the water molecule. The interaction parameters for Zn were taken from the default OPLS forcefield as implemented in GROMACS package.

Properties have been calculated considering a time step of 2 fs with data collected every 0.01 ps. The cubic cells were equilibrated for 200 ps and for the equilibration process we have simulated 1 ns. The systems were kept at the appropriate temperature and pressure via Berendsen4 and Parrinello-Rahman schemes, with constant couplings of 0.1 and 1.0, respectively. All bond lengths were constrained via the SHAKE algorithm. A cutoff distance of 1.2 nm for the LJ interactions was employed, while the Coulomb interactions were treated by using the PME algorithm. Production run was carried out for 5ns.

The calculations of the transfer free energy have been performed using the thermodynamic integration scheme with the integrator for stochastic dynamics. Free energies of solvation have been computed by decoupling a solute molecule from the solvent using the identity:

$$\Delta G = \int_0^1 \left\langle \frac{dH(\lambda)}{d\lambda} \right\rangle d\lambda \qquad (2.44)$$

where H is the parametrized Hamiltonian. The coupled state (λ = 1) corresponds to a simulation with the solute fully interacting with the solvent and the uncoupled state (λ =0) corresponds to a simulation considering the solute without interaction with the solvent.

Simulations conducted at different values of λ allow us to plot a ∂H/∂λ curve, from which ΔG is derived. The value of λ was varied from 0 to 1 with interval of 0.1. The soft core Lennard-Jones potential parameters were taken as α= 0.5, p = 1.0 and σ = 0.3.

3 Chapter 3: Carboxylic and Diglycolamic Acid functionalized Carbon Nanotubes

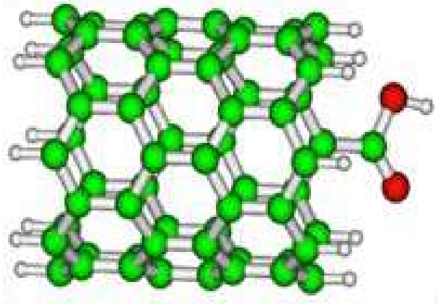

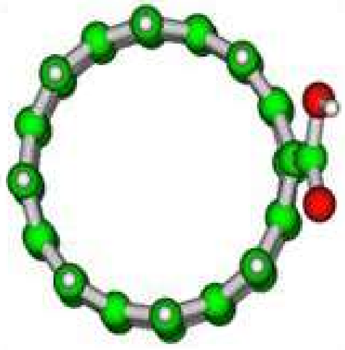

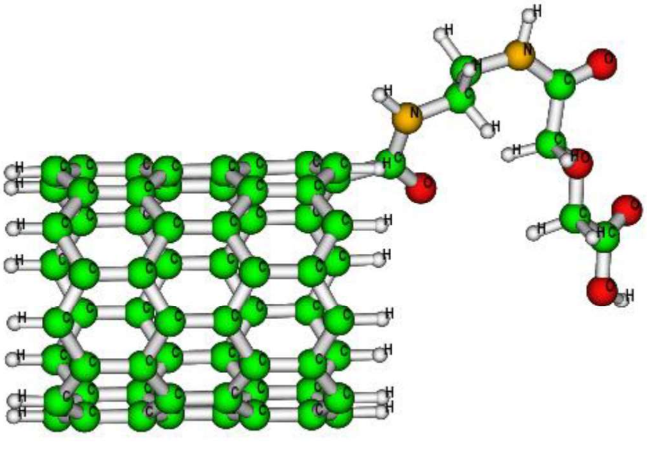

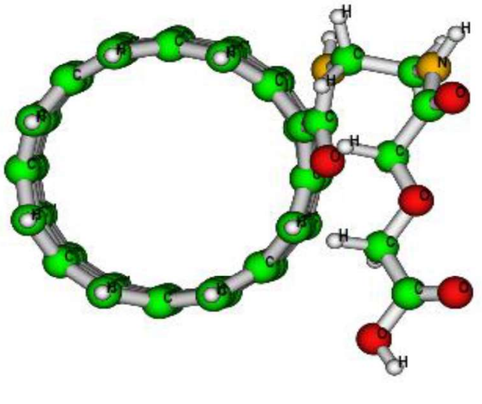

3.1 Adsorption of Th(IV) ions with CNT-COOH and CNT-DGA[167]

Thorium is a long-lived naturally occurring radionuclide widely distributed over the earth crust. The use of thorium as a source of fissile material for the manufacture of nuclear fuel as well as the reprocessing of nuclear fuel can also concentrate this element.[222] The presence of thorium metal ion in the environment is of important concern due to its toxicity and health effects on human. Efficient removal of thorium from waste stream before discharging it to environment is, hence, an essential field to explore. One indirect importance of thorium separation studies is that, it has only +IV stable oxidation state in solution and hence, has been selected as a chemical analogue for other tetravalent actinides.[223]

Separation of tetravalent thorium, Th(IV), from aqueous solution by pristine multi-walled carbon nanotues (MWCNTs) and oxidized MWCNTs have been reported.[224-227] Diglycolamic acid [124] , a tridentate and CHON based ligand, -functionalized CNTs[228] were used for separation of Th(IV) from aqueous solution in our previous paper. From these studies it has been seen that oxidized CNTs have better adsorption performances than that of pristine and DGA functionalized CNTs. The presence of bi-dentate carboxylic acid ligands on the surface of the CNT enhances the Th(IV) binding up to adsorption capacity of 132 mg g^{-1}.[226] Whereas tridentate DGA ligand on CNT have shown nearly ten time lower adsorption. [228] These interesting observations may be understood by considering the molecular approach of complexation of Th(IV) metal ion with pristine, oxidized and DGA-functionalized CNTs. Recent research has revealed that the presence of oxidized (carboxylated) fullerene enhances the

Th(IV) adsorption efficiency of oxidized CNTs[226]. This interesting observations can also be theoretically examined parallel with above calculations to understand the nature of binding of Th(IV) with different kinds of carbon nanomaterials . Here, quantum chemical calculations for the interaction of Th(IV) ion with pristine (p-CNT), oxidized or carboxylic acid (COOH) functionalized (CNT-COOH) and DGA functionalized CNTs (CNT-DGA) have been extensively studied by density functional theory (DFT). Electronic structures, energetics and thermodynamics of the interaction of Th(IV) ions with pristine CNT, CNT-COOH and CNT-DGA were described to look insight the complexation and hence, adsorption efficiencies of these carbon nano-structures towards Th(IV). The interactions of Th(IV) with oxidized fullerene was compared with the oxidized CNT.

3.1.1 Computational *Study*

3.1.1.1 **Computational Protocol**

The optimized geometry, total energy and vibrational IR frequency of tetravalent thorium ion complexes with different type of CNTs were computed using BP86 density functional employing SVP basis set [229] as implemented in Turbomole suite of program[181, 230] i.e. O (7s4p1d)/[3s2p1d], N(7s4p1d)/[3s2p1d], C(7s4p1d)/[3s2p1d], H(4s1p)/[2s1p], Th(14s13p10d8f1g) / [10s9p5d4f1g]. The zero point energy and thermodynamic correction to the total energy were made to compute the free energy at T=298.15K. Further, single point energy calculation was performed on all the optimized complexes using hybrid B3LYP functional [231, 232] and TZVP basis set[181] i.e. O (11s6p2d1f)/[5s3p2d1f], N (11s6p1d)/[5s3p1d], C(11s6p2d1f)/[5s3p2d1f], H(5s2p1d)/[3s2p1d]. BP86 functional consists of Becke B88 exchange functional [233] and Perdew P86 correlation functional [234] and was found to be successful in predicting molecular geometries of lanthanides and actinides complexes[235-238]. The solvent effect in the energetic was incorporated employing conductor line screening model (COSMO) [210].

3.1.1.2 **Structural Parameters**

The chemical species of interest are hydrated thorium and hydrated thorium nitrate, and hence these species are optimized and the structures are presented in **Figure 3.1**. In hydrated Th^{4+}-$(H_2O)_8$, the central Th metal ion was coordinated to 8 water molecules in distorted octa coordinated fashion. The calculated Th-O (see **Table 3.1**) bond distance of

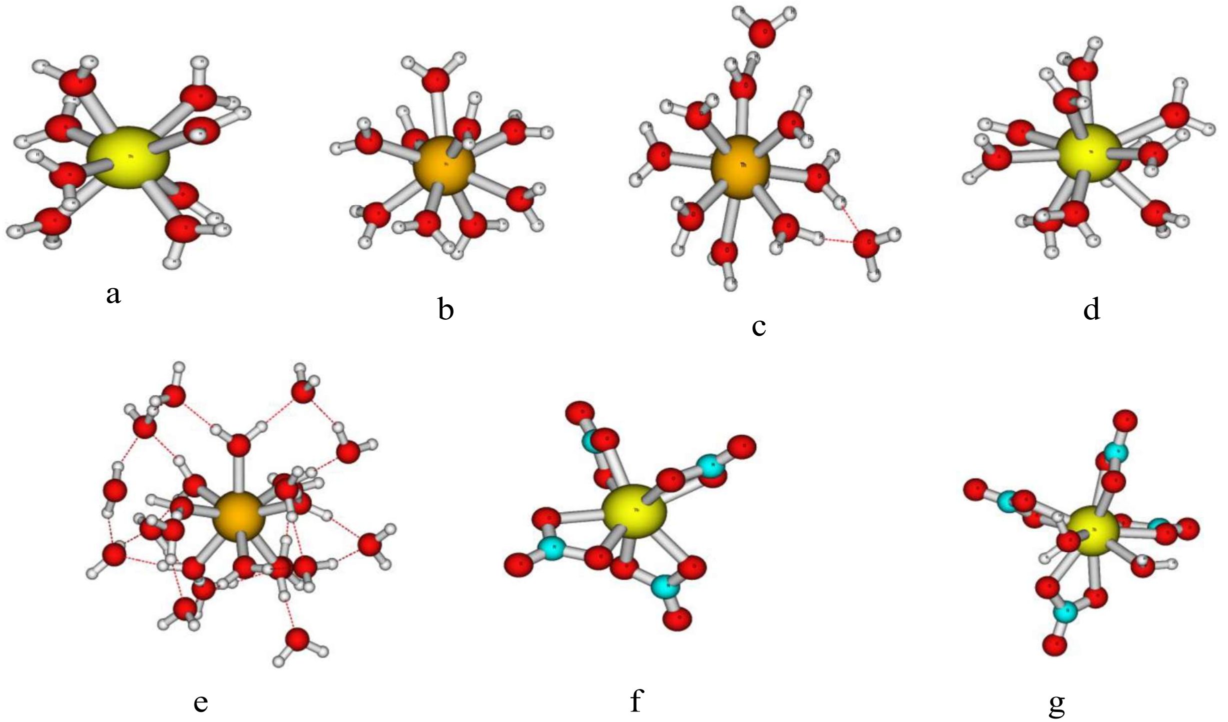

Figure 3.1 Optimized structures of hydrated Th^{4+} ions and $Th(NO_3)_4$ at the BP/SVP level of theory: (a) Th^{4+}-$(H_2O)_8$ (b) Th^{4+}-$(H_2O)_9$ (c) Th^{4+}-$(H_2O)_{10}$ (d) Th^{4+}-$(H_2O)_{11}$ (e) Th^{4+}-$(H_2O)_{24}$ (f) $Th(NO_3)_4$ (g) $Th(NO_3)_4(H_2O)_2$

2.48 Å was found to be very close to the experimental results of 2.45 Å and hence confirm the reliability of the present method of calculation. The coordination of 8 water molecules was reported earlier using LUX experiment.[239]

But, EXAFS studies reported a varied coordination number of Th^{4+} ion of 9-11[240-242] with a Th-O distance of about 2.45Å. Hence, further, hydrated Th^{4+} with 9, 10 and 11 numbers of H_2O molecules were optimized and shown in **Figure 3.1** The calculated Th-O (see **Table 3.1**) bond distances of 2.52 Å (Th^{4+}-$(H_2O)_9$) and 2.55Å (Th^{4+}-$(H_2O)_{10}$) were found to be higher compared to the experimental results.

It can clearly be seen from the structure of Th^{4+}-$(H_2O)_{11}$ that 11 water molecules cannot be accumulated in the first sphere of solvation shell; 9 water molecules reside in the first shell and rest 2 nest in the second solvation shell. The average Th-O bond distances of the H_2O's of first solvation shell are same (2.52 Å) as Th^{4+}-$(H_2O)_9$ which is higher compared to the experimentally reported values. Owing to the impact of second water coordination sphere in the hydration of Th^{4+}, a structure of 24 H_2O hydrated Th^{4+} was optimized and it is seen that 8 H_2O molecules occupy the first coordination sphere with 2.45 Å Th-O bond length which is exactly same with experimental results. In order to find out the most stable hydrated species, free energy of hydration was calculated after inclusion of standard state entropy correction.[243]

The calculated results are presented in **Table 3.2**. From the table it is seen that the free energy of hydration for Th^{4+}-$(H_2O)_8$ ion is higher than that of Th^{4+}-$(H_2O)_9$ (by -0.1kcal/mol), Th^{4+}-$(H_2O)_{10}$ (by -7.1kcal/mol) and Th^{4+}-$(H_2O)_{24}$ (by -19.9kcal/mol) indicating its higher stability and hence higher chance of occurrence in the aqueous environment.

Table 3.1 Structural parameter of hydrated species of Th^{4+} and $Th(NO_3)_4$.

Chemical Species	M-O_H (Å)	M-O_N (Å)
$Th^{4+}(H_2O)_8$	2.48 *(2.45)	
$Th^{4+}(H_2O)_9$	2.52	
$Th^{4+}(H_2O)_{10}$	2.55	
$Th^{4+}(H_2O)_{24}$	2.45, 4.54 (1st shell, 2nd shell)	
$Th(NO_3)_4$		2.44
$Th(NO_3)_4(H_2O)_2$	2.59 (2.57)	2.48 (2.46)

*Experimental values are given in parenthesis

Although the difference in Gibb's hydration energy between Th^{4+}-$(H_2O)_8$ and Th^{4+}-$(H_2O)_9$ or Th^{4+}-$(H_2O)_{10}$ is small, Th-O bond length of latter does not tally with the experimental one whereas former shows very similar length. On the other hand, although the Th-O bond length is very good match with experimental one for Th^{4+}-$(H_2O)_{24}$, the free energy of hydration is quite lower than that of Th^{4+}-$(H_2O)_8$. Therefore, aqueous Th^{4+} ion is modelled using Th^{4+}-$(H_2O)_8$ species. In presence of nitric acid, the nitrate ions displace the water molecules from the first shell of solvation leading to the formation of $Th(NO_3)_4$ which is confirmed from the free energy of reaction (**Table 3.2**).

Table 3.2 Free energy of hydration (in kcal/mol) for hydrated species of Th^{4+} and $Th(NO_3)_4$

Chemical reaction	**Gas Phase**	**Aqueous Phase**
$Th^{4+} + 8H_2O = Th^{4+}\text{-}(H_2O)_8$	-693.9	-1325.3
$Th^{4+} + 9H_2O = Th^{4+}\text{-}(H_2O)_9$	-716.4	-1325.2
$Th^{4+} + 10H_2O = Th^{4+}\text{-}(H_2O)_{10}$	-725.1	-1318.2
$Th^{4+} + 24H_2O = Th^{4+}\text{-}(H_2O)_{24}$	-932.7	-1305.4
$Th^{4+}\text{-}(H_2O)_8 + 4\ NO_3 = Th(NO_3)_4 + 8H_2O$	-913.2	-60.23
$Th(NO_3)_4 + 2H_2O = Th(NO_3)_4 – (H_2O)_2$	-13.9	-13.23

The optimized structure of $Th(NO_3)_4$ is presented in **Figure 3.1**. All four nitrate ions are found to be coordinated in bidentate mode. It is interesting to check whether the $Th(NO_3)_4$ species remains as hydrated form in the aqueous environment. In view of this, di-hydrated structure of $Th(NO_3)_4$ is optimized and the structure is shown in **Figure 3.1**. In $Th(NO_3)_4(H_2O)_2$, the central Th metal ion was coordinated to the 4 nitrate ion in bidentate mode and 2 water molecules leading to deca coordination. The formation of $Th(NO_3)_4(H_2O)_2$ was confirmed by the negative free energy of reaction (**Table 3.2**).

For our modelling studies, we have considered pristine CNT, COOH and DGA functionalized CNT. The CNT considered here is a (8, 0) zigzag single-walled CNT which consists of four unit cells with tubular length of 5.78 Å width of 6.40 Å. We have considered one COOH and DGA unit anchored on the open pore of the (8, 0) zig-zag CNT with 4 unit cells as earlier studied[63]. The optimized geometry of pristine and COOH and DGA functionalized CNT is displayed in **Figure 3.2**.

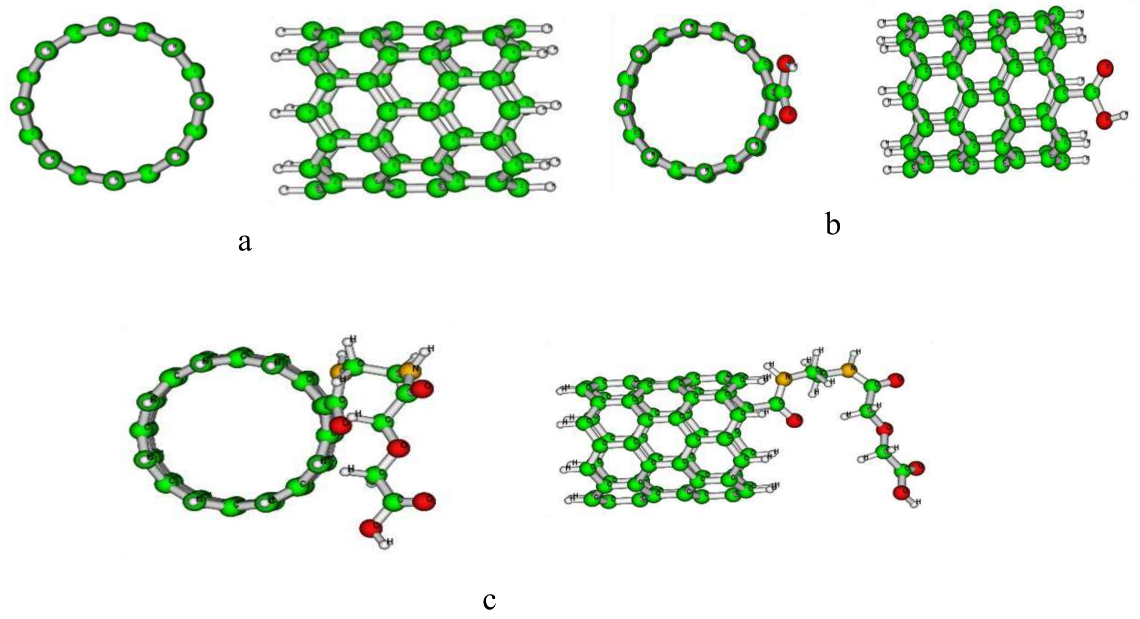

Figure 3.2 Optimized geometries of pristine and COOH and DGA functionalized CNT at the BP/SVP level of theory (a) (8, 0) zigzag CNT; (b) (8, 0) zigzag CNT-COOH; (c) (8, 0) zigzag CNT-DGA

In the optimized structures, the C-C and C-H bond distance of CNT unit was found to be 1.44Å and 1.10Å. In CNT-COOH, the -COOH group was found to be aligned along the axis of the CNT. It has been seen that the diglycolamic acid group was wrapping around the cylindrical backbone of nanotubes (**Figure 3.2**). In the DGA unit, the carbonyl, C=O bond distance was found to be 1.22 Å and carboxylate C=O bond distance was found to be 1.31 Å. The ethereal C-O bond distance was found to be 1.39Å. Three oxygen donor atoms are projecting in similar directions like in free diglycolamic acid. The bond length of two C=O groups of DGA unit was found to be 1.21Å and 1.22Å respectively.

The optimized structures of complexes of Th^{4+} with p-CNT with and without nitrate ions are presented in **Figure 3.3**. Although open edges are more reactive than the sidewall surface of p-

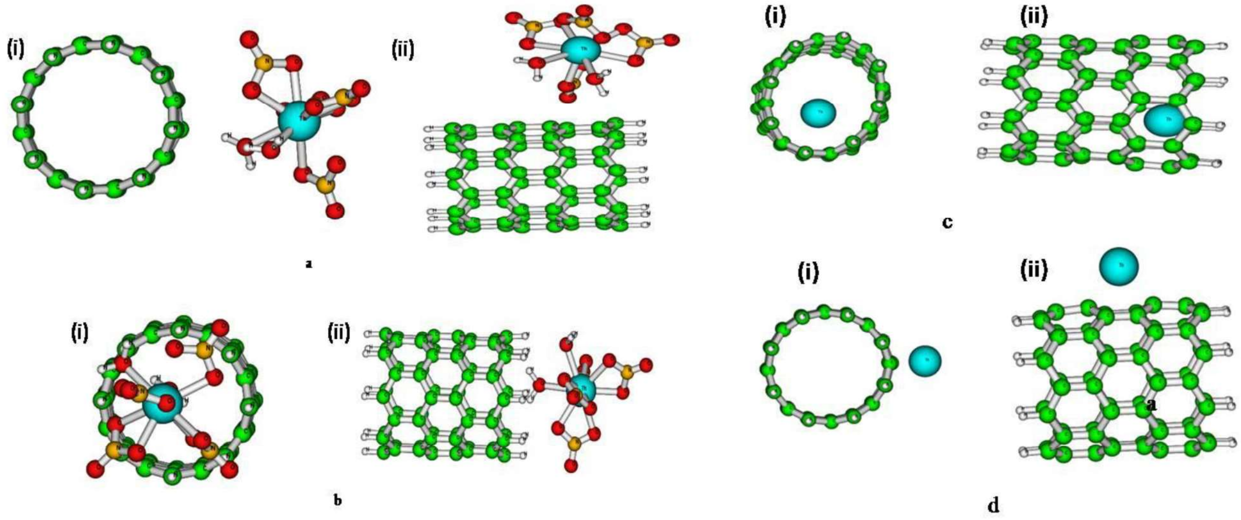

Figure 3.3 Optimized structures of complexes of Th^{4+} with non-functionalized/pristine CNT along with nitrate ion: (a) Interaction from sidewall of CNT (CNT_s) and (b) from open edges of CNT (CNT_o) (c) Interaction from sidewall of CNT without nitrate ion (CNT_s) and (d) from open edges of CNT (CNT_o); (i) tail view (ii) side view, at the BP/SVP level of theory

CNT, we have considered the binding of thorium from both directions. The $Th(NO_3)_4(H_2O)_2$ species was found to be lying outside of the side surface and open end of the CNT. The calculated Th-O (O from NO_3 and H_2O) and Th-C are displayed in **Table 3.3**.

The optimized structure of complex of Th^{4+} with functionalized CNT-COOH and CNT-DGA in absence of nitrate ion is presented in **Figure 3.4** and the characteristic bond distances are shown in the Figure as well as given in **Table 3.3**.

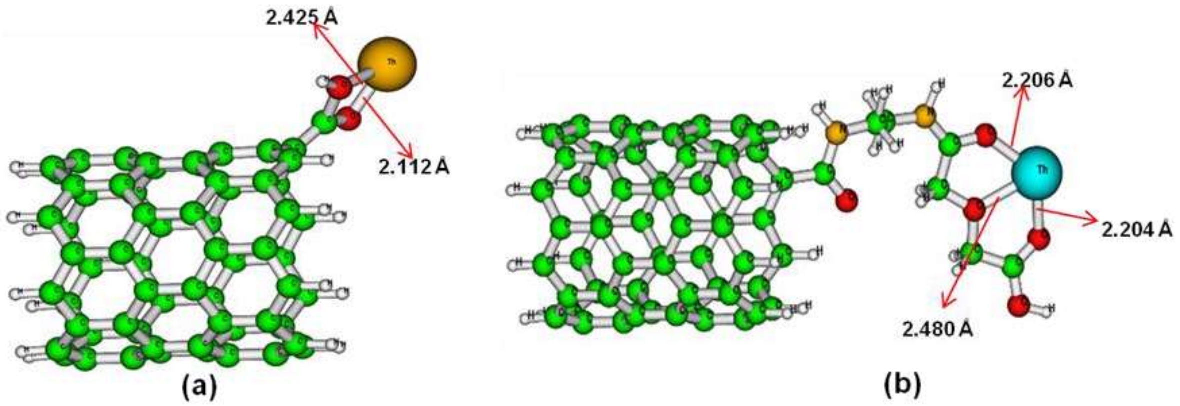

Figure 3.4 Optimized structures of Th^{4+} complex with (a) COOH and (b) DGA functionalized CNT in absence of nitrate ions at the BP/SVP level of theory

Table 3.3 Bond distances in Å from Th^{4+} metal centre for complexes/system under consideration

Bond	**System of Th^{4+} bonded with**					
	CNT-Side Surface (in presence of NO_3 and H_2O)	**CNT-Open End (in presence of NO_3 and H_2O)**	**CNT-COOH (in absence of NO_3& H_2O)**	**CNT-DGA (in absence of NO_3& H_2O)**	**CNT-COOH in presence of NO_3& H_2O)**	**CNT-DGA (in presence of NO_3& H_2O)**
Th-O(NO3)	2.49	2.49	-	-	2.52	2.47
Th-O(H2O)	2.56	2.58	-	-	2.63	2.45
Th-C* (CNT)	5.451	-	-	-	-	-
Th-H(CNTedge)	-	4.703	-	-	-	-
$\text{Th-O}^{\#}$(COOH)	-	-	2.11, 2.42	-	2.36,3.82	-
$\text{Th-O}^{¥}_{\text{carbonyl}}$[124]	-	-	-	2.21	-	2.62
$\text{Th-O}_{\text{ether}}$[124]	-	-	-	2.48	-	2.71

*M-C: distances between metal and nearest six carbon atoms of a hexagon the CNT; # first one is the distance of M--O=C bond and second one is of M--O-C of –COOH group; ¥ Average bond distance of two $\text{Th-O}_{\text{carbonyl}}$ of DGA unit of CNT-DGA.

From the **Figure 4(a)** it is seen that the COOH group is little tilted from the axis of the CNT after complexation with Th^{4+} ion. Th-O bond distance was found to be 2.11Å and 2.42Å. In Figure 4(b), the Th^{4+} ion is found to be directly coordinated to the three donors O atoms of the DGA moiety. All three donor O atoms and the coordinated metal ion are lying in the same plane. It is interesting to mention that though the metal ions and three donor O atoms are lying in the same plane, the M-O bond length with three O atoms are not same in length. The M-O (O of C=O group) bond length were found to be 2.20 and 2.21Å and one M-O (ethereal O) bond length was found to be 2.48Å. The shorter M-O bond length for C=O group compared to M-O bond length of ethereal O suggest that former has stronger interaction ability than the later. In order to find out the effect of CNT on the interaction, we have performed the calculation by replacing CNT with H atom in the CNT-COOH and CNT-DGA motifs. The optimized structures are presented in **Figure 3.5** and characteristics bond distances are shown in **Table 3.4**.

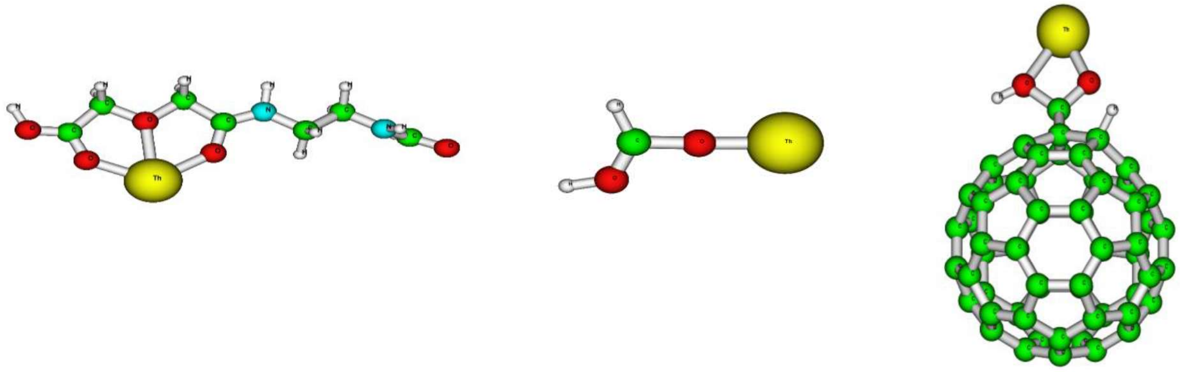

Figure 3.5 Optimized structures of Th^{4+} complexes with DGA and COOH unit (connected to CNT in CNT-DGA and CNT-COOH, respectively), and with C_{60}-COOH at the BP/SVP level of theory.

Table 3.4 Calculated structural parameters (in Å) of Th^{4+} ion with HCOOH, DGA and C60-COOH at the BP/SVP level of theory

Species	**M-O distance (Å)**			
	amide O	**carboxy O**	**ethereal O**	**alcoholic O**
HCOOH		1.994		4.146
DGA	2.182	2.198	2.495	
C60-COOH		2.078		2.357

The optimized structure of complex of Th^{4+} ion with functionalized CNT-COOH and CNT-DGA in presence of nitrate ion is presented in **Figure 3.6** and the characteristic bond distances are shown in the Figure as well as given in **Table 3.3**. From the Figure 6(a) it is seen that the only the carbonyl O of COOH group (unlike in case of Th^{4+} complex with CNT-COOH in absence of nitrate ions where both the O centres were bonded to metal ions) is coordinated to the Th^{4+} ion and it is lengthened to 2.36 Å in presence of nitrate ion from 2.11Å in absence of nitrate ions. The presence of nitrate ions and water molecules made the carboxylic group to bind in monodentate mode with more electro-donating carbonyl O centre. Thorium ion coordinated to four nitrate ion in

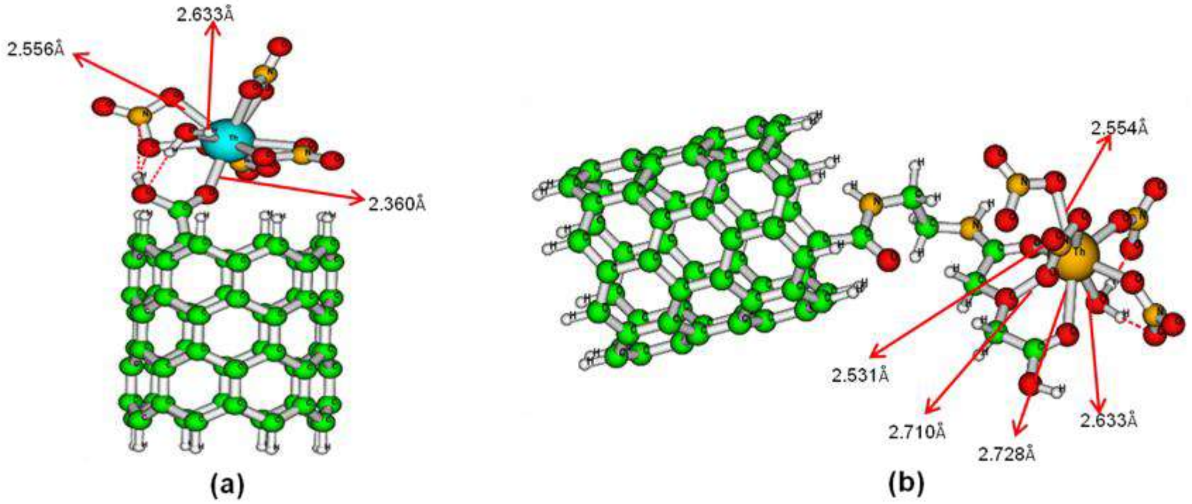

Figure 3.6 . Optimized structures of Th^{4+} complex with (a) CNT-COOH and (b) CNT-DGA in presence of nitrate ion

bidentate mode and one each with water and carbonyl O of COOH group. The Th-O (O of NO_3) bond distance was lengthened due to the strong coordination from the carbonyl O atom of CNT-COOH adsorbent. In CNT-DGA complex, Figure 6(b), The Th^{4+} ion is found to be directly coordinated to the three donor O atoms of the DGA moiety, six donor atoms from four nitrate ions (two bidentate and two monodentate mode) and one from aqua leading to deca coordination. The Th-O (oxygen of NO_3) is found to be varied from 2.32Å to 2.59Å and the Th-O (carbonyl oxygen of DGA) is found to be varied from 2.53 to 2.72Å indicating asymmetrical nature of bonding from the identical carbonyl bonding. The Th-O (etheric oxygen of DGA) is found to be 2.71Å. Further, the M-O bond length in hydrated species was found to be larger than the M-O bond length of H_2O attached to the CNT-DGA-Th complex. The M-O bond distance of NO_3^- ion is found to be smaller than the M-O of H_2O indicating the stronger interaction of metal ions with NO_3^- ion group than H_2O. In the complex of Th^{4+} ionwithCNT-DGA, the elongation of the of the two carbonyl C=O bonds (1.31, 1.30 Å) from free CNT-DGA (1.21, 1.22 Å) and ethereal C-O bonds (1.45 Å) from free CNT-DGA (1.39 Å) refers to its participation in the binding, whereas the same carboxylic C=O bond distance before (1.30 Å) and after (1.31 Å) binding refers its non-participation in the complexation. The shorter Th-O bond of the C=O (2.36 Å) of the CNT-COOH than that of C=O (2.62 Å) of CNT-DGA clearly aimed towards the greater affinity of CNT-COOH for Th^{4+} adsorption than CNT-DGA.

3.1.1.3 **Binding energy/free energy of complexation in absence of nitrate ions**

The gas phase binding energy, which plays an important role in the initial screening as well as predicting adsorption capacity of an adsorbent material towards metal ions, is calculated using different possible reaction routes. The calculated values of binding energy are presented in **Table 3.5**. The gas phase binding energy of p-CNT with bare metal ion was found to be quite high; the interaction of Th^{4+} from sidewall and open edge surface of p-CNT have nearly similar binding enegy.

Table 3.5 Electronic and thermodynamic energies (in kcal mol^{-1}) of Th^{4+} ion with non-functionalized and functionalized CNT in absence of nitrate ion

Complexation reaction	**ΔE**	**ΔS**	**ΔH**	**ΔG**	**ΔG_{aq}**
$Th^{4+} + CNT_S = CNT_S\text{-}Th^{4+}$	-759.6	-0.029	-759.2	-750.4	-86.8
$Th^{4+} + CNT_O = CNT_O\text{-}Th^{4+}$	-754.5	-0.03	-754.1	-745.2	-22.3
CNT-COOH + Th^{4+}= CNT-COOH-Th^{4+}	-792.8	-0.02	-792.0	-783.8	-105.6
CNT-DGA + Th^{4+}= CNT-DGA-Th^{4+}	-875.6	-0.04	-874.2	-861.9	-114.5
$Th^{4+}(H_2O)_8 + CNT_S = CNT_S\text{-}Th^{4+} + 8H_2O$	24.9	0.238	14.6	-56.5	33.3
$Th^{4+}(H_2O)_8 + CNT_O = CNT_O\text{-}Th^{4+} + 8H_2O$	29.9	0.238	19.6	-51.3	97.8
CNT-COOH + $Th^{4+}(H_2O)_8$ = CNT-COOH-Th^{4+} +$8H_2O$	-8.2	0.239	-18.5	-89.9	48.8
CNT-DGA + $Th^{4+}(H_2O)_8$ = CNT-DGA-Th^{4+} +$8H_2O$	-90.9	0.225	-100.8	-168.0	39.8

[CNTs and CNTo refers to the surface side and open end of CNT; Unit of ΔE, ΔH and ΔG = kcal/mol; ΔS = kcal/mol/K]

The aqueous phase free energy of the binding is four times higher for sidewall interaction than that of open edges of p-CNT; may be the consequence of interaction of water molecules with the reactive dangling bonds at the open edges of CNT. It is seen that the binding energy of bare Th^{4+} ion with CNT-COOH and CNT-DGA in gas phase in absence of nitrate ion is very high. The CNT-DGA shows more electronic binding capacity than CNT-COOH. This might be due to the more number of donor atom (3 in

CNT-DGA) than CNT-COOH (2 donor atoms). In order to have further insights, NPA (**Table 3.6**), HOMO-LUMO (**Table 3.7**) and NBO (**Table 3.8**) analyis was performed.

Table 3.6 Gas phase NPA of Th^{4+} binding with for complexes/system under consideration

NPA parameters		**System of Th^{4+} bonded with**			
		CNT-Side Surface	**CNT-Open End**	**CNT-COOH**	**CNT-DGA**
Charge on Th^{4+} metal ion		1.902	1.892	1.719	1.768
Electron population on the orbital of	s	4.201	4.20	5.312	5.179
	p	11.998	11.998	11.973	11.962
	d	11.056	11.059	10.643	10.788
	f	0.835	0.844	0.349	0.299
	g	0.004	0.004	0.002	0.002

Table 3.7 Calculated various molecular descriptors (eV)

	E_{HOMO}	**E_{LUMO}**	**$E_{(LUMO-HOMO)}$**	**χ**	**η**	**$\Delta N(Th^{4+})$**	**$\Delta N(Th^{4+}-(H_2O)_8)$**
Th^{4+}	-56.23	-34.09	22.13	45.16	11.06		
$Th^{4+}-(H_2O)_8$	-25.46	-17.58	7.87	21.52	3.93		
CNT-DGA	-4.32	-3.91	0.41	4.11	0.205	1.820	2.101
CNT-COOH	-4.24	-3.83	0.40	4.03	0.200	1.824	2.111
C60-COOH	-5.85	-4.14	1.70	4.99	0.85	1.684	1.725

Table 3.8 Average second order stabilization energies $E_{ij}^{(2)}$ for the complexes of Th^{4+} using NBO analysis at the B3LYP/TZ2P level of theory as implemented in ADF

Complex	Donarnbo (i)	Accepter nbo (j)	Avg. $E_{ij}^{(2)}$ kcal/mol
CNT-COOH	LP-O	LV-Th	10.38
CNT-DGA	LP-O	LV-Th	7.43

LP = Lone Pair; LV = energy-sorted lone vacant orbitals

There is a considerable transfer of charge to the ligands as evident from the residual charge values in **Table 3.6** on the metal centre leading to higher interaction energy. Increase of electronic population in the s, d and f orbitals of the metal ions after complexation signals to the strong covalent bonding between the metal and ligands. The absolute electronegativity and absolute hardness of CNT-COOH and CNT-DGA are almost close, the HOMO-LUMO gap of CNT-COOH and CNT-DGA is also identical (**Table 3.7**). These has also been reflected in the identical values of ΔN which indicates that their interation with Th^{4+} ion should be very close (**Table 3.7**). But actually, the gas phase interaction energy of CNT-DGA is higher that that of CNT-COOH and hence, ΔN unable to corelate the interaction energy values. Further it was seen that the higher interaction of CNT-DGA compared to CNT-COOH is reflected neither from the residual charge on the thorium metal ion which is found to be higher for the former than of latter (NPA analysis) nor from the stabilization energy by NBO analysis in **Table 3.8**. NBO analysis resulted higher stabilization energy for Th^{4+}-CNT-COOH interaction than that of Th^{4+}-CNT-DGA establishing higher binding energy for the former. In order to investigate the role of CNT in the functionalized CNT-COOH and CNT-DGA unit, the interaction energy of the metal ions was further evaluated by replacing the CNT unit with H atom in the CNT-

COOH and CNT-DGA motif. The gas phase interaction energies were found to be reduced considerably in absence of CNT (see **Table 3.9**). The selectivity trend remains the same.

Table 3.9 Calculated values of interaction energies (kcal/mol)

Various stoichiometric reaction	**ΔE**
CNT-DGA + Th^{4+} = CNT-DGA-Th^{4+}	-875.6
CNT-COOH + Th^{4+} = CNT-COOH-Th^{4+}	-792.8
C60-COOH +Th^{4+} = C60-COOH-Th^{4+}	-627.0
HCOOH= Th^{4+} = HCCOH-Th^{4+}	-292.6
HDGA + Th^{4+} = HDGA-Th^{4+}	-581.4

In aqueous phase, though the CNT-DGA shows higher free energy, the value has been reduced considerably due to the solvent dielectric screening on the interaction (**Table 3.5**). Since the metal ion mainly exist in hydrated form in the solution, the binding energy was evaluated using the stable hydrated Th^{4+}-$(H_2O)_8$ ion species. The gas phase interaction as well as free energy was found to be reduced considerably. Even, the free energy of complexation has become positive indicating no adsorption of metal ion from the solution either by CNT-COOH or CNT-DGA if the modelling is carried out without nitrate ion in the complexation reaction. In addition, The HOMO-LUMO analysis in the aqueous phase is also not in accord with the calculated interaction energies values; the fraction of electron transfer should have been more for CNT-DGA than that of CNT-COOH (**Table 3.7**).

One interesting observation can be seen from entropy change values of the eight reactions considered in **Table 3.5**. The first four reactions where Th^{4+} taken as a bare metal ions ΔS values are negative whereas in the next four reactions where Th^{4+} taken as octa-hydrated it is positive. The adsorption of Th^{4+} metal ions from aqueous to the surface of the CNTs involve two steps: (i) partial or complete dehydration of the hydrated Th^{4+} metal ions, and (ii) condensation of the dehydrated metal ion onto the surface of CNTs by chemical and/or physical adsoption process. The ΔS of the first step is positive as it releases the bonded water molecules from the hydrated cluster, whereas, ΔS of the second step is negative. The dehydration step is not required for the initial four reactions of **Table 3.5** and hence owing to the condensation of random bare Th^{4+} ions onto the CNT surface the entropy change turn as negaive. The negative free enrgy of these entropy disfavoured reactions has come from the high and negative entahlpy chage values (**Table 3.5**). In the case of the reactions involving the octa-hydrated Th^{4+}, although reactions are entropy favoured due to the positive or less negative values of electronic enthalpy change, the free energy change turned to be positive. Thus for the complexation reactions of hydrated Th^{4+} with CNTs the electronic effect dominate over the entropy effect in the calculation of Gibb's free energy.

3.1.1.4 **Binding energy/free energy of complexation in presence of nitrate ions**

In view of the failure of the model without nitrate ion, next we have calculated the binding/free energy for the above complexation reaction in presence of nitrate ion and the calculated values are presented in **Table 3.10**. In case of p-CNT, for both the surface and open face of CNT, the interaction energy of thorium nitrate species in gas phase was found to be negative whereas the free energy was found to be positive. Further, the CNT surface have slightly higher electronic interaction energy comapared to open face of the CNT. Furthermore, the free enegy of adsorption for thorium nitrate with either type of pristine CNT shows positive value confirming its inability to adsorp in solution phase which is also observed from experiments.[224, 225]

Table 3.10 Electronic and thermodynamic energies (in kcal mol^{-1}) of Th^{4+} ion with non-functionalized and functionalized CNT in presence of nitrate ion at the B3LYP/TZVP level of theory

Complexation reaction	**ΔE**	**ΔS**	**ΔG**	**ΔG_{aq}**
$Th(NO_3)_4(H_2O)_2$ + CNT_S = CNT-$Th(NO_3)_4(H_2O)_2$	-8.2	-0.04	4.0	11.1
$Th(NO_3)_4(H_2O)_2$ + CNT_O = CNT-$Th(NO_3)_4(H_2O)_2$	-5.7	-0.03	4.1	16.4
Scheme - 1				
CNT-COOH + Th^{4+}+ $4NO_3$ + H_2O = CNT-COOH-$Th(NO_3)_4(H_2O)$	-1699.0	-0.22	-1629.3	-200.9
CNT-DGA + Th^{4+}+ $4NO_3$ + H_2O = CNT-DGA-$Th(NO_3)_4(H_2O)$	-1696.8	-0.23	-1620.5	-188.9
Scheme - 2				
CNT-COOH+$Th^{4+}(H_2O)_8$+$4NO_3$=CNT-COOH-$Th(NO_3)_4(H_2O)$+ $7H_2O$	-914.4	0.047	-935.4	-46.4
CNT-DGA+$Th^{4+}(H_2O)_8$+$4NO_3$ = CNT-DGA-$Th(NO_3)_4(H_2O)$+ $7H_2O$	-912.2	0.03	-926.6	-34.4
Scheme - 3				
$Th(NO_3)_4(H_2O)_2$ + CNT-COOH = CNT-COOH-$Th(NO_3)_4(H_2O)$+H_2O	-9.2	-0.009	-8.2	-7.2
$Th(NO_3)_4(H_2O)_2$ + CNT-DGA = CNT-DGA-$Th(NO_3)_4(H_2O)$+ H_2O	-7.0	-0.02	1.1	5.3

[Unit of ΔE, ΔH and ΔG = kcal/mol; ΔS =kcal/mol/K]

The next question arises whether oxidised CNT can adsorp Th^{4+} metal ion from the solution or not. In view of that, the binding energy and free energy for bare Th^{4+} metal ion in presence of nitrate ion in gas phase is evaluated and the values are presented in **Table 3.10**. It is interesting to note that both the binding energy and free energy of complexation of Th^{4+} ion was found to be higher with CNT-COOH than that of CNT-DGA in presence of nitrate ion which was inverse in absence of nitrate ion (Scheme – 1).

Although, the role of entropy is similar as observed in the absence of nitrate ion (see **Table 3.5**). Even in solution phase also, CNT-COOH shows higher adsorption capacity than CNT-DGA and matter of fact is that the experimental results also show the same trend of adsorpion capacity by this two CNT-based sorbents[224-228]. As we know that the metal ion in solution phase remains as hydrated form and hence next calculation is performed using stable hydrated Th^{4+}-$(H_2O)_8$ ion species. The binding and free energy both in gas and solution phase follows the same trend i.e. CNT-COOH shows higher binding capacity over CNT-DGA (Scheme – 2). Recently, there is a practice of considering hydrated ion pair of actinide nitrate instead of their isolated species in higher nitric acid concentration.[150] In view of this, we have also calcuated the binding and free energy of complexation using hydrated ion pair (Scheme - 3). The calculated results are presented in **Table 3.10**. The calculated binding and free energy values both in gas and solution phase for thorium nitrate with CNT-COOH is shown to be negative. For CNT-DGA , binding energy is negative but the free energy is positive either in gas and solution phase. This clearly indicates that the hydrated nitrate ion pair of Th^{4+} ion seems to be unsuitable for modeling the adsorption reaction of ions with functionalized CNT.

3.1.1.5 **Effect of presence of C_{60}-COOH**

Oxidized/carboxylated form of fullerene has also been emerging as more efficient adsorbent in recent times. Presence of hyroxylated and carboxylated fullerene (C_{60}) enhances the adsorpion capacity of oxidized CNT has been established by experimentation[226]. Calculations have been performed for the interactions of Th^{4+} with carboxylated C_{60} fullerene (C_{60}-COOH), the optimized structure of the realted complex has been shown in **Figure 3.5**, characteristic Th-O bond lengths are shown in **Table 3.4**, and energetic results are displayed in **Table 3.9**. It is evident from the binding energy values that C_{60}-COOH can enhance the adsorpion while companying CNT; interaction energy (- 697 kcal mol^{-1}) is more than twice as compared with formic acid, replacing C_{60} with H in C_{60}-COOH, (- 292 kcal mol^{-1}). The higher absolute electonegativity and HOMO-LUMO gap (see **Table 3.7**) of C_{60}-COOH also indicate for the strong interaction with thorium ions. It can also be seen that for the complexation with Th^{4+} or hydrated Th^{4+} the C_{60}-COOH has lower ΔN values than that of CNT-COOH and CNT-DGA. This supports the fact that former have lower binding energy (-627.0 kcal/mol) than the later (-792.8 and -930.2 kcal/mol, respectively) (**Table 3.9**) but the considerable binding energy of C_{60}-COOH is sufficient to increase the adsorption capacity of CNT-COOH (or CNT-DGA) for Th^{4+} adsorption when C_{60}-COOH would be added with the functionalized CNT.

3.1.1.6 **Comparison with dispersion-corrected DFT (DFT-D)**

The DFT-D optimized geometric structures of pristine-CNT, CNT-COOH and CNT-DGA were also optimized. It was seen that all structures are similar with the DFT optimization, except the orientation of the DGA unit on CNTs is different in free CNT-DGA structure; although the Th^{4+} complexes of CNT-DGA structures are similar for both the cases. Due to the dispersive interaction the DGA molecule have taken a different orientation from the DFT optimized structure. Other conformations of the CNT-DGA may also possible owing to the flexible nature of the DGA unit attached with the CNT. But once Th^{4+} ion bonded with the DGA unit through tridentate chelation, the flexibility of the unit would nearly diminish and that is why geometrical structures of Th^{4+} complex of CNT-DGA are similar for DFT and DFT-D optimization. **Table 3.11** compares the characteristic bond distances of Th^{4+} complexes with CNTs, CNT-COOH and CNT-DGA without and without optimization at DFT and DFT-D. It is found that all the bond lengths are almost same and refers to identical binding environment around the metal ion.

Table 3.11 Comparison of bond distances in Å from Th^{4+} metal centre for complexes/system under consideration without nitrate with and without dispersion-corrected DFT of Grimme's D3 scheme

Bond	**With Dispersion DFT calculation**				**Without dispersion DFT calculation**			
	System of Th^{4+} bonded with							
	CNT-Side Surface	**CNT-Open End**	**CNT-COOH**	**CNT-DGA**	**CNT-Side Surface**	**CNT-Open End**	**CNT-COOH**	**CNT-DGA**
Th-C* (CNT)	2.552	-	-	-	2.542	-	-	-
Th-H(CNTedge)	-	4.013	-	-	-	3.935	-	-
Th-O[#](COOH)	-	-	2.265	-	-	-	2.265	-
Th-O[#]$_{carbonyl}$[124]	-	-	-	2.192	-	-	-	2.205
Th-O$_{ether}$[124]	-	-	-	2.440	-	-	-	2.480

*M-C: distances between metal and nearest six carbon atoms of a hexagon the CNT; [#] Average of two similar Th-O distances.

Adsorption binding energies of CNTs, CNT-COOH and CNT-DGA with Th^{4+} were calculated by considering bare and hydrated metal ions. The results are depicted in **Table 3.12**.

Table 3.12 Electronic and thermodynamic energies (in kcal/mol) of Th^{4+} ion with non-functionalized and functionalized CNT in absence of nitrate ion with dispersion-corrected DFT of Grimme's D3 scheme.

Complexation reaction	**ΔE**
$Th^{4+} + CNT_S = CNT_S\text{-}Th^{4+}$	-764.2
$Th^{4+} + CNT_O = CNT_O\text{-}Th^{4+}$	-765.8
$CNT\text{-}COOH + Th^{4+} = CNT\text{-}COOH\text{-}Th^{4+}$	-793.9

CNT-DGA + Th^{4+}= CNT-DGA-Th^{4+}	-884.5
$Th^{4+}(H_2O)_8$ + CNT_S = CNT_S-Th^{4+} + $8H_2O$	35.1
$Th^{4+}(H_2O)_8$ + CNT_O = CNT_O-Th^{4+} + $8H_2O$	33.5
CNT-COOH + $Th^{4+}(H_2O)_8$ = CNT-COOH-Th^{4+} +$8H_2O$	5.4
CNT-DGA + $Th^{4+}(H_2O)_8$ = CNT-DGA-Th^{4+} +$8H_2O$	-85.1

It is clearly found that the binding energy values are very close to the DFT based calculations. Difference in the energy values between DFT and DFT-D calculation is more when hydrated metal ions are considered for the complexation. This is evident as, in casae of hydrated model, the presence of water molecules near the CNT surface create more dispersion interaction compared to bare Th^{4+} ions. Binding energy of the interactions were also compared between the energy calculations at DFT level after structural optimization at DFT-D level and the energy calculations at DFT-D level after structural optimization at DFT-D of theory (**Table 3.13**) and it is seen that the difference in the adsorption binding energy values are not significant. Although the adsorption binding energy values are not same, but the treand of binding energy of adsorption of Th^{4+} by CNT-open edge, CNT-side surfae, CNT-COOH and CNT-DGA are identical with the DFT calculation. Hence, there would not be any difference in the adsorption preferences of Th^{4+} towards above four types of CNTs considered between computational calculations done at DFT and DFT-D.

Table 3.13 Comparison of interaction energies (in kcal/mol) of Th^{4+} ion in absence of nitrate ion: (i)# optimization at the BP with Grimme's D3 dispersion correction/SVP & single point energy at the B3LYP/TZVP level and (ii)† optimization at the BP with Grimme's D3 dispersion correction/SVP & single point energy at the B3LYP with Grimme's D3 dispersion correction /TZVP level

Complexation reaction	**ΔE (i)#**	**ΔE (ii)†**
Th^{4+} + CNT_S = CNT_S-Th^{4+}	-760.61	-764.28
Th^{4+}+ CNT_O = CNT_O-Th^{4+}	-754.62	-765.84
CNT-COOH + Th^{4+}= CNT-COOH-Th^{4+}	-792.83	-793.96
CNT-DGA + Th^{4+}= CNT-DGA-Th^{4+}	-891.37	-884.54
$Th^{4+}(H_2O)_8$ + CNT_S = CNT_S-Th^{4+} + $8H_2O$	22.98	35.14
$Th^{4+}(H_2O)_8$ + CNT_O = CNT_O-Th^{4+} + $8H_2O$	28.97	33.58
CNT-COOH + $Th^{4+}(H_2O)_8$= CNT-COOH-Th^{4+} +$8H_2O$	–9.23	5.46
CNT-DGA + $Th^{4+}(H_2O)_8$ = CNT-DGA-Th^{4+} +$8H_2O$	–107.77	-85.11

3.2 Selectivity of Eu(III) over Am(III) with CNT-DGA[168]

In the spent fuel reprocess process, The high level radioactive waste (HLW) stream contains the long lived minor actinides (MA) such as ^{237}Np, ^{241}Am, ^{243}Am, and ^{245}Cm along with fission product elements (FPs) such as ^{90}Sr, ^{137}Cs, ^{106}Ru, etc. and structural elements such as Fe, Cr, Zr, etc. The deep geological disposal and storage of this vitrified HLW has been followed worldwide. Isolation of the long lived MA and fission products like ^{99}Tc, ^{93}Zr, and ^{129}I from HLW is desirable for minimizing the long term radiological risk. Partitioning of actinides from the bulk of short lived and inactive material are investigated from long time and various partitioning processes are suggested. However, None of these processes can mutually separate between the trivalent trans plutonium actinides, An(III) (Am(III), Cm(III), etc.) and the lanthanides, Ln(III) due to their similar chemical behaviour. Partitioning between Ln(III) and An(III) is also important in view of the formation of larger amount of lanthanides (20–30 times) over that of the minor actinides in fission reaction. The high neutron absorption cross section of some isotopes of lanthanides can reduce the efficiency of transmutation process where long-lived radionuclides will be transmuted in high energy high flux reactors or accelerator driven sub-critical system. It is desirable, therefore, to develop a suitable agent that can mutually separate trivalent lanthanides from trivalent actinides.

Diglycolamic acid [124] derivatives, a CHON type anionic tridentate ligand, are emerging as potential candidate for trivalent lanthanide-actinide separation. Therefore, we have studied the separation of Eu(III) and Am(III) by DGA-functionalized-CNTs (DGA-CNTs). Multi-walled-CNTs have been modified by introducing DGA groups on its surface through chemical covalent functionalization and studied for adsorption of Eu(III) and Am(III). Theoretical investigation of the extraction of Eu(III) and Am(III) by this material has also been carried out using density functional theory as implemented in the Turbomole program.

3.2.1 Computational Study

3.2.1.1 Computational Protocol

The same methodology has been used as in Sec. 3.1.1.1.

3.2.1.2 Structural Parameters

We have considered one DGA unit anchored on the open pore of the (8,0) zig-zag CNT with 4 unit cells as earlier studied for one unit of carboxylate anchored on CNT.[39] The optimized structures of complexes of Eu^{3+} and Am^{3+} with functionalized CNT-DGA in absence of nitrate ion are presented in **Figure 3.7**. Both the Eu^{3+} and Am^{3+} ions are found to be directly coordinated to the three donor O atoms of the DGA moiety. All three donor O atoms and the coordinated metal ion are lying in the same plane. The calculated structural parameters are given in **Table 3.14**. The bond length of two C=O groups of DGA unit was lengthened to 1.248Å and 1.275Å for Eu^{3+} ion and 1.244Å and 1.271 Å for Am^{3+} ion after complexation. It is interesting to mention that though the metal ions and three donor O atoms are lying in the same plane, the M-O bond length with three O atoms are not same in length.

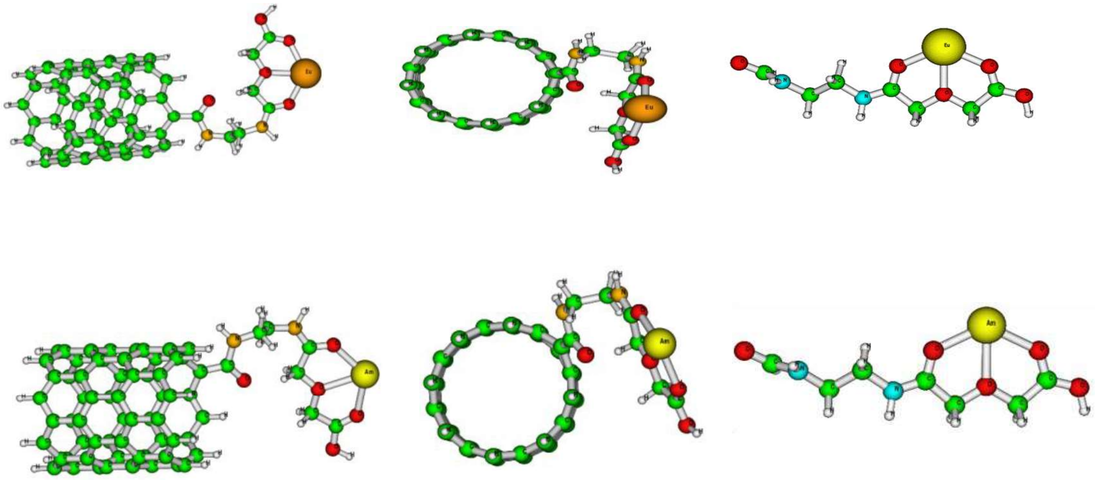

Figure 3.7 Optimized structure of complexes of Eu^{3+} and Am^{3+} ions with DGA functionalized (8, 0) CNT and non-functionalised DGA in absence of nitrate ion.

Table 3.14 Calculated structural parameters of complexes of Eu^{3+} and $Am3^{+}$ with CNT-DGA at the BP86/SVP level of theory

d_{M3+-O} (Å)of	with Nitrate		without Nitrate	
	Am^{3+}	Eu^{3+}	Am^{3+}	Eu^{3+}
$NO_3(1)$	2.448	2.459	-	-
	2.425	2.449		
$NO_3(2)$	2.456	2.475	-	-
	2.463	2.534		
$NO_3(3)$	2.457	2.475	-	-
	2.515	2.483		
DGA-C=O	2.457	2.566	2.419	2.391
	2.665	2.694	2.324	2.292
DGA-C-O-C	2.618	2.611	2.596	2.520

The M-O (O of C=O group) bond length was found to be 2.292 and 2.391Å and one M-O (ethereal O) bond length was found to be 2.520Å for Eu^{3+} ion, whereas for Am^{3+} ion it was 2.324, 2.419 and 2.596Å respectively. The shorter M-O bond length for C=O group compared to M-O bond length of ethereal O suggest that former has stronger interaction ability than the later.

The shorter bond length of Eu^{3+} compared to Am^{3+} ion in absence of nitrate ion might be due tothe higher covalency in Eu-O bond compared to Am-O bond which is found to be reversed of the Eu-S and Am-S bond covalency.[148, 244] The larger –C=O distances and smaller M-O distances for Eu^{3+} compared to Am^{3+} points towards strong interaction of the former with the CNT-DGA than the later. It is interesting to study the effect of CNT on the interaction energy in the CNT-DGA unit. In order to find out the effect of CNT on the interaction energy, we have performed the calculation by replacing CNT with H atom in the CNT-DGA motif and the optimized structure is presented in **Figure 3.7**. The optimized structure of Eu^{3+} and Am^{3+}ion in presence of nitrate ion is displayed in **Figure 3.8**.

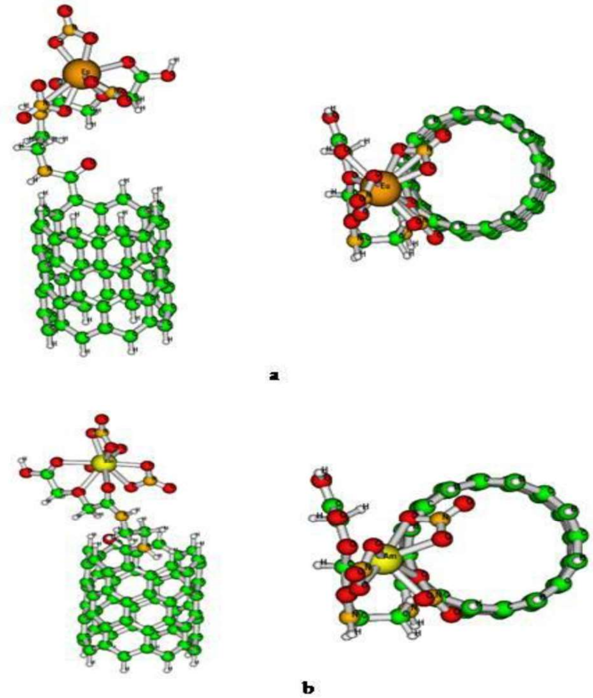

Figure 3.8 Optimized structure of complexes of (a) Eu^{3+} and (b) Am^{3+}ions with DGA functionalized (8, 0) CNT in presence of nitrate ion.

Both the Eu^{3+} and Am^{3+}ions are found to be nona coordinated through 3 donor atoms from DGA and six donor atoms from three nitrate ions in bidentate mode. The Eu-O (oxygen of NO_3) is found to be varied from 2.449 to 2.534Å whereas Am-O (oxygen of NO_3) is found to be varied from 2.425 to 2.515Å. The Eu-O (carbonyl oxygen of DGA) is found to be varied from 2.566 to 2.694Å and for Am-O (carbonyl oxygen of DGA) is found to be in the range of 2.457 to 2.665Å indicating asymmetrical nature of bonding from the identical carbonyl bonding. The Eu-O (etheric oxygen of DGA) is found to be 2.611Å and for Am^{3+} it is determined to be 2.618Å. The close M-O bond distance bears the fact that trivalent lanthanides and actinides have similar chemical properties. The optimized structure of hydrated Eu^{3+} and Am^{3+} ion are also presented in **Figure 3.9**. The calculated Eu-O bond distance was found to be varied from 2.454-2.539Å, whereas, the

Am-O bond distance was found to be varied form 2.508-2.589Å suggesting that the hydration energy of Eu^{3+} ion should be more than that of Am^{3+} ion due to shorter bond length of Eu-O over Am-O. The higher solvation free energy of Eu^{3+} ion over Am^{3+} ion has been reported earlier from abinito and semi-empirical calculation.[245-248] Further, the M-O bond length in hydrated species was found to be larger than the M-O bond length of C=O group of DGA ligand. The M-O bond distance of NO_3^- ion is found to be smaller than the M-O of H_2O indicating the stronger interaction of metal ions with NO_3^- ion group than H_2O.

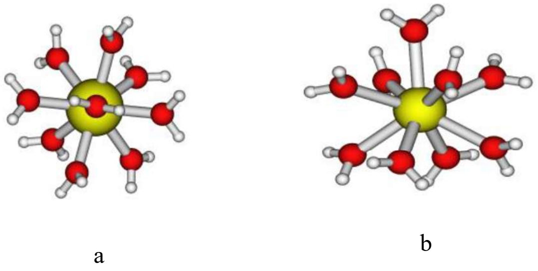

Figure 3.9 Optimized structure of hydrated complexes of (a) Eu^{3+} and (b) Am^{3+} ions.

3.2.1.3 **Gas phase binding energy/free energy of complexation**

The origin of preferential selectivity for a particular metal ion towards a coordinating ligand may be electronic or entropy driven or solvent mediated. Hence, the gas phase binding energy, which plays an important role in the initial screening as well as in the origin of selectivity of the metal ions, is calculated using the following complexation reaction (Equation 1) in gas phase as

$$M^{3+} + CNT - DGA + 3NO_3^- = M(NO_3)_3.CNT - DGA \qquad (3.1)$$

$$\Delta E_{(gp)} = \Delta E_{CNT-DGA-M(NO_3)_3(gp)} - (\Delta E_{M^{3+}(gp)} + 3\Delta E_{NO_3^-(gp)} + \Delta E_{CNT-DGA(gp)} \qquad (3.2)$$

Where $\Delta E_{CNT-DGA-M(NO_3)_3(gp)}$, $\Delta E_{M^{3+}(gp)}$, $\Delta E_{NO_3^-(gp)}$ and $\Delta E_{CNT-DGA(gp)}$ represent the total energy of the metal ion-ligand-nitrate complex, metal ion, nitrate ion and the ligand respectively. The calculated values of binding energy are given in **Table 3.15**.

Table 3.15 Calculated interaction energies, ΔE (kcal/mol) and thermodynamical parameters in gas phase for bare metal ions (kcal/mol)

Complexation reaction in gas phase	**ΔE**	**ΔH**	**ΔS***	**ΔG**
$Eu^{3+} + DGA \rightarrow DGA - Eu^{3+}$	-416.4	-416.0	-0.027	-407.8
$Am^{3+} + DGA \rightarrow DGA - Am^{3+}$	-334.4	-333.9	-0.029	-325.2
$Eu^{3+} + CNT - DGA \rightarrow CNT - DGA - Eu^{3+}$	-600.9	-595.8	-0.041	-583.5
$Am^{3+} + CNT - DGA \rightarrow CNT - DGA - Am^{3+}$	-550.4	-545.3	-0.035	-534.6
$Eu^{3+} + 3NO_3^- + CNT - DGA \rightarrow CNT - DGA - Eu(NO_3)_3$	-1062.5	-1061.0	-0.154	-1015.0
$Am^{3+} + 3NO_3^- + CNT - DGA \rightarrow CNT - DGA - Am(NO_3)_3$	-1040.5	-1039.1	-0.153	-993.2

*the unit is kcal/mol/K

It is seen that the binding energy of Eu^{3+} ion with CNT-DGA either in presence or absence of nitrate ion is found to be higher than that of Am^{3+} ion. The value of gas phase binding energy, ΔE for Eu^{3+} ion (-600.9kcal/mol) was found to be higher than that of Am^{3+} ion (-550.4kcal/mol) by -50.5kcal/mol. It is interesting to study the effect of CNT on the interaction energy in the CNT-DGA unit. In order to find out the effect of CNT on the interaction energy, we have performed the calculation by replacing CNT with H atom in the CNT-DGA motif. The gas phase interaction energy was found to be reduced considerably in absence of CNT (see the **Table 3.15**).The selectivity trend remains the same. In order to find out the reason of higher binding energy of Eu^{3+} ion over Am^{3+} ion, the NPA was performed to compute the charge on the metal ion and the atomic orbital population. The calculated value of residual charge on the metal ions and the atomic orbital population is presented in **Table. 3.16**.

Table 3.16 Calculated charge and orbital population using NBO analysis in gas phase

Complex species	Charge on Metal ion (esu)	n(s)	n(p)	n(d)	n(f)	n(g)
$CNT-DGA-Eu^{3+}$	1.82	4.02	11.99	10.16	6.99	0.0003
$CNT-DGA-Am^{3+}$	1.69	4.15	11.99	10.18	6.97	0.0004
$CNT-DGA-Eu(NO_3)_3$	1.78	4.16	1.99	10.80	6.24	0.001
$CNT-DGA-Am(NO_3)_3$	1.84	4.18	11.99	10.76	6.20	0.001

From NPA, it is seen that there is small extra orbital contribution to the inner s, d and f subshells of the metal ion indicating that the interaction of metal ion with CNT-DGA ligand has some covalent character. The f subshells were found to be more diffused than the s and d subshells in absence of nitrate ion. The contribution from g subshells is nearly negligible. In presence of nitrate ion, there is a change in the orbital population. The d subshells were found to be more diffused than the s and f subshells in presence of nitrate ion. The contribution from f subshells is reduced considerably. Unexpectedly, in absence of nitrate ion the residual charge on Eu^{3+} ion (1.82au) was found to be more compared to Am^{3+} ion (1.69au) indicating that the interaction energy should be more with Am^{3+} ion over Eu^{3+} ion, but actually the calculated binding energy was found to be higher with Eu^{3+} ion over Am^{3+} ion. But, it was seen to be reversed in the presence of nitrate ion, where, the residual charge on the Am^{3+} metal ion (1.84au) was found to me more compared to Eu^{3+} metal ion (1.78au). This is reflected in the interaction energies i.e., the interaction energies with nitrate ion are higher than without nitrate ion for both Eu^{3+} and Am^{3+} complexes with CNT-DGA. The transfer of charge was found to be higher in Eu^{3+} ion compared to Am^{3+} ion. The substantial charge on the metal atom obtained from natural population analysis (**Table 3.16**.) indicates the charge-dipole type interaction.

The transfer of charge was found to be much higher in the presence of nitrate ion which in turn increases the interaction energy further. Further, in order to understand the nature of interaction, E_{HOMO} and E_{LUMO} and their energy gap for free metal ion and ligand was evaluated and is displayed in **Table. 3.17**.

Table 3.17 Calculated Quantum chemical descriptorsin gas phase

	E_{HUMO}(eV)	E_{LUMO}(eV)	$E_{HUMO\text{-}LUMO}$(eV)	χ (eV)	η(eV)	ΔN
Eu^{3+}	-37.16	-31.95	5.20	34.55	2.60	5.42
Am^{3+}	-32.40	-28.45	3.95	30.43	1.97	6.03
$CNT - DGA$	-4.32	-3.91	0.41	4.11	0.20	-

The E_{HOMO} and $E_{LUMO}$are a measure of electron-donor and electron-acceptor capacity, respectively, and consequently determine donors and acceptors in charge-transfer interactions. The $E_{HOMO\text{-}LUMO}$ of Eu^{3+} ion (5.2eV) was found to be higher than that of Am (3.95eV) indicating the softer nature of Am^{3+} compared to Eu^{3+} ion. Even the calculated value of absolute electronegativity, χ, and absolute hardness, η for Eu^{3+} ion was found to be higher than that of Am^{3+} ion suggesting its strong accepting nature. The tridentate DGA ligand with hard O donor represents the class of hard base as evident from the value of $E_{HOMO\text{-}LUMO}$ (0.41eV) and the value of χ (4.11eV) and η (0.20eV). According to Pearson's SHAB principle[249], the interaction of Eu^{3+} ion with DGA should be more compared to softer acceptor i.e. Am^{3+} ion and same is reflected in the higher binding energy of Eu^{3+} ion over Am^{3+} ion. Further, the amount of charge transfer, ΔN was also evaluated for the donor acceptor reaction and the values are presented in **Table. 3.17**. The higher the value of charge transfer, ΔN, higher is the metal-ligand interaction. But, in the present case, the value of ΔN was found to be higher with Am^{3+} over Eu^{3+} ion and cannot be correlated with the binding energy trend.

The thermodynamic free energy of complexation, ΔG for Eu^{3+} and Am^{3+} complexes in gas phase has also been computed and the values are presented in **Table 3.15**. It is seen that the change in enthalpy, ΔH of the complexation reaction is negative indicating an enthalpic favorable process. The value of ΔH is found to be more negative in the presence of nitrate ion. Further the value of ΔH found to be higher for Eu^{3+} compared to Am^{3+} ion towards CNT-DGA. The calculated value of entropy change ΔS is also given in the same table. The value of ΔS is found to be negative suggesting entropy unfavorable process. It is known that the metal ion ligand complexation from aqueous phase is structure breaking and structure making process. The metal ion complexation is a structure making process, whereas during complexation the hydrated ion is dehydrated leading to release of water molecule, which is a structure breaking process. The former leads to negative entropy contribution whereas later leads to positive entropy contribution. This can be explained as follows. Though, the release of water molecules during dehydration is a structure breaking process, the released water molecules form a stable water cluster through hydrogen bonding, which in turn fails to add the high positive entropy contribution due to assembling of remaining reactant species. But, point to be noted, that though the entropy is negative, it cannot surpass the high enthalpy value leading to negative free energy indicating favorable complexation reaction. The value of free energy change, ΔG is found to be smaller than that of ΔH as TΔS is negative. It is also interesting that the value of TΔS is found to be more negative in the presence of nitrate ion (see **Table 3.15**). This is obvious as more species are involved in the complex formation.

3.2.1.4 **Free energy of extraction using thermodynamic cycle in solvent phase**

Though gas phase free energy of complexation was sufficient to capture the experimental selectivity of Eu^{3+} ion over Am^{3+} ion towards CNT-DGA, it will be more realistic if the calculation is performed in solution phase. The metal ions are extracted from the aqueous environment, where it remains in a strongly hydrated form. Hence it is essential to compute the solvation energy of the metal ions in aqueous environment for accurate prediction of extraction energy. In order to account for the aqueous solvent effect, we have followed the earlier reported cluster water model[243]

$$M^{3+}_{(gp)} + (H_2O)_{9(aq)} \rightarrow M^{3+}(H_2O)_{9(aq)} \qquad (3.3)$$

The cluster of 9 water molecules for Eu^{3+} and Am^{3+} was used for geometry optimization and total energy calculation as earlier considered.[245, 246]The optimized structures of hydrated $[Eu(H_2O)_9]^{3+}$ and $[Am(H_2O)_9]^{3+}$ clusters are also presented in **Figure 3.9**. In the case of hydrated clusters of Eu^{3+} and Am^{3+} the Eu-O (2.457-2.539Å) and Am-O (2.507-2.589Å) bond distances are found to be longer than the values observed in its complexes with CNT-DGA indicating the strong complexing nature of CNT-DGA with Eu^{3+} and Am^{3+} ions.In case of nitrate ion, solvation free energy from our earlier study was used.[250] The gas phase optimized structure was used to calculate single point energy using COSMO solvation model to obtain the solvation free energy.The computed values of free energy of solvation after standard state entropy corrections for Eu^{3+} and Am^{3+} ions are -820.2 and -799.4 kcal/mol respectively. The reported experimental solvation energy of Eu^{3+} ion is -803.8kcal/mol[251] and hence gives the confidence in using the present solvation energy methodology. Further, the difference in solvation energy (20.8kcal/mol) of Eu^{3+} and Am^{3+} ion is found to be very close to the reported[247, 248] value of 22.2kcal/mol by David et al. using a simple model based on the line of Born electrostatic model where calculation of hydrated ion thermodynamic properties were calculated by taking into account of various basic interactions between an ion and surrounding water molecules namely: ionic radius, the coordination number, the cation–oxygen distance, the number H of water molecules in the second hydration shell and the effective charge Z_{eff} of a cation.In aqueous phase, the calculation of free energy for ions was performed using standard state entropy corrections[243] as practiced by Bryantsev et al. Interesting to note that though the solvation free energy of Eu^{3+} ion is much higher than that of Am^{3+} ion, Eu^{3+} ion is preferentially selected over the Am^{3+} ion. This preferential selectivity of Eu^{3+} ion over Am^{3+} ion can be well addressed by calculating the free energy of extraction of the ions with the ligands. The free energy of extraction, ΔG_{ext} for Eu^{3+} and Am^{3+} with CNT-DGA from aqueous phase was calculated using Born-Haber thermodynamic cycle (**Figure 3.10**). The free energy of solvation of CNT-DGA and its complexes with Eu^{3+} and Am^{3+} with and without nitrate ion in the aqueous phase are calculated and given in **Table 3.18**. The binding energy, ΔE for Eu^{3+} and Am^{3+} with and without nitrate in aqueous phase is also presented in **Table 3.18**.

$$\begin{tikzcd}
M^{3+}_{(gp)} \arrow[d, "\Delta G_{sol(M)}"] & + & 3NO_3^{-}{}_{(gp)} \arrow[d, "\Delta G_{sol(NO3-)}"'] & + & L_{(gp)}\Delta G_{gp} \arrow[d, "\Delta G_{sol(L)}"] \arrow[r, "\Delta G"] & ML_3(NO_3)_{3(gp)} \arrow[d, "\Delta G_{sol(ML(NO3)3}"] \\
M^{3+}_{(aq)} & + & 3NO_3^{-}{}_{(aq)} & + & L_{(aq)}\Delta G_{ext} \arrow[r, "G_{ext}"'] & ML(NO_3)_{3(aq)}
\end{tikzcd}$$

Figure 3.10 Thermodynamic cycle for calculation of free energy of extraction for Eu^{3+} and Am^{3+} ion with CNT-DGA.

Table 3.18 Calculated interaction energies, ΔE (kcal/mol) and thermodynamical parameters in aqueous phase for bare metal ions (kcal/mol)

Complexation reaction in aqueous phase	ΔE	ΔH	ΔS*	ΔG
$Eu^{3+} + CNT - DGA \rightarrow CNT - DGA - Eu^{3+}$	-81.9	-76.8	-0.041	-64.5
$Am^{3+} + CNT - DGA \rightarrow CNT - DGA - Am^{3+}$	-71.5	-66.3	-0.035	-55.7
$Eu^{3+} + 3NO_3^{-} + CNT - DGA \rightarrow CNT - DGA - Eu(NO_3)_3$	-100.1	-98.7	-0.154	-52.6
$Am^{3+} + 3NO_3^{-} + CNT - DGA \rightarrow CNT - DGA - Am(NO_3)_3$	-110.0	-108.5	-0.153	-62.7

*the unit is kcal/mol/K

It is seen that the aqueous phase binding energy of Eu^{3+} ion with CNT-DGA in absence of nitrate ion is found to be higher than that of Am^{3+} ion.The value of aqueous phase binding energy, ΔE for Eu^{3+} ion (-81.9kcal/mol) was found to be higher than that of Am^{3+} ion (-71.5kcal/mol) by -10.4kcal/mol in absence of nitrate ion, whereas, the opposite trend was observed in presence of nitrate ion i.e., Am^{3+} shows higher aqueous phase binding energy over Eu^{3+} ion. Point to be noted that the binding energy is reduced drastically from the gas phase value due to screening of the metal ion charge by the dielectric of the water molecules. Further, it is interesting to study how the solvent change the charge, orbital population and HOMO-LUMO of the metal ion ligand system and hence dictates the interaction. In view of this, the NPA was performed to compute the charge on the metal ion and the atomic orbital population in aqueous phase also. The calculated value of residual charge on the metal ions and the atomic orbital population is presented in **Table 3.19**. From NPA, it is seen that there is small extra orbital contribution to the inner d and f subshells of the metal ion indicating that the interaction of metal ion with CNT-DGA ligand has some covalent character. The f subshells were found to be more diffused than the s and d subshells in absence of nitrate ion.

Table 3.19 Calculated charge and orbital population using NBO analysis in aqueous phase

Complex species	Charge (esu)	n(s)	n(p)	n(d)	n(f)	n(g)
$CNT-DGA-Eu^{3+}$	1.88	4.01	11.99	10.11	6.99	0.0002
$CNT-DGA-Am^{3+}$	2.27	4.02	11.99	10.11	6.58	0.0004
$CNT-DGA-Eu(NO_3)_3$	1.61	4.15	11.99	10.72	6.50	.0001
$CNT-DGA-Am(NO_3)_3$	1.86	4.18	11.99	10.75	6.19	0.001

The contribution from g subshells is nearly zero. Further, though the diffused nature of s and f orbital of Eu^{3+} ion remains same, it was found to be reduced for Am^{3+} ion in aqueous phase compared to gas phase. In presence of nitrate ion, the aqueous phase binding energy was found to be reversed i.e., the binding energy of Am^{3+} ion was found to be higher than that of Eu^{3+} ion by 9.8kcal/mol. There is a change in the orbital population also. The d subshells were found to be more diffused than the s and f subshells in presence of nitrate ion. The contribution from f subshells is reduced considerably. The residual charge on Eu^{3+} ion (1.88au) in absence of nitrate ion was found to be small compared to Am^{3+} ion (2.27au) indicating that the interaction energy should be more with Eu^{3+} ion over Am^{3+} ion and same is observed as revealed from the aqueous phase binding energy (**Table. 3.18**). In presence of nitrate ion, the residual charge on Eu^{3+} ion (1.61au) was also found to be small compared to Am^{3+} ion (1.86au) indicating that the interaction energy should be more with Eu^{3+} ion over Am^{3+} ion but actually reverse trend was noticed. Further, in order to understand the nature of interaction in aqueous phase, the energy of HOMO and LUMO and their gap for free metal ion and ligand was evaluated in aqueous phase and is displayed in **Table 3.20**. The $E_{HOMO-LUMO}$ of Eu^{3+} ion (5.2eV) and Am^{3+} (3.95eV) was seen to be unchanged from the gas phase. The calculated value of absolute electronegativity, χ, and absolute hardness, η for Eu^{3+} ion was found to be reduced in the aqueous phase compared to gas phase but the trend remains same. Similar is the case for the tridentate DGA ligand. The amount of charge transfer, ΔN was also evaluated for the donor acceptor reaction in aqueous phase without nitrate ion and the values are presented in **Table.3.20**. The value of ΔN was found to be higher with Eu^{3+} (1.54) over Am^{3+} (1.27) ion which can be correlated with the higher binding energy of Eu^{3+} over Am^{3+} ion.

Table 3.20 Calculated Quantum chemical descriptors in aqueous phase

	E_{HUMO}(eV)	**E_{LUMO}(eV)**	**$E_{HUMO-LUMO}$(eV)**	**χ (eV)**	**η(eV)**	**ΔN**
Eu^{3+}	-14.82	-9.61	5.20	12.21	2.60	1.54
Am^{3+}	-11.10	-7.14	3.95	9.12	1.97	1.27
$CNT-DGA$	-3.88	-3.61	0.26	3.75	0.13	-

The free energy of complexation for Eu^{3+} and Am^{3+} ions with CNT-DGA is also presented in **Table.3.18**. The free energy of complexation in solution was found to be reduced considerably compared to gas phase (**Table. 3.15**). The solvent-metal ion interaction in the aqueous phase decreases the interaction of metal ion with ligand thereby decreasing the free energy value. The value of ΔG for Eu^{3+} ion was found to be higher than that of Am^{3+} ion in absence of nitrate ion, whereas, it was reversed in the presence of nitrate ion i.e. Am^{3+} ion is preferentially selected over Eu^{3+} ion. This may be due to consideration of simple complexation reaction where all the species are considered to be implicitly solvated. Further, to check this anomaly of selectivity, the free energy of extraction was calculated in absence of nitrate ion using the thermodynamic cycle and the results are listed in **Table 3.21**.

Table 3.21 Calculated value of thermodynamic parameters (kcal/mol) for the extraction of Eu^{3+} and Am^{3+} ions in absence of nitrate anion with CNT-DGA

M^{3+}	$\Delta G_{(gp)}$	$\Delta G_{sol(M)}$	$\Delta G_{sol(CNT-DGA)}$	$\Delta G_{sol(CNT-DGA-M(NO3)3)}$	ΔG_{ext}	$\Delta\Delta G_{sol}$
Eu	-583.5	-820.2	-34.6	-286.1	-14.8	568.7
Am	-534.6	-799.4	-34.6	-291.3	8.0	542.7

Here also, the free energy of extraction was found to be higher for Eu^{3+} ion over Am^{3+} ion. From Eq. 3.3, it is seen that the free energy of extraction, ΔG_{ext} has two contributory components, one is assigned from the gas phase and other one is from the solvent phase. The calculated values of $\Delta\Delta G_{sol}$is presented in Table **3.22**.

Table 3.22 Calculated value of thermodynamic parameters (kcal/mol) for the extraction of Eu^{3+} and Am^{3+} ions in presence of nitrate anion with CNT-DGA

M^{3+}	$\Delta G_{(gp)}$	$\Delta G_{sol(M)}$	$\Delta G^{*}_{sol(NO3)}$	$\Delta G_{sol(CNT-DGA)}$	$\Delta G_{sol(CNT-DGA-M(NO3)3)}$	ΔG_{ext}	$\Delta\Delta G_{sol}$
Eu	-1015.0	-820.2	-54.2	-34.6	-46.8	-44.3	952.9
Am	-993.2	-799.4	-54.2	-34.6	-43.8	-40.3	935.1

*reference [243]

From the **Table 3.15** and **Table 3.22**, it is seen that in presence of nitrate ion, the value of ΔG_{gas} supersedes the positive value of $\Delta\Delta G_{sol}$ for both Eu^{3+} and Am^{3+} leading to negative value of ΔG_{ext} (see **Table 3.22**). The free energy of Eu^{3+} ion was found to be higher than that of Am^{3+} ion by 3.98kcal/mol. It is interesting to note that using the simple complexation reaction in solution phase where all the energy calculations are done using implicit solvation leads to higher selectivity for Am^{3+} ion over Eu^{3+} ion in the presence of nitrate ion, whereas using more reliable thermodynamic cycle the selectivity order becomes reversed i.e. Eu^{3+} ion is extracted preferentially over Am^{3+} ion. The suitability of the methodology can be validated only by performing the experiments which is the topic of the next section.

3.2.2 Experimental Study

3.2.2.1 **Batch adsorption and IR spectral studies**

Preparation and characterization of CNT-DGA was performed successfully[252] . (~25 mg) of CNT-DGA was equilibrated for 2 hours with aqueous solution spiked with ^{241}Am (III)(or $^{(152+154)}$Eu (III)) tracer at pH 2 and 298 K. The black colored solution was centrifuged at 10,000 rpm. Radioactivity of ^{241}Am (III)and $^{(152+154)}$Eu (III)in supernatant clear solution was measured using a well-type NaI(Tl) scintillation detector. The solid phase distribution ratio (K_d) of metal ion was determined using Eq. (3.4)

$$K_d = \frac{A_i - A_f}{A_f} \times \frac{V_{aq}}{W_s} \tag{3.4}$$

Where A_i and A_f are the initial and final gamma activity of the metal ions in the aqueous phase, V_{aq} is the volume of the aqueous phase (1ml) and W_s is the weight of the sorbent used for the equilibration studies. The distribution constant of Eu^{3+} and Am^{3+} ion was estimated to be 496ml/g and 337ml/g respectively. From the estimated distribution constant, it is indisputably established that the Eu^{3+} ion is preferentially extracted over Am^{3+} ion and hence confirm the acceptance of the explicit cluster model for ion solvation free energy and thermodynamic cycle for the evaluation of free energy of extraction in solution phase.

FTIR spectra of the synthesized CNT-DGA was also recorded and compared with the calculated one (**Figure 3.11**). The carbonyl stretching frequency of the DGA group was clearly visible at 1605 cm^{-1} in experimental spectra which is equivalent to 1648 cm^{-1} peak of the calculated one and hence confirms the acceptance of present computational methodology used for the calculation of the IR spectra. Further, the strong coordinating ability of carbonyl oxygen was confirmed from the significant red shift of the –C=O stretching frequency in the calculated IR spectra of complexes of Eu^{3+} ion (1441 cm^{-1}) and Am^{3+} ion (1550 cm^{-1}). The stronger interaction of DGA with Eu^{3+} over Am^{3+} is also reflected from the large extent of red shift in former metal ion.

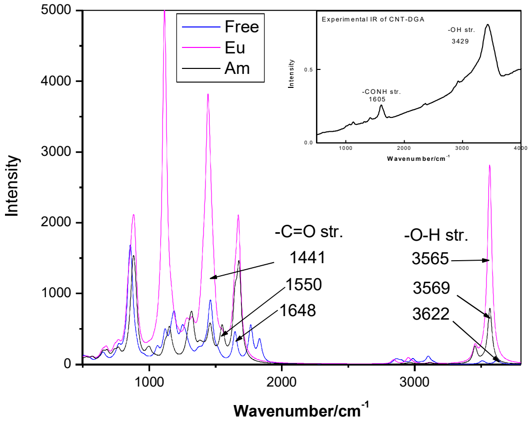

Figure 3.11 Experimental and calculated IR spectra of free CNT-DGA and its complexes with Eu^{3+} and Am^{3+} ions

3.3 Adsorption of Pu^{4+}, PuO_2^{2+} and Am^{3+} by CNT-DGA[169]

The appropriate ligand functionality attached to the CNT was expected to enhance the sorption efficiency as well as selectivity of the targeted actinide ions. In previous section amide functionalized CNTs were found to improve the extraction efficiency for tetra and hexavalent actinides[253, 254].

In view of these, the present investigation focused on understanding the sorption behaviour of Pu^{4+}, PuO_2^{2+} and Am^{3+} using diglycolamic acid functionalized multiwalled carbon nano tubes (DGA-CNT). Different isotherm and kinetics modes were employed to get more insight into the sorption procedure. The stripping, radiolytic stability and selectivity study was also carried out for evaluation of the overall performance. The coordination environment and nature of interaction can be predicted by the theoretical calculations using the density functional theory (DFT). Therefore, DFT calculation was carried out to locate the coordination mode of the functionalized ligand with an aim to understand the complexation of Pu^{4+}, PuO_2^{2+} and Am^{3+} with DGA-CNT.

3.3.1 Experimental Study

3.3.1.1 **Extraction profiles as a function of aqueous feed acidity**

The K_d values for Am^{3+}, Pu^{4+} and PuO_2^{2+} were found to increase with increase in aqueous feed acidity upto 3 M HNO_3, while plateau were observed beyond 3 M HNO_3(**Figure 3.12**). The initial increase in Kd values with aqueous feed acidity can be attributed to the participation of the nitrate anion during the complexation. Beyond 3M HNO_3, due to the presence of sufficient amount of H^+ ion into the aqueous phase, it competes with the metal ions leading to the insensitivity of their $K_d$values with aqueous feed acidity

$$H^{+} + DGA - CNT + NO_3^{-} = HNO_3.DGA - CNT \qquad (3.5)$$

The K_d values for for the actinides were found to follow the trend $Am^{3+} > Pu^{4+} > PuO_2^{2+}$. The better sorption of tetra valent plutonium compared to hexavalent can be attributed to the high chemical potential of the tetra valent ion. The unusually higher extraction of Am^{3+} over Pu^{4+} might be attributed to the aggregation behaviour of DGA moieties which was also reported in case of several DGA functionalized ligands.[226, 255-259]

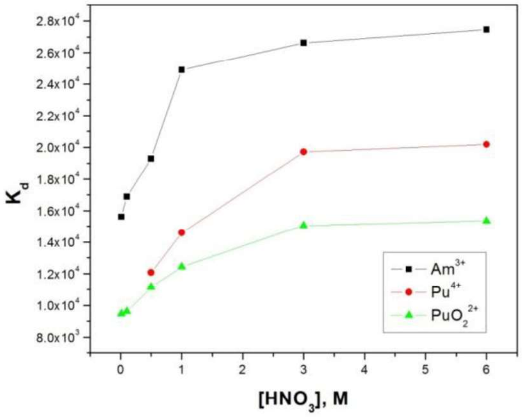

Figure 3.12 The extraction profiles for Am^{3+}, Pu^{4+} and PuO_2^{2+} as a function of aqueous feed acidity

A comparative study was carried out to evaluate the efficiency of DGA-CNT over CNT, CNT with different functionality and nano diamonds on sorption of actinides in different oxidation states reported in the literatures (**Table 3.23**).

Table 3.23 Comparison of the performance of DGA-CNT with other carbon based sorbent reported in literature

Sorbent	Actinides	K_d(mLg^{-1})	Comment	Conditions	Ref
CNT	Pu^{4+}	2.44E+03	low K_d value, only effective in the pH region	pH 6.0, 0.1 M $NaClO_4$ medium, 20 ± 2 °C	260
	UO_2^{2+}	1.10E+03	low K_d value, only effective in the pH	pH 3.0, 298 K	261

			region		
	Eu^{3+}	40%	very low *% sorption*, only effective in the pH region	pH 3.0, 298 K	257
Amide-CNT	Pu^{4+}	5.40E+03	Efficient, selective and total evaluation of sorption behaviour, kinetics, stripping, radiolytic stability, processing SHLW	3 M HNO_3, 25 ± 2 °C	
	PuO_2^{2+}	1.60E+03			253
	UO_2^{2+}	1.40E+03			254
	Th^{4+}	1.10E+04			
Nano diamonds	Am^{3+}	92%	Moderate to low % sorption value, effective in pH region	pH 4	255
	Pu^{4+}	95%			
	UO_2^{2+}	60%			
Oxidized CNT	Th^{4+}	80%	Moderate % sorption, effective in pH region	pH3	226
	U^{4+}	80%		pH 7	256
DGA-CNT	Am^{3+}	2.6 E+04	Efficient, selective and total evaluation of sorption behaviour, kinetics, stripping, radiolytic stability, processing SHLW	3 M HNO3	Present Investigation
	Pu^{4+}	1.90E+04			
	PuO_2^{2+}	1.5 E+04			

3.3.1.2 **Analysis of Sorption isotherm**

To understand the nature of sorption behaviour different models (Langmuir, Freundlich, Dubinin-Rodushkevich (D-R) andTempkin) of isotherms based on certain assumptions were utilized in the present investigation. The regression analysis was taken as the basis for the particular isotherm to be operative. The isotherm parameters as described in Table 2.5 and 2.6, are calculated from the fitted data. **Figure3.13** shows the analysis of different isotherm models while **Table 3.24** summarizes the constants obtained from these isotherm analyses. The Langmuir maximum sorption capacity for the actinides were found to follow the trend q_m (Am^{3+}) > q_m (Pu^{4+}) > q_m (PuO_2^{2+}). This trend was found to be similar as observed for their $K_d$values. The sorption energy for hexavalent plutonium was found to be the maximum followed by trivalent americium and tetravalent plutonium. The regression coefficient for Langmuir isotherm analysis was found to be very close to unity revealing the highest possibility of this isotherm to be operative during sorption process.

The 'n' values of Freundlich isotherm model which is the indication of strength of adsorption followed the same trend as observed for their K_d values. The 'n' values for all the actinides were evaluated as less than 1 revealing the cooperative nature of the sorption process. The linear regression coefficients for Am^{3+}, Pu^{4+} and PuO_2^{2+} were found to be 0.99980, 0.99975 and 0.99990, respectively. Though the linear regression coefficients were having very close proximity to unity, till that of Langmuir isotherm were found to be slightly superior.

To distinguish between physi-sorption and chemi-sorption, Dubinin–Radushkevich isotherm, based on an empirical model, is used to express the sorption mechanism with a Gaussian energy

distribution onto a heterogeneous surface. The sorption energy values calculated from followed the trend: Am^{3+} (21.4 kJ mol^{-1}) > Pu^{4+} (18.9 kJ mol^{-1})> PuO_2^{2+} (17.0 kJ mol^{-1}).

The sorption energy values revealed that the sorption processes are 'chemi-sorption' indicating the chemical interaction of actinides ion to the DGA moieties on carbon nanotubes. The X_m value, which is the indication of sorption capacity was found to follow similar trend as seen in case of Langmuir isotherm and the values were found to be in good agreement. the linear regression coefficients of Am^{3+}, Pu^{4+} and PuO_2^{2+} were found to be 0.99819, 0.87761 and 0.95728, respectively. These values were found to be poorer with respect to the other two isotherms analyzed earlier, suggesting the non existence of this isotherm during sorption.

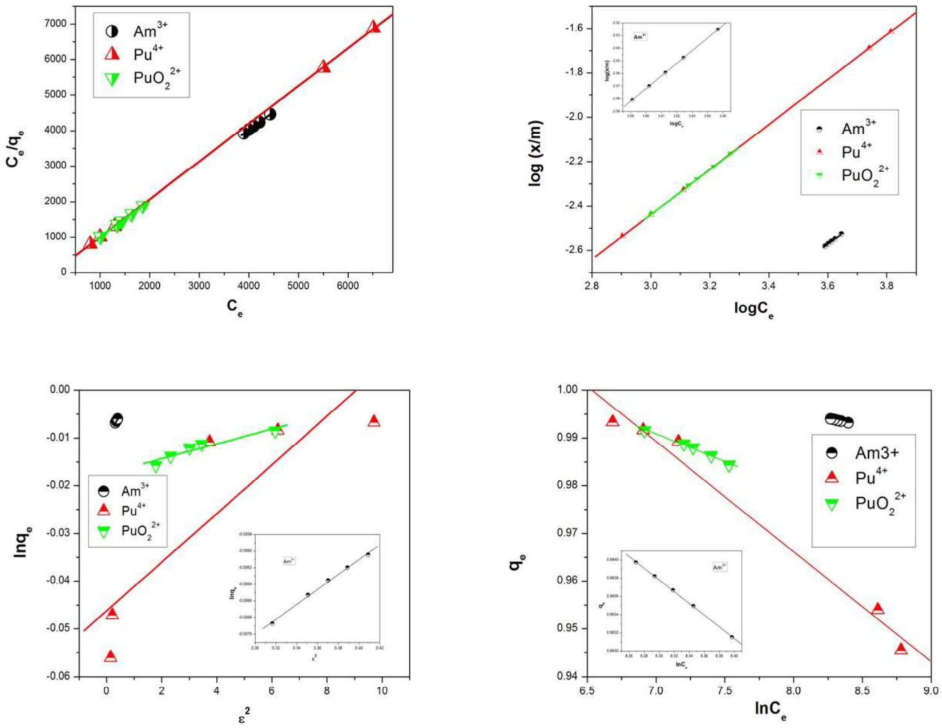

Figure 3.13 Analyses of Langmuir, D-R, Freundlich and Tempkin isotherms (curve inside is forAm^{3+})

The Temkin isotherm constant b values followed the trend $Am^{3+} > PuO_2^{2+} > Pu^{4+}$ whereas A_T values followed $PuO_2^{2+} > Am^{3+} > Pu^{4+}$ with the linear regression coefficients 0.99970, 0.99177 and 0.99477 for Am^{3+}, Pu^{4+} and PuO_2^{2+}, respectively. This also suggested that probably Tempkin isotherm was not operative during sorption of actinides on DGA functionalized CNT.

Table 3.24 The analyses of different sotherms with their regression coefficients

Langmuir			
Metal	q_0 (mg g^{-1})	b (L mol^{-1})	χ2
Am^{3+}	98.71	3.72	0.99999
Pu^{4+}	94.06	1.86	0.99998
PuO_2^{2+}	97.61	6.04	0.99999
D-R			
	E (kJ mol^{-1})	X_m (mg g^{-1})	χ2
Am^{3+}	21.4	99.03	0.99819
Pu^{4+}	18.9	95.48	0.87761
PuO_2^{2+}	17.0	98.26	0.95728
Freundlich			
	n	K_f(mg g^{-1})	χ2
Am^{3+}	0.99	100.6	0.99980
Pu^{4+}	0.98	200.1	0.99975
PuO_2^{2+}	0.94	222.7	0.99990
Tempkin			
	b (Lmg^{-1})	A_T (Lmg^{-1})	χ2
Am^{3+}	38.72	24.0	0.99970
Pu^{4+}	10.81	21.7	0.99177
PuO_2^{2+}	21.59	50.5	0.99477

3.3.1.3 **Sorption kinetics**

The K_d values for these actinides were monitored as a function of equilibration time. In case of Am^{3+}, the K_d values were found to increase with increase in equilibration time upto 120 min followed by a plateau. This observation indicated that almost 2 hours are required for achieving equilibration. In case of Pu^{4+} and PuO_2^{2+}, the K_d values were found to increase upto 60 min followed by almost no change in the K_d values. This indicated that 1 hour was sufficient for their equilibrium. Comparatively slower kinetics for Am^{3+} might be attributed to the extra time required for pre-organization of DGA moieties which was also responsible for the higher efficiency of sorption for Am^{3+} compared to Pu^{4+}.

To get into more insight of sorption, the kinetics data were also fitted into different models for sorption: Lagergren first order, intra particle diffusion and pseudo-second-order kinetics model. The rate constants and the q_e values for these actinides were summarized in **Table 3.25**. The linear regression coefficients for Am^{3+}, Pu^{4+} and PuO_2^{2+} were evaluated as 0.98024, 0.84719 and 0.93549, respectively. This revealed that the Lagergren first order kinetics were not operative for the sorption of these actinides on DGA-CNT.

Table 3.25 The sorption kinetics for Am^{3+}, Pu^{4+} and PuO_2^{2+} using different models

	Lagergren first order		
Metal	k_1	q_e	χ^2
Am^{3+}	0.053	50.75	0.98024
Pu^{4+}	0.019	13.07	0.84719
PuO_2^{2+}	0.037	11.08	0.93549
	Intra-particle diffusion model		
	k_i(mg g^{-1} min^{-1})	C	χ^2
Am^{3+}	190.4739	11.58	0.88989
Pu^{4+}	34.21018	5.95	0.73252
PuO_2^{2+}	13.12283	3.94	0.81424
	Pseudo second-order model		
	k_2(mg g^{-1} min^{-1})	q_e(mg g^{-1})	χ^2
Am^{3+}	2.10E-05	1.19E+02	0.99999
Pu^{4+}	1.40E-04	6.00E+01	1.00001
PuO_2^{2+}	3.60E-04	3.97E+01	0.99999

The above analysis of sorption kinetics led to fit the experimental data into other isotherm models. The 'intra particle diffusion' model was used to fit the kinetic data. The plots of q vs $t^{0.5}$ for Am^{3+}, Pu^{4+} and PuO_2^{2+} were shown in **Figure 3.14**. Intra-particle diffusion was not the only rate determining step as revealed from the positive intercept values for the actinides. The boundary layer thickness was found follow the trend Am^{3+}> Pu^{4+}> PuO_2^{2+} as indicated from the C values. The linear regression analyses were found be even poorer for this model compared to Lagergren first order kinetics model revealing that intra particle diffusion model was not operative during the sorption of Am^{3+}, Pu^{4+} and PuO_2^{2+} on DGA-CNT.

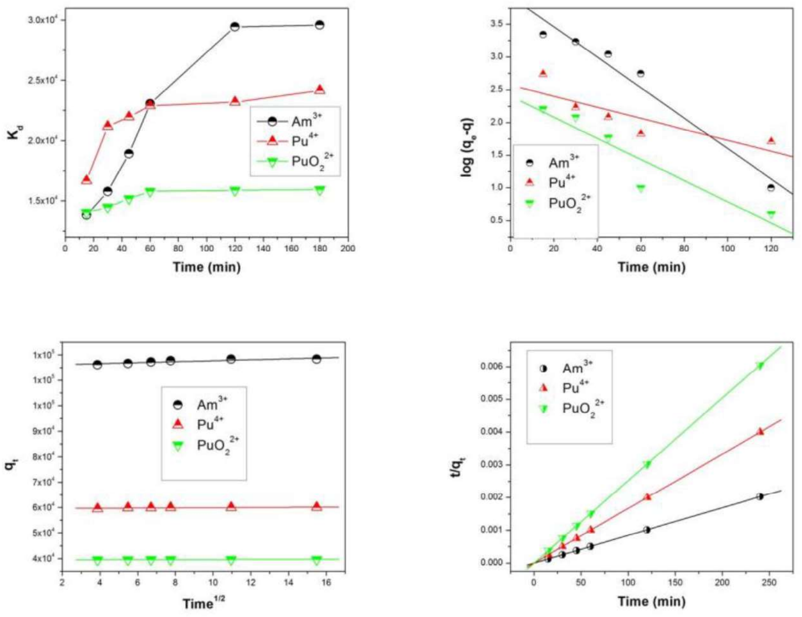

Figure 3.14 The sorption kinetics plot and kinetic data modeling for Am^{3+}, Pu^{4+} and PuO_2^{2+} using Lagergren first order, intra particle diffusion and pseudo-second-order kinetics model

The pseudo-second-order kinetics was the model of our choice. The plots of of t/q vs t were shown in **Figure 3.14.** The rate constant for Am^{3+} was found to be almost an order of magnitude lower compared to that of Pu^{4+} and PuO_2^{2+}. The linear regression coefficients were found to have very close proximity to the unity. This revealed that the sorption of Am^{3+}, Pu^{4+} and PuO_2^{2+} on DGA-CNT proceeded via pseudo second order rate kinetics. **Table 3.25** summarizes the constants evaluated from the analysis sorption kinetics models.

3.3.1.4 **Back extraction of the actinides from DGA-CNT**

Though, DGA-CNT was found to be highly efficient sorbent material for actinides like Am^{3+}, Pu^{4+} and PuO_2^{2+}, the recovery of these actinides from DGA-CNT is one of the important aspects should be looked into. A variety of stripping solutions were explored for the quantitative back extraction of these actinides. For Am^{3+}, 0.01 M EDTA, 0.01 M oxalic acid and 0.01 M Na_2CO_3 were found to strip almost 98 %, 86% and 78 % of loaded Am^{3+} from DGA-CNT. In case of Pu^{4+} the % stripping values were found to be ~ 90 %, 99% and 59 % while that for PuO_2^{2+} were ~ 83 % , 65% and 99 % for 0.01 M EDTA, 0.01 M oxalic acid and 0.01 M Na_2CO_3, respectively. This investigation led to the conclusion that EDTA was successful in stripping of trivalent actinides while for tetra and hexavalent actinides the suitable strippant was found to be oxalic acid and sodium carbonate, respectively (**Figure3.15**).

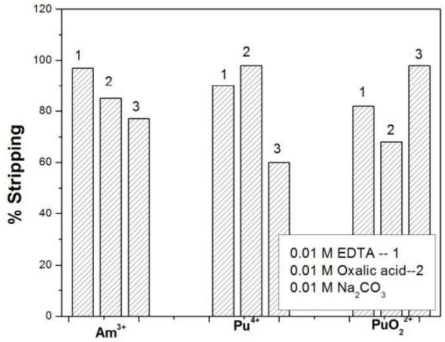

Figure 3.15 Back extraction of Am^{3+}, Pu^{4+} and PuO_2^{2+} from DGA-CNT

3.3.1.5 **Radiolytic stability**

During the processing of the actinides, the sorbent materials are exposed to different radio-toxic emissions like alpha, beta, gamma etc. These radiations deposit energy when they pass through different medium. Due to this energy the weakest bond is expected to break. As a consequence the efficacy of the materials might be questionable. In view of this, the DGA-CNT was exposed to various gamma dose using ^{60}Co source and the changes in the K_d values were monitored for Am^{3+}, Pu^{4+} and PuO_2^{2+} (**Figure 3.16**). On 500 kGy gamma exposure the K_d value for Am^{3+} was found to be ~ 83 % of its original value while on 1000 kGy exposure it was found to become ~ 71 % of the original. On 500 kGy exposure, for Pu^{4+} and PuO_2^{2+} the K_d values were found to become ~ 78 % and 69 % of their original values where as they became 71% and 55 % on 1000 kGy exposure. This study revealed that upto 500 kGy DGA-CNT system showed good radiolytic stability towards extraction of all the actinides encountered in the present investigation.

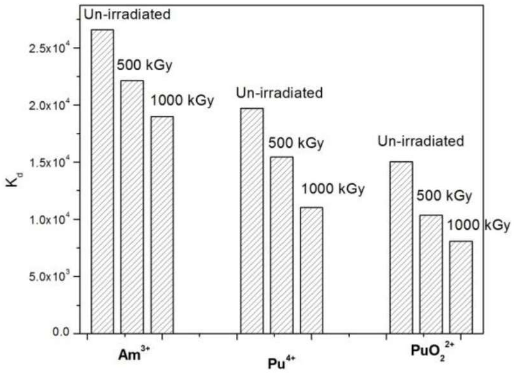

Figure 3.16 Radiolytic stability of DGA-CNT

3.3.1.6 Processing of simulated high level waste solution of Research reactor and Fast Breeder reactor origin

The success of any sorbent materials lied on processing the high level nuclear waste solutions. In view of this DGA-CNT was used for the processing of synthetic high level waste solutions obtained from research reactor and Fast breeder reactor origin. The raffinate was directly fed into plasma for the ICP-AES analysis as shown in **Table 3.26**. The analytical results revealed that even after processing with DGA-CNT, most of the common metallic constituents viz: Al, Ag, Ba, Ca, Cd, Cr, Fe, Mg, Mn, Na, Ni, Sr, Ru, Mo, Pd were not adsorbed on the DGA-CNT and hence found in the raffinate solution. DGA-CNT was found to be highly efficient and selective sorbent for actinides and lanthanides.

Table 3.26 Analytical results for SHLW solutions from RR and FBR origin after processing with DGA-CNT

		FBR		RR	
Element	**Analytical line (nm)**	**Initial (mgL^{-1})**	**Final (mgL^{-1})**	**Initial (mgL^{-1})**	**Final (mgL^{-1})**
Al	396.152	-	-	250	230±10
Ag	243.779	5	4.8±0.2	-	
Ba	455.404	70	68±3	100	96±4
Ca	396.847	-		400	320±20
Cd	361.051	5	4.9±0.2	300	290±10
Cr	284.984	-		400	300±20
Fe	244.451	-		1500	1480±10
Mg	280.27	-		300	270±10
Mn	257.611	-		500	490±20
Na	588.995	-		500	490±20
Ni	227.021	-		300	250±10
Sr	407.771	30	26±1	50	29±2
Ce	413.38	200	1.3±0.1	100	1.0±0.1
La	379.478	75	0.01±0.001	100	0.05±0.001
Pr	414.311	50	0.05±0.001	-	
Nd	401.225	30	0.03±0.001	-	
Sm	359.26	50	0.02±0.001	-	
Zr	339.198	15	1.2±0.1	-	
Ru	245.644	10	6.0±0.3	7.5	5.9±0.3
Mo	281.615	1.5	1.3±0.1	30	29±2
Pd	324.27	5	4.9±0.2	-	-
Gd	335.047	5	0.01±0.002	-	-
Dy	353.17	5	0.04±0.003	-	-
Eu	381.967	5	0.02±0.004	-	-

3.3.1.7 **Luminescence investigation**

3.3.1.7.1 Local environment of metal ion

The local environment of the metal ion in the complex form was very well probed by photoluminescence investigation using Eu^{3+} as probing metal ion[187, 262-265]. **Figure3.17** represented the emission spectra for Eu^{3+} in aqueous system and in complex with DGA-CNT and their decay profiles. The difference in the emission spectra revealed that the nature of the species is quite different. On complexation with DGA-CNT, the overall emission intensity was found to be increased which was attributed to the allowance of Laporte forbidden f-f transitions by mixing of the orbital from ligating moieties. The overall l emission spectra were found to have mainly 4 prominent components: peak ~ 593 nm was attributed to $^5D_0 \rightarrow ^7F_1$ transition which is magnetic dipole transition and insensitive to the ligand field perturbation. The peak ~ 611 nm was attributed to $^5D_0 \rightarrow ^7F_2$ transition which is an electric field dipole transition and hypersensitive to the ligand field perturbation. The ratio of the intensity of these two transition was termed as 'Asymmetry Ratio (A)', which is a measure of the asymmetry of the Eu^{3+} in the complex with respect to point of inversion symmetry[266, 267]. On complexation , the A value was found to increase in DGA-CNT compared to Eu_{aq} system. The A values were reported to be even high for the complexation with Tetra octyldiglycolamide (TODGA) , tripodaldiglycolamide (TDGA), Calix[4]arenes functionalized by diglycolamide (CDGA) in ionic liquid (IL)[268-270]. The presence of inner sphere water molecules in the Eu complex was evaluated from the life time value[266, 271-274]. In case of Eu_{aq} system the life time value revealed the presence of 9 water molecules in the primary co-ordination sphere while in DGA-CNT complex absence of inner sphere water molecule was observed. Similar observations were also reported in case of the Eu^{3+} complex with different DGA based ligands. the mono exponential nature of the decay profile also confirmed the presence of single species on complexation with DGA-CNT.

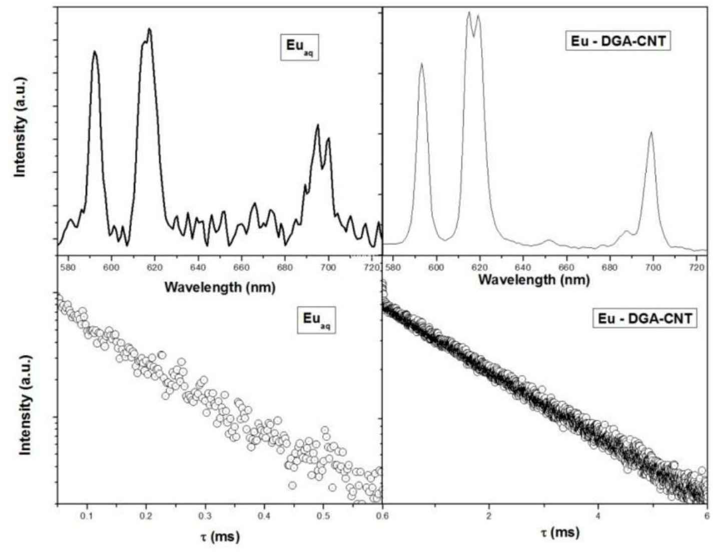

Figure 3.17 Photo-luminescence emission spectra and decay profiles for Eu_{aq} and Eu complex of DGA-CNT

3.3.1.7.2 Calculation of J-O parameters and other photo-physical properties

To get into the more detail on the complexation the J-O parameters (Ω_2 and Ω_4), which are mainly the measure of covalency of the metal-ligand bond were evaluated for Eu-DGA-CNT complex using the emission intensity of different transitions[275-280]. The covalency for Eu_{aq} complex was reported to be the least among the different Eu complex. The Ω_2 value for DGA-CNT complex was found to be more than that of TODGA and complex but less than CDGA complex. This revealed the stronger covalent interaction of Eu^{3+} with the DGA moieties impregnated on CNT. The other J-O parameter (Ω_4), measure of long range order followed the trend: Eu$_{aq}$<Eu-DGA-CNT <Eu-CGDA <Eu-TODGA <Eu-TDGA. The magnetic dipole transition probability (A$_{md}$) for Eu$_{aq}$and all other Eu-complex was found to be nearly same revealing its insensitivity towards ligand field perturbation. The electric dipole transition probabilities (A$_{2ed}$, A$_{4ed}$) of Eu-DGA-CNT complex for both the transitions $^5D_0 \rightarrow {}^7F_2$ and$^5D_0 \rightarrow {}^7F_4$) were found to be much higher compared to that of Eu$_{aq}$ system and they were of similar order with reported values for different DGA based complexes. The quantum efficiency (η) for DGA-CNT complex was found to be much higher compared to that of Eu$_{aq}$ system. The presence of 9 inner sphere water molecules in Eu$_{aq}$ system led to the additional non-radiative path ways for relaxation of the excited complex.

Table 3.27 Comparison of J-O parameters and photo-physical properties of DGA based different Eu complex

Parameters	Eu- DGA-CNT	Eu$_{aq}$	Eu-TODGA	Eu-TDGA	Eu-CDGA
Ω_2	4.33E-20	1.62 E-20	4.13E-20	3.97E-20	4.48E-20
Ω_4	4.96E-20	3.87 E-20	5.23E-20	5.35E-20	5.07E-20
η	0.38	0.05	0.44	0.49	0.34
A	1.88	0.416	1.98	2.34	2.73
τ (ms)	1.92	0.115	2.17	2.25	1.52
N_{H2O}	0	9	0	0	0
β_1	0.20	0.19	0.19	0.20	0.19
β_2	0.49	0.42	0.48	0.47	0.52
β_4	0.29	0.20	0.30	0.31	0.28
A_{md}	42.09	42.5	42.59	42.78	42.59
A_{2ed}	104.55	71.8	107.14	102.43	117.17
A_{4ed}	65.66	69.5	67.01	68.44	64.37
Reference	Present work				

Consequently, the radiative emission decreases and hence led to lowering in the η value. The η value for DGA-CNT was found to be comperable to that reported in the literature. The branching ratio (β) values for different transitions were found to follow the similar trend of $\beta_2 > \beta_1 > \beta_4$ as observed for similar Eu complexes[266, 271-274, 281]. **Table 3.27** summarizes the J-O parameters and different photo-physical constants for DGA-CNT complex and other Eu complex reported in the literature.

3.3.2 Computational Study

3.3.2.1 **Computational Protocol**

Theoretical investigation on the electronic structures, geometry, energy and thermochemistry related to the sorption of Am^{3+}, Pu^{4+} and PuO_2^{2+} by DGA-CNT was carried out by using DFT as described in Sec. 3.1.1.1 [181, 230]. For the ease of computation time, CNT considered here is a (8, 0) zigzag single-walled CNT which consists of four unit cells with tubular length of 5.78 Å width of 6.40 Å. Diglcolamic acid [124] unit was attached to the open end of the CNT owing to the higher reactivity of the open end dangling carbon atoms[282].Coordination complex structures of DGA-CNT with Am^{3+}, Pu^{4+} and PuO_2^{2+}metal ions in presence of nitrate anions and no water molecules (as luminescence study would show later) were considered. DFT calculations were performed with the B3LYP functional, a hybrid Hartree–Fock/DFT method that includesBecke's three-parameter functional (B3) with the Lee, Yang and Parr (LYP) correlation functional[231, 232] in conjunction with def-SVP[229] basis set (for geometry optimization) and triple-zeta def-TZVP[181] basis sets (vibrational frequency and single point energy calculation). To take scalar relativistic effect in consideration, Dirac–Fock effective core potentials (ECPs)[283] was used for plutonium. This potential replaces 60 inner core electrons with the pseudo potentials, and whereas the remaining 34 (for Pu) electrons are described the respective basis sets. The polarized all electron basis sets were used for the light atoms C, H, O, and N. The gas phase energy of the DGA-CNT and its complexes with Am^{3+}, Pu^{4+} and PuO_2^{2+} metal ions in presence of nitrate anions was first calculated. The cavity radii of C, O, N, H, Am and Pu in the aqueous solvent continuum were taken as 2.000, 1.720, 1.830, 1.300, 1.990, and 2.223Å, respectively.

3.3.2.2 **Structural Parameters**

The optimized geometrical structures of the DGA-CNT and its complexes with Am^{3+}, Pu^{4+} and PuO_2^{2+} in presence of nitrate ions are shown in **Figure 3.18**.

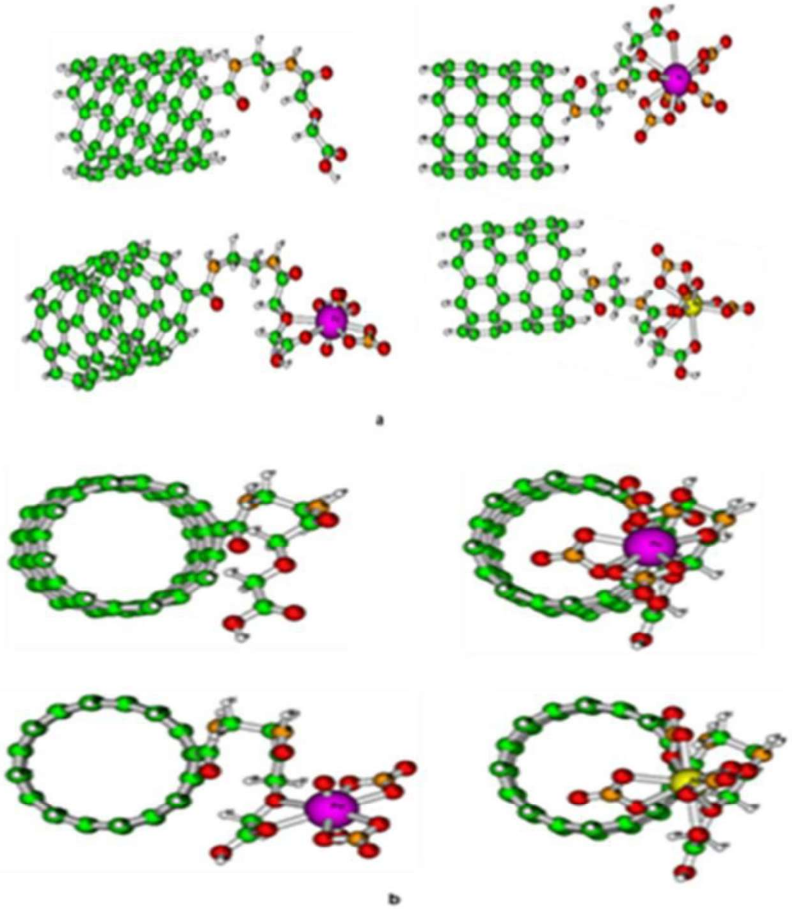

Figure 3.18 Optimized structures of DGA-CNT, and its complexes of Pu^{4+} $PuO_2^{2+}$and Am^{3+}in presence of NO_3^- (a) side view, and (b) front view

The metal to donor atom bond distances in the optimized complex structures is shown in **Table 3.28**, whereas **Table 3.29** depicts the distances of bonds mostly altering their strength due to complexation.

Table 3.28 Metal to donor oxygen bond distances in the optimized complex geometries (in Ǻ).

Molecular System	M-$O_{carbonyl}$	M-$O_{etheric}$	M-$O_{nitrate}$
$Pu(NO_3)_4$(DGA-CNT)	2.47, 2.81	2.73	2.42
$PuO_2(NO_3)_2$(DGA-CNT)	2.57, 3.52	2.77	2.43
$Am(NO_3)_3$(DGA-CNT)	2.55, 2.66	2.63	2.47

Table 3.29 Characteristic C-O and Pu-O bond distances in the optimized geometries

Molecular System	C=$O_{carbonyl}$	C-O_{ether}	Pu-O
DGA-CNT	1.20	1.39	
$Pu(NO_3)_4$(DGA-CNT)	1.22	1.40	
$PuO_2(NO_3)_2$(DGA-CNT)	1.21	1.41	1.72
$Am(NO_3)_3$(DGA-CNT)	1.22	1.40	
PuO_2^{2+}			1.67

The diglycolamic acid moiety is located rear from the CNT tube projecting the two carboxyl and one ether oxygen in the same direction. The little difference in lengths between two C=Ocarbonyl and C-Oetherbond (Table 3.28) is arisen from the dissimilar bonding environment of these groups. Both the Pu^{4+} and Am^{3+} are coordinated to the three oxygen donors of the DGA-CNT, whereas Pu is bonded to two oxygen donors (one from carbonyl and another from ether oxygen) in PuO_2^{2+} complex.

In Pu^{4+}-DGA-CNT complex, four nitrates are coordinated in bidentate mode and DGA group is bonded in tridentate mode with the Pu meal ion, giving rise to 11-coordinated complex. Pu is octa coordinated in PuO_2^{2+}-DGA –CNT complex, four from two nitrate ions, two from DGA group and two from oxo group. Am is nona coordinated in Am^{3+}-DGA-CNT complex where six coordination is derived from three bidentate nitrate and rest three from DGA unit. The two Pu-$O_{carbonyl}$ bond distances in Pu^{4+}-DGA-CNT complex (2.479 and 2.817 Å) are shorter than that in PuO_2^{2+}-DGA-CNT (2.576 and 3.523 Å) complex, whereas Am-$O_{carbonyl}$ bond length is in between, i.e., 2.553 and 2.668 Å (Table 6). On the other hand, M-O_{ether} bond is strongest in Am^{3+} (2.636 Å) complex and weakest in PuO_2^{2+} (2.778 Å) complex. M-$O_{nitrate}$ bond distances are shortest in Pu^{4+} complex and longest in Am^{3+} complex. The extent of deviation of C=O and C-O_{ether} bond distances in the complex structures from the free sorbent DGA-CNT structure would measure the degree of involvement of the carbonyl and other oxygen donors in the metal coordination process. As it can be seen from the **Table 3.29**, deviation of C=O is maximum in Pu^{4+} complex and minimum in PuO_2^{2+} complex, whereas deviation of C-Oether is maximum in PuO_2^{2+} and minimum in Pu^{4+} complex. The elongation of Pu-O bond in PuO_2^{2+} complex compared to PuO_2^{2+} signifies the strong complexation of nitrate and DGA–CNT with the plutonium metal centre.

3.3.2.3 **Binding energy/free energy of complexation in presence of nitrate ions**

The strength of the complexation has also been calculated from the interaction binding energy and free energy of the sorption reaction of individual metal ions as expressed in equation 2 to 4, and shown in **Table 3.30**. The binding energy of sorption with DGA-CNT of Pu^{4+} is higher than that of PuO_2^{2+} both in gaseous and aqueous phase, whereas for Am^{3+} it is higher than PuO_2^{2+} but less than Pu^{4+}.

Table 3.30 Interaction energy (kcal/mol) parameters for the sorption by DGA-CNT

Complexation of DGA-CNT	**Gas phase**			**Aqueous phase**	
	ΔE	**ΔS***	**ΔG**	**ΔE**	**ΔG**
Pu^{4+}	-3757.9	-0.197	-3690.8	-257.5	-190.3
PuO_2^{2+}	-1525.3	-0.101	-1489.9	-90.8	-55.4
Am^{3+}	-2534.0	-0.137	-2487.1	-111.3	-64.4

*Unit of ΔS is kcal/mol.K

The decrease in energy values in aqueous phase in compared to gas phase is due to the screening of the solvent dielectric continuum in the interaction. The change in entropy is most negative in case of Pu^{4+} complexation and least for PuO_2^{2+}, which is a consequence of the association of the nitrate anions in the complex formation reaction. The free energy of sorption is also highest for Pu^{4+} uptake and lowest for PuO_2^{2+} both in gaseous and aqueous phase. This observation inferred that DGA-CNT sorbs Pu^{4+} and Am^{3+} strongly than PuO_2^{2+}.

3.3.2.4 **Quantum chemical molecular descriptors**

The binding capability of DGA-CNT for the three metal ions has also been analyzed by quantum chemical molecular descriptors and calculated values are depicted in **Table 3.31**. DGA-CNT is a hard base having lower value of χ and η, whereas the Pu^{4+} is the hardest acid among the three hard base metal ions having higher values of χ and η.

Thus, according to the Pearson's SHAB principles[38] Pu^{4+} coordination should be the strongest and PuO_2^{2+} be the weakest among the three metal ion complexation systems. This is also reflected from the amount of charge transfer (ΔN) values of the metal ion and DGA-CNT pairs; it is higher in Pu^{4+} (7.380) and Am^{3+} (7.660) compared in PuO_2^{2+}

(3.358). Thus chemical descriptor values are in good congruence with the bond distances and energetic analysis for the complexation of Am^{3+}, Pu^{4+} and PuO_2^{2+} with DGA-CNT.

Table 3.31 Calculated various molecular descriptors (in eV)

	E_{HOMO}	E_{LUMO}	Gap ($E_{HOMO-LUMO}$)	χ	η	$\Delta N(Th^{4+})$
Pu^{4+}	-46.39	-41.39	4.96	43.89	2.50	7.38
PuO_2^{2+}	-23.93	-19.11	4.81	21.52	2.40	3.35
Am^{3+}	-32.19	-28.63	3.56	30.41	1.78	6.66
DGA-CNT	-4.16	-3.75	0.41	3.95	0.20	

3.4 Conclusion

The structures, interaction, bonding and thermodynamic parameters for the complexation of Th^{4+} ion with pristine CNT, oxidizedCNT or CNT-COOH and CNT-DGA using DFT levels of theory are reported here. The free energy of adsorption for Th^{4+} ion bythe three CNT based ligands was computed using the hybrid B3LYP density functional and TZVP basis set in conjunction with COSMO solvation approach. Gas phase results though provide qualitative idea about the complexation reaction it is not realistic as it does not represent the real system which takes place in solution phase. Results of aqueous phase calculation are comparable with the experimentally obtained trend of adsorption capacity of Th^{4+} with p-CNT, CNT-COOH and CNT-DGA. The p-CNT has positive free energy of adsorption implying zero interaction with Th^{4+} in aqueous phase. DGA being tridentate ligand compared to bidentate –COOH, CNT-DGA was expected to be shown higher interaction/complexation with Th^{4+} metal ion. But, CNT-COOH has higher free energy of adsorption than that of CNT-DGA; same is reflected from their experimental Th^{4+} adsorption capacity values. Carboxylated C_{60}

fullerene has quite high value of binding energy with Th^{4+} indicating enhancement of adsorption by CNT-COOH in presence of C60-COOH. The present study was a modest attempt to model the complex chemical problem like the complexation reaction of Th^{4+} ionpristine as well as COOH and DGA functionalized CNT and can be used further for future design of functionalized CNT for the removal of Th^{4+} and other radionuclides ion from nuclear waste.

The structures, interaction, bonding and thermodynamic parameters for the complexation of Eu^{3+} and Am^{3+} ion with functionalized CNT-DGA using DFT levels of theory are reported here. The hybrid B3LYP density functional and TZVP basis set in conjunction with COSMO solvation approach can be used successfully to predict the free energy of transfer for Eu and Am ion with functionalized CNT-DGA. Further, gas phase results though provide qualitative idea about the complexation reaction it is not realistic as it does not represents the real system which takes place in solution phase. The simple complexation reaction in solution phase where all the energy calculations are done using implicit solvation fails to predict the correct selectivity order in the presence of nitrate ion. From the estimated distribution constant, it is indisputably established that the Eu^{3+} ion is preferentially extracted over Am^{3+} ion and hence confirm the acceptance of the explicit cluster model for ion solvation free energy and thermodynamic cycle for the evaluation of free energy of extraction in solution phase. Finally, this is the first study where the functionalized CNT-DGA was tested both theoretically and experimentally for the extraction of Eu^{3+} and Am ions. The present study was a modest attempt to model the complex chemical problem like the complexation reaction of Eu^{3+} and Am^{3+} with functionalized CNT-DGA and can be used further for future design of functionalized CNT for the separation of minor actinides from the lanthanides. Work in this direction is in progress in our computational and experimental laboratory.

DGA-CNT was demonstrated as highly efficient sorbent for Am^{3+}, Pu^{4+} and PuO_2^{2+} with the trend in the K_d values: $Am^{3+} > Pu^{4+} > PuO_2^{2+}$. Based on the linear regression coefficients, the Langmuir isotherm was found to be predominating with the sorption capacity 98.71 mg g^{-1}, 94.06 mg g^{-1} and 97.61 mg g^{-1}, for Am^{3+}, Pu^{4+} and PuO_2^{2+}, respectively. The sorption energy calculated from the D-R isotherm revealed that there was chemical interaction between DGA-CNT and the actinide ions i.e. chemi-sorption. The sorption was found to proceed via pseudo 2nd order kinetics with the rate constants 2.10E-05, 1.40E-04 and 3.60E-04 mg g^{-1} min^{-1} for Am^{3+}, Pu^{4+} and PuO_2^{2+}, respectively. Suitable stripping agents were also identified for the back extraction of the actinides of different oxidation states from DGA-CNT. The sorbent was also found to have good radiolytic stability. The photoluminescence investigation revealed that the Eu^{3+} in complex with DGA-CNT exists as single species. On complexation, the water molecules in the primary coordination sphere were replaced by the donating atoms from ligating moieties and subsequently the overall assymmetry of the Eu^{3+} enhanced. The complexation also led to the increase in covalency between Eu^{3+} and O bond from ligand functionality. The magnetic dipole transition probability was found to be insensitive towards ligand field perturbation while electric dipole transition of ${}^5D_0 \rightarrow {}^7F_2$ was hypersensitive. Density functional theory reveals the tridentate coordination mode of the DGA moiety towards Pu^{4+} and $Am^{3+}$and bidentate coordination mode towards PuO_2^{2+}.

The binding energy of sorption with DGA-CNT of Pu^{4+} is higher than that of PuO_2^{2+} both in gaseous and aqueous phase, whereas for Am^{3+} it is higher than PuO_2^{2+} but less than Pu^{4+}. The free energy of sorption is also highest for Pu^{4+} uptake and lowest for PuO_2^{2+} both in gaseous and aqueous phase. The theoretical observation inferred that DGA-CNT binds Pu^{4+} and Am^{3+} strongly than PuO_2^{2+} and the same is corroborated from the sorption experiment.

4 Chapter 4: Amidoamine and Ploy(amidoamine) functionalized Carbon Nanotubes

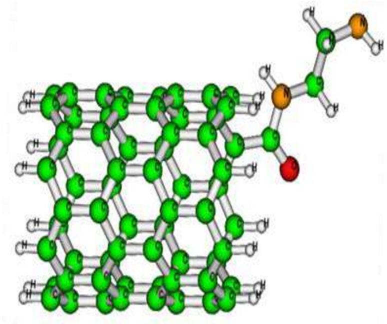

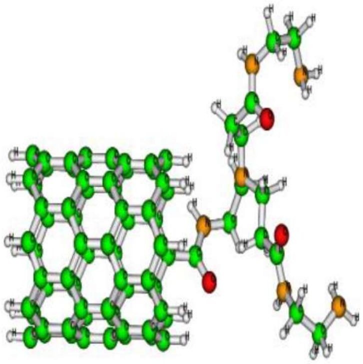

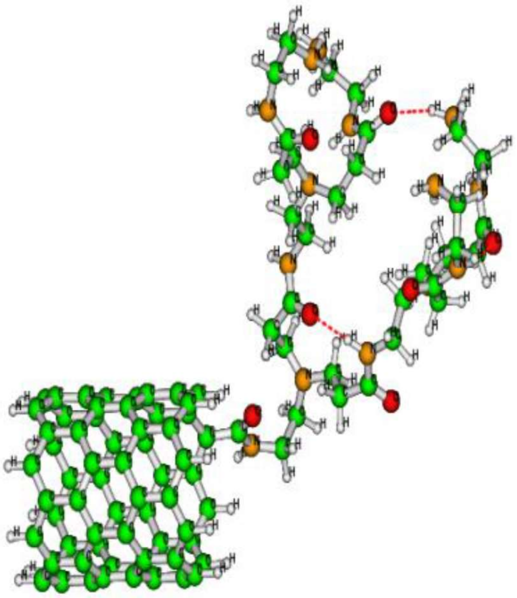

4.1 Sorption of U(VI), Am(III) &Eu(III) by CNT-AA[170]

Functionalization or modification of carbon nanotubes has attracted increasing attention over the past years. Carboxylate groups have been introduced onto the surface of carbon nanotubes by reaction with strong oxidizing agents such as HNO_3 [284].Recently researchers have been interested to investigate the possible role of CNT in radioactive waste management. Initially multi-walled carbon nanotubes (MWCNTs) were found to have very large sorption capacity for heavy metals like Cd^{2+} and Pb^{2+} under aerobic conditions[285, 286]. Specific literature on CNTs for the application in nuclear waste management is still sparse but interesting studies have been carried out. Oxidized MWCNTs were found to have extraordinarily high adsorption capacity for Am(III) and the mechanism of sorption was surface complexation[287]. It was also reported that uranyl acetates are efficiently sorbed by single-walled carbon nanotubes (SWCNTs) due to filling of the inside cavities[288]. Uranium sorption in surface oxidized CNT was found to increase over un-functionalized SW CNT at lower pH [289][17].MWCNT was found to show extraordinarily high Am(III) sorption capacity ($\geq$ 40 mg/g) from aqueous medium which was reported to be due to strong surface complexation. Sorption and desorption of lanthanide ion Eu(III) on MWCNT showed very high adsorption and retention capacity which was explained by surface complexation and/or chemisorptions mechanism[290]. Th(IV) [224] and Sr(II)[291, 292] sorption have also been reported using MWCNT where also the mechanism was found to be surface complexation. These exciting uses are reported to be possible due to unique nature of interaction between 5f electrons of actinides and p electrons of carbon materials[168, 293].

The aim of the present chapter is to functionalize MWCNT with novel functional group-amido-amine, characterize the functionalized MWCNT, study its sorption behavior for Am(III) and U(VI). Various parameters were investigated to determine the mechanism of extraction and adsorption capacity of the functionalized MWCNT. Density functional theory was also been applied for understanding the mechanism of actinide extraction in MWCNT as well as energy of binding.

4.1.1 Experimental Study

4.1.1.1 Kinetic sorption studies

Kinetics of the sorption process using MWCNT-AA was studied for both ^{241}Am and ^{233}U. The kinetic data are given in **Figure 4.1** (A & B).

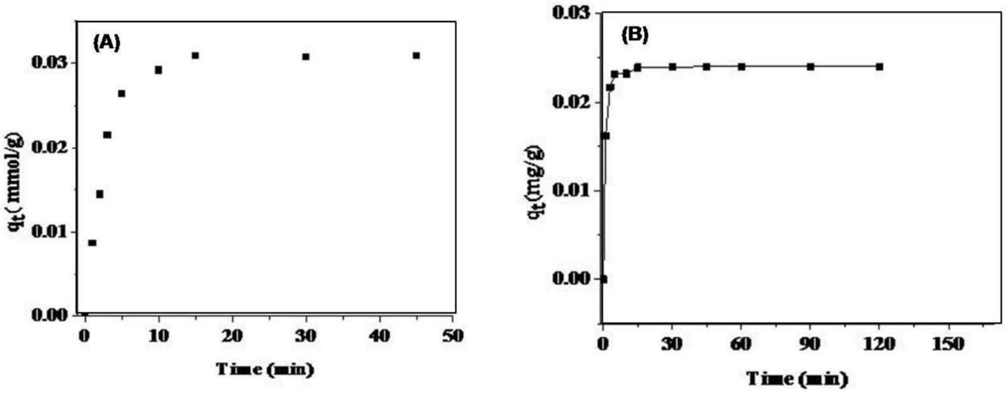

Figure 4.1 Effect of sorption time on the equilibrium sorption capacity of MWCNT-AA for (A) ^{233}U and (B) ^{241}Am

For both the radionuclides, the equilibrium was found to be achieved within 15 minutes of contact time and hence in further experiments the contact time was kept at 1h to attain complete equilibrium. Literature reports are widely varied as far as time of equilibration for different types of MWCNT is concerned. Wang et al[287] reported that 5-7 min is enough to attain equilibrium for multiwalled CNTs whereas Sr absorption by functionalized carbon nanotubes required ~15 min of equilibration time. But Chen et al[294] reported that for Eu absorption on MWCNT/ iron oxide nano composite requires 2 days to attain the equilibrium and similarly sorption of U(VI) by MWCNT/iron oxide composite was reported to be requiring ~8 h for attainment of equilibrium (Zong et al [295]). Generally it is described that at the initial stages there are vacant surface sites available for sorption hence the sorption increases quickly at the initial stage. But at the later stages the remaining vacant surface sites are difficult to occupy due to the repulsion from the sorbate molecules.

When the kinetic data were tried to be modeled with the different kinetics models, it was observed that both 233U and 241Am sorption kinetics could be modeled by pseudo-second- order rate equation described by [194]. The linear curves of t/qt vs. time were acquired according to equation mentioned in Table 2.4 and are shown in **Figure 4.2** (A & B).

The corresponding coefficient (R^2) of 0.999 and 0.997 for U and Am respectively corroborate to the fact that sorption process follows the pseudo-second-order kinetics model. The corresponding coefficients for pseudo-first-order kinetic equation were found to be 0.966 and 0.958 for U and Am respectively. The plots are given in **Figure 4.3**.The values corresponding to pseudo-first-order and pseudo-second-order eqn. are given in **Table 4.1**.

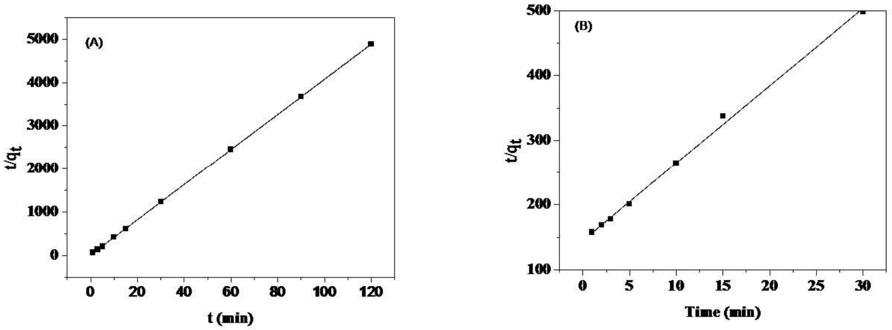

Figure 4.2 Pseudo-second-order kinetics model for the sorption of (A) U and (B) Am by MWCNT-AA

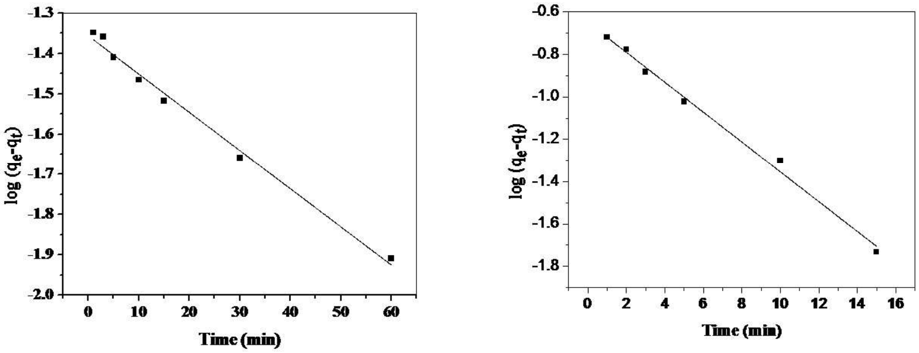

Figure 4.3 Pseudo-first-order plot for the sorption of ^{241}Am by MWCNT-AA and Pseudo-first-order plot for the sorption of ^{233}U by MWCNT-AA

The corresponding coefficient (R^2) of 0.999 and 0.997 for U and Am respectively corroborate to the fact that sorption process follows the pseudo-second-order kinetics model. The corresponding coefficients for pseudo-first-order kinetic equation were found to be 0.966 and 0.958 for U and Am respectively. The plots are given in **Figure 4.3**.The values corresponding to pseudo-first-order and pseudo-second-order eqn. are given in **Table 4.1**.

Table 4.1 Parameters for pseudo-second-order and pseudo-first-order kinetics modeling for the sorption of ^{241}Am and ^{233}U by MWCNT-AA

Radionuclide	**Pseudo-second-order**			**Pseudo-first -order**
	R^2	**q_e (mg/g)**	**k_2(g/(mg · min))**	**R^2**
^{233}U	0.999	19.84	0.012	0.966
^{241}Am	0.997	15.92	0.055	0.958

4.1.1.2 **Effect of pH**

The sorption of metal ions by CNT is strongly dependent on the pH of the aqueous solution[287, 296] . The results on the sorption efficiency of Am(III) and U(VI) with varying pH of the solution are shown in **Figure 4.4 (A & B)**. pH was found to have profound effect on the sorption efficiency for both U(VI) and Am(III). For U(VI) the percentage sorption increases with increasing pH of the solution in the range of 1.0-7.0. But at pH > 7.0, the percentage sorption of U(VI) decreases with increasing pH value. This can be explained on the basis of electrostatic attraction between U(VI) and the surface charges of functionalized MWCNT which are affected by pH of the solution. Further, the protonation-deprotonation of the functional groups could enhance or suppress U(VI) sorption. From the potentiometric acid-base titration, the surface of functionalized MWCNT was found to be positively charged at pH < 4.8 . The dominant species of U(VI) is UO_2^{2+} at pH < 5 [297] and so the electrostatic repulsion between positively charged functionalized MWCNT and UO_2^{2+} leads to low sorption of U(VI) onto MWCNT. With further increase in pH of the medium, the functional groups on the surface of MWCNT becomes negatively charged and so the interaction between MWCNT and the dominant species of U(VI) [$(UO_2)_3(OH)_5^+$/$UO_2(OH)^+$] in the pH range of 5.0-7.0 leads to increase in sorption efficiency.

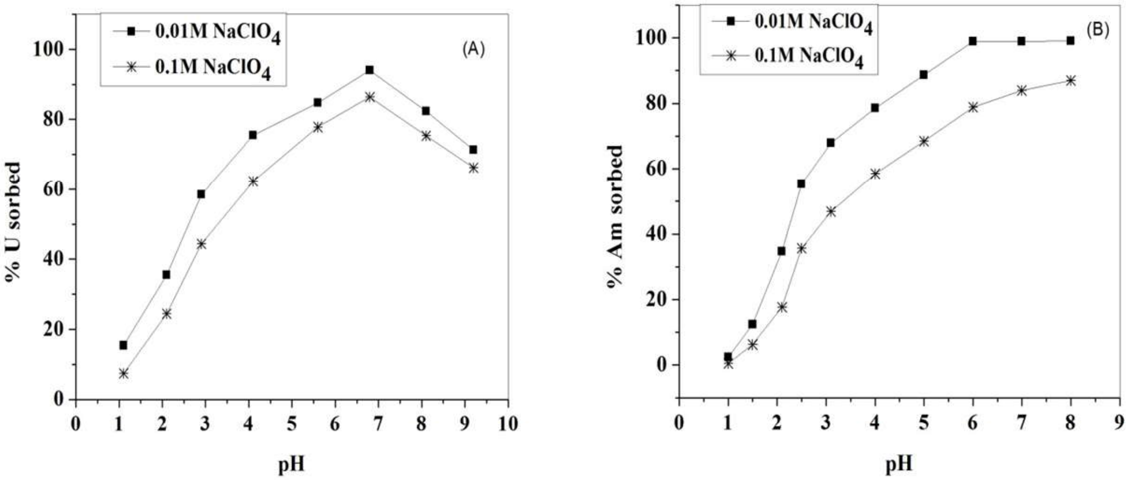

Figure 4.4 Effect of pH of aqueous solution on the sorption of (A) ^{233}U and (B) ^{241}Am by MWCNT-AA

Above pH 7, the dominating species of U(VI) is $UO_2(OH)_3^-$ and the repulsion between the negatively charged species and negative surface charge of functionalized MWCNT leads to decrease in sorption efficiency for U(VI) above pH 7. The sorption efficiency of Am(III) follows an increasing trend from pH 1 to 6 and high values of sorption are maintained above pH 6. The species formed by Am(III) at different pH medium includes Am^{3+} (major species up to pH 6), $Am(OH)^{2+}$ (mostly formed from pH 6 to 8), $Am(OH)_2^+$ (predominant species above pH 8 up to pH 12) with little contribution from $Am(OH)_3$ above pH 11 [243]. So for pH range studied, Am(III) is present as positively charged species and the interaction with negative surface charge of functionalized MWCNT leads to increase in sorption efficiency. A striking feature of both the graphs is the change in %

sorption of both U(VI) and Am(III) with change in ionic strength. With increasing ionic strength, % sorption was found to decrease for both the actinides studied. As the mechanism of sorption for both the actinides involves interaction between two charged species as discussed above, increase in ionic strength of the medium will lead to more stabilization of the charged species. This creates a barrier for the ionic interactions between two charged species and hence the % sorption decreases at higher ionic strength.

4.1.1.3 **Sorption Isotherm**

To understand the sorption mechanism and calculate the maximum sorption capacity of the functionalized MWCNT, isotherm studies were carried out using Eu and U. Due to low pH value of radioactive waste water, isotherm studies were carried out at pH 6. The isotherm for U(VI) and Eu(III) are shown in **Figure4.5**. As evident from the Figures, initially the amount of metal sorption increased quickly with increasing metal concentration in the solution and then arrives at a plateau. The maximum sorption capacity of Eu(III) and U(VI) was found to be 16.13 and 20.65 mg/g respectively. The experimental data were fitted with Langmuir and Freundlich isotherm models. The plots for Langmuir and Freundlich isotherms are shown **Figure 4.6**. The various parameters obtained from different isotherms are shown in **Table 4.2**. Langmuir isotherm model fits the experimental data more than Freundlich model as is evident from **Table 4.2**. Maximum sorption capacities of functionalized MWCNT for Eu(III) and U(VI) was observed to be 16.1 and 20.66 mg/g respectively which are in excellent agreement with that of experimentally determined maximum sorption capacity. Thus the sorption of Eu(III) and U(VI) on the functionalized MWCNT proceeds via a chemical reaction and it

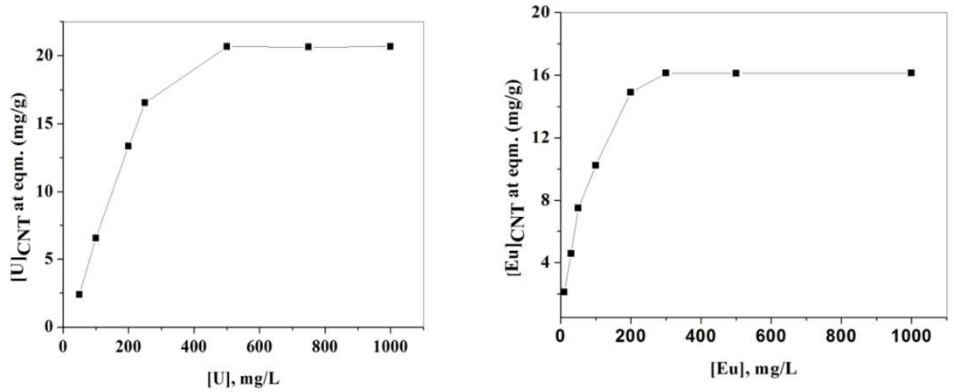

Figure 4.5 Effect of initial concentration of ^{233}U and $^{152+154}$Eu on q_e for sorption by MWCNT-AA

is limited by the availability of the ligand complexing sites due to saturation effect according to Langmuir model and it is also proved that there is no multilayer sorption of Eu(III) or U(VI).

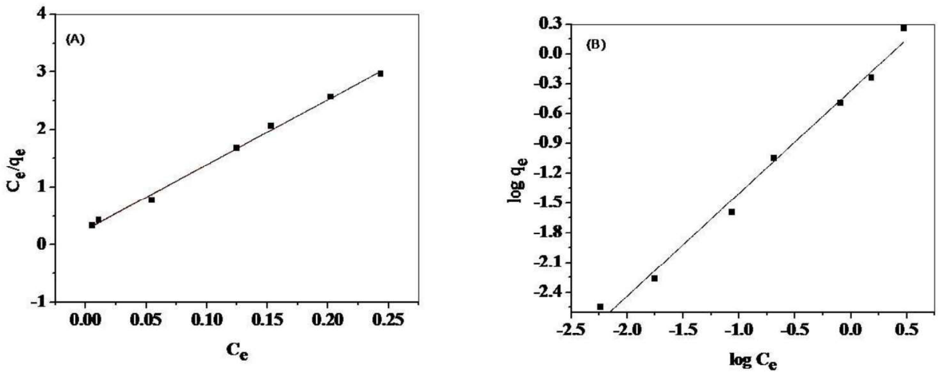

Figure 4.6 Isotherm plots for the sorption of $^{152+154}$Eu by MWCNT-AA: (A) Langmuir plot (B) Freundlich plot

Table 4.2 Different isotherm constants and corresponding R^2 values for the sorption of Eu(III) and U(VI) by MWCNT-AA

	Langmuir			**Freundlich**		
Radionuclide	**q_{max}(mg/g)**	**b (L/mmol)**	**R^2**	**K_f (mmol^{1-n}L^n g^{-1})**	**n**	**R^2**
Eu(III)	16.1	42.89	0.995	0.37	0.97	0.981
U(VI)	20.66	8.86	0.996	0.49	0.752	0.989

4.1.1.4 Comparison between non-functionalized and functionalized CNT

In order to prove the efficiency of our functionalization procedure, we tried to compare the sorption behavior of $^{152+154}$Eu for untreated MWCNT, carboxylic acid functionalized MWCNT and amido-amine functionalized MWCNT. Physical separation of untreated MWCNT during sorption experiment was a problem and it required lengthy separation time with high speed centrifugation (60 min at a rpm of 18000) and the maximum sorption capacity of 152+154Eu was found to be ~10 mg/g. Carboxylic acid functionalized MWCNT was also found to be difficult to separate out after sorption experiment and the kinetics of equilibration was found to be very slow. It was already reported that only 85% Am(III) was sorbed by carboxylic acid functionalized MWCNT after 4 days[287] and our results also confirmed the observation. Desorption of sorbedAm(III) from loaded carboxylic acid functionalized MWCNT was also reported to be very slow. The maximum sorption capacity of Eu(III) by carboxylic acid functionalized MWCNT was found to be 25.14 mg/g which was somewhat lower than that reported for Am(III) [287]. Thus amido-amine functionalized MWCNT offered higher sorption capacity compared to untreated MWCNT, faster kinetics of sorption and desorption over carboxylic acid functionalized MWCNT along with significantly high sorption capacity for both ^{233}U and $^{152+154}$Eu.

4.1.1.5 Reusability study

Desorption of Am(III) and U(VI) was studied using 1M HNO3 solution and it was observed that quantitative desorption of the radionuclides is possible from the amido amine functionalized MWCNT in two contacts. Reusability studies for the functionalized MWCNT showed that there is no change in the sorption efficiency for successive six cycles of operation. The MWCNT-AA was also found to highly radiation stable with respect to gamma radiation[171].

4.1.2 Computational Study

4.1.2.1 Computational Protocol

The molecular structures and interaction energies were computed using density functional theory (DFT) as implemented in Turbomole suite of program[181, 230].The CNT considered here is a (8, 0) zigzag single-walled CNT consists of four unit cells with tubular length of 5.78 Å width of 6.40 Å. For sake of calculation, a single amido-amine group was attached to the more reactive dangling edge carbon atom of CNT structure. The geometric structures of amido-amine-CNT and its complexes with UO_2^{2+} and Am^{3+} were optimized at the B3LYP[231, 232] density functional employing SVP[229] basis set. Relativistic effective core potentials (RECP) with 60 electrons in the core of U has been used in the basis set, while for the light atoms C, H, O, and N all electrons have been included in the basis set. The vibrational IR frequencies of the molecular structures were also evaluated at the same level of theory. Further, single point energy calculation was performed on all the optimized molecular structures using hybrid B3LYP[231, 232] functional and TZVP [181] basis set.

4.1.2.2 Structural Parameters

1:1 complex between the actinide ion and CNT-AA in presence of nitrate ions are considered following the complexation reaction mentioned in equation 4.1.

$$M^{n+}+nNO_3^-+CNT-AA\rightarrow M(NO\ \ CNT-AA \qquad (4.1)$$

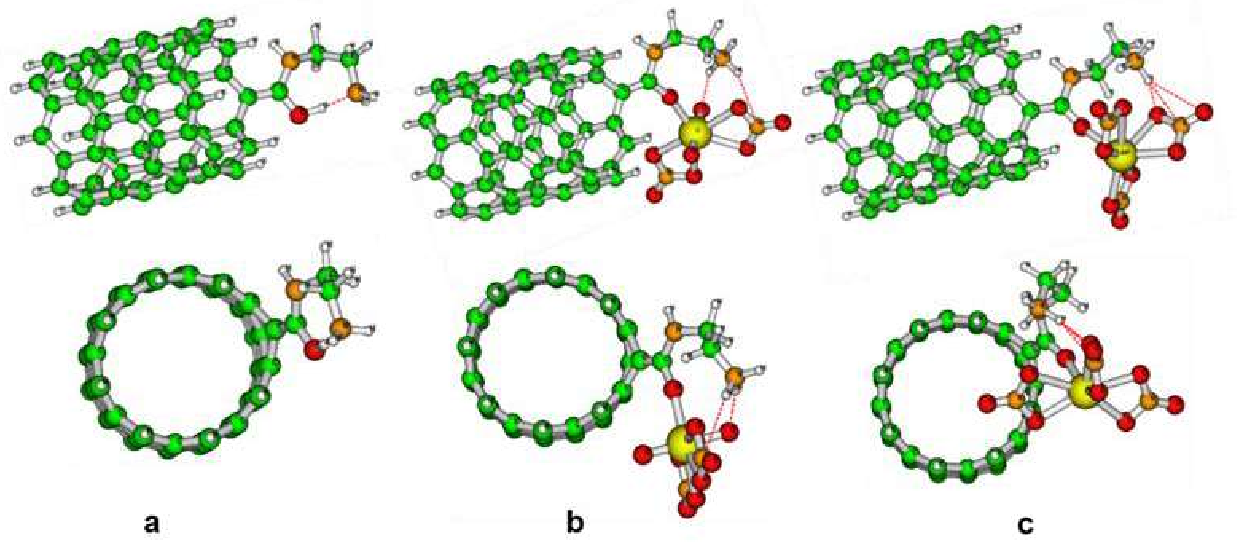

Figure 4.7 Optimized structures of the (a) CNT-AA, (b) $UO_2(NO_3)_2$CNT-AA complex, and (c) $Am(NO_3)_3$CNT-AA complex

The optimized structures of the CNT-AA are shown in **Figure 4.7(a).** The amido-amine unit attached with a carbon atom at the open edge of the CNT is projected outward. The optimized complex structures of the U(VI) and Am(III) with CNT-AA in presence of NO_3^- ions are shown in **Figure 4.7(b)** and **4.7(c)**, respectively. Only NO_3^- ions are considered in the first coordination shell of the actinide ions owing to the stronger coordination ability of NO_3^- than H_2O molecules. The carbonyl oxygen of amide part and the nitrogen of the amine part of the amidoamine unit in CNT-AA are coordinated with the metal ion. As shown in the **Figure 4.7(a)**, for uranium complex, two NO_3^- coordinate to the central U in bidentate mode, amidoamine unit of CNT coordinates in bidentate mode, give rise to 8- coordinated complex including the two coordination from two oxo groups. For, Am(III) complex, bidentate coordination from three $NO_3^-$and same for the amidoamine also result in 8-coordination environment. The bond distances between the metal coordination center and the donor atom (O and N) for the optimized structures are summarized in **Table 4.3**. For both of the complexes, smaller M-O(C=O) bond length than that of M-O(NO_3) indicates that amide carbonyl has stronger coordination ability than the nitrates.

Again, for both of the complexes, Smaller metal to carbonyl oxygen distance than that of metal to nitrogen suggests that carbonyl oxygen have stronger coordination ability than the amine nitrogen. The M-O(C=O) bond length is smaller (2.378 Å) for the U(VI) complex compared to the Am complex (2.399 Å). This indicates that CNT-AA has stronger complexation ability for U(VI) compared to Am(III). The coordination nature of amide carbonyl oxygen and amine nitrogen can also be seen from the elongation of C=O (1.267 or 1.260 Å from 1.230 Å) and C-N (1.468 and 1.475 Å from 1.454 Å) bonds after complexation which is the result of coordination with the metal ions by the donor sites.

Table 4.3 Calculated M-O and M-N distances in Åfor the CNT-AA and its complexes with UO_2^{2+} and Am^{3+} in presence of nitrate ions

Bonds	**Molecular System**			
	$UO_2(NO_3)_2$CNT-AA	**$Am(NO_3)_3$CNT-AA**	**$Eu(NO_3)_3$CNT-AA**	**CNT-AA**
M-O(C=O)	2.378	2.399	2.4086	
M-N(NH_2)	2.689	2.615	2.610	
M-O(NO_3)*	2.503	2.474	2.460	
C=O(Amide)	1.267	1.260	1.251	1.230
C-N(Amine)	1.468	1.475	1.471	1.454

*Averages of all the M-O distances between M and NO_3^-.

4.1.2.3 Binding energy/free energy of complexation in presence of nitrate ions

The binding energy and free energy change of the complexation reaction (equation 4.1) for U(VI) and Am (III) are shown in **Table 4.4**. The ΔG values for the two actinide ions are very negative both in gas and aqueous phase, indicating favorable nature of the adsorption of these radionuclides on the CNT-AA as depicted by our experiments. It can also be seen from the table that ΔE or ΔG values are reduce significantly from gas phase to solution phase, suggesting that the solvation/hydration of the metal ions plays a crucial role in the complexation process.

The role of solvation of metal ions can clearly be understood from the table that the gas phase ΔEgas or ΔGgas is higher for Am(III) compared to U(VI), whereas, the solution phase ΔEaq or ΔGaq is higher for U(VI) (-168.3 kcal mol-1 or -105.3 kcal mol-1) compared to Am(III) (-107.9 kcal mol-1 or -56.6 kcal mol-1) which is good agreement with our experimental adsorption studies that CNT-AA have higher capacity for U(VI) (20.66 mg g-1) than Am(III) (16.10 mg g-1). In order to get inside of the coordination nature in the complexation, natural population analysis (NPA) [167] was performed with the complex molecules and the results is shown in **Table 4.5**.

Table 4.4 Calculated ΔE and ΔG in kcal mol-1of complexation reactions in gas and aqueous phase between the metal ions and MWCNT-AA in presence of nitrate ions

Complexation of	ΔE_{gas}	ΔG_{gas}	ΔE_{aq}	ΔG_{aq}
UO_2^{2+}	-591.6	-528.6	-168.3	-105.3
Am^{3+}	-1041.6	-990.3	-107.9	-56.6
Eu^{3+}	-1062.8	-1011.8	-96.8	-45.9

Table 4.5 Natural charges (Q) on the actinide acceptor and donor oxygen (O) and nitrogen (N) by NPA analysis in the complexes obtained

Complexation of	Q(M)	Q(O), Amide C=O	Q(N) Amine NH_2	$Q(O)^{\#}$, NO_3
UO_2^{2+}	1.736	-0.620	-0.759	-0.393
Am^{3+}	1.872	-0.722	-0.841	-0.528

[#] Average values of the natural charges of 4 and 6 O donors from U and Am complexes, respectively.

The less positive charge on U(VI) (1.736) compared to Am(III) (1.872) indicates stronger complexation of the former than the latter. The charge on oxygen and nitrogen coordinating sites of the amidoamine unit of the CNT-AA is lower for U(VI) than that of Am(III), suggesting more charge transfer from these atoms to the metal acceptor center which in turn strengthen the coordination with U(VI). Thus NPA analysis also corroborates the experimental results.

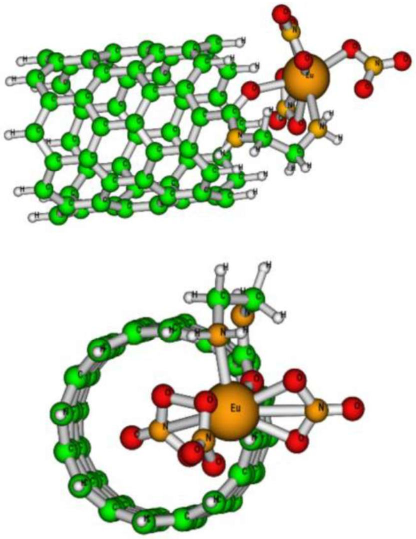

Figure 4.8 Optimized molecular structures of the Eu(NO$_3$)$_3$CNT-AA complex at the B3LYP/SVP level of theory.

Similar DFT calculation for the complexation of Eu(III) with CNT-AA are also performed to compare the results with Am(III) ion. The optimized molecular structures of the Eu(NO3)3CNT-AA complex was shown in **Figure 4.8**. The bond distance between metal to oxygen donor centre of AA is highest for Eu compared to Am and U (**Table 4.3**). This shows that CNT-AA form stronger complex with Am compared to Eu. The same is also attributed from the aqueous phase free energy values of complexation in Table **4.4**.

The experimental extraction has been carried out in slight acidic pH condition where protonation of basic groups would take place due to the presence of protons (H+) in the ambient surrounding; it is imperative to investigate the effect of protonation of the surface groups of CNTs on the complexation of uranyl and americium ions. In view of this, calculation was performed with protonated SWCNT-AA. The bond distances of these three systems are depicted in **Table 4.6**. In the optimized geometric conFigureuration, the proton (H^+) is stabilized in the middle of amine nitrogen and carbonyl oxygen atom of the amidoamine ligand on the SWCNT with interatomic distance of 1.644 and 1.106Å, respectively.

Table 4.6 Bond Distances of protonated SWCNT-AA and its complexes with uranyl and americium in presence nitrate anions

Structure	**Distances in Å of the bond -**						
	C=O	**N-H$_{(proton)}$**	**O-H$_{(proton)}$**	**N-H$_{(amine)}$**	**U-O$_{(C=O)}$**	**U-N$_{(amine)}$**	**U-O$_{(NO3)}$**
SWNT-AA-H^+	1.326	1.644	1.016	1.020 1.022			
SWNT-AA-H^+-$UO_2(NO_3)_2$	1.314	1.043	2.272	1.025 1.048	2.237	3.719	2.423
SWNT-AA-H^+-$Am(NO_3)_3$	1.296	1.036	3.297	1.025 1.064	2.239	4.203	2.420 2.374 2.515 2.490 2.433 2.627

That is the proton is more strongly bonded to the carbonyl oxygen atom. It can be seen that due to the stronger coordination ability of carbonyl oxygen towards positively charged Am(III) and U(VI) ion, the proton has shifted to amine nitrogen center. This is clear from the increase in the O-Hproton distance from 2.272Å (for uranyl) and 3.927Å (for Am(III)), and decrease in N-Hproton distance from 1.644Å to 1.043Å (for uranyl) and 1.036Å (for Am(III)) in the complex structure. Unlike in un-protonated form, the AA unit here is coordinating as mono dentate donor, as the amine nitrogen binding has ceased due to the close vicinity of the proton. This reflects in the enhancement in M-Namine distances in complexes with proton from the un-protonated system [3.719 Å (uranyl) or 4.203Å (Am), **Table 4.6** from 2.689Å (uranyl) or 2.615Å (Am), respectively, **Table 4.3**]. The decrease in the M-OC=O bond distance [2.237Å (uranyl) or 2.239Å (Am), **Table 4.6** from 2.378Å (uranyl) or 2.399Å (Am), respectively, **Table 4.3**] compared to the un-protonated complex reveals the stronger coordination of the carbonyl group. The binding energy and free energy change associated with the complexation in presence of proton has also been computed and presented in **Table 4.7** with comparison against energy values in absence of proton.

Table 4.7 Calculated ΔE and ΔG in kcal mol^{-1} of complexation reactions in gas and aqueous phase between the metal ions and MWCNT-AA with protonation of the RNH2 unit in presence of nitrate ions

Protonation of amidoamine	Complexation of	ΔE_{gas}	ΔG_{gas}	ΔE_{aq}	ΔG_{aq}
No	UO_2^{2+}	-591.6	-528.6	-168.3	-105.3
	Am^{3+}	-1041.6	-990.3	-107.9	-56.6
Yes	UO_2^{2+}	-536.7	-491.2	-115.4	-69.9
	Am^{3+}	-1016.2	-956.1	-93.6	-33.5

It is evident that the strength of complexation has decreased as the binding energy or free energy of complexation are decreased due to the presence of proton which perturb amine to take part in binding with metal ion. The aqueous phase free energy is higher for U(VI) (-69.938 kcal mol^{-1}) compared to Am(III) (-33.500 kcal mol^{-1}) which is good agreement with our experimental adsorption studies that CNT-AA have higher capacity for U(VI) than Am(III) in slightly acidic pH. In order to further gain insights into the nature of bonding, the distribution of the highest occupied (HOMO) and lowest unoccupied (LUMO) molecular orbitals of CNT-AA, and its complexes with U(VI) than Am(III) is depicted using iso-surface value of 0.011 (e bohr^{-3}) in **Figure 4.9**. The frontier molecular orbitals of CNT-AA are redistributed after complexation with both the metal ions, which confirms the coordination between the metal and ligands on CNT. The decrease in HOMO-LUMO energy gap in uranyl complex (0.40eV) and increase in case of americium (1.30eV) from the gap in CNT-AA (0.41eV) may be correlated with the higher free energy of complexation for the former compared to the later. Effect of solvation is

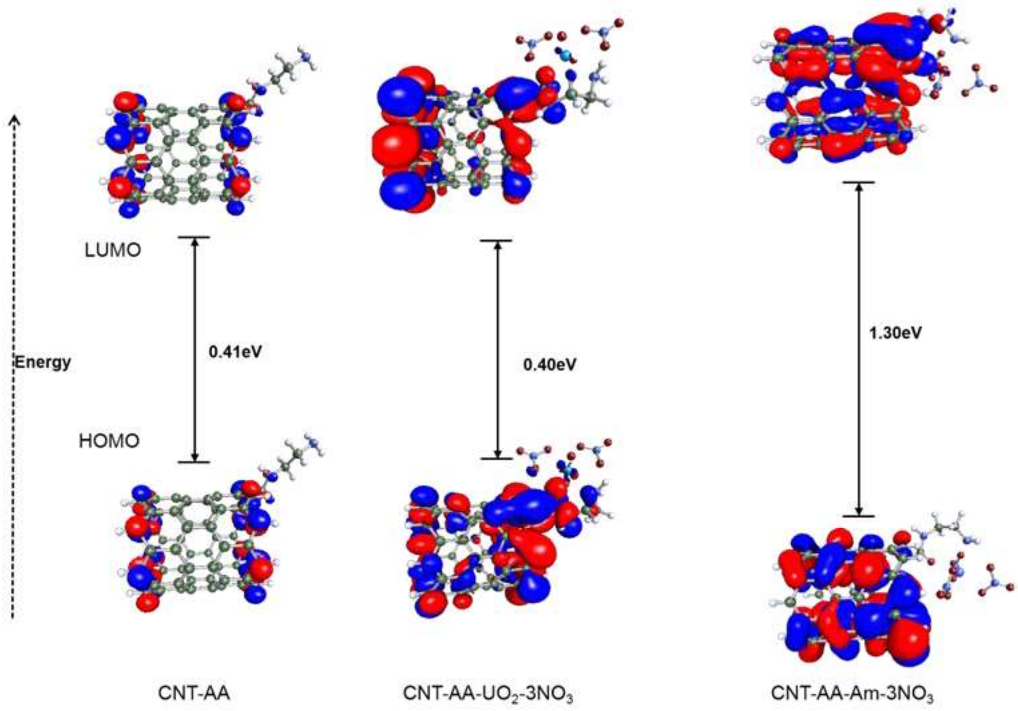

Figure 4.9 The distribution of the HOMO and LUMO orbitals of CNT-AA, and its complexes with UO$_2^{2+}$ and Am^{3+} ions in presence on nitrate anions, at isosurface value of 0.011e.bohr^{-3}

very complicated in determining the sorption energies by DFT theory. Various model for the hydration and then partial or complete dehydration of metal ions during coordination process have been followed in metal –ligand complexation theoretical studies[298]. The aqueous phase calculation in **Table 4.4** was carried out by implicit solvation model where bare metal ions are immersed into dielectric continuum of water using COSMO solvation model. Now, following explicit solvation model, the hydrated U(VI) and Am(III) were sorbed on protonated SWCNT-AA. Based on the nature of dehydration during complexation, monomer solvation approach (where released water molecules are considered free) and cluster solvation approach (where released water molecules form cluster owing to the strong intermolecular H-bonding) are considered. The aqueous phase free energy was calculated using standard state entropy corrections as practiced by Bryantsev et al.[243]. The results are shown in **Table 4.8**.

Table 4.8 Calculated Gibbs free energy change of complexation reactions in aqueous phase between the metal ions and protonated SWCNT-AA considering hydration of the metal ions

Hydration model	Complexation of	ΔG_{aq} (kcal mol^{-1})
Monomer water	UO_2^{2+}	5.9
	Am^{3+}	8.4
Cluster water	UO_2^{2+}	23.9
	Am^{3+}	35.5

Although the free energy become positive for both of the metal ions, the experimental trend of higher uranyl adsorption by CNT-AA compared to americium is maintained, i.e., ΔG_{aq} values for uranyl complexation is less positive than that for americium in both the solvation model.

4.2 Sorption behaviour of Pu^{4+} and PuO_2^{2+} on CNT-AA[171]

Various technologies exist for the removal of Plutonium, which include filtration, solvent extraction, ion exchange and adsorption. Adsorption is considered one of the most attractive processes for Pu removal from solution, since adsorbents are generally easy to handle in the case of radioactive metals and can be used for various situations.[299] In sorption techniques minimum amount of solvent are used and due to this it Is eco-friendly. Functionalized CNT-AA have been considered as the most preferred solid phase sorbent material for removal of organic pollutants,[300-302] heavy metals[286, 303-306] from aqueous medium and pre-concentration of lanthanides[290, 307] and actinides[253, 258, 287] from acidic aqueous medium. Additionally density functional theoretical (DFT) calculation has been performed to study the nature of coordination and interaction of the Pu^{4+} and PuO_2^{2+} ions towards the MWCNT-AA. Therefore, DFT calculation was carried out to find the coordination mode of the functionalized ligand with an endeavor to know the complexation of Pu^{4+} and PuO_2^{2+} with MWCNT-AA.

4.2.1 Experimental Study

4.2.1.1 **Effect of aqueous feed acidity on the K_d values of Pu^{4+} and PuO_2^{2+}**

For extraction profile of Pu^{4+} and PuO_2^{2+}, K_d values as a function of feed acidity were taken into consideration and it was observed (**Figure 4.10**) that for both the metal ions the K_d values were found to increase with increase in HNO3 concentration. The increase in K_d values with aqueous feed acidity might be due to the participation of NO_3^- anion on complexation.

$$Pu^{4+}_{aq} + AA - MWCNT + 4NO^{-}_{3\,aq} = Pu(NO_3)_4 . AA - MWCNT \qquad (4.2)$$

$$PuO_{2\,aq}^{2+} + AA - MWCNT + 4NO_{3\,aq}^{-} = PuO_2(NO_3)_2\,.AA - MWC \qquad (4.3)$$

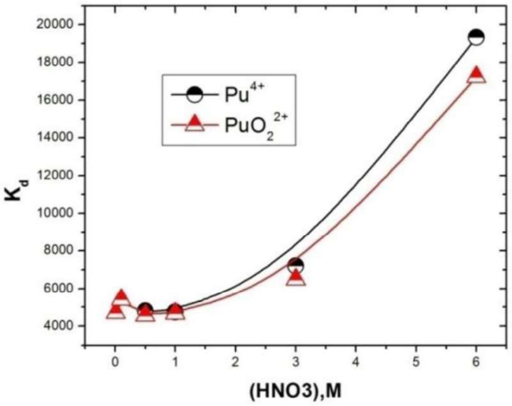

Figure 4.10 Effect of feed acidity on the K_d values of Pu^{4+} and PuO_2^{2+}

4.2.1.2 Understanding the sorption mechanism through isotherm

To understand the sorption mechanism involved, different sorption isotherms are explored as empirical models which are obtain from the regression analysis of experimental data. Present investigation deals with the fitting of sorption isotherm data for Pu^{4+} and PuO_2^{2+} in the four most widely accepted sorption isotherm models, Langmuir, Dubinin–Radushkevich(D–R), Freundlich and Temkin isotherms. The fitting plots and evaluated parameters are given in **Figure 4.11 and Table 4.9,** respectively. The main objective behind this is to understand the sorption mechanism based on the best linear regression. Langmuir isotherm model describes the monolayer formation in between adsorbate and the outer surface of the adsorbent, and after that no further adsorption takes place. Langmuir represents the equilibrium distribution of metal ions between the solid and liquid phases. This isotherm is valid only for monolayer adsorption onto a surface containing a finite number of identical sites. In this model no transmigration of adsorbate in the plane of the surface.

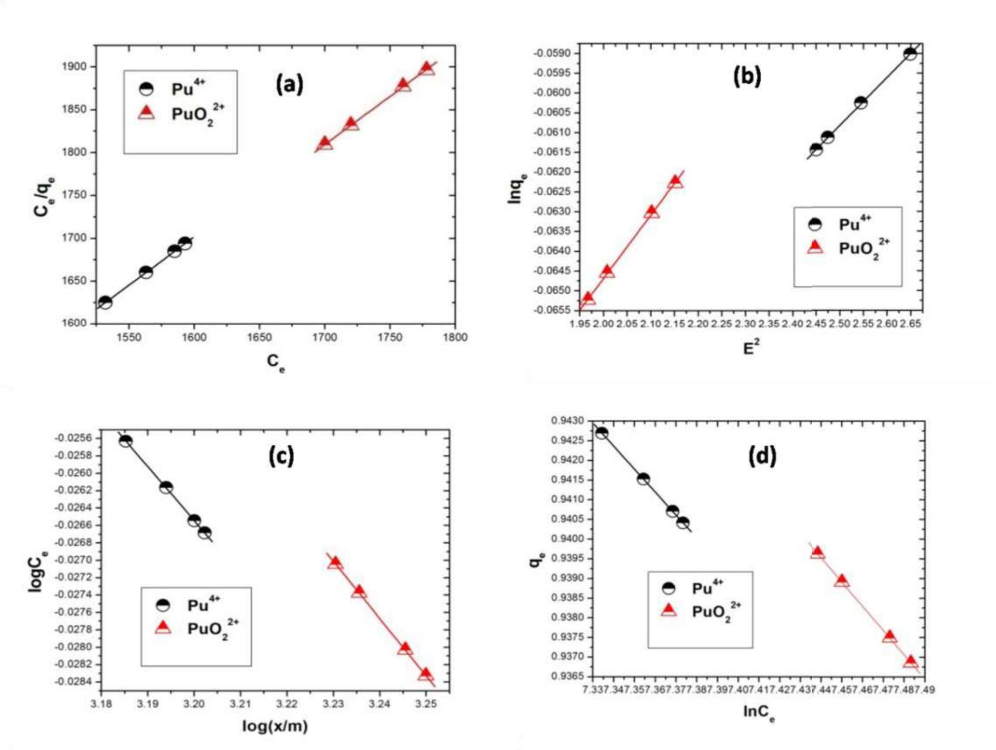

Figure 4.11 (a) Langmuir, (b) D–R, (c) Freundlich and (d) Tempkin isotherms for Pu^{4+} and PuO_2^{2+} on MWCNT-AA

The Langmuir sorption capacity of PuO_2^{2+} (89.4 mg g^{-1}) was found higher than that of Pu^{4+}(91.2 mg g^{-1}). Sorption energy (b) values also follow the same trend. The linear regression coefficients for Langmuir isotherm were found to be 1.00003 and 1.00005 for Pu^{4+} and PuO_2^{2+} on MWCNT-AA respectively, as shown in **Table 4.9**. The Langmuir adsorption not explains the surface roughness and in-homogenity of the adsorbent. It also neglects multiple site sorption and influence of neighboring sorption sites. In view of this, the experimental data were tried to analyze by other isotherm models.

Dubinin–Radushkevich isotherm, an empirical model initially conceived for the subcritical vapors onto micro pore solids by pore filling mechanism, is used to express the sorption mechanism with a Gaussian energy distribution onto a heterogeneous surface. This isotherm is mainly used for distinguishing physi-sorption and chemi-sorption. The energy values (E_a) for Pu^{4+} and PuO_2^{2+} were found to be 12.41 and 10.59 kJ mol^{-1}, respectively, showing the chemical interaction between amidoamine group and Plutonium ion in both the oxidation states. Moreover, this interaction was found to be greater in case of Pu^{4+} compared to PuO_2^{2+}. Similar observation was also noticed in case of $K_d$values for Plutonium. The linear regression coefficients for this model were found be 0.99885 and 0.99882, respectively for Pu^{4+} and PuO_2^{2+}. These linear regression coefficient values were inferior compared to the Langmuir model.

Freundlich Isotherm is commonly used to describe the adsorption characteristics for the heterogeneous surface. It describes the relation between adsorbate concentrations on the surface to the adsorbate concentration in liquid. This isotherm can be applied to multilayer adsorption. The Freundlich isotherm constant, k_f gives an approximate estimation of adsorption capacity of Pu^{4+} and PuO_2^{2+} on MWCNT. The 'n' is an indication of the strength of sorption. If $n = 1$ then the partition of metal ion between the solid and liquid phases are independent of the concentration of metal ion. The n value above one indicates the normal sorption whereas below one indicates cooperative adsorption. In the present investigation the 'n' values for Pu^{4+} as well as PuO_2^{2+} were found to be well above 1. The higher k_f value for Pu^{4+} revealed its higher sorption capacity over PuO_2^{2+}on MWCNT-AA. This was in good agreement with that obtained by Langmuir isotherm. The regression coefficients for Pu^{4+} and PuO_2^{2+} for Freundlich isotherm were evaluated as 0.99978 and 0.99968 for tetra and hexavalent plutonium, respectively.

Table 4.9 Different constants obtained from Langmuir, D.R., Freundlich and Tempkin isothem.

Langmuir isotherm			
	q_e(mgg^{-1})	b(Lmol^{-1})	χ^2
Pu^{4+}	91.2	0.016	1.00003
PuO_2^{2+}	89.4	0.009	1.00005
Dubinin-Radushkevich isotherm			
	X_m(mgg^{-1})	E(KJmol^{-1})	R
Pu^{4}+	91.6	12.41	0.99885
PuO_2^{2+}	90.0	10.59	0.99882
Freundlich isotherm			
	K_f(mgg^{-1})	n	R
Pu^{4+}	102.1	16.11	0.99978
PuO_2^{2+}	90.2	15.19	0.99968
Temkin isotherm			
	A_T(Lmg^{-1})	b	R
Pu^{4+}	64.0	42.6	0.99988
PuO_2^{2+}	14.4	40.3	0.99989

Temkin Isotherm model is based on that the heat of adsorption of all molecules in the layer decrease linearly (not by logarithmic nature) with a uniform distribution of binding energies.[308-310] The model equation and parameters are discussed in Section 2.6.1.3 in chapter 2. For present experiment it was observed that the A_T value for Pu^{4+} was found to be ~ 4.5 times greater than PuO_2^{2+}.But the regression coefficients for Pu^{4+} and PuO_2^{2+} on MWCNT-AA isotherms were found to be 0.99988 and 0.99989, respectively. Based on the linear regression analysis, the sorption process was found to follow Langmuir isotherm, i.e. through mono layer, without interaction of the neighboring sorbent sites and considering all the binding sites are equivalent.

4.2.1.3 **Kinetics study**

Kinetics is one of the important sections of sorption study which should be looked into. If C_t and C_{te} are the metal ion concentration on MWCNT-AA at time'‘t’ and at equilibrium, then the fractional attainment of the equilibrium (F) can be expressed as[311],

$$F = \frac{C_t}{C_{te}} \qquad (4.4)$$

A plot of 1-F as the function of time (**Figure 4.12**) revealed that with increase in time the 1-F values decreased drastically upto 45 min followed by gradual decrease. This study primarily revealed that, 45 minutes is essential for attaining the equilibrium. To get into the detailed of sorption kinetics, the experimental data were fitted on different models: Lagergren first order, intra particle diffusion model and finally pseudo second-order reaction. The fitted plots are shown in **Figure 4.12** and the simulated model parameters are depicted in **Table 4.10**. The pseudo-frst order rate constant k_{ads} for Pu^{4+} was found to be more compared to PuO_2^{2+}, while the linear regression coefficients were evaluated as 0.8672and 0.8059for Pu^{4+} and PuO_2^{2+}, respectively. The linear regression coefficients were found to be poor in the present model. The linear relationship between q_t and $t^{0.5}$ in intra particle diffusion model revealed that the sorption process is controlled by intra-particle diffusion only. However, multi -linear graphs indicate two or more steps influence the sorption process. The intra particle diffusion rate constant for $PuO_2^{2+}$and Pu^{4+} found to be almost similar. C values, were found to be almost similar suggesting the same boundary layer thickness for the sorption. The linear regression coefficients for the above analysis were also found to be poor as like obtained by the Lagergren pseudo first order kinetics.

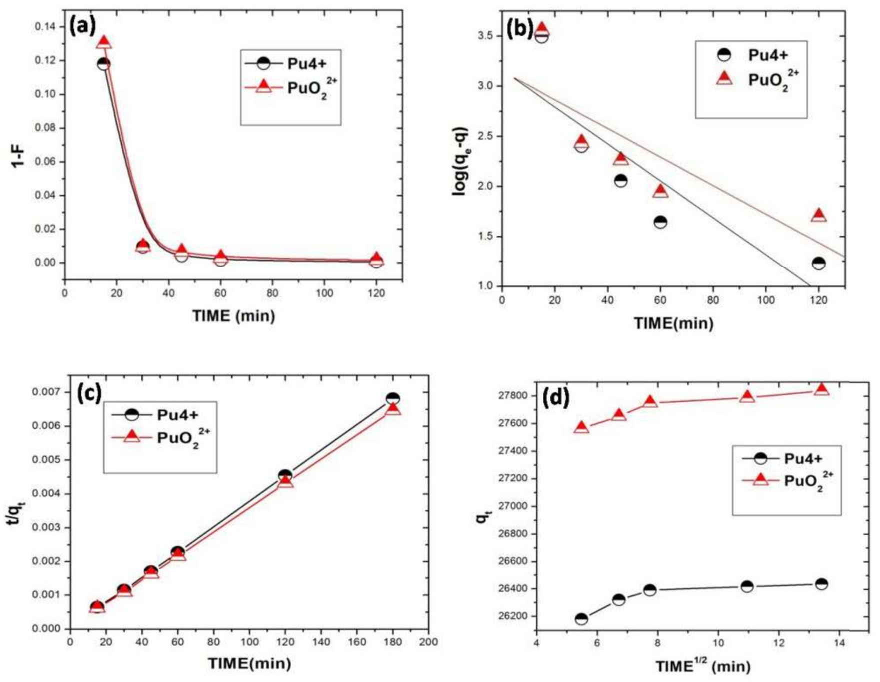

Figure 4.12 Sorption kinetics for Pu^{4+} and PuO$_2^{2+}$ on MWCNT-AA: (a) Plot of 1-F vs time, (b) pseudo-first order, (c) pseudo-second-order, and (d) intraparticle diffusion fitting

Table 4.10 Different constants obtained from the Langmuir, D–R, Freundlich, and Tempkin isotherms

Lagergren first order kinetics			
	q$_e$	k$_{ads}$	R
Pu^{4+}	1454.5	0.042	0.86728
PuO$_2^{2+}$	1414.2	0.032	0.80590
Intra particle diffusion model			
	k$_p$	C	R
Pu^{4+}	26.1	26115.6	0.82965
PuO$_2^{2+}$	30.8	27445.0	0.91974
Pseudo second order			
	q$_e$	k$_2$	R
Pu^{4+}	26617.6	3.8E-05	0.99995
PuO$_2^{2+}$	28049.3	3.1E-05	0.99994

A plot of t/q vs. t gave straight lines for both the cases with high degree of linear regression coefficients. Slope of this plot give q$_e$ value while the intercept gave the pseudo second order rate constants. The rate constant for Pu^{4+} was found to be almost 1.2

times of that for PuO_2^{2+}. The overall analyses of the sorption kinetics also revealed that sorption of Plutonium on MWCNT-AA take place through pseudo 2nd order rate kinetics.

4.2.1.4 **Back extraction of Pu from MWCNT-AA**

During processing of radiotoxic matal ions, it is imperative that the method should be developed for back extraction of both the oxidation states of plutonium from loaded MWCNT-AA. This is very important on the basis of precious metal accounting and also for its further processing either in nuclear reactor or as waste for disposal. In view of this several agents were used to serve the purpose. Out of them only 0.01 M oxalic acid, 0.01 M sodium carbonate and 0.01 M EDTA were found to be successful for at least more than equal to 70 % elution of the metal ion in both the oxidation states (**Figure 4.13)**.

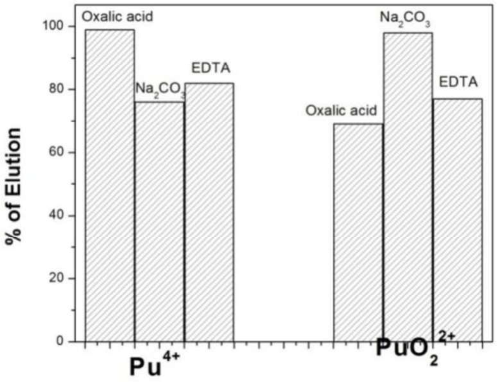

Figure 4.13 Elution behaviour of tetra and hexavalent plutonium from MWCNT-AA

It was also observed that for tetravalent plutonium 0.01 M oxalic acid was the best for almost quantitative (more than 99 %) recovery of plutonium. In case of hexavalent plutonium 0.01 M sodium carbonate showed the most promising results of ~ 99 % stripping from loaded MWCNT-AA.

4.2.1.5 **Radiolytic degradation**

During processing of radio-toxic metal ion, alpha, beta and other particles alongwith the high energy gamma rays deposit energy on the medium. As a result, the weakest bond of the sorbent will break. This may lead to the degradation of the performance of the sorbent either by reducing the sorbent efficiency or by decreasing selectivity. The sorbent with maximum radiation resistance is always desirable. In this context, the MWCNT-AA was exposed to a variety of radiation dose upto 1500 kGy and with that irradiated MWCNT-AA, sorption efficiency for tetra and hexavalent plutonium were determined. The results were shown in **Figure4.14**. On gamma 500 kGy, 1000 kGy and 1500 kGy of irradiation, the sorption efficiency for Pu^{4+} was found to become ~ 94.9 %, 90.7 % and 86.5 %, respectively, whereas that for PuO_2^{2+} became 93.6 %, 88.4 % and 84.1 %, respectively. This study revealed that MWCNT-AA had high radiation stability towards gamma irradiation.

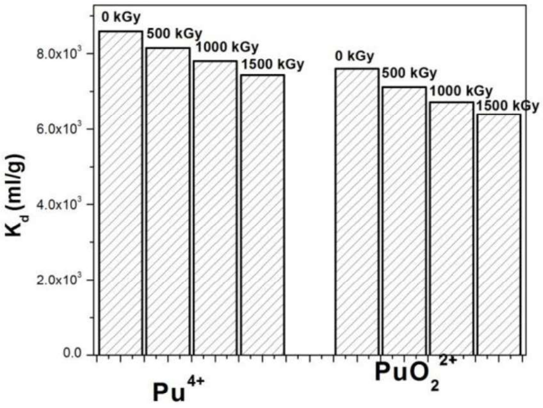

Figure 4.14 The radiolytic stability of MWCNT-AA

4.2.1.6 **Selectivity of MWCNT-AA**

The success of a sorbent depends in the efficient and selective separation of the targeted metal ion from actual waste composition. In this regards, simulated high level waste of research reactor origin was processed by using MWCNT-AA. The sorption of most of the metal ion present in the nuclear waste i.e. Al, Ba, Ca, Cd, Cr, Fe, Mg, Mn, Na, Ni, Sr, Ru and Mo was found to be negligibly small while Ce and La were found to be extracted on the solid phase. **Table 4.11** summarizes the analytical results obtained after processing the SHLW by MWCNT-AA followed by feeding the aqueous phase directly into the plasma.

Table 4.11 The analytical results obtained by ICP-AES after processing the SHLW with MWCNT-AA

Metal ions	**Analytical line (nm) for measuring in ICP-OES**	**Initial (mgL^{-1})**	**RR Final (mgL^{-1})**	**K_d (mLg^{-1})**
Al	396.152	250	245±16	0.20
Ba	455.404	100	94±4	0.60
Ca	396.847	400	388±19	0.30
Cd	361.051	300	292±11	0.26
Cr	284.984	400	366±15	0.85
Fe	244.451	1500	1476±20	0.16
Mg	280.270	300	273±14	0.90
Mn	257.611	500	499±15	0.02
Ni	227.021	300	288±17	0.40
Sr	407.771	50	46±3	0.80
Ce	413.380	100	0.95±4	9.50
La	379.478	100	0.96±4	9.60
Ru	245.644	7.5	7.1±0.3	0.53
Mo	281.615	30	28±3	0.66

4.2.2 Computational Study

4.2.2.1 **Computational Protocol**

DFT calculation was conducted for the electronic structures, geometry, energy and thermochemistry related to the sorption of Pu^{4+} and PuO_2^{2+} by CNT-AA as given in Sec.

3.1.1.1. A (8, 0) zigzag single-walled CNT (SWNT) with four unit cells with tubular length of 5.78 Å width of 6.40 Å was considered for the calculation. Amidoamine (AA) unit was attached to the open end of the CNT owing to the higher reactivity of the open end dangling carbon atoms.[282] Orbital population analysis on the optimized structures was performed using natural population analysis (NPA).[220]The charge transfer(ΔN)[312] between Pu metal centre and AA donor of SWNT-AA was evaluated using absolute electronegativity (χ) and absolute hardness (η) of metal ion and sorbent. By using Koopmans' theorem[313],χ and η can be calculated from the energy of highest occupied (HOMO) and lowest unoccupied (LUMO) molecular orbital of the metal and sorbent, which are inputs from the DFT calculation.

4.2.2.2 **Structural Parameters**

The optimized geometrical structures of the SWNT-AA, and its complexes with Pu^{4+} and PuO_2^{2+} with nitrate anions are shown in **Figure 4.15**. The Pu-O and Pu-N bond distances involved in the complexation reaction are shown in **Table 4.12**. The AA and all the nitrate anions are coordinated to Pu metal centre in bidentate mode for both Pu^{4+} and PuO_2^{2+} complexes. Thus Pu is deca-coordinated (two from each of four nitrates and one AA) in the former complex and octa-coordinated (two from each of two nitrates and one AA, and one from each of two oxo group) in the later.

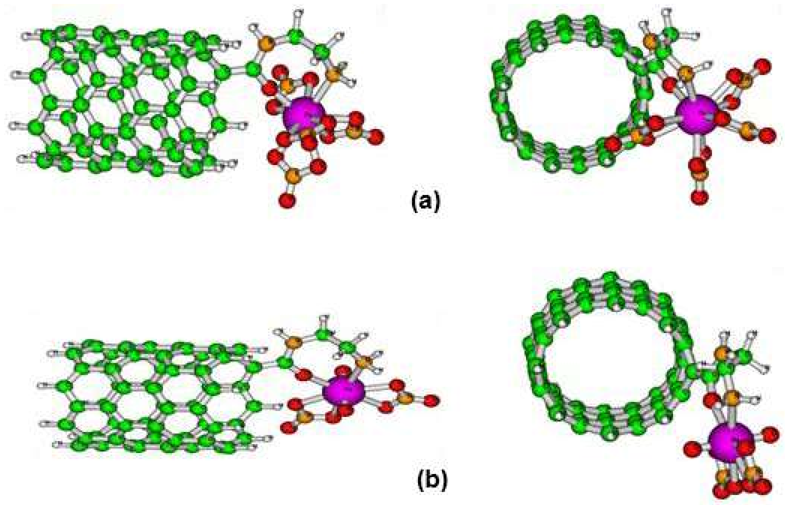

Figure 4.15 The optimized structures for the Pu^{4+} (a), and PuO_2^{2+} (b) complexes with SWNT-AA in presence of nitrate anions

Table 4.12 Characteristic Pu-O and Pu-N bond distances in the optimized geometries

	Bond distances (Å)		
Molecular System	**Pu-O(C=O)**	**Pu-N(NH_2)**	**Pu-O(NO_3)**
$Pu(NO_3)_4$(SWNT-AA)	2.24	2.60	2.45
$PuO_2(NO_3)_2$(SWNT-AA)	2.42	2.67	2.47

The Pu-O(C=O) bond distance is shorter (2.24 Å) for Pu^{4+} complex compared to PuO_2^{2+} (2.42Å), whereas the Pu-N and Pu-O(NO3-) bonds are of nearly similar strength for both the complexes. This implies formation of more stable complex by Pu^{4+} than that of PuO_2^{2+} with SWNT-AA. For further insight of the binding in these two complexes, calculated natural population analysis (NPA) results of the optimized complex and bare ions are summarized in **Table 4.13**. The f-shell of both complexes are populated by more numbers of electrons compared to their free corresponding tetravalent and hexavalent-oxo plutonium cation.

Table 4.13 Calculated f orbital population and natural charges on the Pu atoms

Species	Gas phase			Aqueous phase		
	f_{pop}	**Q**	**ΔQ***	**f_{pop}**	**Q**	**ΔQ**
$Pu(NO_3)_4$(SWNT-AA)	5.15	1.45	2.55	5.43	1.29	2.71
Pu^{4+}	4.0	4.0		4.0	4.0	
$PuO_2(NO_3)_2$(SWNT-AA)	5.19	1.43	1.03	5.49	1.25	1.40
PuO_2^{2+}	4.88	2.46		4.78	2.65	

This population enhancement in f-shell is more in aqueous phase compared to gas phase (e.g. for Pu^{4+}-complex 4.0 increases to 5.15 in gas phase, whereas 4.0 increases to 5.43 in aqueous phase) signifying involvement of water in the complexation. The natural charges (Q) on Pu atom in gas phase are changes from 4.0 and 2.46 in free metal ion to 1.45 and 1.43 in the complex strictures of Pu^{4+} and PuO_2^{2+}, respectively. This also reveals the more interaction by Pu^{4+} than PuO_2^{2+}, as cationic charge neutralization is more in the former (2.25) case than the later (1.03); same observations are seen in aqueous phase, only the charge neutralization on the Pu metal is more (2.27/1.40) due to the participation of the water molecules in the coordination. The quantum mechanical descriptors for the Pu acceptor and SWNT-AA donor was calculated from their energy of HOMO and LUMO using Koopmans's theorem and summarized in **Table 4.14**. The higher HOMO-LUMO gap, electronegativity, and hardness of Pu^{4+} (4.96, 43.89, and 2.50 eV, respectively)compared to PuO_2^{2+} (4.81 eV, 21.52, and 2.40 eV,respectively) signify the better acceptor property of the former. On the other hand, with lower values of HOMO-LUMO gap, electronegativity, and hardness (0.27, 3.79, and 0.13 eV, respectively), SWNT-AA has strong donor capacity. Thus the amount of charge transfer (ΔN) is higher in Pu^{4+}(7.60) than that in PuO_2^{2+}(3.48) leading to stronger complexation for the former case.

Table 4.14 Calculated various molecular descriptors

	E_{HOMO}(eV)	E_{LUMO}(eV)	Gap ($E_{HOMO-LUMO}$(eV))	χ (eV)	η(eV)	ΔN
Pu^{4+}	-46.39	-41.39	4.96	43.89	2.50	7.60
PuO_2^{2+}	-23.93	-19.11	4.81	21.52	2.40	3.48
SWNT-AA	-3.93	-3.66	0.27	3.79	0.13	

4.2.2.3 Free energy of complexation in gas as well as in aqueous phase

In order to estimate the stability of the Pu-amidoamine bonds in the two complexes, the free energy of complexation of of Pu^{4+} and PuO_2^{2+} with SWNT-AA in presence of nitrate ions are calculated in gas phase and aqueous solution. As shown in **Table 4.15**, the free energy of complexation is almost three times higher for Pu^{4+} than PuO_2^{2+} both in gas and aqueous phase. The decrease in aqueous phase energy values is due to extra solvent-metal ion interaction. This confirms the higher sorption of Pu^{4+} compared to PuO_2^{2+} by SWNT-AA.

Table 4.15 Calculated free energy of complexation (kcal/mol) of Pu^{4+} and PuO_2^{2+} with SWNT-AA

Complexation reaction	ΔG_g	ΔG_{aq}
$Pu^{4+} + SWNT - AA + 4NO_3^- \rightarrow Pu(NO_3)_4(SWNT - AA)$	-1751.3	-326.6
$PuO_2^{2+} + SWNT - AA + 2NO_3^- \rightarrow PuO_2(NO_3)_2(SWNT - AA)$	-512.5	-110.9

4.3 Sorption of NpO_2^+ and NpO_2^{2+} on CNT-AA[172]

Amide functionalized carbon nanotubes were extensively studied for the separation of uranium, plutonium and thorium while neptunium remained un-extracted. The safe disposal of highly radiotoxic waste arising out of the nuclear establishment is one of the prerequisites of the energy programme. Neptunium being one of minor actinides having long half-life is to be monitored carefully. Due to the predominance existence of neptunium in pentavalent oxidation state, which is having less chemical potential, its complexation is very difficult. Either its conversion to hexavalent or tetra valent oxidation state is necessary for its complexation. Therefore, the literatures focused on neptunium separation/complexation are very few. in view of this, an attempt was made to demonstrate the efficient sorption behaviour of NpO2+ and NpO22+ on amidoamine functionalized multiwalled carbon nanotube. This includes the analysis of four isotherm models to understand the sorption mechanism; analysis of three different kinetics models to throw lights on sorption kinetics, effect of gamma irradiation on the sorption efficiency of MWCNT-AA on extraction of Np, stripping of Np from adsorbed MWCNT-AA. It is worthwhile to explore the sites of coordination and nature of interaction between NpO_2^+ and NpO_2^{2+} with MWCNT-AA. Density functional theory (DFT) has been proven to be very useful in elucidating the coordinates sites and type on interaction[167, 168, 314, 315]. Therefore, DFT calculation was performed to establish the coordination mode of the functionalized ligand with an aim to understand the complexation of NpO_2^+ and NpO_2^{2+} with MWCNT-AA.

4.3.1 Experimental Study

4.3.1.1 Effect of aqueous feed acidity on the K_d values

The sorption efficiency as a function of aqueous feed acidity is shown in **Figure 4.16**. The K_d values for NpO_2^{2+} was found to be more than that of NpO_2^+ due to the higher chemical potential of the former, The K_d values were found to increase with aqueous feed acidity drastically up to 3 M HNO_3 followed by slow increase. The initial rise in K_d values is the artifact of the participation of NO_3^- in complex formation while at higher feed acidity the availability of large amount of H^+ led to the competition with Np ion.

$$NpO_{2\,aq}^{+} + MWCNT - AA + NO_{3\,aq}^{-} = NpO_2(NO_3).MWCNT - AA \quad (4.5)$$

$$NpO_{2\,aq}^{2+} + MWCNT - AA + 2NO_{3\,aq}^{-} = NpO_2(NO_3)_2\,.MWCNT - AA \quad (4.6)$$

$$H_{aq}^{+} + MWCNT - AA + NO_{3\,aq}^{-} = HNO_3\,.MWCNT - AA \quad (4.7)$$

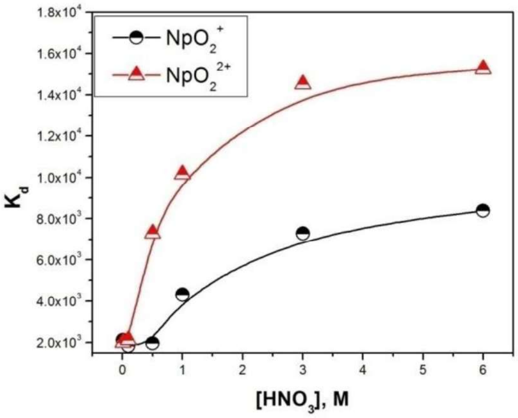

Figure 4.16 Effect of feed acidity on the K_d values of NpO_2^+ and NpO_2^{2+}

4.3.1.2 **Sorption Isotherm**

For understanding the nature of the sorption, and mechanism isotherm analysis was carried out using Langmuir isotherm, Dubinin–Rodushkevich (D–R) isotherm, Freundlich Isotherm and Temkin Isotherm models and conclusions were made based on their linear regression analysis [316, 317]. **Table 4.16** summarizes the results obtained from the linear regression analysis of linear plots (not shown here) of the respective models.

Table 4.16 The isotherm analysis using different models

Langmuir isotherm			
	q_m(mgg^{-1})	b(Lmol^{-1})	χ^2
NpO_2^+	60.2	0.029	0.99971
NpO_2^{2+}	82.5	0.022	0.99992
Dubinin-Radushkevich isotherm			
	X_m(mgg^{-1})	E(KJmol^{-1})	R
NpO_2^+	65.8	9.88	0.97141
NpO_2^{2+}	85.2	11.05	0.98909
Freundlich isotherm			
	K_f(mgg^{-1})	n	R
NpO_2^+	62.6	10.2	0.99689
NpO_2^{2+}	88.0	9.3	0.99893
Temkin isotherm			
	A_T(Lmg^{-1})	b	R
NpO_2^+	12.6	32.2	0.99588
NpO_2^{2+}	10.1	28.7	0.99861

The Langmuir sorption capacity (q_m) for NpO_2^{2+} was found to be more than that of NpO_2^+ while there is only a moderate change in the sorption energy (b) was observed from Langmuir analysis. The sorption capacities for UO_2^{2+}, Th^{4+}, Pu^{4+} and PuO_2^{2+} on amide functionalized carbon nanotubes were reported to be 32.5, 47.1, 91.9 and 84.9 mg g^{-1}, respectively[253, 254] . The D-R isotherm analysis revealed the sorption energy (E) for NpO_2^+ and NpO_2^{2+} to be 9.88 and 11.05 kJ mol^{-1}, respectively suggesting the chemical interaction between the amidoamine functionality and the Np ion. The maximum sorption capacities for Np in penta and hexavalent oxidation states were found to be of similar order as obtained from Langmuir isotherm and K_f values in Freundlich isotherm. Additionally, the strength of sorption 'n' values obtained from Freundlich isotherm has its own significance as follows: 1)n = 1 then the partition of metal ion between the solid and liquid phases are independent of the concentration of metal ion; 2)the n value above one indicates the normal sorption; 3)below one indicates cooperative adsorption. The present sorption was found to be a case of 'normal sorption'. The 'normal sorption' was also reported for UO_2^{2+} and Th^{4+} on amide functionalized carbon nanotubes while cooperative mechanism was reported for tetra and hexavalent Pu on same sorbent. The linear regression analysis revealed that the sorption of Np on MWCNT-AA proceeded via Langmuir isotherm with regression coefficients 0.99971 and 0.99992 for NpO_2^{+} and NpO_2^{2+}, respectively. The experimental sorption capacities for NpO_2^{+} and NpO_2^{2+} was evaluated as 58.1 and 83.9 mg g^{-1}, respectively; which were very close to the values observed by Langmuir isotherm model.

4.3.1.3 **Sorption kinetics**

Lagergren pseudo first order rate kinetic, Intra-particle diffusion model and Pseudo second-order model were employed to understand the sorption kinetics [80-83].F is the fractional attainment of the equilibrium at time t. A plot of 1-F as the function of time (**Figure 4.17**) revealed that with increase in time the 1-F values decreased drastically upto120 min followed by plateau for both penta and hexavalent Np. Therefore, 120 minutes are required for achieving complete equilibrium. The linear regression analysis of the kinetics using different models is shown presented in **Table 4.17**. Lagergren 1st order kinetics revealed that the rate constants (k_{ads}) for both penta and hexavalent Np are nearly similar while the regression coefficients for this model were not found to be satisfactory (NpO_2^{+} =0.86728, NpO_2^{2+} = 0.80590).

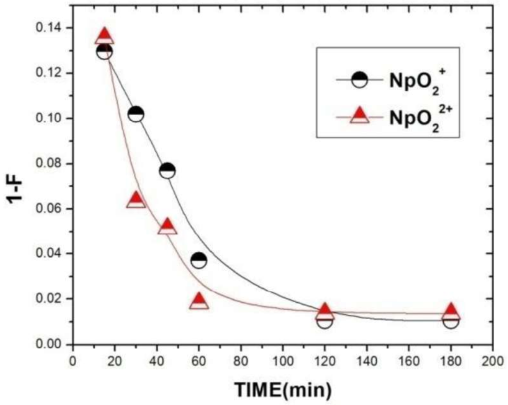

Figure 4.17 Sorption kinetics of NpO_2^+ *and* NpO_2^{2+} *on MWCNT-AA*

In view of this the intra particle diffusion model has been employed for the diffusion-controlled sorption process on a porous sorbent. The regression coefficients were found to be improved by this model with the rate constants 27.8 and 32.2 mg $g^{-1}min^{-1}$ for NpO_2^+ and NpO_2^{2+}, respectively. The constant, C (mg g^{-1}), evaluated from the intercept, proportional to the boundary layer thickness was found to follow the trend NpO_2^{2+}> NpO_2^+.

Table 4.17 The analysis of sorption kinetics via different models

Lagergren first order kinetics			
	q_e	k_1	R
NpO_2^+	13.24	0.024	0.86728
NpO_2^{2+}	12.15	0.020	0.80590
Intra particle diffusion model			
	k_p(mg g^{-1} min^{-1})	C	R
NpO_2^+	27.8	16.8	0.90530
NpO_2^{2+}	32.1	28.2	0.78593
Pseudo second order			
	q_e(mg g^{-1})	k_2 (mg g^{-1} min^{-1})	R
NpO_2^+	69.3	5.13E-04	0.99992
NpO_2^{2+}	92.7	3.85E-04	0.99997

The pseudo-second-order kinetics model was found to be best fitted in the experimental data revealing the sorption rate as 5.13 x 10^{-4} and 3.85 x 10^{-4} mg g^{-1} min^{-1} for penta and hexavalent neptunium, respectively.

4.3.1.4 **Radiolytic stability**

The gamma ray exposure basically led to the deposition of energy into the medium or the sorbent. The sufficient energy deposition on the amidoamine functionalized MWNCT might lead to breakage of weaker bonds (**Figure 4.18**). Consequently, there was a possibility of modification of functionalities of the sorbent molecules. Due to these radiations induced change of the sorbent, there might be modification in its performance. During the processing of radio toxic elements, the sorbent continuously had to suffer the high energy irradiation (particle as well as gamma), and hence the sorbent should be as robust as possible. In view of this, the radiolytic stability of the sorbent was investigated. To understand the radiation chemistry of amidoamine functionality detailed investigation on the degradation products need to be carried out and that would be a separate study which is beyond our scope and hence the radiation products were not investigated while the degradation in the sorption performance was studied. The sorbent, proposed to be used for processing of radiotoxic metal ion should have high radiolytic stability. The gamma irradiated MWCNT-AA was used for evaluating the sorption efficiency for penta and hexavalent neptunium. On 500 kGy gamma exposure the K_d values for NpO_2^+ and NpO_2^{2+}, were found become 94% and 90 % of their initial values while on 1000 kGy gamma exposure they became 82 % and 78 %. Upto this gamma exposure the sorbent was found to have very good radiolytic stability. A highly extensive gamma exposure of

1500 kGy was found to decrease the K_d values drastically to ~ 58% and 50 % of the original values of NpO_2^+ and NpO_2^{2+}, respectively. **Figure 4.19**, depicts the radiolytic stability study.

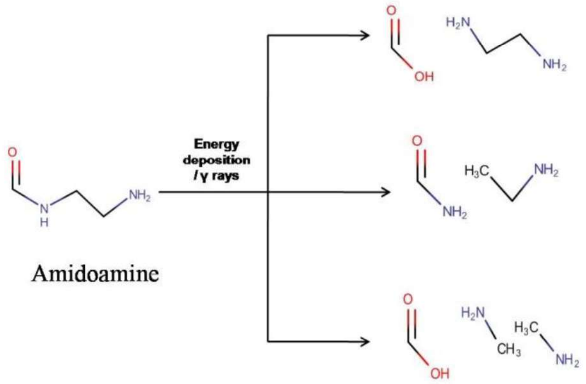

Figure 4.18 Probable radiolytic degradation route for amidoamine functionality on gamma irradiation

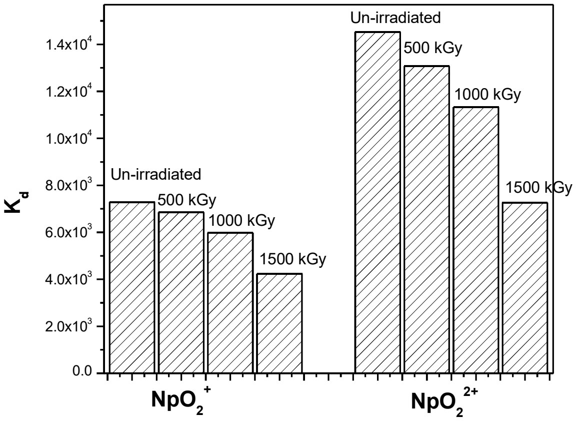

Figure 4.19 Radiolytic stability of MWCNT-AA

4.3.1.5 Back extraction of NpO_2^+ and NpO_2^{2+}

Several stripping agents have been used for quantitative back extraction of NpO_2^+ and NpO_2^{2+} from MWCNT-AA. 0.01 M oxalic acid was found to be ineffective for both the oxidation states. 0.01 M EDTA and 0.01 M Na_2CO_3 were found to successful for quantitative back extraction of penta (~98%) and hexa (~99%)valent neptunium, respectively.

4.3.2 Computational results

4.3.2.1 **Computational Protocol**

Similar computational methodology and level of DFT theory as in Section 4.2.2.1 were employed for optimization of structures and energetics.

4.3.2.2 **Structural Parameters**

The optimized structures of the complexes of NpO^{2+} and $NpO_2^{2+}$with SWNT-AA in presence of nitrate anions are shown in **Figure 4.20**.

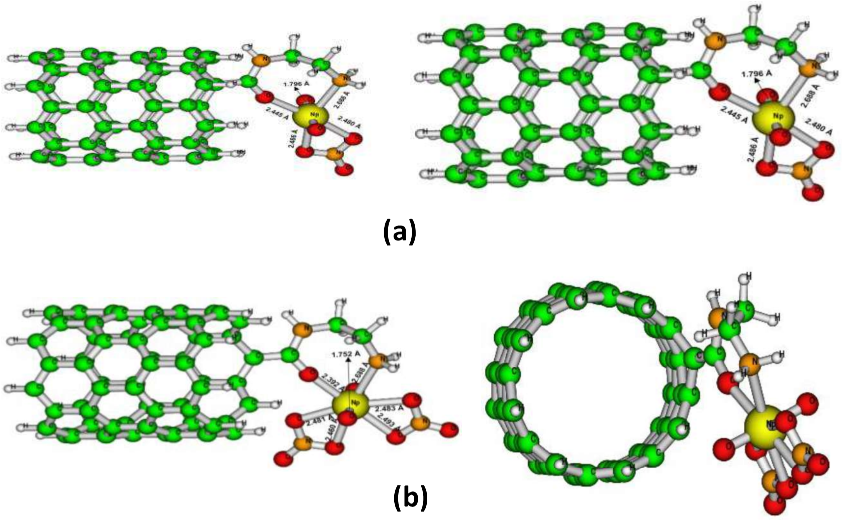

Figure 4.20 The optimized structures for the NpO_2^+ (a), and NpO_2^{2+} (b) complexes with SWNT-AA in presence of nitrate anions. The green, white, red, orange, and yellow balls represent carbon, hydrogen, oxygen, nitrogen, and neptunium

The AA and all the nitrate anions are coordinated to Np metal center in bidentate mode for both NpO_2^+ and NpO_2^{2+} complexes. Thus Npishexa-coordinated (two from sole nitrate, two from one AA, and two from two oxo groups), and octa-coordinated (two from each of two nitrates and two from one AA, and two from two oxo group) in the NpO_2^+ and NpO_2^{2+} complexes, respectively. The Np-O(C=O) bond distance is shorter (2.39 Å) for NpO_2^{2+} complex compared to NpO_2^+ (2.44Å) one, whereas the Np-N_{NH2} (2.68Å) and Np-O_{NO3-} (2.48Å) bonds are of similar strength for both the complexes. This clearly indicates the formation of more stable complex by NpO_2^{2+}compared to NpO_2^+ with SWNT-AA due to the higher charge on the neptunyl(VI) compared to neptunyl(V).

The charge and f orbital population of the neptunyl atom before and after complexation were evaluated from NPA analysis and shown in **Table 4.18**. The charge of the Np atom decreased considerably from the bare penta and hexavalent neptunyl ion due to the interaction with SWNT-AA for both of the complexation reaction. The charge neutralization due to complexation (ΔQ) is 1.07 for neptunyl(VI) and 0.42 for neptunyl(V) in gas phase. Again, due to the coordination of bare neptunyl ion with SWNT-AA and nitrates, the electronic population of the f orbitals have enhanced for both the complexation, and this f orbital population enhancement due to complexation (Δf_{pop}) is 0.36 for neptunyl(VI) and 0.01 for neptunyl(V) in gas phase.

Table 4.18 Calculated natural charges (Q), f orbital population and their difference after bonding on the Np atoms

Species	**Gas phase**				**Aqueous phase**			
	Q	**ΔQ**	**f_{pop}**	**Δf_{pop}**	**Q**	**ΔQ**	**f_{pop}**	**Δf_{pop}**
$NpO_2(NO_3)_4$(SWNT-AA)	1.72	0.42	4.18	0.01	1.78	0.59	4.14	0.09
NpO_2^+	2.14		4.17		2.37		4.05	
$NpO_2(NO_3)_2$(SWNT-AA)	1.51	1.07	4.07	0.36	1.35	1.45	4.34	0.74
NpO_2^{2+}	2.58		3.71		2.8		3.6	

The higher values of ΔQ and $\Delta f_{pop}$for NpO_2^{2+} compared to NpO_2^{+} confirm the stronger coordination of former with SWNT-AA. The ΔQ and Δf_{pop}values are higher in aqueous phase compared to gas phase calculation which indicates involvement of water in the complexation. The quantum mechanical descriptors for the Np acceptor and SWNT-AA donor was calculated from their energy of HOMO and LUMO using Koopmans's theorem and summarized in **Table 4.19**. The higher values of HOMO-LUMO gap, electronegativity, and hardness of neptunyl ions and lower values of SWNT-AA reveal that neptnyl ions are acceptor or acid and SWNT-AA is donar or base. The amount of charge transfer between the SWNT-AA and neptunyl ion (ΔN) calculated from the absolute electronegativity and absolute hardness values of the donar and acceptor species is higher for NpO_2^{2+}(3.87)compared to NpO_2^{+} (1.49). This also clearly indicates the stronger coordination of the neptunyl(VI) with SWNT-AA.

Table 4.19 Calculated various molecular descriptors

	E_{HOMO}(eV)	E_{LUMO}(eV)	Gap ($E_{HOMO-LUMO}$(eV))	χ (eV)	η(eV)	ΔN
NpO_2^{+}	-13.09	-8.63	4.46	10.86	2.23	1.49
NpO_2^{2+}	-22.85	-18.73	4.12	20.79	2.05	3.87
SWNT-AA	-3.93	-3.66	0.27	3.79	0.13	

4.3.2.3 **Binding energy/free energy of complexation**

The binding energy and free energy of the sorption processes in gas as well as in aqueous phase are shown in **Table 4.21**. The gas phase binding energy (ΔE) for neptunyl (VI) sorption is higher by -352.54 kcal/mol compared to neptunyl(V) sorption. The free energy change (ΔG) due to sorption of NpO_2^{2+} is higher by -344.23 kcal/mol compared to NpO_2^{+} sorption, in gas phase. The same results are also obtained in aqueous phase calculation.

The free energy change (ΔG) due to sorption of NpO_2^{2+} is higher by -344.23 kcal/mol compared to NpO_2^{+} sorption, in gas phase. The same results are also obtained in aqueous phase calculation; ΔEof NpO_2^{2+}sorption is higher by -61.91 kcal/mol than that of NpO_2^{+}, and ΔG of NpO_2^{2+}sorption is higher by -53.60 kcal/mol than that of NpO_2^{+}.

Table 4.20 Calculated binding energy and free energy of complexation in kcal/mol

Complexation of	**Gas phase**		**Aqueous phase**	
	ΔE	**ΔG**	**ΔE**	**ΔG**
NpO_2^{+}	-205.57	-176.80	-72.20	-43.43
NpO_2^{2+}	-558.11	-521.03	-134.11	-97.03

These results are in good congruence with experimentally observed higher adsorption capacity of MWCNT-AA for NpO_2^{2+}compared to NpO_2^{+}. It is interesting to note that the difference between the aqueous phase and gas phase energy values are due to extra solvent-metal ion interaction indicate the role of solvation energy in the sorption of neptunyl ions on SWNT-AA.

4.4 Uptake of Hg(II) by MWCNT-AA[173]

Despite being excessively toxic in nature, mercury is used in various industrial processes and eventually the mercury enter the wastewater directly or leach into water from disposal sites.[318]The tolerance limit of mercury in drinking water[319] is 0.001 mg/L and the CPCB, India guided discharge limit of mercury in industrial waste water is 0.01 mg/L. Thus, in order to minimize its grave impacts, wastewater containing mercury needs to be treated before being discharged into the receiving environment. This has led to a number of techniques being developed for removal of mercury from wastewater over the years.

Over the years, a new member to the carbon family, carbon nanotubes (CNTs) have received considerable attention because of their potential to act as extremely successful adsorbents against chemical as well as biological contaminants.[320] Their applications for removal of toxic pollutants from gaseous as well as aqueous streams has been extensively studied due to its porous and hollow structure, large surface area, light mass density, higher thermal, chemical, mechanical and radiation stability.[321] CNT based technologies have thus been found for water treatment applications in numerous fields, like sorbents, membranes, filters and catalysts, while many others are still in the development stage.[322]

Functionalization on the surface of CNTs further increases the capacity as well as selectivity towards adsorption application. Functionalization introduces organic ligands or functional groups on the CNT surface. Chemical covalent functionalization route offers better control on the modification of the surface functionality.[323] Several functional groups such as carboxylic acid[324], amine[325], amide[326], dithiocarbamate[327], diglycolamide[228], have been attached on the walls of the CNTs and tested for adsorption metal ions and organic molecules.

In the present study, we have systematically carried out batch adsorption studies to measure the uptake of Hg^{2+} ions from aqueous solution by MWCNT-AA. The adsorbent was prepared by chemical covalent functionalization and characterized by FTIR, XRD, XPS, TGA and DLS analysis. Although the same material has been called amide or amino-MWCNTs in previous studies reported[326, 328, 329], it is legitimate to refer to it as amidoamine-MWCNTs, as the functional group on the surface of nanotubes possesses both amide (-CONH-)and amine ($-NH_2$) units. The effect of pH, contact time, initial metal ion concentration and temperature on the adsorption of Hg^{2+} ions by MWCNT-AA has been studied and optimized adsorption parameters were set. Desorption and regeneration cycles were carried out to prove the renewability of the synthesized adsorbent. A small-scale fixed bed column study was performed to give an insight into the scale-up process. In addition, density functional theory (DFT) calculations were performed to understand the structure of the synthesized adsorbent, as well as the mechanism and selectivity of interaction between metal ions and MWCNT-AA.

4.4.1 Experimental Study

4.4.1.1 pH Studies

The pH of any solution plays a significant role in determining the adsorption of metal ions from it. Hg (II) adsorption increases from pH 2 to 7, after which, it is seen to decrease (**Figure 4.21**). The capacity of MWCNT-AA increases from 13.21 to 34.51 as the pH of the solution changes from 2 to 7. The steep decrease in adsorption by lowering the pH from 4 to 2 is a consequence of two factors. The competition between Hg^{+2} ions and H^+ ions in the solution, which leads to a decrease in the amount of Hg^+ ions adsorbed. Secondly, the predominant species in the presence of Cl^- ions is $HgCl_2$ at pH<4. While lowering the pH from 4 to 2 by addition of dilute HCl, the formation of $HgCl_2$increases, and Hg(II) sorption by MWCNT-AA decreases. At pH>4, depending on the Cl^- ion concentration various species like $Hg(OH)^+$, $Hg(OH)_2$, HgOHCl, $Hg(OH)_3^-$ would be available in the solution. From pH 4 to 7, Hg^{2+} and $Hg(OH)^+$ are dominating species, which bind strongly with amidoamine groups, and hence the sorption enhanced. The decrease in sorption beyond pH 7 may be attributed to the predominant formation of

$Hg(OH)_2$, $Hg(OH)_3^-$ like species, which being neutral or negatively charged have less affinity for binding with MWCNT-AA.As just below pH4 and very above pH7 the sorption sharply decreases, the optimum pH of the metal ion solution used for further studies was decided to be 6 for easy and insured adjustment, and all further experiments were carried out at this optimum pH. Similar observation and pH optimization has been reported earlier.[28]

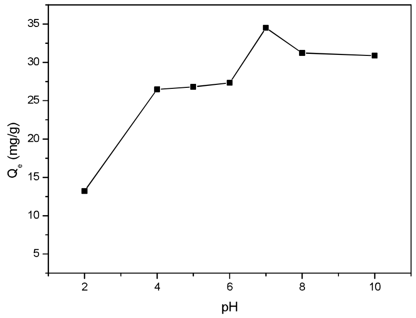

Figure 4.21 Effect of pH on adsorption of Hg^{2+} by MWCNT-AA

4.5.2. Isotherm. Non-linear two parameter and three parameter models were employed to simulate the experimental equilibrium data as shown in **Figure 4.22**(a) and (b).

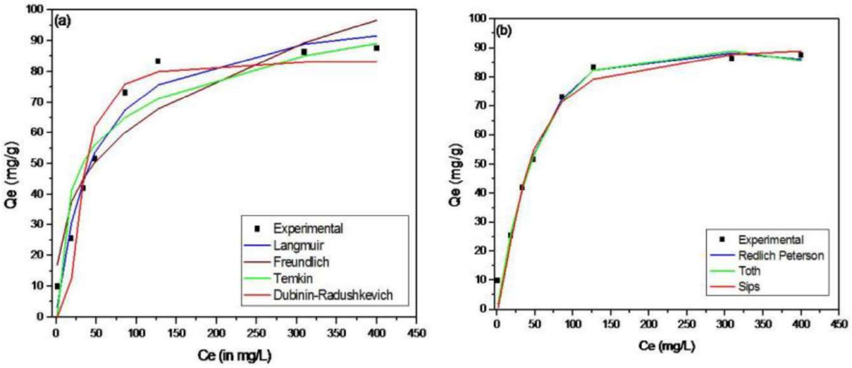

Figure 4.22 Hg^{2+} sorption equilibrium data fitting using (a) two parameter, and (b) three parameter isotherm models using MWCNT-AA sorbent

The values of the calculated theoretical parameters for all the models, coefficient of correlation (R^2) and chi-squared distribution has been provided in **Table 4.21**.The sharp initial slopes for all the non-linear models clearly indicates that the synthesized nanoparticles have a high efficiency when there is low Hg(II) concentration, and the decreasing slope with increasing concentration depicts saturation of active sites on the adsorbent surface.

Table 4.21 Hg^{2+}adsorption isotherm parameters for MWCNT-AA

No. of Parameters	**Model**	**Fitted parameters**		**R^2**
2	Langmuir	b	0.023 L/mg	0.96808
		q_m	101.35 mg/g	
2	Freundlich	K_f	15.24 (mg/g) $(L/g)^n$	0.88591
		n	3.24	
2	Temkin	B_t	15.66	0.89568
		K_t	0.74 L/g	
2	D-R	Q_o	83.64 mg/g	0.92875
		B_{DR}	$1.2 \times 10^{-4} mol^2/kJ^2$	
		Ea	64.65 kJ/mol	
3	Redlich-Peterson	K_{RP}	1.51 L/g	0.98854
		a_{RP}	$2.2 \times 10^{-3} (L/g)^g$	
		g	1.32	
3	Toth	K_{th}	9113.82 mg/g	0.98821
		a_{th}	166.22 L/g	
		t	0.59	
3	Sips	K_s	0.37	0.98015
		a_s	0.004 L/mg	
		b_s	1.52	

Amongst the two parameter models for MWCNT-AA, the Langmuir model (R^2=0.96808) offers the best fit for the experimentally observed data. It assumes that the surface is homogeneous with constant adsorption energy on each site. Each site can thus adsorb only a single molecule, i.e. monolayer adsorption which occurs at finite localized sites with no interaction between any of the adsorbed Hg(II) molecules.At low adsorbate concentrations, the Langmuir isotherm effectively reduces to a linear isotherm and thus follows Henry's law.Fitting with Langmuir model thus supports the idea of the surface of MWCNT-AA being homogeneous in nature. The theoretical monolayer maximum sorption capacity is calculated to be 101.35 mg/g. Separation factor (R_L) is a dimensionless constant represented as:

$$R_L = \frac{1}{1+bC_o} \tag{4.8}$$

where C_o is the initial metal concentration in mg/L. R_L is indicative of the adsorption nature. It indicates the adsorption to be irreversible (R_L=0), favorable (0<R_L<1), linear (R_L=1) and unfavourable (R_L>1).

R_L calculated for MWCNT-AA was found to be within 0.8148 to 0.79315 for initial concentrations of 10 to 500 mg/L Hg (II) indicating that adsorption by MWCNT-AA was favourable as 0<R_L<1.

For the three parameter models, the good fit is obtained for the Redlich-Peterson model which is based on a hybrid model featuring Langmuir and Freundlich isotherms. This model has a linear dependence on concentration in the numerator and an exponential function in the denominator to represent adsorption equilibria over a wide range of concentration. Redlich-Peterson model can be applied either in homogeneous or heterogeneous systems due to their versatility. This suggests heterogeneousness of the MWCNT-AA surface which may arise due to the functionalization of the homogeneous surface of MWCNTs.

4.4.1.2 **Kinetics**

The experimental kinetic data were fitted with pseudo first order and second order kinetic equations and shown in **Figure 4.23**. It is evident from the graphs that the initial stage of adsorption is characterized by a relatively rapid adsorption rate, after which it slowly decreases and finally attains a stable value in approximately 180 minutes.

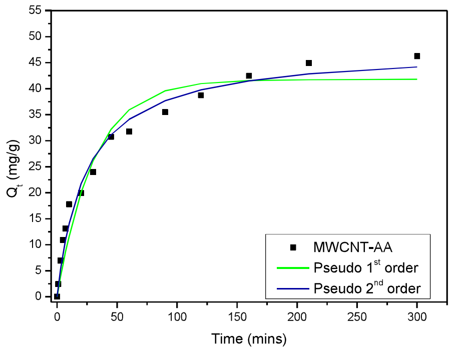

Figure 4.23 Kinetic model fitting for Hg^{2+} sorption by MWCNT-AA

The calculated kinetic parameters and correlation coefficients are given in **Table 4.22**. The pseudo second-order model (R^2=0.973) displayed superior fitness as compared to pseudo first order model. The pseudo second order model estimated the equilibrium capacity value of MWCNT-AA to be 45.05 mg/g, which lies closer to the experimentally observed value at the same initial metal ion concentration. Conformity of the pseudo second-order model clearly indicated chemical nature of interactions between the Hg (II) ions and the surface of MWCNT-AA, that is, ion exchange and surface complexation.

Table 4.22 Kinetic parameters for Hg^{2+} sorption by MWCNT-AA

Model	**Parameters Value**		**R^2**
Pseudo 1st order	q_e	39.33 mg/g	0.95293
	k_1	0.040 1/min	
Pseudo 2nd order	q_e	45.05 mg/g	0.97279
	k_2	1.12×10^{-3}g/mg min	

The intraparticle diffusion equation (**Table 2.6**) calculates the rate constant k_i and C, a constant related to the thickness of the boundary layer. If the plot of $q_t$vs $t^{1/2}$ (Weber-Morris plot) produces a straight line, then the entire adsorption process is governed solely by intraparticle diffusion. If multi-linear plots are obtained, then there are more steps governing the entire adsorption process.The Weber-Morris plot is shown in **Figure 4.24**. It is clear from the plot that mercury removal is a multi-step process involving adsorption to external surface and diffusion. The mechanism is assumed to have the following steps: (i) mass transfer of the adsorbent through the water film to the adsorbent surface. This step is referred to as film diffusion, (ii) pore diffusion of the adsorbate occurs, and (iii) occupation of a surface site on the adsorbent by physisorption or chemisorption and attainment of equilibrium.The slopes of each of the three parts give the rate of adsorption of that stage. The first stage can be seen to be the fastest, involving external diffusion to the surface of the adsorbent. The second stage involving pore diffusion is a relatively slower process of gradual adsorption. Due to the decrease in the number of Hg ions in the solution as well as active sites on the adsorbent surface, the third and final stage which shows the attainment of equilibrium is the slowest.

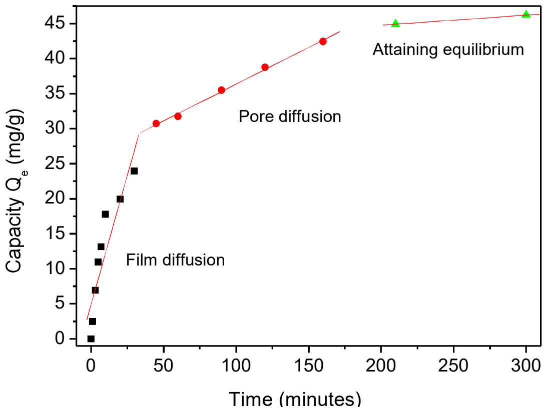

Figure 4.24 Intraparticle diffusion model for MWCNT-AA Kinetics

4.4.1.3 **Thermodynamics**

The effect of temperature on the adsorption of Hg(II) ions on MWCNT-AA has been shown in **Figure 4.25** where $\ln K_d$ is plotted against 1/T. The value of ΔH^o and ΔS^o were calculated using the slope and intercept of the linear plot as per the Van't Hoff equation (Equation 9). The evaluated thermodynamic parameters and the correlation coefficient calculated is shown in **Table 4.23** The positive value of ΔH^o revealed that the adsorption process is endothermic in nature. The value of ΔG^o lies between -17.325and -19.514kJ/mol for the temperature range 40^{o}C to 80^{o}C. A negative value of ΔG^o implies that the adsorption process is spontaneous. An increasing value of ΔG^o with increasing temperature means that adsorption of Hg ions on MWCNT-AA is more favourable at higher temperatures. The positive values of enthalpy change can be arisen due to the higher endothermicity of the dehydration step than exothermocity of the complexation process. The positive value of ΔS^o reflects the affinity of MWCNT-AA towards the Hg

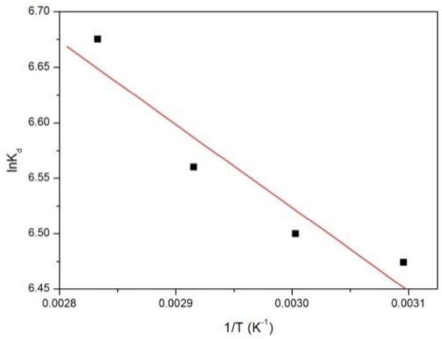

Figure 4.25 lnK_d vs 1/T plot for Hg^{2+} sorption by MWCNT-AA

ions present in the solution as well as an increase in the degree of freedom of the adsorbed species.It can be attributed to the release of water molecule produced by the interaction of Hg ions with functional groups and surface sites of MWCNT-AA.

Table 4.23 Thermodynamic parameters for Hg^{2+} sorption by MWCNT-AA

ΔH^0 (kJ/mol)	**ΔS^0 (kJ/mol.K)**	**Temperature (K)**	**ΔG^0 (kJ/mol)**	**R^2**
6.239	0.073	323	-17.32	0.9013
		333	-18.05	
		343	-18.78	
		353	-19.51	

4.4.1.4 Selectivity

Binary selectivity of Hg^{2+}over a number of other metal ions present in typical mercury plant waste water[330] was measured. **Figure 4.26** depicts the capacity for Hg^{2+} in comparison to other metal ions (Cd, Mg, Si, Na, Li, Na, Ca) by MWCNT-AA. MWCNT-AA was found to be highly selective for Hg(II) in all the pair studied. This may be due to strong soft acid (Hg^{2+})-soft base (amido group[331]) interaction, owing to the soft nature of Hg^{2+} ions compared to other metals. Except Cd^{2+}, all metal ions do not have significant adsorption in the binary solution with Hg^{2+} ions. About 23.09% of Cd was removed in comparison to 56.5% Hg by MWCNT-AA in the binary mixtures. The less selectivity of

Hg(II) with Cd may be attributed to the chemical similarity between Hg and Cd, as both are adjacent members in group 12 of the periodic table. Compared to other metal ions studied Hg^{2+} is ‘soft acid’ metal ions and amido group behaves like a soft base.

4.4.1.5 **Desorption and Regeneration**

EDTA was tested for desorption of Hg(II)-loaded MWCNT-AA due to the ability of EDTA to form strong complexes with Hg ions with very high stability constant (21.80). Desorption was then carried out by maintaining varying concentrations of EDTA and it was found that 0.01M EDTA solution is able to render 99% desorption in single cycle of desorption. The synthesized adsorbent was used in six successive adsorption-desorption cycles to check its feasibility for the use in scaled up applications. **Figure 4.27** shows variation in the equilibrium adsorption capacities with the number of adsorption-desorption cycles. It is evident that the MWCNT-AA can be used multiple times, as the adsorption capacity falls by just 2.92% even after sixth cycle compared to the initial cycle. An average of 99.7 % desorption is also attained in all the cycles. 0.05 M EDTA solution was used for desorption from the

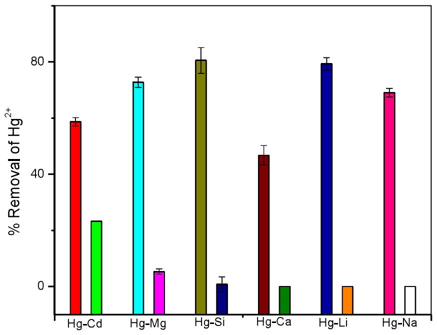

Figure 4.26 Binary selectivity of Hg^{2+} ions with other metal ions present in wastewater

mercury laden adsorbent in each cycle of operation. Higher and quicker desorption can also be attained by increasing the concentration of EDTA used, however, optimum amount is used to avoid particle destruction[6] and settling of the EDTA particles on the adsorbent leading to difficulties in separation of CNTs. Thus the investigated adsorbent can be reused many times after simple regeneration with EDTA treatment with little or no decrease in efficiency.

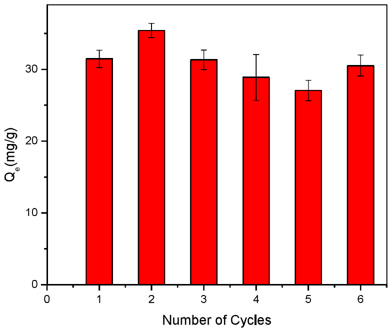

Figure 4.27 Regeneration of used MWCNT-AA up to six cycles

4.4.1.6 **Fixed bed column Studies**

The breakthrough curve obtained for the adsorption of Hg (II) on MWCNT-AA is shown in **Figure 2.22**. The flow rate of the 500 mg/L solution was kept constant at 0.7 mL/min by means of a peristaltic pump. 390 mL of the solution was made to flow through 0.3720 g of MWCNT-AA packed in the glass column. It can be seen from the breakthrough curve (**Figure 4.28(a)**) that breakthrough is achieved (C_o/C_i=0.05) when 22 mL of the solution is collected, or t_b is approximately 31.43 minutes. Similarly, exhaustion of the bed (C_o/C_i=0.95) occurs when 341 mL of the effluent has been collected. Thus t_e is approximately 487.14 minutes. No difference in Hg(II) concentration in the influent and effluent is attained once 390 mL solution is collected.

The total amount of Hg(II) ions adsorbed (Equation 2.9) by the fixed bed column is calculated by plotting the area under the curve of Co-Ci against volume collected, and its value is 37.7504 mg. The equilibrium capacity is thus obtained by Equation 2.10 as 101.48 mg/g. This value lies extremely close to the maximum capacity obtained by the Langmuir isotherm model which was calculated as 101.35 mg/g. The height of the mass transfer zone (h_z) comes out to be 4.68 cm by using Equation 2.12. The desorption curve is shown in **Figure 4.28**(b) and it is seen that 97.9 % desorption occurs after passing 50 mL of 0.05M EDTA solution. The calculation showed that 36.96mg of metal was successfully desorbed from the adsorbed 37.75mg of Hg(II). This reiterates the regeneration and multiple cycle use of the MWCNT-AA in the continuous mode of operation.

Figure 4.28 (a) Breakthrough and (b) desorption curve of the fixed-bed column study for the separation of Hg^{2+} ions by MWCNT-AA

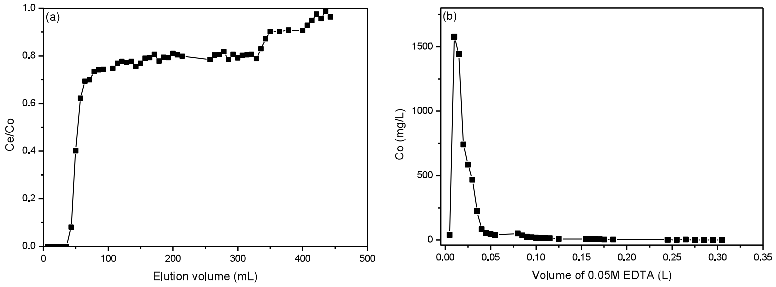

a b

The adsorption performance of MWCNT-AA was compared with activated carbon, strong cation exchange resin, MWCNTs, and MWCNT-COOH through batch method. MWCNT-AA showed the highest adsorption capacity for mercury ion removal from the above other adsorbents. As suggested by the batch studies, MWCNTs column would show lower Hg^{2+}

removal efficiency. A comparative column removal studies conducted between MWCNTs and MWCNT-AA, reiterate the better separation efficiency of functionalized CNTs column.

4.4.2 Computational Results

4.4.2.1 Computational Protocol

Similar computational methodology and level of DFT theory as in Section 4.2.2.1 were employed for structural optimization and energetics.

4.4.2.2 Interaction of Hg^{2+} ions with CNT-AA

Amidoamine group attached on the surface of the SWNT may covalently link with the sp^2 carbon atom located either on the sidewall or at the open end of the nanotube, as both position contain defects from which functionalization initiates.[332]Again, occurrence of sidewall functionalization should be compared to that on the open end owing to the very high aspect ratio and surface area of CNTs.[332] In view of this, structure of both, the amidoamine group attached on the sidewall and at the open end of SWNT, are optimized and shown in **Figure 4.29**. From the structures it can be seen that SWNT-AA may complex with Hg^{2+} ions through amine nitrogen and/or carbonyl oxygen donors. Hence two types of complexation have been looked at, (i) monodentate binding of only amine group with metal centre, and (ii) bidentate coordination from amidic carboxyl and amine. Thus **Figure 4.29** (a) and (b) show the complexation of Hg^{2+} ions with sidewall amidoamine of SWNT-AA through monodenate and bidentate mode of, respectively. Similarly **Figure4.29** (c) and (d) depicts the coordination of mercury ions with edge amidoamine of SWNT-AA through monodenate and bidentate mode of, respectively.

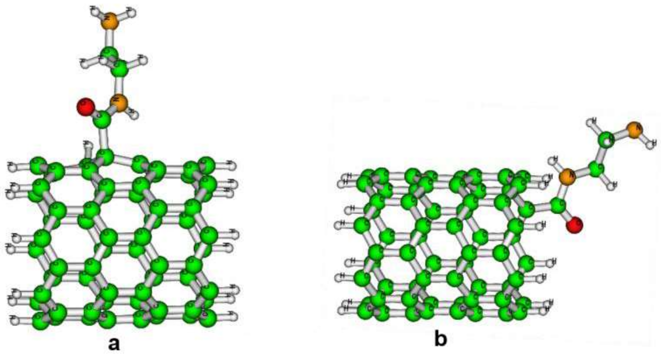

Figure 4.29 Optimized structures of SWNT-AA (a) sidewall, and (b) open end

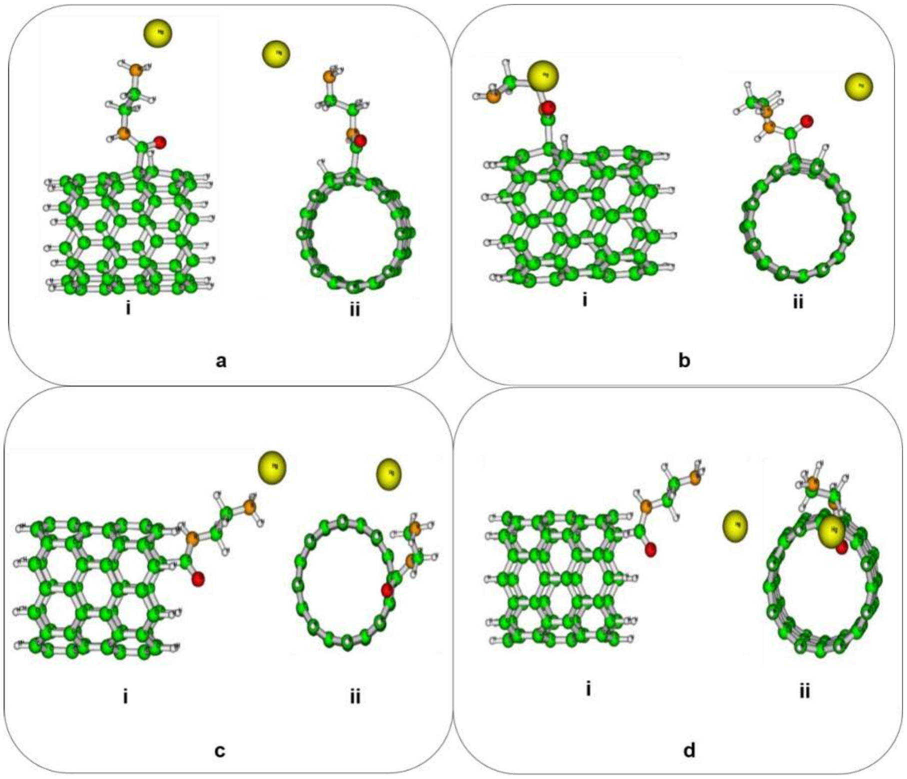

Figure 4.30 Optimized geometric structures of side-wall and open edged functionalized SWNT-AA bonded with Hg^{2+} ion; sidewall (a) mono, (b) bi-dentate mode on, and open edge (c) mono, (d) bi-dentate mode

Table 4.24 The characteristic bond distances in the optimized structures of Hg^{2+} complexed SWNT-AA

Structure	**Hg-O**	**Hg-N**	**C-N(NH_2)**	**C=O**
swmt-aa-sidewall			1.456	1.219
swnt-aa-sidewall-hg-monodent		3.671	1.443	1.217
swnt-aa-sidewall-hg-bident	3.792	6.159	1.460	1.21
swmt-aa-edge			1.454	1.230
swnt-aa-edge-hg-monodent		3.640	1.441	1.224
swnt-aa-edge-hg-bident	5.832	3.690	1.448	1.224

The characteristic bond distances are shown in **Table 4.24**. The C=O and C-N bond distances are nearly same whether the amidoamine unit is at sidewall or open edge. By analysing the distance from coordinating donor N and/or O atom to metal ion, it can be said that in mono-dentate mode of binding, the edge functionalized CNT has relatively stronger interaction with mercury ion compared to sidewall one, as former has lower Hg-N distance. In bi-dentate mode, the Hg-O bond length (3.792Å) is short and Hg-N bond (6.159Å) is long for sidewall interaction, whereas for edge side interaction the Hg-N bond length (3.690Å) is short and Hg-O bond (5.632Å) is long.

Thus in order to get the exact strength of complexation depending on location of the amidoamine on the CNT and its binding mode, the binding energy (ΔE) of the interaction of Hg^{2+} ion with SWNT-AA are calculated based on the complexation reaction (equation 4.8), using equation 4.9.

$$SWNT - AA + Hg^{2+} \rightarrow Hg - SWNT - AA \qquad (4.9)$$

$$\Delta E = E_{Hg-SWNT-AA} - (E_{SWNT-AA} + E_{Hg^{2+}}) \qquad (4.10)$$

Where E_x represents the energy of the 'x'. First, gas phase binding energy was calculated and then to get the more realistic energy values, aqueous phase interaction energy was calculated and shown in **Table 4.25**. The decrease in ΔE in aqueous phase, as compared to gaseous phase is due to the screening of aqua molecules on the complexation of mercury ions by the donor atoms of SWNT-AA.

Table 4.25 Interaction energy (kcal/mol) for the binding of Hg^{2+} ion with SWCNT-AA in various binding modes

Structure	ΔE_g	ΔE_{aq}
swnt-aa-sidewall-hg-monodent	-388.6	-199.1
swnt-aa-sidewall-hg-bident	-395.2	-200.4
swnt-aa-edge-hg-monodent	-381.9	-190.3
swnt-aa-edge-hg-bident	-381.8	-189.4

It is evident from the Table that interaction from sidewall is stronger than edge of the SWNT for both, mono-and bi-dentate mode of binding. Among four complexation environs, the sidewall bi-dentate binding is strongest. Although the stabilization energy of bi-dentate from mono-dentate is very small (<1kcal/mole), this was also reflected by the small change in bond length.

4.4.2.3 **Interaction of $HgCl_2$ Ions with CNT-AA**

.As the experimental extraction studies were carried out using $HgCl_2$ aqueous solution, it is imperative to study the effect of chloride ions on the interaction between MWCNT-AA and Hg^{2+}. The significance also originates from the fact that in aqueous solution, $HgCl_2$ exists exclusively (~99%) as $HgCl_2$ molecule. Thus, **Figure 4.31**(a) and (b) shows the complexation of $HgCl_2$ ions with sidewall amidoamine of SWNT-AA through monodenate and bidentate mode of, respectively. Similarly, **Figure 4.31** (c) and (d) depicts the coordination of mercury chloride with edge amidoamine of SWNT-AA through monodenate and bidentate mode, respectively. In all the optimized structures, the metal to donor bond lengths is below 3Å, which are the characteristic coordination bond lengths. **Table 4.26** shows these bond distances. Deviation in C-N, C=O and Hg-Cl bond in the complex structures from the native molecules reflects the coordination of the N/O donor with Hg centre of the $HgCl_2$ unit. **Table 4.26** reveals little stronger interaction for bi-denate coordination from open edged side ligands, as both Hg-O and Hg-N bond distances are smaller compared to sidewall interaction. Binding energy of the interaction between $HgCl_2$ and SWNT-AA in four possible modes is also calculated using equations similar to 4.8 and 4.9. The observed results are shown in **Table 4.27**. The bi-dentate mode of complexation from sidewall ligand are proven to be slightly (~1 kcal/mol in aqueous phase) more stable than other means of complexation.

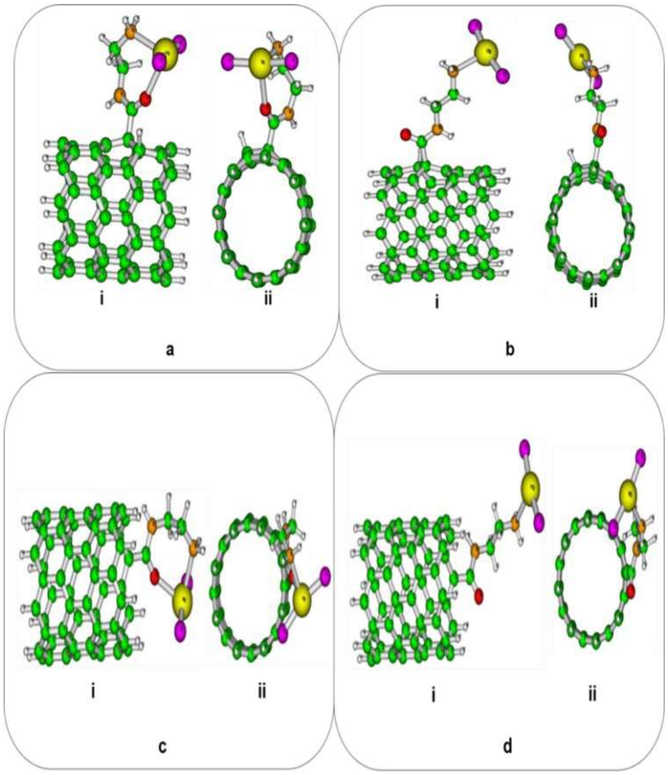

Figure 4.31 Optimized geometric structures of side-wall and open edged functionalized SWNT-AA bonded with $HgCl_2$ molecule; sidewall (a) mono, (b) bi-dentate mode on, and open edge (c) mono, (d) bi-dentate mode

Table 4.26 The characteristic bond distances Å of $HgCl_2$ complexed SWNT-AA

Structure	Hg-O	Hg-N	C-N(NH_2)	C=O	Hg-Cl
$HgCl_2$					2.322, 2.322
swnt-aa-sidewall-hgcl2-monodent		2.681	1.465	1.217	2.360, 2.350
swnt-aa-sidewall-hgcl2-bident	2.708	2.687	1.468	1.225	2.387, 2.363
swnt-aa-edge-hgcl2-monodent		2.640	1.469	1.229	2.356, 2.354
swnt-aa-edge-hgcl2-bident	2.601	2.668	1.467	1.241	2.392, 2.379

Table 4.27 Interaction energy (kcal/mol) of $HgCl_2$ ion with SWCNT-AA in various binding modes

Structure	ΔE_g	ΔE_{aq}
swnt-aa-sidewall-hgcl2-monodent	-12.1	-9.0
swnt-aa-sidewall-hgcl2-bident	-15.0	-9.7
swnt-aa-edge-hgcl2-monodent	-10.3	-8.2
swnt-aa-edge-hgcl2-bident	-11.4	-7.6

4.4.2.4 Hg^{2+} Selectivity of CNT-AA

The binding energy (BE) for the reactions between other metal ions and SWNT-AA were also calculated and showed in **Table 4.28**. Bi-dentate complexation of CNT-AA from edge side was considered for all the metal ions studied as it showed the strongest interaction. It can be easily concluded that MWNT-AA is extremely selective for Hg(II) as the system has the lowest binding energy (-381.9 kcal/mol) in comparison to any other metal ion studied both in gas and aqueous phase. As observed via experimental results, the binding energy of Cd is close to that of Hg,which is due to the structural similarity between Cd and Hg. Thus preferential selectivity of metal ions by SWNT-AA shows the following trend by calculation, $Hg^{2+} > Cd^{2+} > Mg^{2+} > Ca^{2+} > Li^{+} > Na^{+} > K^{+}$.

Table 4.28 Calculated values of binding energy (kcal/mol) for reaction of Hg^{2+} and metal ions with SWCNT-AA

Metal ion	ΔE_g	ΔE_{aq}	Metal ion	ΔE_g	ΔE_{aq}
Hg	-381.9	-190.3	Na	-67.0	-10.6
Cd	-312.6	-114.9	K	-46.2	-4.87
Mg	-290.1	-37.2	Li	-94.2	-24.7
Ca	-214.4	-51.4			

4.5 Sorption behavior of Pu^{4+} on CNT-PAMAM[174]

Dendrimer is repetitively branched molecules and is typically symmetric around the core, and may have three-dimensional morphology[333-336]. PAMAM, is the most well known dendrimer. Lower generations can be thought of as flexible molecules (1st and 2nd) with no appreciable inner regions, while medium-sized (3rd and 4th) do have internal space that is essentially separated from the outer shell of the dendrimer. Very large (7th or greater) dendrimers can be thought of more like solid particles with very dense surfaces due to the structure of their outer shell.

In this present investigation the lower generation PAMAM functionalized carbon nanotube was used for efficient and selective separation of Pu^{4+}. This study also includes understanding the sorption mechanism through different isotherm, kinetics through different model, radiolytic stability of the dendrimer, and stripping characteristics.

4.5.1 Experimental Study

4.5.1.1 Effect of feed acidity on the K_d value

The extraction efficiency is a function of the aqueous feed acidity [317], therefore, extraction profiles for Pu^{4+} were established at various aqueous feed acidity using MWCNT-$PAMAM_{G1}$ and MWCNT-$PAMAM_{G2}$. K_d values for Pu^{4+} on both materials were found to increase with increase in feed acidity upto3 M HNO_3, followed by a plateau [**Figure 4.32**]. The initial increase in K_d values for Pu^{4+}can be in accordance with the law of mass action due to the participation of NO_3^- anion on complexation. With increase in feed acidity, the enhancement in the availability of the H^+ would lead to the competition of H^+ with Pu^{4+} resulting plateau. The sorption efficiency of Pu^{4+} was found to be more for MWCNT-$PAMAM_{G2}$ compared to that of MWCNT-$PAMAM_{G1}$ might be due to the availability of more functional group in the former for the interaction with the Pu^{4+} ion.

$$Pu_{aq}^{4+} + PAMAM_{Gn} + 4NO_{3\ aq}^{-} = Pu(NO_3)_4 . PAMAM_{Gn} \qquad (4.11)$$

$$H_{aq}^{+} + PAMAM_{Gn} + NO_{3\ aq}^{-} = HNO_3 . PAMAM_{Gn} \qquad (4.12)$$

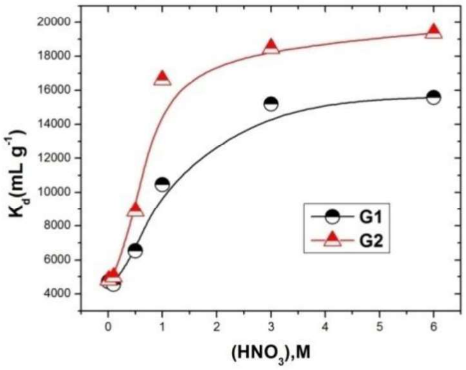

Figure 4.32 The variation of K_d values of Pu^{4+} as a function of aqueous feed acidity

4.5.1.2 **Sorption isotherm**

To have insight into the sorption process it is useful to analyze experimental data into different sorption models. In view of this, four most popularly used isotherm models, Langmuir, D–R and Tempkin isotherms were employed[260, 337-339] . The equilibrium data were fitted with linear plots of the respective isotherm models an shown in **Figure 4.33**. Characteristic parameters of each model were evaluated from these plots and depicted in **Table 4.29**. The Langmuir adsorption capacity of MWCNT-PAMAM$_{G2}$ (92.48 mg g^{-1}) was found higher than that of MWCNT-PAMAM$_{G1}$ (89.22 mg g^{-1}). These capacity values are well above the efficiency of activate carbon (12 mg g^{-1}) and nanocast mesoporous carbon (58 mg g^{-1}). The sorption energy values follow the sametrend.The linear regression coefficients for langmuir isotherm were found to be 0.99998 and 0.99999 for Pu^{4+} on MWCNT-PAMAM$_{G1}$ and MWCNT-PAMAM$_{G1}$, respectively. The sorption energy values evaluated from D-R isotherm fitting for MWCNT-PAMAM$_{G1}$ and MWCNT-PAMAM$_{G2}$ were found to be 10.07 and 16.95 kJmol^{-1}, respectively, showing the chemical interaction between amidoamine group and Pu^{4+} i.e. the sorption preceded via chemi-sorption. Moreover, this interaction was found to be greater in case of second generation dendrimer compared to the first generation dendrimer might be due to the presence of more ligating sites. The linear regression coefficients for this model were found be 0.99013 and 0.98945, respectively for 1st and 2nd generation of dendrimers. These linear regression coefficient values were inferior compared to the Langmuir model. The maximum sorption capacities for these dendrimers from two generation were found to be similar and follow similar trend as that of Langmuir isotherm.

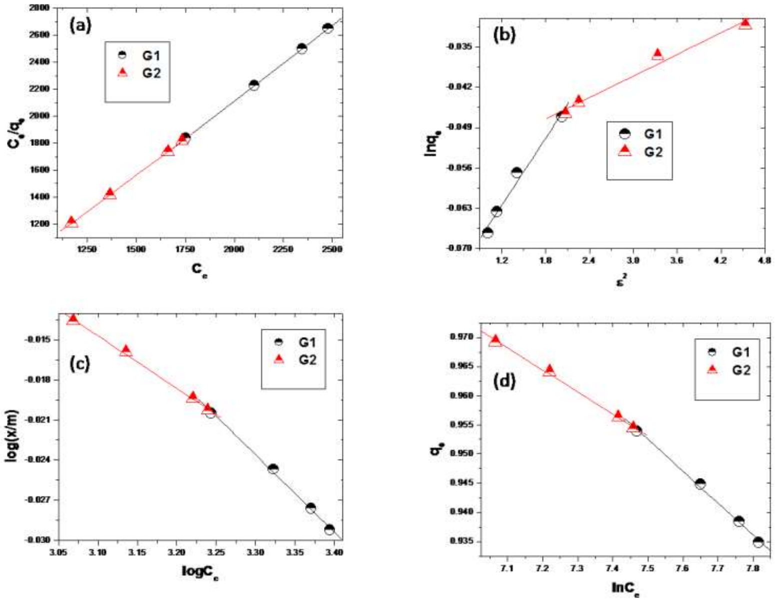

Figure 4.33 (a) Langmuir, (b) D–R,(c) Freundlich and (d) empkin isotherms for Pu^{4+}on MWCNT-$PAMAM_{G1}$(G1) and MWCNT-$PAMAM_{G2}$(G2).

Table 4.29 Different constants obtained from Langmuir, D.R., Freundlich and Tempkinisothem.

	Langmuir isotherm		
	q_e(mgg^{-1})	b(Lmol^{-1})	χ^2
$PAMAM_{G1}$	89.22	0.008	0.99998
$PAMAM_{G2}$	92.48	0.018	0.99999
	Dubinin-Radushkevich isotherm		
	X_m(mgg^{-1})	E(KJmol^{-1})	χ^2
$PAMAM_{G1}$	91.77	10.07	0.99013
$PAMAM_{G2}$	94.29	16.95	0.98945
	Freundlich isotherm		
	K_f(mgg^{-1})	n	χ^2
$PAMAM_{G1}$	87.08	17.26	0.99875
$PAMAM_{G2}$	96.22	25.45	0.99882
	Temkin isotherm		
	A_T(Lmg^{-1})	b	χ^2
$PAMAM_{G1}$	94.50	45.57	0.99888
$PAMAM_{G2}$	96.11	66.01	0.99890

The 1/n value of Freundlich isotherm model below one indicates a chemi-sorption, normal sorption while above one indicates cooperative adsorption. Sorption becomes more heterogeneous as 1/n value gets closer to zero. If n = 1 then the partition between the two phases are independent of the concentration[338].The sorption of Pu^{4+} on MWCNT-$PAMAM_{G1}$ and MWCNT-$PAMAM_{G2}$ followed chemi-sorption, normal sorption since 'n' value for MWCNT-$PAMAM_{G1}$ and MWCNT-$PAMAM_{G2}$ were found above unity i.e., 17.26and 25.45, respectively. Similar conclusion was also drawn from the energetic of D–R isotherm analysis. The k_f value for MWCNT-$PAMAM_{G1}$ and MWCNT-$PAMAM_{G2}$ were 87.08 mg g^{-1} and 96.22mg g^{-1} respectively.

Based on the linear regression analysis, the sorption process was found to follow Langmuir isotherm, i.e. through mono layer, without interaction of the neighbouring sorbent sites and considering all the binding sites are equivalent

4.5.1.3 **Kinetics study**

A plot of 1-F as the function of time (**Figure 4.34**) revealed that with increase in time the 1-F values decreased drastically upto120 min followed by gradual decrease. This study primarily revealed that, 180 minutes is essential for attaining the equilibrium (as there is only marginal change in 1-F values beyond 180 min).

To get into the detailed of sorption kinetics, the experimental data were fitted on different models: Lagergren first order, intra particle diffusion model and finally pseudo second-order model. The fitted plots are shown in **Figure 4.34** and evaluated kinetic parameters are shown in **Table 4.30**. The pseudo second order model found to be best suited a can been seen the regression constant value . The 2nd order rate constant for MWCNT-

PAMAM$_{G2}$ was found to be almost 1.2 times of that for MWCNT-PAMAM$_{G1}$. **A** pseudo second order reaction is a chemical reaction between two reactants, and is thus a third order reaction, which appears to be a second order reaction because one of the reactants Pu^{4+} is in such small quantity (tracer level less than μM) that it is not easily noticed.The other explanation of pseudo 2nd order kinetics in sorption process is that the rate-limiting step may be chemical sorption or chemisorption involving valency forces through sharing or exchange of electrons between sorbent and sorbate[194].

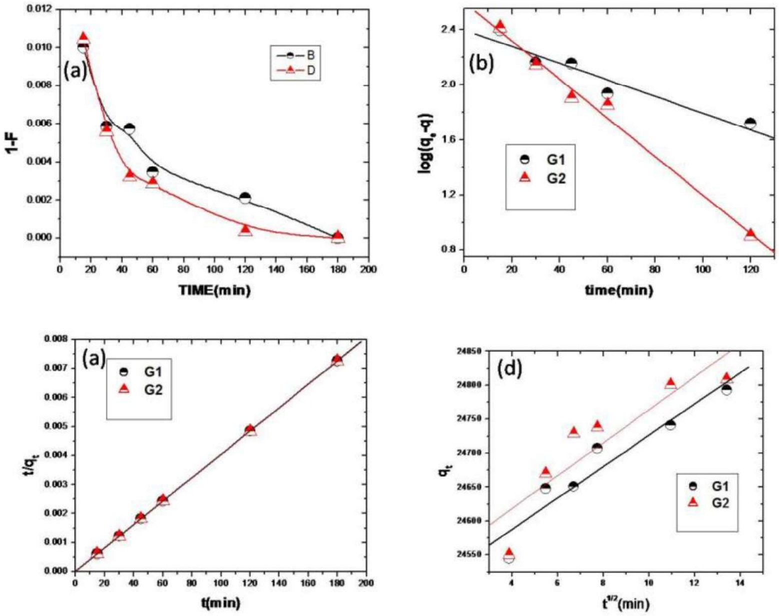

Figure 4.34 Sorption kinetics fitted plots of Pu^{4+}on PAMAM$_{G1}$ (G1), PAMAM$_{G2}$ (G2): (a) 1-F vs Time, (b) Lagergren first order, (b) pseudo second-order model, and (d) intra particle diffusion model

Table 4.30 Sorption kinetic model parameter for Pu^{4+} on $PAMAM_{G1,G2}$

Lagergren first order kinetics			
	q_e	k_{ads}	χ^2
$PAMAM_{G1}$	250.351	0.013	0.95469
$PAMAM_{G2}$	396.85	0.032	0.99423
Intra particle diffusion model			
	k_p(mg g^{-1} min^{-1})	C	χ^2
$PAMAM_{G1}$	23.11	24.49	0.95131
$PAMAM_{G2}$	24.26	24.52	0.89756
Pseudo second order			
	Q_e(mg g^{-1})	k_2(mg g^{-1} min^{-1})	χ^2
$PAMAM_{G1}$	248.13	0.00016	1
$PAMAM_{G2}$	248.37	0.00020	1

4.5.1.4 **Radiolytic stability**

Since in this present investigation, we are looking for highly efficient sorbent material for Pu^{4+}, it is imperative that the sorbent will be exposed to different kind of high energy particles like α, β and high energy radiation like γ. As a matter of fact, they will certainly deposit appreciable amount of energy to the sorbent material. This may lead to

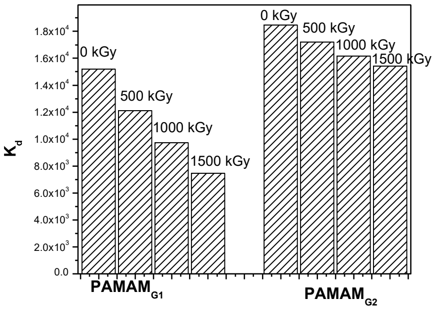

Figure 4.35 The radiolytic stability for $PAMAM_{G1}$ and $PAMAM_{G2}$

deformation or degradation of the sorbent functionality responsible for interaction with the metal ion and ultimately, this will lead to degradation of the performance[254, 317]. In view of this, both the 1st and 2nd generation dendrimers are exposed to sufficient amount of gamma dose and degradation of their performance was monitored.

It was observed that on 500 kGy gamma exposure, the $K_d$values became 79 % and 93 % of its original value for 1st and 2nd generation dendrimer, respectively where as the 1000 kGy gamma expossure made it 64 % and 87 % respectively. After a large dose of 1500 kGy, they became 52 % and 83 %, respectively. This study revealed that upto 500 kGy, dendrimer of both the generation is highly radiolytically stable. The overall radiolytic stability for 2ndgeneration was found to be more than that of 1st generation. The radiolytic stability of these sorbent is pictorially presented in **Figure 4.35**.

4.5.1.5 **Back extraction of Pu^{4+} from PAMAM-MWCNT**

During the processing of the radiotoxic metal, it is no advisable to keep the metal ion on the sorbent for long time. This will not only reduce the performance of the sorbent due to constant contact dose but also make the situation complicated to recover the Pu for its further application. In view of this, several stripping agents were investigated to demonstrate process for complete back extraction of Pu^{4+} from these sorbent materials. Out of all 0.01 M oxalic acid, 0.01 M Na_2CO_3 and 0.01 M EDTA showed appreciable back extraction i..e. more than 50 % stripping All these stripping solutions were made by dissolving required amount of Na_2CO_3, oxalic acid and EDTA in quartz doubly distilled water (based on their concentration).For both the sorbent materials, 0.01 M oxalic acid was found to be the most successful for almost ~ 95 % and 97 % stripping of plutonium from 1st and 2nd generation dendrimer, respectively. On the other hand EDTA was able to strip 56 % and 65 % adsorbed Pu^{4+} whereas 0.01 M Na_2CO_3 could manage 72 % and 88 %, for 1st and 2nd generation dendrimer, respectively.

4.6 Sorption of Am^{3+} on CNT-PAMAM[175]

4.6.1 Experimental Study

4.6.1.1 Effect of feed acidity on the K_d value

The extraction efficiency is a function of the aqueous feed acidity[340], therefore, extraction profiles for Am^{3+} were established at various aqueous feed acidity using MWCNT-$PAMAM_{G1}$ and MWCNT-$PAMAM_{G2}$. The K_d values for Am^{3+} on both materials were found to increase initially with increase in feed acidity upto 0.5 M HNO_3, followed by a gradual decrease **(Figure 4.36)**. The K_d values for Am^{3+} were found to be higher for second generation dendrimer as compared to the first generation throughout the acidity range observed in the present case. The initial increase in Kd values with aqueous feed acidity might be due to the participation of NO_3^- anion on complexation. But with increase in aqueous feed acidity, due to the availability of large amount of H^+ ion, it competes with the Am^{3+} resulting decrease in K_d values.

$$Am^{3+}_{aq} + PAMAM_{Gn} + 3NO_3^-{}_{aq} = Am(NO_3)_3\,.PAMAM_{Gn} \qquad (4.13$$

$$H^{+}_{aq} + PAMAM_{Gn} + NO_3^-{}_{aq} = HNO_3\,.PAMAM_{Gn} \qquad (4.14)$$

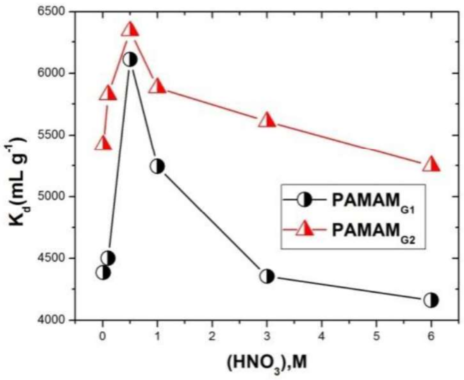

Figure 4.36 The variation of K_d values of Am^{3+} as a function of aqueous feed acidity

4.6.1.2 **Sorption isotherm**

To have insight into the sorption process it is useful to analyze experimental data into different sorption models. In view of this, four most popularly used isotherm models, Langmuir, Freundlich, D–R and Tempkin isotherms were employed. From the linear fitted plots, isotherm parameters involving in each models are calculate and shown **Table 4.31.** Langmuir model is proved to be most suited as suggested by linear regression coefficient value. The Langmuir sorption capacity of MWCNT-PAMAM$_{G2}$ (97.62 mg g^{-1}) was found higher than that of MWCNT-PAMAM$_{G1}$ (82.59 mg g^{-1}). The D-R model evaluated sorption energy values for MWCNT-PAMAM$_{G1}$ and MWCNT-PAMAM$_{G2}$ were found to be 27.38 and 50.49 kJ mol^{-1}, respectively, showing the chemical interaction between amidoamine group and Am^{3+}. Moreover, this interaction was found to be greater in case of second generation dendrimer compared to the first generation dendrimer might be due to the presence of more ligating sites. Similar observation was also noticed in case of $K_d$values for Am^{3+}. The n of Freundlich model indicate the strength of sorption. The sorption of Am^{3+} on MWCNT-PAMAM$_{G1}$ and MWCNT-PAMAM$_{G2}$ followed chemi-sorption, normal sorption since 'n' value for MWCNT-PAMAM$_{G1}$ and MWCNT-PAMAM$_{G2}$ were found above unity i.e., 10.04 and 15.09, respectively.

Table 4.31 Different constants obtained from Langmuir, D.R., Freundlich and Tempkin isothem

Langmuir isotherm			
	q_m(mg. g^{-1})	b(L.mg^{-1})	χ^2
PAMAM$_{G1}$	82.59	8.40	0.99998
PAMAM$_{G2}$	97.62	3.54	0.99994
Dubinin-Radushkevich isotherm			
	X_m(mg.g^{-1})	E(kJ mol^{-1})	χ^2
PAMAM$_{G1}$	86.48	27.37	0.99339
PAMAM$_{G2}$	95.73	50.49	0.97992
Freundlich isotherm			
	K_f(mg. g^{-1})	n	χ^2
PAMAM$_{G1}$	101.5	10.04	0.99924
PAMAM$_{G2}$	92.5	15.09	0.99698
Tempkin isotherm			
	A_T(Lmg^{-1})	b	χ^2
PAMAM$_{G1}$	14.82	28.44	0.99937
PAMAM$_{G2}$	13.89	63.41	0.99737

4.6.1.3 **Kinetics study**

A plot of 1-F as the function of time revealed that with increase in time the 1-F values decreased drastically upto 60 min followed by gradual decrease. This study primarily revealed that, 60 minutes is essential for attaining the equilibrium. To get into the detailed of sorption kinetics, the experimental data were fitted on different models (Lagergren first order, intra particle diffusion model and finally pseudo second-order) and calculated parameters are shown in **Table 4.32**. Best fitting has come from pseudo second order model as suggested by regression coefficient value. The pseudo second order rate constant for MWCNT-PAMAM$_{G1}$ was found to be almost 1.6 times of that for MWCNT-PAMAM$_{G2}$.

Table 4.32 Sorption kinetics of Am^{3+} on $PAMAM_{G1}$, $PAMAM_{G1}$

Lagergren first order kinetics

Metal ion	q_e(mg. g^{-1})	k_{ads}(min^{-1})	χ^2
$PAMAM_{G1}$	114.24	0.034	0.9271
$PAMAM_{G2}$	200.78	0.041	0.9967

Intra particle diffusion model

Metal ion	k_p(mg g^{-1} min^{-1})	C	χ^2
$PAMAM_{G1}$	2.44	145.02	0.9211
$PAMAM_{G2}$	4.66	144.06	0.8413

Pseudo second order kinetics

Metal ion	q_e(mg g^{-1})	k_2 (mg g^{-1} min^{-1})	χ^2
$PAMAM_{G1}$	1.46E+02	8.61E-05	1.001
$PAMAM_{G2}$	1.45E+02	5.38E-05	0.99999

4.6.1.4 **Radiolytic stability of $MWCNT\text{-}PAMAM_{G1,G2}$**

To observe the radiolytic stability, the MWCNT-PAMAM was exposed to different amount of gamma irradiation. With the irradiated dendrimer materials the K_d values for Am^{3+} were calculated and compared with un-irradiated MWCNT-PAMAM. With increasing gamma dose the K_d values were found to decrease for Am^{3+}. On 500 kGy exposure, the K_d values for 1st and 2nd generation became 3.5×10^3 and 4.5×10^3, respectively (which were originally ~ 4.3×10^3 and 5.6×10^3). On 1000 kGy exposure they became ~ 2.7×10^3 and 3.5×10^3. Though a considerable decrease in sorption efficiencies were observed for 1000 kGy of gamma exposure, till the K_d values are very high for efficient sorption of Am^{3+}. Moreover, the radiolytic stability study also revealed that upto 500 kGy, these materials were found to behave satisfactorily.

4.6.1.5 **Stripping of metal ion**

Back extraction of metal from aqueous solution of sorbent is of equal importance during processing of radio toxic materials. Out of several stripping agents, EDTA, Na_2CO_3 and oxalic acid were found to show considerable back extraction of Am^{3+} from the dendrimer of 1st and 2nd generations. **Figure 4.37** summarizes the % stripping data for these aqueous complexing agents. The % stripping for Am^{3+} was found to be ~ 95% when 0.05 M EDTA was used as a stripping agent for MWCNT-PAMAM$_{G1}$ whereas ~ 85% when 0.05 M oxalic acid was used. But only less than 80% back extraction of Am^{3+} was found to be possible using 0.05 M Na_2CO_3 solution. Similarly in MWCNT-PAMAM$_{G2}$, EDTA, Na_2CO_3 and oxalic acid of same concentration were found to back extract ~ 90%, 70 % and 82%, respectively. This study revealed that 0.05 M EDTA was the best strippant among these three.

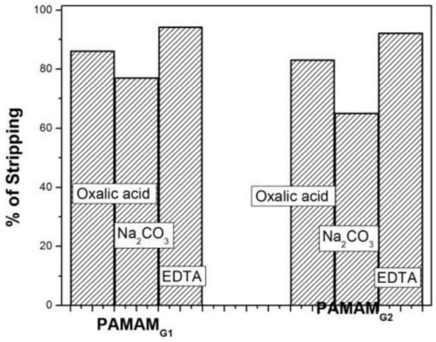

Figure 4.37 Stripping of Am^{3+} from G1 and G2-MWCNT-PAMAM

4.6.1.6 Selectivity of MWCNT-PAMAM$_{G1,G2}$

Finally both the dendrimers were applied for the processing of SHLW solution of FBR origin. The waste solution was chosen in the context of generation of minor actinides like Am^{3+} from plutonium bearing nuclear fuel. After processing the SHLW solution was fed into plasma for direct analysis by ICP-AES. The analytical results were summarized in **Table 4.33**. This study revealed that dendrimer of both the generations was highly selective for the separation of Am^{3+}.

Table 4.33 The processingof SHLW of FBR origin on G1, G2- MWCNT-PAMAM

Metal	**Analytical line (nm), ICP-OES**	**Initial (mg L^{-1})**	**PAMAM$_{G1}$ Final (mg L^{-1})**	**K$_d$**	**PAMAM$_{G2}$ Final (mg L^{-1})**	**K$_d$**
Al	396.152	-	-	-		
Ag	243.779	5	3.159	2.91E-01	3.647	1.85E-01
Ba	455.404	70	9.278	3.27E+00	5.983	5.35E+00
Ca	396.847	-	-	-		
Cd	361.051	5	3.95	1.33E-01	4.62	4.11E-02
Cr	283.563	-	-	-	-	-
Fe	244.451	-	-	-	-	-
Mg	280.27	-	-	-	-	-
Mn	257.611	-	-	-	-	-
Na	588.995	-	-	-	-	-
Ni	227.021	-	-	-	-	-
Sr	407.771	30	2.804	4.85E+00	1.84	7.65E+00
Ce	413.38	200	26.411	3.29E+00	16.546	5.54E+00
La	379.478	75	14.28	2.13E+00	9.212	3.57E+00
Pr	414.311	50	3.766	6.14E+00	2.338	1.02E+01
Nd	401.225	30	22.308	1.72E-01	26.294	7.05E-02
Sm	359.26	50	9.563	2.11E+00	1.314	1.85E+01
Zr	339.198	15	2.797	2.18E+00	1.742	3.81E+00
Ru	245.644	10	7.019	2.12E-01	5.398	4.26E-01
Mo	281.615	1.5	1.15	1.52E-01	0.89	3.43E-01
Gd	335.047	5	1.623	1.04E+00	1.118	1.74E+00
Dy	353.17	5	0.517	4.34E+00	0.434	5.26E+00
Eu	381.967	5	2.17	6.52E-01	1.34	1.37E+00

4.6.2 Computational Protocol

The optimized geometry, total energy and vibrational IR frequency of trivalent Eu and Am complexes with CNT-PAMAM were computed using the method given in Sec. 3.1.1.1.

4.6.2.1 **Computational Result**

The minimum energy structures of free CNT-PAMAM$_{G1}$ and CNT-PAMAM$_{G2}$ are displayed in **Figure4.38**, whereas the complexes are shown in **Figure4.39**. The calculated structural parameters for the complexes are presented in **Table. 4.34**. The average M-O and M-N bond distances of Eu complex with CNT-PAMAM-$_{G1}$ were found to be slightly shorter than that of corresponding Am-O and Am-N bond distances. Similar trend was also observed with the complexes with CNT-PAMAM-$_{G2}$. For G2, two type of stoichiometry was assumed for metal-ligand (M:L) complexation: 1:1 and 2:1. Further, the complexation ability of the PAMAM functionalized CNT was evaluated by computing the free energy of complexation in aqueous solution and the results are presented in **Table. 4.35**.

From the calculated value of ΔG, the selectivity of Am^{3+} and Eu^{3+} ions for CNT-PAMAM-$_{G1}$ was found to be almost identical. The extraction ability of CNT-PAMAM-$_{G2}$ was higher over CNT-PAMAM-$_{G1}$ for both Am^{3+} and Eu^{3+} ions as expected because with increasing generation the donor numbers also increases.

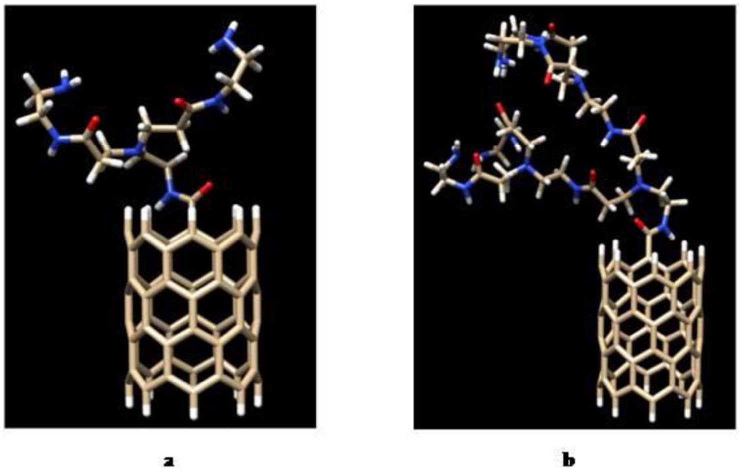

Figure 4.38 Optimized structures of free (a) CNT-PAMAM$_{G1}$ and (b)CNT-PAMAM$_{G2}$

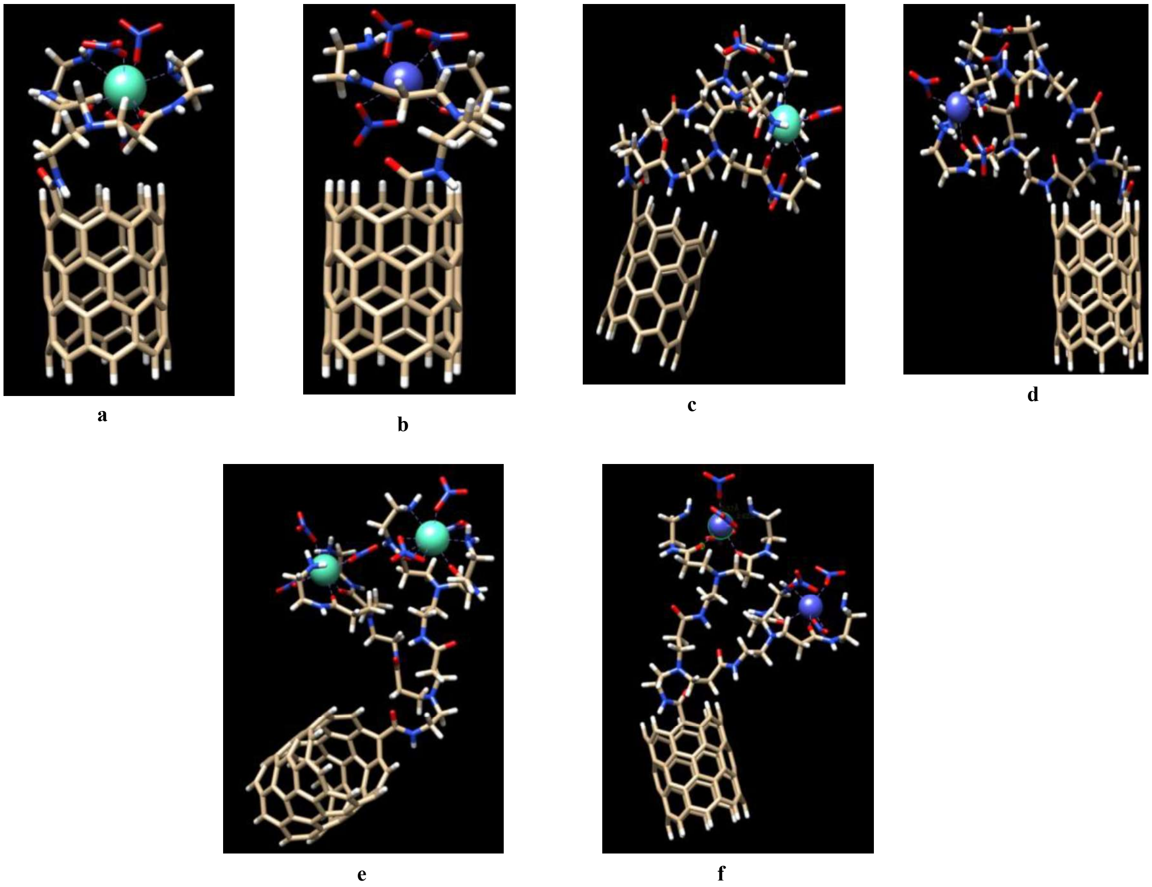

Figure 4.39 Optimized structures of complexes of ions: (a) CNT-PAMAM$_{G1}$ -Eu(NO$_3$)$_3$ (b) CNT-PAMAM$_{G1}$ -Am(NO$_3$)$_3$ (c) CNT-PAMAM$_{G2}$ -Eu(NO$_3$)$_3$ (d) CNT-PAMAM$_{G2}$ -Am(NO$_3$)$_3$ (e) CNT-PAMAM$_{G2}$ -(Eu(NO$_3$)$_3$)$_2$ and (f) CNT-PAMAM$_{G2}$ -(Am(NO$_3$)$_3$)$_2$

Table 4.34 Calculated various structural parameters (Å)

System	Bond distances (Å)		
	N_{NH2}-M	$O_{C=O}$-M	O_{NO3}-M
CNT-PAMAM-$_{G1}$-Eu$(NO_3)_3$	2.64, 2.65	2.38, 2.44	2.30, 2.35, 2.48, 3.00
CNT-PAMAM-$_{G1}$-Am$(NO_3)_3$	2.65, 2.64	2.46, 2.40	2.35,2.38, 2.55, 2.52
CNT-PAMAM-$_{G2}$-[Eu$(NO_3)_3]_2$	2.59	2.42	2.32
CNT-PAMAM-$_{G2}$-[Am$(NO_3)_3]_2$	2.62	2.45	2.37

The selectivity of Am^{3+} is high compared to Eu^{3+} for G2. The probable metal-ligand stoichiometry was also predicted using the calculated value of ΔG. The value of ΔG for G2 was found to be smaller than G1 when 1:1 M:L stoichiometry was taken into consideration. But, from experimental results, it was observed that the distribution constant for G2 was higher than that of G1. The correct trend of enhanced complexation was recovered when 2:1 M:L stoichiometry was considered.

Table 4.35 Calculated values of free energy of complexation, ΔG (kcal/mol).

System	ΔG (kcal/mol)
CNT-PAMAM-$_{G1}$-Eu$(NO_3)_3$	-74.4
CNT-PAMAM-$_{G1}$-Am$(NO_3)_3$	-74.4
CNT-PAMAM-$_{G2}$-Eu$(NO_3)_3$	-61.5
CNT-PAMAM-$_{G2}$-Am$(NO_3)_3$	-60.2
CNT-PAMAM-$_{G2}$-[Eu$(NO_3)_3]_2$	-133.7
CNT-PAMAM-$_{G2}$-[Am$(NO_3)_3]_2$	-135.7

4.7 Sorption Np(V) on CNT-PAMAM[176]

^{237}Np is an important alpha emitting long-lived radionuclide (Q_a = 4.959 MeV, $T_{1/2}$ = 2.14 9 10_6 years), which can be a serious threat to the environment and requires proper mitigation steps in case of nuclear fallouts. Although, the biological effects of neptunium in human beings have not been investigated well but studies on animals have shown that $_{237}$Np exposure can induce cancers of bone, lung, and liver [341]. Neptunium has five oxidation states (+3, + 4, + 5, + 6, and + 7) and out of which only +5 is predominant and stable. Np(V) has a unique chemistry and because of its low chemical potential, its complexation and separation is difficult and requires special measures. Our recent publication on the sorption of pentavalent and hexavalent neptunium onto amide functionalized MWCNTs have shown promising results[342] and from that, it seems plausible to use functionalized MWCNTs for the separation/preconcentration of neptunium from nuclear waste solutions.

Dendrimer functionalized MWCNTs has been synthesized in order to enhance the surface property and thus to increase the sorption efficacy[174, 175] . We have used 1st and 2nd enerations of PAMAM dendrimer functionalized MWCNTs for the sorption of plutonium[174] and americium[175] as discussed in above sections. In this study, sorption of pentavalent neptunium onto these two PAMAM dendrimer functionalized MWCNTs, i.e., MWCNT–PAMAM$_{G1}$ and MWCNT–PAMAM$_{G2}$ will be discussed.

4.7.1 Experimental Study

4.7.1.1 **Effect of feed acidity on the K_d value**

The sorption profiles of Np(V) onto MWCNT–PAMAM$_{G1}$ and MWCNT–PAMAM$_{G2}$ were established by plotting the K_d values as a function of HNO_3 concentration in the aqueous phase. The K_d values for Np(V) on both the sorbents were found to increase with an increase in the feed acidity (**Figure 4.40**). The acidity constant (pKa) of the interior tertiary amine group of PAMAM dendrimer is ~6.0 whereas for the terminal primary amines it is ~ 9.0[343] . Even at the lowest concentration of HNO_3 in the study (0.01 M or pH 2), all the amine groups are expected to remain protonated and thus the amide carbonyl groups will serve the purpose of ligating sites. The sorption performance is expected to decrease with the increase in HNO_3 concentration due to the competitive nature of H^+ ions for the binding sites (Equation 4.13). On the other hand, the participation of nitrate ion in the complexation of metal ions increases the sorption performance which is a direct consequence of the law of mass action (Equation 4.12). A very similar trend has been reported for the sorption of Np(V) and Np(VI) onto amidoamine functionalized MWCNT (MWCNT–AA)[172] and also for the sorption of Pu^{4+} onto MWCNT–$PAMAM_{Gn}$ [174]. The computational calculation, done for the sorption of Np(V) ion onto amidoamine functionalized MWCNT (MWCNT–AA) resulted in a hexa-coordinated structure for Np(V) ion where two nitrate ions were found to coordinate with neptunium[172]. Glycerol modified binary layered double hydroxide nanocomposites were synthesized for effective removal of uranium[344] . Extended X-ray absorption fine structure technique was used for understanding the complexation and the experimental data were supported by the density functional theory calculation. The competitive interaction of UO_2^{2+} and Sr^{2+} on graphene oxides was also reported in the literature using EXAFS analysis supported by DFT calculations[345]. The adsorption and desorption of UO_2^{2+} on functionalized graphene oxides were reported by batch experiments, EXAFS technique, and theoretical calculations in understanding the mode of coordination[346]. In the present case, an increase in the K_d values with an increase in HNO_3 concentration was due to the participation of nitrate ions in the complexation process. As the concentration of HNO_3 increased in the aqueous medium, more number of nitrate ions were available for the evident for the graph that though the increase in HNO_3 concentration was many folds, the complexation of neptunium ion which was marked by a gradual rise in the K_d values.

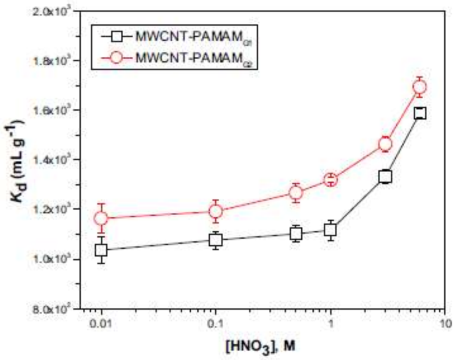

Figure 4.40 Distribution coefficient (K_d) values of Np(V) as a function of aqueous feed acidity

It is also increase in K_d values was significantly low. This behavior is a direct consequence of the competitive nature of H_3O^+ ions for the binding sites which increased with the increasing feed acidity.Also, the sorption capacity of MWCNT–PAMAM$_{G2}$ was found higher than that of MWCNT–PAMAM$_{G1}$ which might be due to more number of ligating sites on the surface of MWCNT–PAMAM$_{G2}$ compared to that on MWCNT–PAMAM$_{G1}$.

4.7.1.2 **Sorption kinetics**

Plot of 1-F as the function of time and kinetic data fitted with three model (Lagergren first order, intra particle diffusion model and finally pseudo second-order) are shown in **Figure 4.41.** First plot revealed that in the case of sorption of Np(V) ion onto MWCNT–PAMAM$_{G1}$, the equilibrium was attained in 2 h of contact time whereas for MWCNT–PAMAM$_{G2}$, the sorption process did not reach the equilibrium point even after 3 h of contact time. This might be due to more number of ligating sites on the that with increase in time the 1-F values decreased drastically upto 60 min followed by gradual decrease. From the next three fitted curves it is clear that pseudo second order kinetic model simulate the experimental data in best manner. The most plausible explanation behind the trend followed in kinetics is the chemical interaction between a sorbate and a sorbent which is the rate-limiting step and governs the whole sorption process.

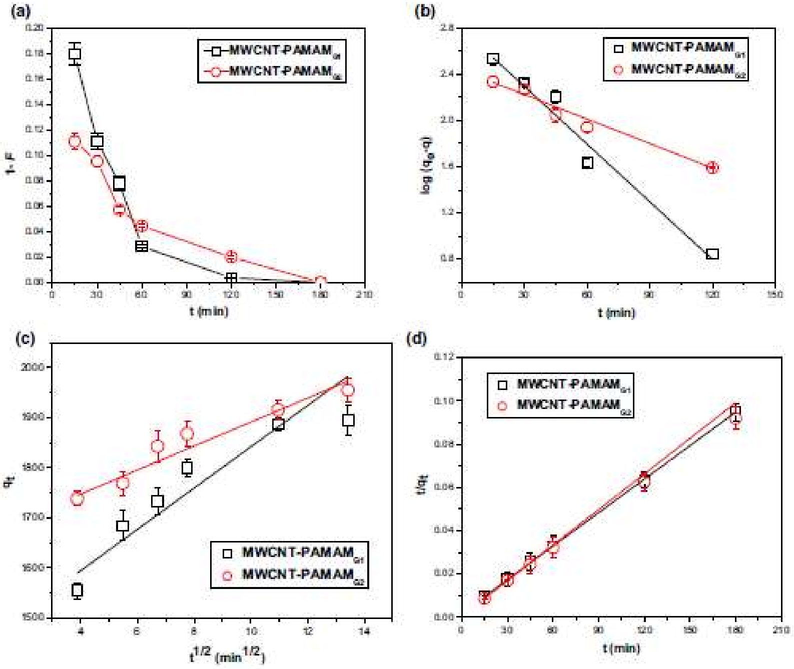

Figure 4.41 Sorption kinetic plots of Np(V) onto MWCNT–PAMAM$_{G1}$ and MWCNT–PAMAM$_{G2}$: (a)plot of 1-F vs t; (b) Lagergren's first order kinetic model; (c) Intra particle diffusion model; (d) Pseudo second order kinetic model

4.7.1.3 **Sorption isotherm**

The equilibrium data for the Np(V) sorption by MWCNT–PAMAM$_{G1}$ and MWCNT–PAMAM$_{G2}$ were simulated with four known isotherm model as Section 4.6.1.2. The Langmuir model was fitted most suitably. The maximum monolayer sorption capacity (q_m) of MWCNT–PAMAM$_{G1}$ and MWCNT–PAMAM$_{G2}$ for Np(V) ions evaluated using Langmuir isotherm model was found to be 56.06 and 58.81mgg-1, respectively. Since the sorption occured by chemical interaction between Np(V) and amidoamine functionality on the surface of MWCNT–PAMAM$_{Gn}$, it can be assumed that the surface of sorbent in the present study is homogeneous and thus the sorption process can be best explained by Langmuir isotherm. Even the linear regression values in the case of Langmuir isotherm model compared to that in Freundlich isotherm model were closer to unity. In most of the literature dealing with the sorption of actinide ions onto the surface of functionalized MWCNT, the sorption process is found to follow Langmuir isotherm model[347].

4.7.1.4 **Back-extraction study**

Back extraction studies were performed using 0.5 M oxalic acid and 0.5 M Na_2CO_3 solution as stripping agents. Oxalic acid was able to strip 90–92% of Np(V) ions sorbed onto MWCNT–PAMAM$_{Gn}$. Although the stripping efficiency of the Na_2CO_3 solution was found lower than that of the oxalic acid (>95%) but as high as 82–87% of sorbed Np(V) was recovered from loaded MWCNT–PAMAM$_{Gn}$.

4.7.2 Computational Protocol

Similar computational methodology and level of DFT theory as in Section 4.6.2.1 were employed.

4.7.2.1 **Computational Results**

The minimum energy structures of complexes of NpO_2^+ and NpO_2^{+2} ions with CNT-PAMAM$_{G1}$ and CNT-PAMAM$_{G2}$ are displayed in **Figure4.42**. The Np to donar atom distances in both of the complexes are shown in **Table 4.36**. The average M-N$_{(Amine)}$ bond distances of Np complex (both in pentavalent and hexavalent state) with CNT-PAMAM-$_{G2}$ were found to be slightly shorter than that with CNT-PAMAM-$_{G2}$, whereas the M-O$_{(Nitrate)}$ distances of G2 has little higher values than the G1. This is a reflective of strong coordination of Np metal ion with G2 donar atoms which are more in number than in G1.

The weakening of the M-O$_{(\text{Nitrate})}$ bond for G2 is indicative of the superior complexation by dendrimer ligands compared to nitrate anions. The M-O$_{(\text{Carbonyl})}$ distance for Np(V) has also strong for G2 compared to G1, but the non-participation of carbonyl oxygen in case of Np(VI) complex needs further investigation.

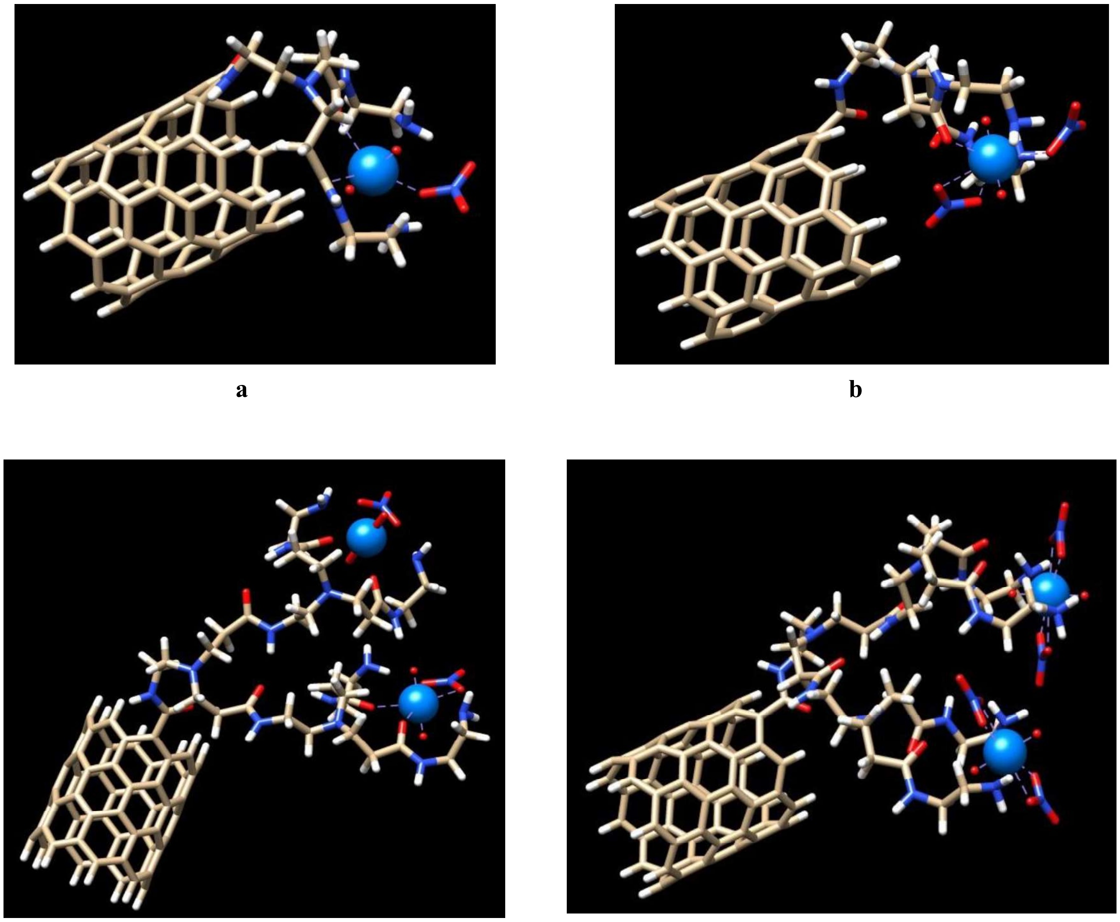

a

b

c

d

Figure 4.42 Optimized structures of complexes of ions: (a) CNT-PAMAM$_{G1}$ -NpO$_2$(NO$_3$) (b) CNT-PAMAM$_{G1}$ - NpO$_2$(NO$_3$)$_2$ (c) CNT-PAMAM$_{G2}$ -(NpO$_2$(NO$_3$))$_2$ and (f) CNT-PAMAM$_{G2}$ -(NpO$_2$(NO$_3$)$_2$)$_2$

Further, the complexation ability of the PAMAM functionalized CNT was evaluated by computing the free energy of complexation in aqueous solution and the results are presented in **Table. 4.37**.

Table 4.36 Calculated various structural parameters (Å)

System	Bond distances (Å)		
	N_{NH2}-M	**$O_{C=O}$-M**	**O_{NO3}-M**
CNT-PAMAM-$_{G1}$-$NpO_2(NO_3)$	2.700, 2.689	2.515, 2.545	2.411
CNT-PAMAM-$_{G1}$-$NpO_2(NO_3)_2$	2.676, 2.915	2.424	2.332, 2.500, 2.547
CNT-PAMAM-$_{G2}$-[$NpO_2(NO_3)$]2	2.659, 2.747, 2.759	2.449, 2.500, 2.656, 2.713	2.525, 2.517, 2.632, 2.646
CNT-PAMAM-$_{G2}$-[$NpO_2(NO_3)_2$]2	2.595, 2.656, 2.590, 2.633		2.480, 2.471, 2.520, 2.530, 2.467, 2.474, 2.505, 2.530

Table 4.37 Calculated values of free energy of complexation, ΔG (kcal/mol)

System	ΔG (kcal/mol)
CNT-PAMAM-$_{G1}$-$NpO_2(NO_3)$	-64.0
CNT-PAMAM-$_{G1}$-$NpO_2(NO_3)_2$	-80.3
CNT-PAMAM-$_{G2}$-[$NpO_2(NO_3)$]2	-97.1
CNT-PAMAM-$_{G2}$-[$NpO_2(NO_3)_2$]2	-169.1

From the calculated value of ΔG, the selectivity of NpO_2^{+2} ion over NpO_2^{+} and was found to be higher for both CNT-PAMAM-$_{G1}$ and CNT-PAMAM-$_{G2}$. The extraction ability of CNT-PAMAM-$_{G2}$ was higher over CNT-PAMAM-$_{G1}$ for both NpO_2^{+} and NpO_2^{+2} ions as observed in the experiments.

4.8 Hg(II) adsorption with MWCNT-PAMAM upto generation 5

Gradual increase of adsorption of Hg(II) was observed with increase in the PAMAM dendrimer generation from 1 to 5 in MWCNT-PAMAM (**Figure 4.43**). Number of binding sites situated in the internal cavity and on the external peripheral of 3D structure of PAMAM increases with increase in generation. This results in more strong complexation of Hg(II) ions in the in higher generation of MWCNT-PAMAM molecular surface.

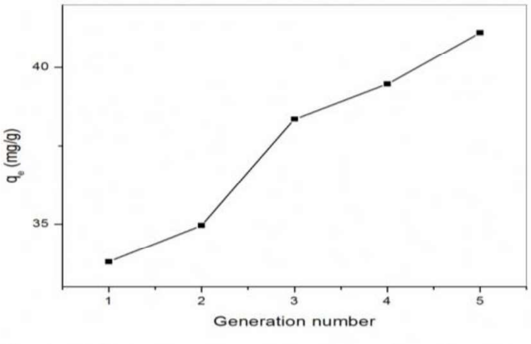

Figure 4.43 Adsorption capacity of MWCNT-PAMAM for Hg (II) uptake up to generation 5.0

4.9 Conclusion

In conclusion, a novel amido-amine functionalized MWCNT was synthesized and showed excellent sorption for the radionuclides ^{233}U and ^{241}Am. The MWCNT-AA showed high sorption capacity for ^{233}U and ^{241}Am. DFT studies proved the experimental observation of higher sorption capacity of ^{233}U compared to ^{241}Am due to stronger complexation strength of U-MWCNT-AA over Am-MWCNT-AA and higher negative solvation energy of U(VI) compared to Am(III).

MWCNT-AA is demonstrated as highly selective and efficient sorbent for tetra and hexavalent plutonium. Different isotherm analysis revealed that, Langmuir isotherm is predominantly operative through mono layer without mutual interaction of the neghbouring complexation sites. The sorption was also found to be chemi-sorption. Based on linear regression analysis the sorption process was found to proceed via pseudo second order reaction. The sorbent was also found to show high radiolytic stability even upto a gamma exposure of 1500 kGy. Density functional theory reveals that MWCNT-AA and all the nitrate anions are coordinated to Pu metal centre in bidentate mode for both Pu^{4+} and PuO_2^{2+} complexes. The present calculated free energy of complexation from DFT is shown to be almost three times higher for Pu^{4+} than PuO_2^{2+} both in gas and aqueous phase. The theoretical results confirm that MWCNT-AA binds Pu^{4+} strongly than PuO_2^{2+}which is also corroborated from the sorption experiment.

MWCNT-AAwas found to be highly efficient sorbent for penta and hexavalent Np and also having high radiolytic stability. The sorption process was found to be chemisorption following Langmuir isotherm.The sorption capacities for NpO_2^{+} and NpO_2^{2+} was evaluated as 58.1 and 83.9 mg g^{-1}, respectively. Thepseudo second order reaction was found to be operative. The quantitative back extraction of penta and hexavalent neptunium was found to be achieved by EDTA and Na_2CO_3, respectively.

Adsorptive removal behaviour of Hg^{2+} ions fromaqueous solution by indigenously prepared functionalized CNTs, MWCNT-AA, were performed. Adsorption process was found to follow pseudo second order kinetic equation and Redlich-Peterson isotherm model, revealing chemical nature of the sorption of mercury ions on the MWCNT-AA surface.The maximum sorption capacity of 101.35 mg/g at pH 6 and room temperature was observed which is higher than conventional absorbents (activated carbon/resin) and pristine MWCNTs. Adsorption was found to be an endothermic and spontaneous process. The adsorbent showed superior selectivity towards Hg(II) ions, as compared with other metal ions generally present in mercury containing industrial waste water. Six adsorption-desorption cycles were successfully carried out without significant loss of uptake using 0.05M EDTA as stripping agent. DFT theoretical calculation showed that sidewall aminoamine functionalization and its bi-dentate complexation with mercuryis more favorable. Binding energy calculation for the selectivity of Hg^{2+} ions with other metal ions fall in congruence with the experimentally observed data. Results demonstrate the possibility of using MWCNT-AA as a material for removal of mercury ions through continuous flow separation in a fixed bed column.

A comparative study was carried out to understand the sorption of Pu4+ on MWCNT-$PAMAM_{G1}$ and MWCNT-$PAMAM_{G2}$. The sorption efficiency was found to increase with increase in aqueous feed acidity followed by plateau for both the sorbent, but the efficiency for 2nd generation dendrimer was found to be more. Based on the linear regression analyses of Langmuir, D-R, Fruendlich and Tempkin isotherms, the Pu^{4+} was found to follow Langmuir isotherm by interaction of the amidoamine functionality with the Pu^{4+} ion. To attain optimum $K_d$values, 180 min was found to be sufficient. The sorption of Pu^{4+} proceeded via pseudo 2ndorder kinetics with the rate constants, 0.00016 and 0.00020 mg g^{-1} min^{-1}, respectively. Both the sorbent showed high radiolytic stability upto 500 kGy while the 2nd generation dendrimer showed better stability compared to the other. More than 95 % Pu^{4+} was found to be back extracted from the sorbent by using 0.01 M oxalic acid. The overall evaluation indicated the potential application of these dendrimer functionalized carbon nano tubes for efficient separation of Pu^{4+} from aqueous acidic waste stream. This 1st and 2nd generation dendrimer was found have more more sorption efficiency for Pu^{4+} compared to other carbonnano tube based sorbents, alumina, silica gel, hydrous titanium oxide, Taunit TOPO, Taunit TBP and Taunit DMDOHEMA[254, 258, 348, 349] . Alumina, silica gel and hydrous titanium oxide showed K_d values for Pu^{4+} as 7.00E+03, 1.00E+03 and 1.00E+04, respectively from 0.1 M Na_2CO_3 medium where as their total evaluation as sorbent i.e. selectivity, stripping and radiolytic stability has not yet been demonstrated. They also showed very slow kinetics. Almost 5 hours were required to establish complete equilibrium. On the other hand multiwalled carbon nanotube without any functionalization showed a K_d value of 2.44 E+03 from pH 6 , 0.1 M $NaClO_4$ medium, which is also not preferred condition for processing high level waste solution whose feed acidity is generally 3 M HNO_3. In our previous investigation amide functionalized multiwalled carbon nano tube showed excellent sorption behaviour with K_d value 1.2 E+04, while the present investigation revealed that even in 1st generation of dendrimer, the Kd value enhanced to 1.5 E+04 which was found to increase further to 1.9 E+04 for the 2nd generation with retaining better radiolytic stability, selectivity and stripping behaviour.

1st and 2nd generation of PAMAM functionalized carbon nano tubes were synthesized and characterized through FTIR spectroscopy and elemental analysis. These materials were found to be highly efficient and selective for Am^{3+} and the efficiency enhances with higher generation. The sorption process followed Langmuir isotherm and pseudo second order rate kinetics. The sorption process was found to follow through chemical interaction of amidoamine group with the Am^{3+} ion. The luminescence investigation revealed that the metal ion complex of 1st generation dendrimer was more asymmetric compared to the higher generation. In both the case there was no water molecule in the primary coordination sphere of the metal ion. The J.O. parameter analysis revealed that the covalency between metal ion and the donor atom was found to be more for lower generation dendrimer. Different photo-physical properties like transition probabilities, radiative and non-radiative life times, branching ratio values, quantum efficiency were evaluated for both the complexes of MWCNT-$PAMAM_{G1}$ and MWCNT-$PAMAM_{G2.}$ EDTA was found to be successful for the effective stripping of the Am^{3+} from the loaded sorbent materials while these materials were found to be radiolytically stable upto 500 kGy.

Poly(amidoamine) dendrimer functionalized multiwalled carbon nanotubes were taken as a solid phase sorbent for the sorption of pentavalent neptunium from aqueous acidic solution. An increase in the feed acidity favored the sorption of Np(V) ions onto MWCNT–$PAMAM_{Gn}$ which was primarily due to the participation of nitrate ion in the complexation process. A thorough investigation of sorption kinetic data revealed that the sorption process followed pseudo second order kinetics with $1.4x10^{-4}$ and $6.84x10^{-4}$ g mg^{-1} min^{-1} as rate constants for MWCNT–$PAMAM_{G1}$ and MWCNT–$PAMAM_{G2}$, respectively. The energy values calculated through D–R isotherm showed that the sorption process proceeded via chemical interaction between Np(V) ions and the functionality on the surface of nanotubes. The experimental data fitted well to Langmuir isotherm model showing that the sorption is monolayer on a homogeneous sorbent surface. A small decrease in the sorption performance (~2%) was recorded for irradiated MWCNT–PAMAM^{G2} whereas for MWCNT–PAMAM$_{G1}$, it was more than 17%, making these two sorbents viable for nuclear waste management. Among the two strippant solutions used, 0.5M oxalic acid was found most suitable for the back-extraction of the sorbed Np(V) ion. From this study, it can be concluded that poly(amidoamine) dendrimer functionalized MWCNTs can be used for the preconcentration of neptunium ions from nuclear waste solutions. Gradual increase of adsorption of Hg(II) was observed with increase in the PAMAM dendrimer generation from 1 to 5 in MWCNT-PAMAM owing to the increase in coordination sites in higher generation dendrimer moiety on the CNT structure.

5 Chapter 5: Sulphur Ligand Functionalized Carbon Nanotubes

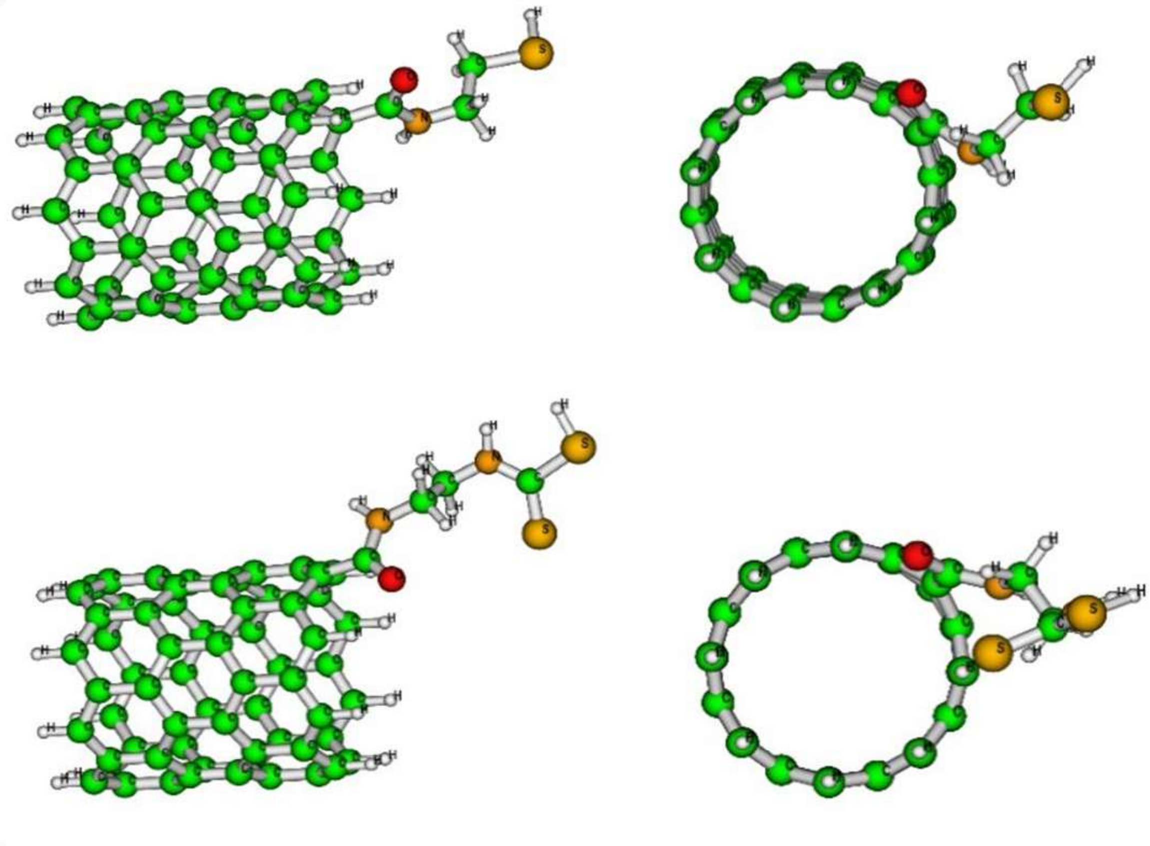

5.1 Introduction

Water crisis is one of the greatest challenges faced today by many parts of the world. There is lack of fresh and clean water which needs to be dealt with. Meanwhile, rapid industrialization has exacerbated the problem, as it is accompanied with a large number of toxic heavy metals having been discharged into the environment in industrial waste water over the past few years [350]. Mercury (Hg) is one such heavy metal, for which the recent estimations suggest global anthropogenic releases to be 1000 tonnes a year[27] . It has been categorized as a "priority hazard substance" by the Agency for Toxic Substances and Disease Registry (ATSDR) because of its toxicity, mobility and a long residence time in the atmosphere[351] . It impairs neurological development and pulmonary function, causes blindness, paralysis, and can even cause breakage of chromosomes[352-354] . Mercury also leads to maladjustment in hormone secretion of organisms [355]. Not only is it non-biodegradable, but it exists in a number of forms in an aqueous environment. The most common species is Hg^{2+}, which readily binds to organic and inorganic matter, thereby posing a threat to aquatic life while also rendering the water unfit for public use [350 353] It also tends to bio-accumulate in the food chain thereby posing a potential risk to human health[356]. Despite being excessively toxic in nature, mercury is used in various industrial processes and eventually the mercury enters the wastewater directly or leach into water from disposal sites[357] . The tolerance limit of mercury in drinking water is 0.001 mg/L and the CPCB, India guided discharge limit of mercury in industrial waste water is 0.01 mg/L [319]. Thus, in order to minimize its grave impacts, wastewater containing mercury needs to be treated before being discharged into the receiving environment.

Over the years, nanomaterials based adsorbents, which are now termed as 'new generation adsorbents', for water treatment has aroused great interest due to their unique properties like are small size, catalytic potential, high reactivity, large surface area, ease of separation, and large number of active sites for interaction with different contaminants[120].Amongst several nanomaterials, Carbon nanotubes (CNTs) have received considerable attention because of their potential to act as extremely successful adsorbents against chemical as well as biological contaminants[321]. Their applications for removal of toxic pollutants from gaseous as well as aqueous streams has been extensively studied due to its porous and hollow structure, large surface area, light mass density, higher thermal, chemical, mechanical and radiation stability. [358] .

Despite their many desirable properties, the hydrophobicity and chemical inertness of CNTs frequently hinders their commercial utilization. To overcome these limitations, CNT surfaces are often tailored using either covalent or non-covalent modification strategies. Covalent surface modification involves the direct incorporation of new elements (e.g., oxygen, fluorine, nitrogen) or organic functionalities (e.g., biomolecules) into the CNT sidewalls. The surface properties of CNTs (e.g., dispersion) can also be changed without modifying their intrinsic structure by non-covalent surface modification strategies that include the adsorption of surfactants, polymers, or biological macromolecules[359]. Chemical covalent functionalization route offers better control on the modification of the surface functionality[360] . Several organic functional groups have been attached on the walls of the CNTs and used for adsorption of metal ions[361].

Mercury, a soft B-group metal, exhibits relatively weak interactions with oxygen containing ligands, moderate strength interactions with nitrogen-containing ligands, and strong interactions with sulfur-containing ligands. Two S-containing functional groups thiol (SH) and dithiocarbamate (DTC) are important in this regards. Covalent linking of –SH on SWCNT[362] and SiO_2 coated Fe_3O_4 nanoparticles[327] and their use in the removal of mercury were investigated. Again attachment of –DTC on MWCNT[363] and graphene oxide[364] were performed and studied for removal of heavy metals (Cd^{2+}, Cu^{2+}, Zn^{2+} and Pb^{2+}). In this chapter, -SH and –DTC functionalized MWCNTs were prepared by following reported synthetic methods[173, 327, 362-364] with little modifications. Further, DFT has been used to study the structure, energetic and thermodynamics of the molecular system presented here. Thus the main objective of this study is to recognize the mercury adsorption characteristics of MWCNT-SH and MWCNT-DTC through comparative experimental investigations and theoretical calculations.

5.2 CNT-SH and CNT-DTC for Hg(II) adsorption

5.2.1 Experimental Study

5.2.1.1 **Effect of pH**

The effect of pH on the adsorption of Hg(II) by MWCNT-SH and MWCNT-DTC are shown in **Figure 5.1.** Hg^{2+} adsorption capacity increases from pH 1 to pH 5, and then either decreases again or remains nearly constant up to pH 8. At pH 4 to 6, Hg(II) ions exist as Hg^{2+} and $HgCl^{+}$ species in water solution. The thiol [365] and dithiocarbamate (-NHCS2H) functional group of MWCNT-SH and MWCNT-DTC would adsorb Hg(II) by forming stable MWCNT-S-Hg-S-MWCNT/MWCNT-S-HgCl and MWCNT-DTC-

Hg/MWCNT-DTC-Hg-DTC-MWCNT/MWCNT-DTC-HgCl complexes, respectively. Since thiol [365] and dithiocarbamate (-NHCS$_2$H) are weak acid chelate group and have great affinity for H$^+$ [356, 366], at low pH (<4) value, the stability of the complexes reduces and the competitive interaction between metal ions and protons with active sites increased, leads to very less adsorption. At high pH (pH>7), precipitation of Hg(II) hydroxide occurs simultaneously with Hg(II) ions[353, 354] . Thus, the optimum pH of the feed metal ion solution used for further studies was decided to be 6, to have maximum adsorption and to avoid hydroxide precipitation.

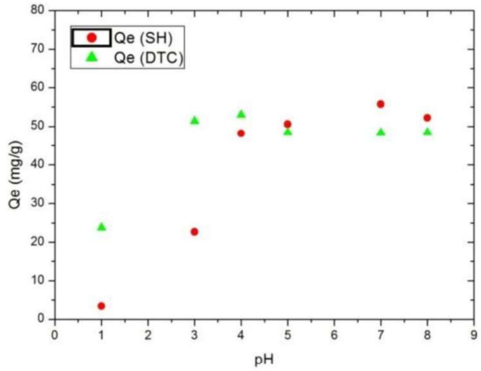

Figure 5.1 Equilibrium capacities of MWCNT-DTC and MWCNT-SH at varying pH

5.2.1.2 Effect of Initial Concentration and Adsorption Isotherms

The effect of initial concentration of Hg^{2+} on its removal by synthesized materials was examined at pH 6 and RT. The experimental results are shown in **Figure 5.2**. It was observed that the amount of Hg^{2+} adsorbed increased as the initial concentration increased from 10 to 600 mg/L. This is because in batch adsorption, the initial concentration of adsorbate is attributed as a driving force to overcome the mass transfer resistance between the aqueous and the solid phases. The increase of initial Hg^{2+} concentration also enhanced the interaction between the adsorbate and the adsorbents, and the data revealed the existence of finite heavy metal binding site on the adsorbents. However, the extent of this adsorption capacity was not proportional to the further increase of the initialHg^{2+} concentration because of the limited sites available for the uptake of cationic Hg^{2+} ions. Both the adsorbents showed saturated behavior when the initial concentration was more than 400 mg/L.

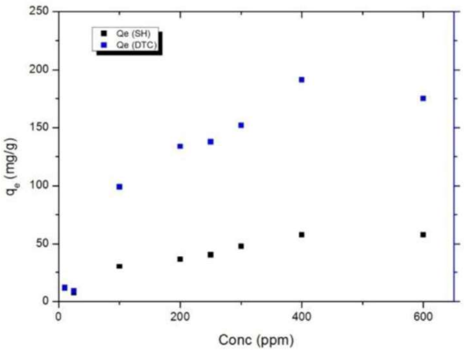

Figure 5.2 Effect of initial feed concentration for the adsorption of Hg(II) by MWCNT-SH and MWCNT-DTC

The adsorption capacity for MWCNT-DTC is higher than that of MWCNT-SH in all feed concentration. This can be attributed from the structure of the adsorbent as shown in **Figure 5.3**. MWCNT-SH has three donor sites (one >C=O, one -NH, and one –SH), whereas MWCNT-DTC has five (one >C=O, two -NH, and two –SH). The adsorption capacity of the functionalized adsorbents is governed by the extent of functionalization and number of donor sites for binding the adsorbate species. The extent of functionalization in the solid phase organic synthesis normally taken as the amount of –COOH linker attached to the MWCNT surface in the oxidation step, and in the proceeding steps MWCNT-COOH are allowed to react with the excess reagents for longer time. Thus extent of functionalization can be assumed to be same for MWCNT-SH and MWCNT-DTC. The number of donor sites present in the functional group would directly determines the relative adsorption capacity of the two MWCNT derivatives. Thus formation of stronger chelating complex is easier for MWCNT-DTC than MWCNT-SH.

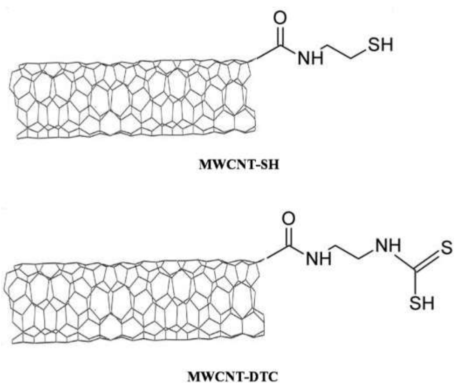

Figure 5.3 Structure of of MWCNT-SH and MWCNT-DTC

The isotherm modeling of the above equilibrium data were carried by using the linearized plots of four models as express in equation 2-5. The Langmuir plots of both the materials are shown in **Figure 5.4** and the parameters calculated from the fittings of models are shown in **Table 5.1**. The values of experimental adsorption capacity are also shown in the Table. By comparing the correlation coefficient (R^2) values and the closeness between the experimental (q_{exp}) and calculated (Q_m) maximum adsorption capacity, for both of the adsorbents, it is evident that he equilibrium isotherm data has good fit with Langmuir model which assumes monolayer sorption of Hg^{2+}ions onto the surface of the sorbent with a finite number of identical sites and without interaction between the adsorbed molecules[196]. The values of Langmuir constants, K_L(L/mg) and Freundlich constant (K_F) which is the related to the sorption capacity and the sorption free energy is consequently higher for MWCNT-DTC than MWCNT-SH. The slope (1/n) of the Freundlich curve for both of the materials is less than unity suggests chemical adsorption process[196]. The higher values of 1/n for MWCNT-DTC are indicative of higher adsorption intensity arising from the stronger adsorbate-adsorbent complex formation [367].

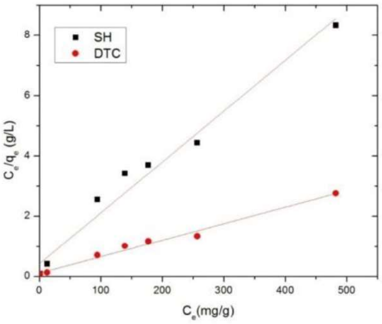

Figure 5.4 Linearized Langmuir Adsorption Isotherm Fitting of equilibrium data for Hg(II) adsorption by CNT-DTC and CNT-SH

Table 5.1 Calculated parameters of the isotherm modeling studies

Isotherm Model	**Parameter**	**CNT-DTC**	**CNT-SH**
	q_{exp}(mg/g)	191.52	57.87
Langmuir	q_m (mg/g)	212.76	61.35
	K_L (L/mg)	0.025	0.023
	R^2	0.97	0.97
Freundlich	1/n	0.44	0.28
	K_F	14.18	10.45
	R^2	0.92	0.98

5.2.1.3 Effect of Contact Time and Adsorption Kinetics

The Typical kinetic experimental curves (**Figure 5.5**) for adsorption of Hg^{2+} on the functionalized MWCNTs showed that adsorption increases sharply during a short contact time (15 mins) and slows down gradually to reach equilibrium. In order to describe the kinetics for Hg^{2+} ion adsorption onto the MWCNTs, the pseudo-first-order and pseudo-second-order kinetics are applied. The fitting of the kinetic data with pseudo-second-order model is shown in **Figure 5.6**. The parameters of the kinetic models and the regression correlation coefficients (R^2) are listed in **Table 5.2**. The R^2 values clearly indicate the applicability of the pseudo-second-order model, which hints for a complexation of Hg^{2+} ions on the surface of MWCNT-DTC and MWCNT-SH.

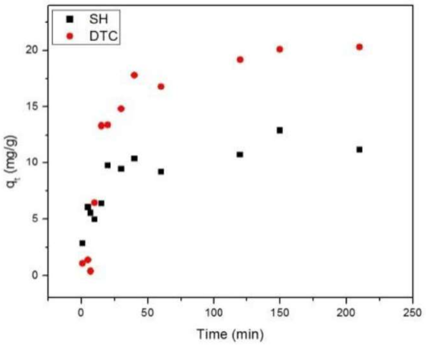

Figure 5.6 Adsorption kinetics of Hg^{2+} adsorption

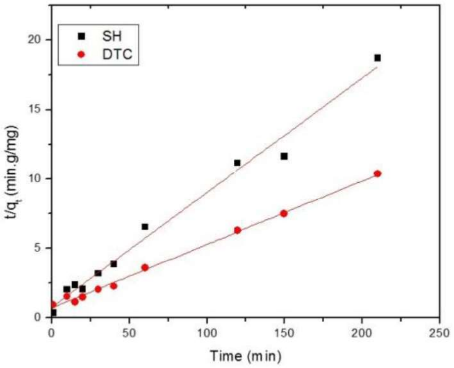

Figure 5.5 Pseudo second-order fitting

Table 5.2 Calculated parameters of kinetic modeling

Equations	Parameters	CNT-DTC	CNT-SH
Pseudo first-order	q_e (mg/g)	15.00	15.84
	k_1 (min^{-1})	0.011	0.002
	R^2	0.83	0.70
Pseudo second-order	q_e (mg/g)	125.00	12.82
	k_2 (g mg^{-1} min^{-1})	0.0004	0.006
	R^2	0.99	0.99

5.2.1.4 Effect of Temperature and Adsorption Thermodynamics

Figure 5.7 depicts the dependence of temperature on the adsorption of Hg(II) ions by MWCNT-DTC/SH. An increase in the adsorption with increase in temperature was observed up to 70^0C, beyond which it remains constant. The thermodynamic parameters of the adsorption process were calculated from the **Figure 5.8.** and shown in **Table 5.3**. The negative free energy of sorption indicate spontaneous and favorable adsorption process for both of the adsorbents. Increase in ΔG with increasing temperature supports the observation of **Figure 5.7** that adsorption capacity increase with temperature. This also suggest an endothermic sorption process which is evident from the positive values of ΔH for both of the sorbents. The positive value of entropy indicates enhance randomness on the CNT-solution interface during complexation of Hg^{2+} ions by the DTC/SH functional groups of MWCNTs due to the release of hydrated water molecules from the metal center before chelation by the ligands situated on the surface[368] . The higher ΔH and ΔG of MWCNT-DTC than

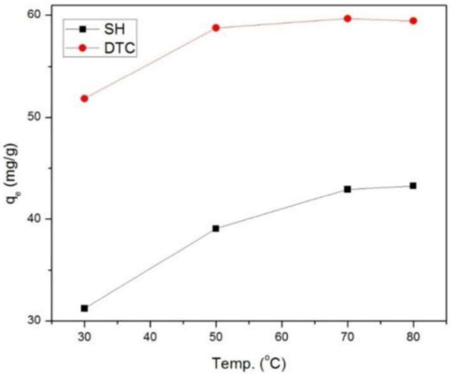

Figure 5.7 Effect of temperature on the sorption of Hg^{2+} with MWCNT-DTC and MWCNT-SH

MWCNT-SH at all studied temperature establishes the superiority of the former for removal of Hg(II) by adsorptive process.

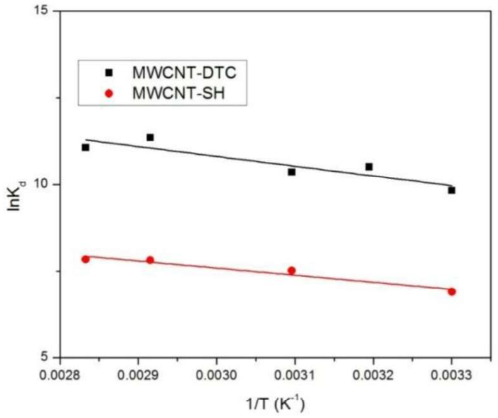

Figure 5.8 Plot of lnKdvs 1/T for Hg(II) separation by MWCNT-DTC and MWCNT-SH

Table 5.3 Calculated thermodynamic parameters

Material	Temperature (K)	ΔG (kJ/mol)	ΔH (kJ/ mol)	ΔS (kJ/mol K)	R^2
CNT-DTC	303	-25.09	23.38	0.16	0.77
	313	-26.69			
	323	-28.29			
	343	-31.49			
	353	-33.09			
CNT-SH	303	-17.58	16.89	0.11	0.92
	323	-19.85			
	333	-20.99			
	343	-22.13			
	353	-23.27			

5.2.1.5 **Selectivity**

The %adsorption of metal ions from a synthetic mixture including Hg(II) with equi-molar concentration are shown in **Figure 5.9**. The results given below indicate high selectivity towards mercury adsorption. This may be originated from the stronger soft-acid (Hg^{2+}

ion) and soft-base (S ligand of MWCNT-DTC/SH) interaction; other metal ions are harder compared to mercury ions[369] . The MWCNT-DTC has higher selectivity than that of MWCNT-SH, adsorbs almost cent percent of Hg^{2+} and almost nil of other metal ions from the mixture, showed its superior adsorbent properties over MWCNT-SH.

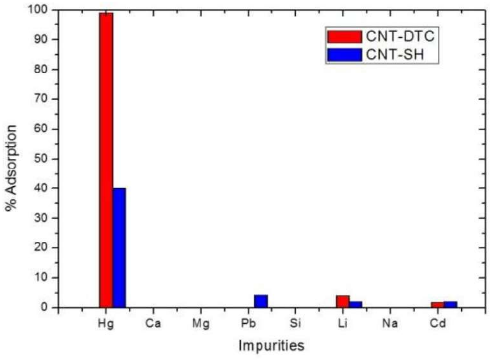

Figure 5.9 Selectivity of MWCNT-SH and MWCNT-DTC for Hg(II) removal from aqueous solution containing equi-molar other metal ions

5.2.1.6 Desorption and Regeneration

In order to reduce the cost of the adsorption process, the investigation for the desorption of Hg^{2+} from the used adsorbents and its regeneration is very necessary. The desorption efficiency of MWCNTs-SH/DTC was evaluated by aqueous solution of HCl, H_2SO_4, HNO_3, EDTA, and CDTA and found that appreciable desorption was not happening in any of the case (**Table 5.4**). Owing to the very strong interaction of Hg(II) with S-ligand on the MWCNTs of MWCNT-SH and MWCNT-DTC, a strong complexing agent of mercury, thiourea solution were used. The Thiourea solution alone was not found to be effective for both of the adsorbents as seen from the Table 6. 5% thiourea solution in aqueous acidic solution has been reported to be an excellent desorbing agent[362]. The concentration of acid was optimized by carrying out desorption at various acidity from

0.001 to 1M of HNO_3 (**Table 5.5**). 5% Thiourea in 0.1M HNO3 was found be best for the quantitative desorption and used for the regeneration of the used MWCNT-DTC/SH. One important aspect to mention here that regeneration of used CNTs requires repetitive dispersion either by ultra-sonication or high shear mixing. This may affect their structure like reduction aspect ratio thereby degrading the properties of the functionalized CNTs and influence the regeneration behavior.

Table 5.4 Desorption of Hg from used MWCNT-SH and MWCNT-DTC with various agent

Desorbing agent Tested	**% Desorption**	
	CNT-SH	**CNT-DTC**
HCl 0.5M	51.20	0.00
HNO3 0.5M	0	0.00
H2SO4 0.5M	23.01	0.67
EDTA 0.05M	43.72	0.00
CDTA 0.05M	4.58	0
Thiourea (5%)	65.30	94.76
Thiourea (2%)	63.21	86.62

Table 5.5 Stripping of Hg(II) from used MWCNT-SH and MWCNT-DTC using 5% thiourea at various acidity of HNO_3

Stripping Agent	**% Desoprtion**	
5% Thiourea in	CNT-SH	CNT-DTC
0.001 M HNO_3	90	75
0.01 M HNO_3	100	74
0.1 M HNO_3	100	84
1 M HNO_3	100	92

5.2.2 DFT Computational Study

5.2.2.1 **Structure and Bonding Analysis**

The thiol and dithiocarbamate unit attached with the MWCNT surface in the structure of MWCNT-SH and MWCNT-DTC as shown in **Figure 5.3** are named as amidothiol (Amd-SH) and amidodithiocarbamate (Amd-DTC). The structures of Amd-SH, Amd-DTC, and its complexes with Hg^{2+} , shown in **Figure 5.10**, were optimized first at B3LYP/TZVP level off theory. The Hg(II) ion is bonded in bidentate fashion with both of the unit. The mercury ion were bonded with the two sulphur donors atoms of Amd-DTC whereas with a sulphur atom and carboxyl oxygen atom of Amd-SH. The bond distances from donor atoms to Hg(II) are listed in **Table 5.6**. A stronger interaction between the mercury ion and Amd-SH may be interpreted from the shorter Hg-S (2.503Å) and Hg-O (2.619Å) bond distances, compared to longer Hg-S (2.449, 3.298Å) bond distances in Amd-DTC. It will be interesting to see how this mercury ion chelation be employed when Amd-SH and Amd-DTC are attached in the surface of MWCNT. The optimized structures of MWCNT-SH and MWCNT-DTC are shown in **Figure 5.11**. The Amd-SH and Amd-DTC unit were attached with the open edge carbon atom of CNT tube owing to the more reactive nature of these dangling carbon atoms. The functional groups containing the electronegative S, N, and O centers are projected outside of the CNT, expectedly because of the presence of π-electron cloud around the tube. The optimized structures of Hg^{2+} bonded MWCNT-SH and MWCNT-DTC are shown in **Figure 5.12**. The bond distances of Hg to coordinating donor atoms are shown in **Table 5.6**.

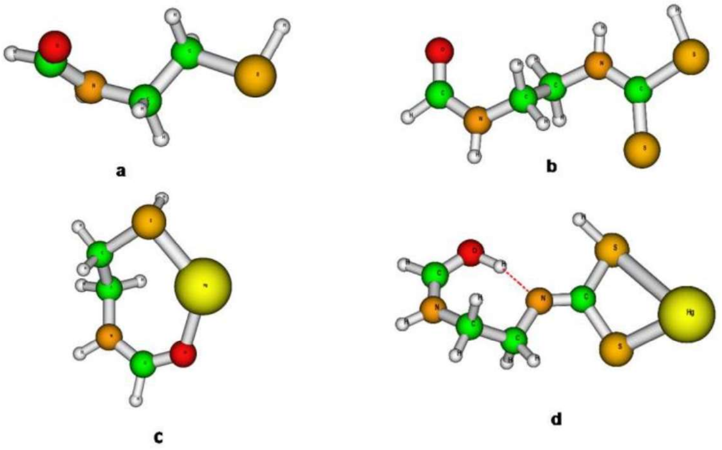

Figure 5.10 Optimized geometrics of (a) Amd-SH, (b)Amd-DTC, (c) Hg^{2+}-Amd-SH, and (d) Hg^{2+}-Amd-DTC.

Table 5.6 Characteristic bond distances in the optimized structures in the DFT study

Optimized structure	**Bond Distances (Å)**		
	S-Hg	**(C=)O-Hg**	**(CNT-Edge)C-Hg**
Amido-SH-Hg	2.503	2.169	
Amido-DTC-Hg	2.449, 3.298		
SWCNT-SH-Hg	3.868	5.502	3.214
SWCNT- DTC-Hg	4.095, 5.825	3.339	5.43
SWCNT- SH-$HgCl_2$	5.262	2.537	4.320
SWCNT- DTC-$HgCl_2$	3.684, 6.170	2.611	4.295

The interaction of mercury ions with the S and O donor atoms can be seen from the bond distances of Hg-S and Hg-O coordination in SWCNT-SH-Hg and SWCNT-DTC-Hg complexes. The same order of bond length is also found between the mercury ion and nearest open edge carbon atom of the CNT tube. This attributes to the interaction of π-electron density of CNT with the positively charged mercury ion. As it is reported that in aqueous solution, $HgCl_2$ exists exclusively (~99%) as $HgCl_2$ molecule, The SWCNT-SH-$HgCl_2$ and SWCNT-DTC-$HgCl_2$ structures are also optimized and shown in **Figure 5.13**.

The Hg-S and Hg-O bond distances in these complexes found to be shorter than that of SWCNT-SH-Hg and SWCNT-DTC-Hg, complexes (**Table 5.6**) indicating stronger interaction of mercury ion with the S and O donar atoms.

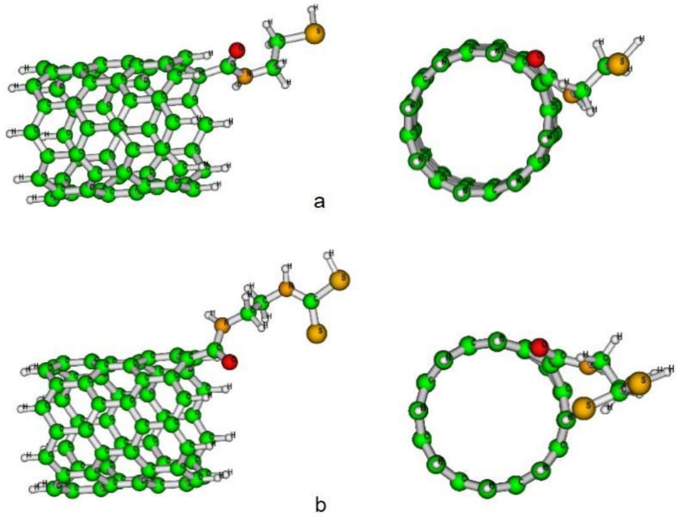

Figure 5.11 Optimized structures of (a) MWCNT-SH and (b) MWCNT-DTC

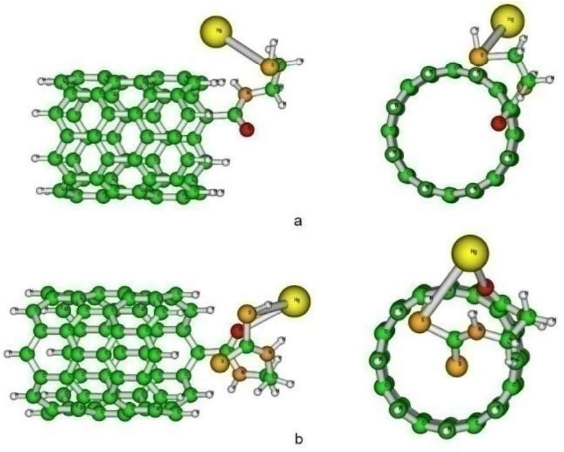

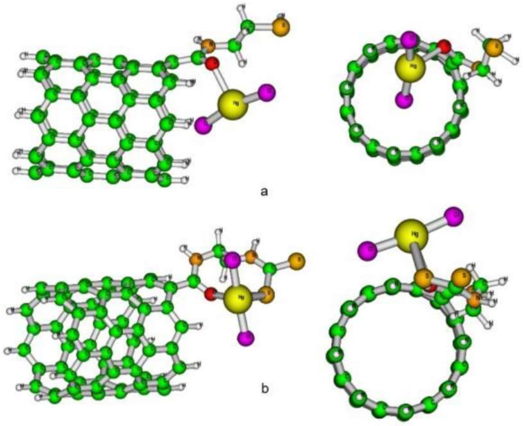

Figure 5.12 Optimized structures of Hg^{2+} complexes; Figure 5.13 Optimized structures of HgCl$_2$ complexes

5.2.2.2 Binding Energy and Free energy of Hg(II) complexation

The electronic binding energy (ΔE**)** between the Hg^{2+} and $HgCl_2$ with Amd-SH, Amd-DTC, SWCNT-SH, and SWCNT-DTC are calculated in gas phase and showed in **Table 5.7**. The free

Table 5.7 Electronic and thermodynamic energies of Hg^{2+} ion with MWCNT-SH and MWCNT-DTC in the gas phase

Reaction considered	Interaction Energies in kcal/mol (kcal/mol/K for ΔS)			
	ΔE	**ΔH**	**ΔS**	**ΔG**
$Amd-SH+Hg^{2+}\rightarrow Amd-SH-Hg^{2+}$	-202.5			
$Amd-DTC+Hg^{2+}\rightarrow Amd-DTC-Hg^{2+}$	-249.8			
$SWCNT-SH+Hg^{2+}\rightarrow SWCNT-SH-Hg^{2+}$	-393.5	-391.0	-0.025	-383.5
$SWCNT-DTC+Hg^{2+}\rightarrow SWCNT-DTC-Hg^{2+}$	-402.9	-400.1	-0.028	-391.8
$SWCNT-SH+HgCl_2\rightarrow SWCNT-SH-HgCl_2$	-20.7	-20.1	-0.038	-8.7
$SWCNT-DTC+HgCl_2\rightarrow SWCNT-DTC-HgCl_2$	-21.7	-22.5	-0.029	-13.8

DTC ligand has higher binding energy (-249.8 kcal/mol) than that of SH (-202.5 kcal/mol) with Hg^{2+} owing to the more binding sites in the earlier. Similarly, the binding energy of SWCNT-DTC is higher for Hg^{2+} and $HgCl_2$ complexation than that of SWCNT-SH (**Table 5.7**). The enthalpy (ΔH) and free energy (ΔG) of adsorption were also calculated in the gas phase and found in similar trend.

As adsorption experiments were carried out in aqueous medium in reality, the DFT energetic calculation was also carried out in aqueous phase and the finding are listed in **Table 5.8**. The decrease in ΔE in aqueous phase, as compared to gaseous phase is due to the screening of aqua molecules on the complexation of mercury ions by the donor atoms of SWCNT-SH/DTC. It is evident from the Table that the binding energy of SWCNT-

DTC is higher for Hg^{2+} and $HgCl_2$ complexation than that of SWCNT-SH. The free energy of adsorption of SWCNT-DTC (-188.0 kcal/mol) for Hg^{2+} binding was unlikely from above found to be lower than that of SWCNT-SH (-189.1 kcal/mol). Although the higher ΔG of SWCNT-DTC (-8.5 kcal/mol) compared to SWCNT-SH (-2.9 cal/mol) in aqueous phase has established with the $HgCl_2$, which is the experimentally found observation. Thus it is better to consider the chloride ions during the calculation of interaction energies of mercury with ligands.

Table 5.8 Electronic and thermodynamic energies of Hg^{2+} ion with MWCNT-SH and MWCNT-DTC in aqueous phase

Reaction considered	**Interaction Energies in Kcal/mol (Kcal/mol/K for ΔS)**			
	ΔE	**ΔH**	**ΔS**	**ΔG**
$SWCNT-SH+Hg^{2+}\rightarrow SWCNT-SH-Hg^{2+}$	-199.0	-196.5	-0.025	-189.1
$SWCNT-DTC+Hg^{2+}\rightarrow SWCNT-DTC-Hg^{2+}$	-199.1	-196.3	0.028	-188.0
$SWCNT-SH+HgCl_2\rightarrow SWCNT-SH-HgCl_2$	-14.9	-14.3	-0.038	-2.9
$SWCNT-DTC+HgCl_2\rightarrow SWCNT-DTC-HgCl_2$	-16.3	-17.2	-0.029	-8.5

5.3 Conclusion

Two sulphur ligand functionalized MWCNTs, MWCNT-SH and MWCNT-DTC were synthesized, characterized and tested for adsorption of mercury(II) ions from aqueous solution. From the batch studies it was found that MWCNT-DTC has higher sorption capacity than that of MWCNT-SH due to the presence of more number of S binding sites. The equilibrium and kinetic adsorption data of both of the adsorbent fits properly with Langmuir and pseudo-second-order model suggesting surface complexation of Hg^{2+} ions on the sulphur binding sites on the surface of MWCNTs. The negative free energy of sorption supports the spontaneous nature of the process. The higher capacity of MWCNT-DTC is reflected from the more negative free energy of adsorption values. Both the materials have good selectivity for Hg(II) with respect to other metal ions tested. Feasibility of continuous fixed bed separation using MWCNT-DTC was successfully carried out. The desorption, regeneration and reusability of the adsorbents were performed using Thiourea solution. In all the experiments MWCNT-DTC were proved to be superior adsorbent than MWCNT-SH for removal of Hg^{2+} ions from aqueous solution. The same trend has been established from the DFT calculation performed for the interaction of mercury(II) ion and mercuric chloride with SWCNT-SH and SWCNT-DTC. DFT results also inferred that the presence of chloride ions in the aqueous phase should be taken into account to arrive at the correct interaction insight.

6 Chapter 6: Crown Ether Functionalized Resin

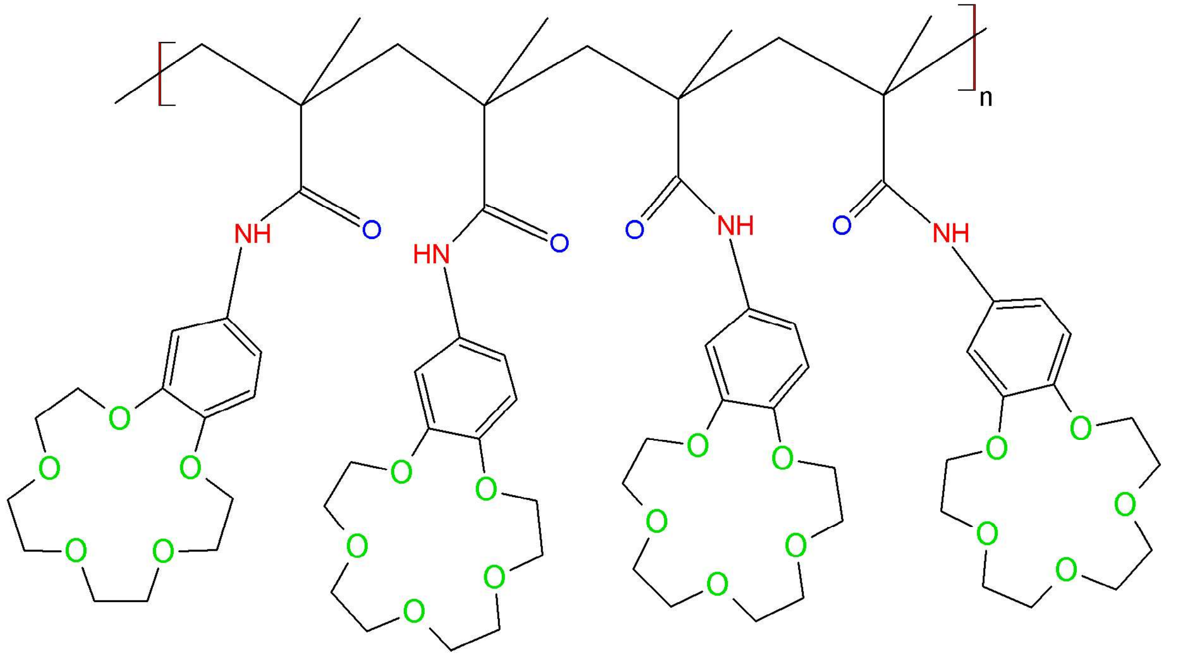

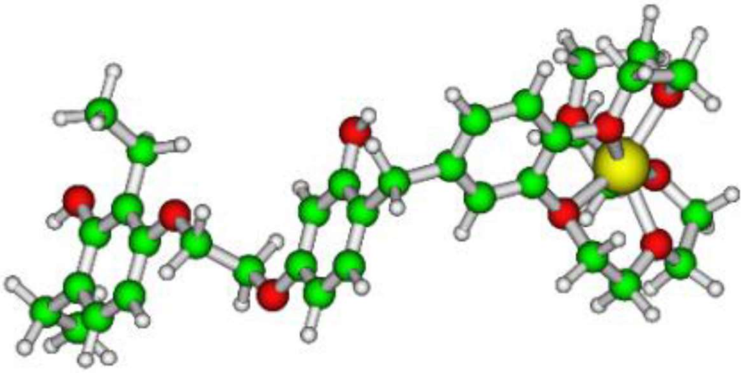

6.1 Introduction

Zinc (Zn), the 24th most abundant element in the Earth's crust, has five stable isotopes of masses 64, 66, 67, 68 and 70 with natural abundances 48.63, 27.90, 4.10, 18.75 and 0.62%, respectively. Isotope separation of Zn is important mainly through two aspects. ^{67}Zn and ^{68}Zn are used as a target materials during (p, n) nuclear transmutation reaction for the production of nuclear medicinally important radioisotope ^{67}Ga ($t_{1/2}$ = 61.8 h, E_γ =185 keV) which is widely used for diagnosis for tumour localization[134, 135]. ^{67}Zn, ^{68}Zn and ^{70}Zn can all be used for the production of the radionuclide ^{67}Cu which have diagnostic and therapeutic application in cancer treatment[136, 137]. ^{66}Zn has been proposed as an alternative target for the production of diagnostically potential ^{64}Cu radioisotopes[138]. Secondly, ^{64}Zn-depleted zinc is used in the primary coolant of nuclear power plant to reduce the formation of radioactive cobalt isotope, ^{60}Co ($t_{1/2}$ = 5.27 y, E_γ =1170 and 1330 keV), presence of which leads to radiation threat to the working personal [139]. During the course of operation, thin corrosion oxide film develops in the coolant circuit of nuclear power reactor and ^{60}Co is one of the components of these films[140]. Zn present in the coolant piping would competes with Co for sites in those films and thus suppresses the build up of ^{60}Co. Additionally, addition of Zn in the form of oxide or acetate prevents stress corrosion cracking in the structural material of the piping of the primary coolant[141]. ^{64}Zn-depleted zinc is used since this most abundant isotope generates highly radioactive ^{65}Zn [$t_{1/2}$ = 244.4 days, E_γ =1116 keV] in the reactor environment.

The physical methods of isotope separation, viz., gas centrifuge, distillation, thermal diffusion, electromagnetic processes, laser based processes, gas diffusion, etc requires relatively large amount of energy and thus pose economic constrains. The chemical exchange isotope separation methods being less energy consumptive and more economical and environmentally clean have been widely studied for several elements. In this context, liquid-liquid solvent extraction and solid-liquid chromatographic isotope separations are two major studied areas. Many scientists have extensively employed these techniques for isotopes separations of various elements [221, 370-379].

Separations of zinc isotopes by liquid-liquid extraction using crown ethers[142] have been reported[143, 144]. Isotope effects in the complex formation of zinc with various crown ethers have been investigated[143]. Stereochemical effect on the isotope separation of zinc by liquid-lquid extraction with crown ether has been recently studied[145]. Crown ether has shown promise for isotope separation albeit small separation factor which can be exploited in chromatography mode. Earlier reduced partition function ratio of various zinc species has been studied using DFT [155, 157]. Isotopic separation factor of complexes of zinc with DCH18C6 has been studied using DFT [156]. In spite of its great potential application, theoretical studies on the Zn isotope separation are found to be rather limited. In view of its technical importance density functional theoretical study (DFT) was performed to identify the suitable cavity of crown ether for zinc isotope fractionation.

6.2 Nano Cavity Induced Isotope Separation of Zinc: DFT Modeling[178]

6.2.1 Structural parameters

The optimized structure of free crown ethers is presented in **Figure 6.1**. The optimized minimum energy structures of various crown ether complexes of Zn^{2+} ion are displayed in **Figure 6.2** and the calculated structural parameters are presented in **Table**

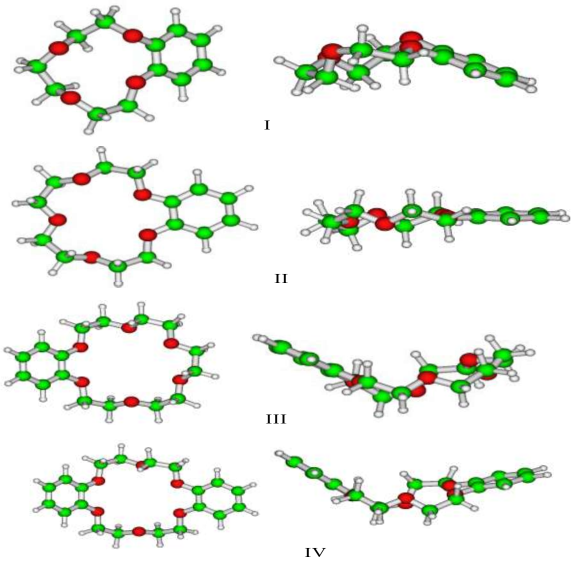

Figure 6.1 Optimized structures of crown ethers: (I) 12C4, (II) 15C5, (III) B18C6 and (IV) DB18C6

6.1. From the Figure it is seen that the Zn^{2+} metal ion is located equidistantly from 4 O donor atoms in benzo-12-crown-4 (B12C4) as confirmed from the Zn-O bond distances (2.00-2.02Å) shown in **Table 6.1**.

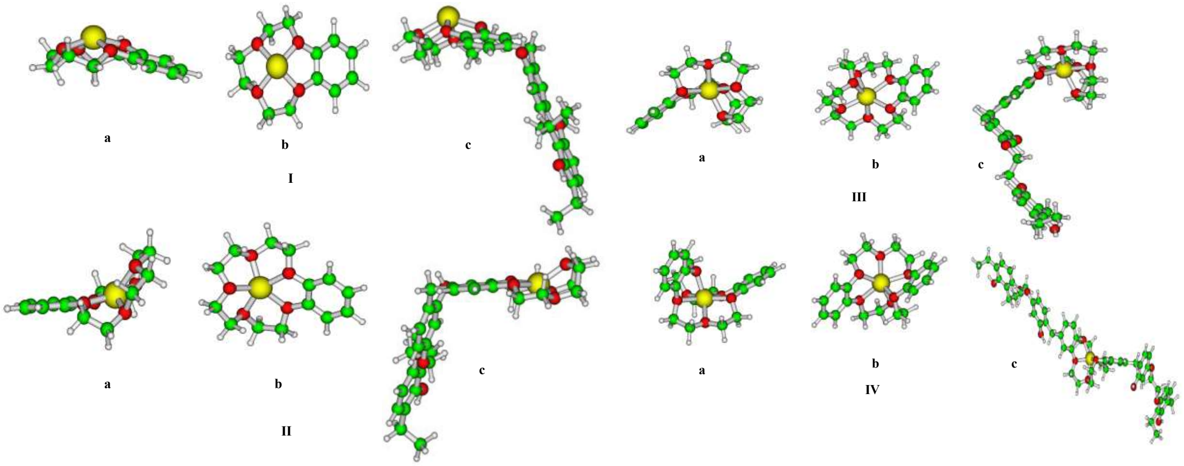

Figure 6.2 Optimized minimum energy structures of Zn complexes with (I) B12C4 (a, b) & EDDP-B12C4 (c); (II) B15C5 (a, b) and EDDP-B15C5(c); (III) B18C6 (a, b) & EDDP-B18C6 (c); and (IV) DB18C6 (a, b) & EDDP-DB18C6 (c)

In Zn^{2+}-B12C4 complex, 4 O atoms bonded equilaterally to the central Zn metal ion which has been pushed outward from the plane of the four O atoms. In case of benzo-15-crown-5(B15C5), five O donor atoms from the crown ring were found to be coordinated to the centrally found to be coordinated to the centrally located Zn^{2+} ion by keeping equidistance Zn-O bond distance (2.08-2.11Å).

Table 6.1 Structural parameters for free crown ethers and zinc-crown ether complexes

Bond	B12C4	Zn-B12C4	B15C5	Zn-B15C5	B18C6	Zn-B18C6	DB18C6	Zn-DB18C6
Zn-O (Å)		2.00		2.08		2.13		2.25
		2.02		2.09		2.13		2.10
		2.02		2.11		2.14		2.13
		2.02		2.09		2.11		2.23
				2.08		2.20		2.14
						2.17		2.12
Diagonal O-O (Å)	4.30	3.85	5.03	3.95	5.55	3.46	3.79	4.35
	3.59	3.78	4.58	3.62	5.63	4.31	4.80	3.30
			4.03	4.06	5.47	3.50	4.40	3.75
			4.02	3.76				
			4.57	3.92				
Cavity Dia. (Å)	1.305	1.175	1.806	1.222	2.91	1.116667	1.69	1.16

Cavity of the crown distorts to accommodate Zn at the centre. Resulting 2 O atoms interact from one orientation and other 3 by 3 different orientation. The Zn-O bond distance was found to be higher than that of in B12C4 due to increased cavity of the B15C5 due to increment of one unit of $–CH_2–CH_2$-O-CH_2-$CH_2–$ link within the B12C4. Further addition of one unit of $–CH_2–CH_2$-O-CH_2-$CH_2–$link leads to benzo-18-crown-6 (B18C6) in which the Zn^{2+} metal ion was found to be coordinated in asymmetrical fashion where four O donor atoms of crown ring were found to produce identical Zn-O bond distance (2.11-2.14Å) and remaining two O atoms leads to slightly higher Zn-O bond distance (2.17-2.20Å). In Zn^{2+}-B18C6 complex, 6 O atoms bonded with central Zn in a shape of distorted octahedron; the vertical Zn-O bonds are heavily bent due to the close structure. Horizontal Zn-O bonds are little distorted from tetragonal plane. The Zn-O bond distance was found to be increased gradually from B12C4 to B18C6 due to increase in cavity size and the same is confirmed from the increased centre to centre diagonal O-O distance (see **Table 6.1**). Similar coordination pattern of Zn^{2+} ion with the six O donor atoms of the dibenzo-18-crown-6 (DB18C6) crown ether was also observed. The cavity of DB18C6 in compared to B18C6 is found to be reduced slightly due to addition of one extra electron withdrawing benzene ring. In Zn^{2+}-DB18C6 complex, Zn^{2+} is in octahedron geometry, two vertical Zn-O bonds bent due to close structure of the cavity. Two benzene rings in the opposite arms of the tetragonal plane keep it planar.

Table 6.2 Structural parameters of EDDP-Crown ethers

Bond	**EDDP-B12C4**	**EDDP-B15C5**	**EDDP-B18C6**	**EDDP-DB18C6**
Zn-O (Å)	2.14	2.10	2.16	2.16
	2.17	2.11	2.15	2.12
	2.16	2.11	2.27	2.18
	2.16	2.09	2.17	2.22
		2.13	2.20	2.14
			2.16	2.21
Diagonal O-O (Å)	3.64	3.78	4.40	4.32
	3.95	3.79	3.82	4.20
		4.06	3.36	4.15
		3.61		
		4.10		

Recently, column chromatography using benzo crown resin having different crown cavity has shown promising results for Zn isotope separation [380-383]. Hence, it is of importance to investigate the various factors that determine the extent of isotope separation using electronic structure calculation with polymeric resin (ethylene dioxydiphenol, EDDP, based) anchored with crown ethers of different cavities. The optimized structure of Zn^{2+} ion complexes with benzo crown resins with different cavities are displayed in **Figure 6.2** and the calculated structural parameters are presented in **Table 6.2**.

Introduction of EDDP group at the benzene ring of B12C4 pushes the Zn ion more outward (Zn-O bond lengths increase) compared to B12C4. Presences of EDDP in B15C5 changes the bonding manner – 2 pair of O atoms coordinate in same orientation whereas rest one differently. In B18C6 anchored on EDDP try to bring the tetragonal Zn-O bonds in more planar mode. In the grafted DB18C6 resin, EDDP group attached with both benzene ring and they are trans to each other. Not significant change in the earlier octahedral geometry. In case of grafted B12C4 and B18C6, the Zn-O bond distance was found to be lengthened by 0.15Å and 0.07Å respectively compared to their free crown part, whereas in case of grafted B15C5 and DB18C6, the Zn-O bond distance remains same as was with free crown ether.

Since the extraction and adsorption of Zn^{2+} ion takes place from solvent phase to the organic phase (solvent extraction) or stationary phase (chromatography) it is necessary to optimize the structure of solvated Zn^{2+} ion. The solvents we have studied here are water, ethanol, acetone and dimethyl ether (dme). For calculation of reduced partition function ratio, we have considered 4 coordinated Zn^{2+} ion and for free energy of solvation we have considered hexa coordinated Zn^{2+} ion as hexa coordinated ion leads to hydration energy very close to the experimental value. The optimized structure of 4 coordinated and 6 coordinated solvated zinc with different solvents are presented in **Figure 6.3**.

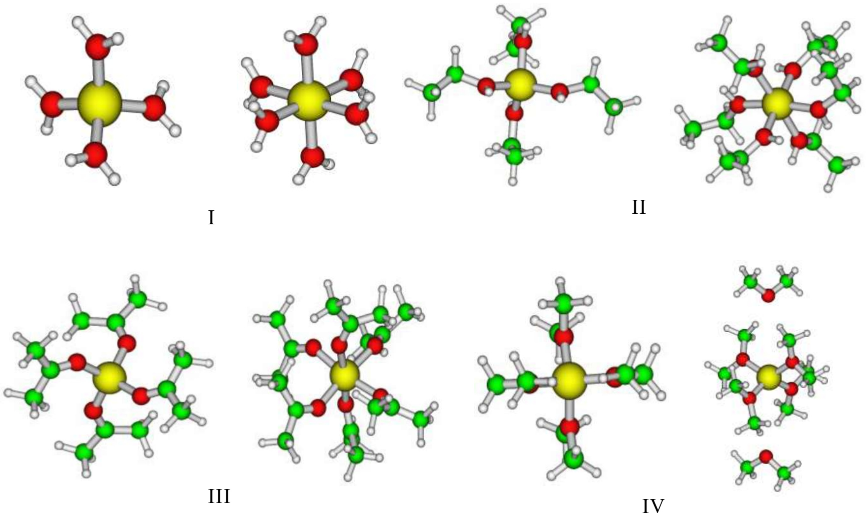

Figure 6.3Optimized minimum energy structures of 4 coordinated and 6 coordinated solvated zinc with (I) water, (II) Ethanol, (III) Acetone, and (IV) Dimethylether

6.2.2 Binding energy and free energy

6.2.2.1 Gas phase and aqueous phase

The calculated values of binding energy for B12C4, B15C5, B18C6 and DB18C6 with Zn^{2+} ion are presented in **Table 6.3**. The binding energy was found to be increased from B12C4 to DB18C6 with increasing number of donor O atoms. Interestingly the binding energy was found to be increased from B12C4 to DB18C6 with increasing cavity size also. Further, the binding energy was also computed to examine the effect of non-covalent interaction using M06-L density functional with TZ2P basis set. The computed values of BE are displayed in **Table 6.3**. The calculated value predicted at M06-L/TZ2P level was found to be very close to the value predicted at B3LYP/TZVP level of theory.

Similar pattern was observed in the free energy of complexation also. The order of free energy of complexation was found to be: DB18C6>B18C6>B15C5>B12C4. The free energy of complexation was found to be reduced compared to enthalpy due to negative contribution of entropy which indicates that metal ion–ligand complexation is a structure making process.

Table 6.3 Energy and thermodynamic parameters of Zn separation by crown ethers in gas phase and in aqueous phase

Medium	**System**	**ΔE (kcal/mol)**	**ΔH (kcal/mol)**	**ΔS (kcal/mol K)**	**ΔG (kcal/mol)**
Gas Phase	B12C4	-288.4 (-281.0)	-287.0	-0.035	-276.5
	B15C5	-327.4 (-322.9)	-324.3	-0.036	-313.5
	B18C6	-344.0 (-341.4)	-340.5	-0.042	-327.8
	DB18C6	-348.0 (-345.8)	-345.0	-0.046	-331.1
Aqueous Phase	B12C4	-51.6	-50.1	-0.035	-39.6
	B15C5	-66.7	-63.6	-0.036	-52.8
	B18C6	-70.0	-66.4	-0.042	-53.7
	DB18C6	-73.2	-70.2	-0.046	-56.2

*Values in parenthesis refers to the BE calculated at MO6-L/TZ2P level

Since most of the complexation process with metal ion takes place from the aqueous environment, it is important to study their interaction and free energy in the aqueous phase also. The effect of aqueous phase was incorporated employing COSMO solvation approach by using dielectric constant of water as 80. The single point energy was calculated in COSMO water phase using optimized geometry of the gas phase. The calculated values of aqueous phase binding energy of Zn^{2+} ion with different crown ethers, presented in **Table 6.3**, was found to be reduced substantially from the gas phase interaction value due to the dielectric screening of the condensed phase water which weakens the interaction. Similarly the free energy of complexation was also reduced drastically in aqueous phase compared to gas phase but the trend remains same i.e

DB18C6>B18C6>B15C5>B12C4. From the gas phase and aqueous phase binding energy it is seen that the crown ether shows considerable affinity towards Zn^{2+} metal ion both in gas and aqueous phase. This strong complexation affinity of crown ether towards Zn^{2+} ion can be exploited for its role in the separation of isotopes of Zn. This is the subject of the next section.

6.2.3 Reduced partition function ratio (RPFR) and isotope separation factor (α)

As described in Equation 2.34 that in order to compute the isotope separation factor for any biphasic system we need to know the value of RPFR for a pair of isotope in the feed solvent phase and the product complex phase. The isotope effect can be clearly seen from the shift in vibrational frequencies between two isotopes (64 and 68) of zinc in different solvents as shown in **Figure 6.4**. Hence, first the RPFR of hydrated Zn^{2+}-$(H_2O)_n$ (n=1-6) cluster system was calculated for different pair of Zn isotope and the values are presented in **Figure 6.5** and **Table 6.4**. From the Figure it is seen that the computed value of RPFR was found to be increased from n=1 then shows maximum at n=4 and then further reduced. The working value of RPFR at n=4 were taken as 1.0098 for Zn (68/64); 1.005 for Zn (66/64) and 1.0047 for Zn (68/66). The highest separation factor is limited by the value of RPFR in water/solvents system. Similarly, the isotope effect between two isotopes (64 and 68) of zinc with different crown ethers can be clearly seen from the shift in vibrational frequencies as shown in **Figure 6.6**. Next, the values of RPFR of complexes of Zn^{2+} ion with different crown ethers were computed and the values are shown in **Table 6.4**. It is interesting to mention that the RPFR was found to be decreased from B12C4 to DB18C6 for all the pair of Zn isotopes studied here. The RPFR was found to be highest with B12C4 and lowest with DB18C6 leading to lowest separation factor in B12C4 and highest separation factor in DB18C6. Further, the separation factor was found

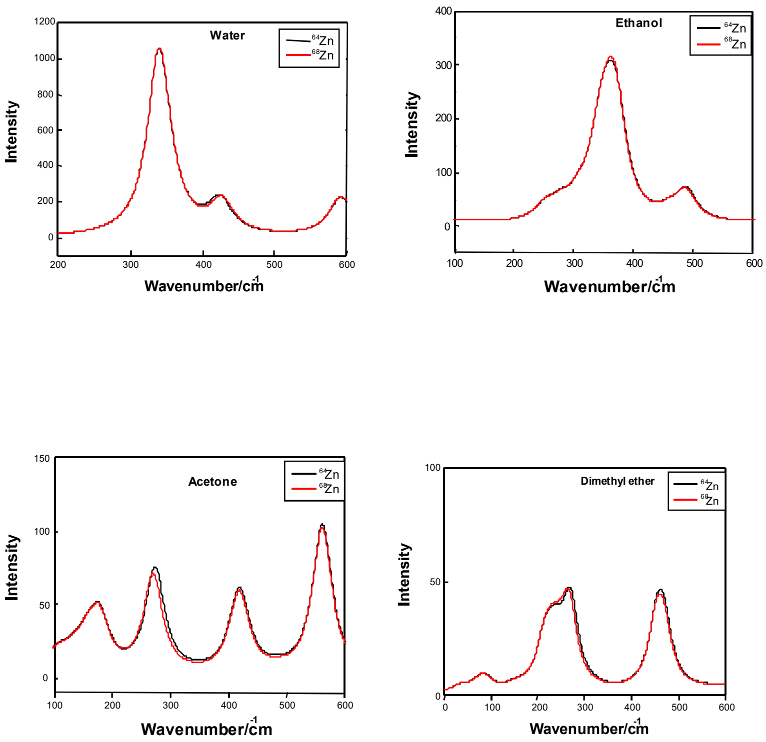

Figure 6.4 Calculated IR frequencies between two isotopes (64 and 68) of zinc in different solvents.

to be highest for Zn (68/64) pair and lowest for Zn (68/66) pair as expected because in the former pair the mass difference is highest. It is worth noting that the RPFR can be correlated with the binding energy and free energy of complexation. The higher the binding/free energy smaller is the RPFR and smaller the binding/free energy higher is the RPFR. This can be further explained as follows that higher the interaction energy means that the complex is strongly bound and hence imparts rigidity to the system leading to smaller RPFR whereas smaller the interaction energy means that the complex is loosely bound and hence more flexibility to the system leading to higher RPFR. This can be further correlated with the cavity size of the crown ether i.e. with increasing cavity size of the crown ether the RPFR was found to be decreased leading to high value of isotope separation factor. The calculated value of separation factor is found to be very close to the value predicted for DCH18C6 crown ether[156].

Table 6.4 RPFR of Zn in aqueous and Zn-crown ether system with separation factor values

System	RPFR			α		
	68/64	66/64	68/66	68/64	66/64	68/66
Zn 4W	1.0098	1.005	1.0047			
B12C4	1.0096	1.0049	1.0047	1.0001	1.0000	0.9999
B15C5	1.0087	1.0044	1.0042	1.0010	1.0005	1.0004
B18C6	1.0079	1.0041	1.0037	1.0018	1.0008	1.0009
DB18C6	1.0075	1.0038	1.0036	1.0022	1.0011	1.0010

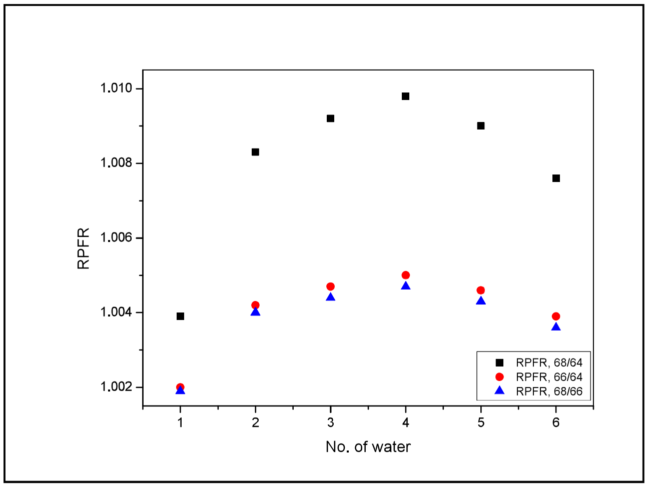

Figure 6.5 Calculated values of RPFR for Zn^{2+}-$(H_2O)_n$ (n=1-6) system

It is well known that the solvent extraction studies are generally carried out using aqueous metal ion solution in contact with suitable non aqueous solvent. Hence, it is worth to examine the effect of non-aqueous solvents on the interaction and free energy of Zn^{2+} metal ion with different crown ethers of different cavity. We have considered chloroform (CF), toluene (TOL) and nitrobenzene (NB) as the representative non-

Table 6.5 Energy and thermodynamic parameters of Zn-crown ether complexes in various organic solvents used in liquid-liquid extraction

Solvent	**Crown Ether**	**ΔE (kcal/mol)**	**ΔH (kcal/mol)**	**ΔS (kcal/moleK)**	**ΔG_{ext} (kcal/mol)**
Nitrobenzene	B12C4	-47.6	-46.1	-0.0352	-35.6
	B15C5	-63.3	-60.2	-0.0361	-49.4
	B18C6	-67.0	-63.4	-0.0427	-50.7
	DB18C6	-70.1	-67.2	-0.0468	-53.2
Chloroform	B12C4	-7.1	-5.7	-0.0352	4.7
	B15C5	-29.4	-26.3	-0.0361	-15.5
	B18C6	-36.6	-33.1	-0.0427	-20.4
	DB18C6	-39.5	-36.5	-0.0468	-22.6
Toluene	B12C4	20.8	22.3	-0.0352	32.8
	B15C5	-5.5	-2.4	-0.0361	8.2
	B18C6	-15.2	-11.6	-0.0427	1.0
	DB18C6	-18.1	-15.1	-0.0468	-1.1

aqueous solvents for examining the extraction capacity of the crown ethers for Zn^{2+} ion. The free energy of extraction, ΔG_{ext} is evaluated using the following complexation reaction

$$M^{2+}_{(aq)} + L_{(org)} = M^{2+}L_{(org)} \qquad (6.1)$$

Here, L stands for B12C4/B15C5/B18C6 and DB18C6. The calculated values of ΔG_{ext} are presented in **Table 6.5**. From the table, it is seen that for a given aqueous-organic biphasic system, ΔG_{ext} was found to be increased with increasing cavity size of the crown ether and follows the trend: DB18C6>B18C6>B15C5>B12C4. Further, ΔG_{ext} was found to be increased with increasing dielectric constant (ε) of the organic solvent and was found to be highest in NB (ε=34.81) and lowest in toluene (ε=2.63). The trend was similar for all the crown ethers. In order to check the effect of cavity of the crown ether and dielectric constant of the organic solvent on the distribution constant, solvent extraction study was performed using zinc chloride solution with B15C5 and DB18C6 in NB, CF and TOL.

The experimentally obtained result that the extraction of zinc metal ions is more with DB18C6 compared to B18C6 was found to be in qualitative correlation with the computed results. But the experimentally found variation of extraction with ε of solvents does not correlate with the calculated one. This should be addressed in future studies.

The separation factor for various pair of Zn isotope was found to be quite small. In view of this small separation factor, recently, column chromatography using polymeric resin anchored with crown ether has been proposed to be used for Zn isotope separation. [380-383] Hence, it will be worthwhile to investigate the various factors that determine the extent of isotope separation using electronic structure calculation with polymeric resin (ethylene dioxydiphenol based benzo crown resin) anchored with crown ethers of different cavities. The calculated RPFR for different pair of Zn isotopes with benzo crown resins having different cavities are presented in **Table 6.6**. In case of B12C4 resin, the value of RPFR for the entire zinc isotope pair was found to be reduced compared to the free B12C4 crown ether which in turn increase the isotope separation factor. Similarly, the value of RPFR for the entire zinc isotope pair was found to be reduced for B15C5 resin compared to the free B15C5 crown ether leading to the enhanced isotope separation factor. But the effect was smaller than that of B12C4. In case of B18C6 resin, the value of RPFR for the entire zinc isotope pair was found to be reduced compared to the free B18C6 crown ether resulting in the increased isotope separation factor. The separation factor was found to be highest for the entire zinc isotope pair with B18C6 resin.

Table 6.6 RPFR and isotope separation factor (α) values for Zn by EDDP-Crown ethers in water

EDDP	RPFR			α		
grafted with	68/64	66/64	68/66	68/64	66/64	68/66
B12C4	1.0049	1.0025	1.0023	1.0052	1.0027	1.0026
B15C5	1.0077	1.0040	1.0037	1.0024	1.0012	1.0012
B18C6	1.0043	1.0010	1.0033	1.005	1.0042	1.0016
DB18C6	1.0070	1.0035	1.0034	1.0031	1.0017	1.0017

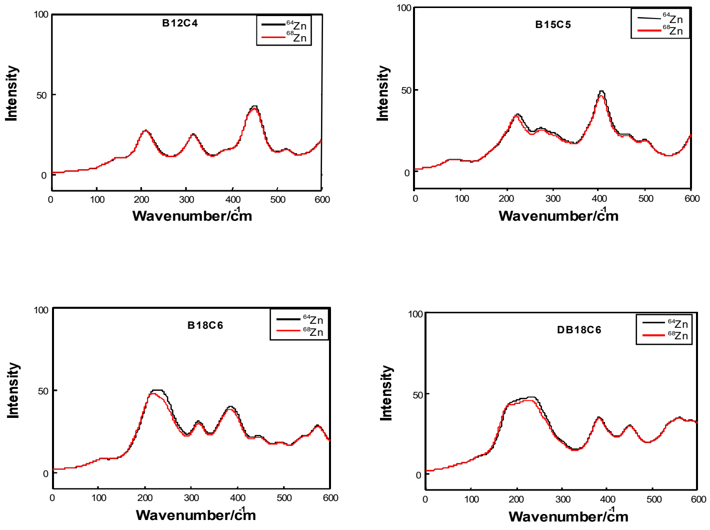

Figure 6.6 Calculated IR frequencies between two isotopes (64 and 68) of zinc with different crown ethers.

Similarly, the value of RPFR for the entire zinc isotope pair was found to be reduced for DB18C6 resin compared to the free DB18C6 crown ether which in turn increases the isotope separation factor. The separation factor with DB18C6 crown resin was found to be higher than that of with B15C5 resin. The separation factor follows the order for a particular isotope pair as: B18C6>B12C4>DB18C6>B15C5 whereas the reported experimental trend was found to be: B15C5>DB18C6>B18C6>B12C4. But point to be mentioned here is that the reported separation factor was for non-aqueous solvents [384]. Hence, RPFR was further calculated in three different non-aqueous solvents namely: acetone, ethanol, and dme. The calculated values of RPFR for different pair of Zn isotopes in different non-aqueous solvents are presented in **Table 6.7**. The calculated value of RPFR for 68/64 pair was found to be almost close for acetone (1.0092), ethanol (1.0094) and dme (1.0092) for n=4 respective solvent molecules. The calculated value of RPFR for 66/64 pair was found to be 1.0047, 1.0048 and 1.0045 for acetone, ethanol and dme respectively whereas it was 1.0045, 1.0045 and 1.0047 for 68/66 pair. **Table 6.8** shows the separation factor, α, values for three concerned isotope pair of zinc in EDDP resin anchored with crown ethers in the three non-aqueous solvents. The calculated value of α for 68/64 pair with EDDP-B12C4 is found to be 1.0043, 1.0044 and 1.0042 for acetone, ethanol and dme respectively.

The α values for 68/64 pair with EDDP-B15C5 is found to be 1.0016, 1.0016 and 1.0014 for acetone, ethanol and dme respectively. The α values for 68/64 pair with EDDP-B18C6 is found to be 1.0049, 1.0050 and 1.0048 for acetone, ethanol and dme respectively. The values of α for 68/64 pair with EDDP-DB18C6 is found to be 1.0023, 1.0023 and 1.0021 for acetone, ethanol and dme respectively. The separation factor follows the order for a particular isotope pair as: B18C6>B12C4>DB18C6>B15C5 whereas the reported experimental trend was found to be: B15C5>DB18C6>B18C6>B12C4. Similar trend was observed for other two pair of isotopes (66/64 and 68/66) also. The contrasting results may be attributed that the experimental results were obtained using real solvents whereas in the present study the calculation has been done in gas phase. Overall the present results capture the cavity effect on the complex chemical phenomena like isotopic separation qualitatively and confirm that the nano cavity based macrocyclic molecule like crown ether can be used for zinc isotope separation process. From the present DFT based molecular modelling study it is shown that B18C6 can be used for zinc isotope fractionation.

Table 6.7 RPFR of Zn in different non-aqueous solvents

Solvent	**n**	**RPFR**		
		68/64	**66/64**	**68/66**
Acetone	1	1.0032	1.0017	1.0016
	2	1.0032	1.0017	1.0016
	3	1.0091	1.0047	1.0044
	4	1.0093	1.0047	1.0045
	5	1.0079	1.0004	1.0038
	6	1.0064	1.0033	1.0031
Ethanol	1	1.0037	1.0019	1.0017
	2	1.0093	1.0047	1.0045
	3	1.0097	1.005	1.0047
	4	1.0094	1.0048	1.0045
	5	1.0083	1.0042	1.004
	6	1.0077	1.0039	1.0037
DME	1	1.004	1.002	1.0019
	2	1.0094	1.0048	1.0045
	3	1.0087	1.0044	1.0042
	4	1.0092	1.0045	1.0047
	5	1.0082	1.0042	1.0039
	6	1.0092	1.0048	1.0044

Table 6.8 Isotope separation factor values for Zn by EDDP-Crown ethers in different non-aqueous solvents

Solvent	EDDP grafted with	α		
		68/64	66/64	68/66
Acetone	B12C4	1.0043	1.0022	1.0022
	B15C5	1.0016	1.0007	1.0008
	B18C6	1.0049	1.0037	1.0012
	DB18C6	1.0023	1.0012	1.0014
Ethanol	B12C4	1.0044	1.0022	1.0021
	B15C5	1.0016	1.0007	1.0007
	B18C6	1.0050	1.0037	1.0011
	DB18C6	1.0023	1.0012	1.0013
DME	B12C4	1.0042	1.0019	1.0023
	B15C5	1.0014	1.0004	1.0009
	B18C6	1.0048	1.0034	1.0013
	DB18C6	1.0021	1.0009	1.0015

6.2.4 Solvation free energy and distribution constant

The present analysis shows that the separation factor is not strongly dependent on the solvent nature but the distribution constant depends on the metal ion solvation energy. In order to examine the effect of solvent on the distribution constant, we have calculated solvation free energy of microsolvated Zn^{2+}-$(sol)_n$ cluster, where sol means water, acetone, ethanol and dme and first solvation shell coordination number, n= 6. The computed value of solvation free energy, ΔG_{sol}, is presented in Table 9 along with the available experimental results [385]. The free energy of solvation is found to be highest in water and lowest in dme. The solvation energy follows the order: water>ethanol>acetone>dme. The higher the solvation energy higher will be the molecular complexation energy required to desolvate the Zn^{2+} ion from the solvent before binding to the ligands. Practically it has been reported in the experiments also where it has been reported that the distribution constant is negligible in water and increased from ethanol to acetone. The predicted solvation free energy of Zn^{2+} ion is further confirmed by performing molecular dynamics simulation of Zn^{2+} ion with different solvent molecules. The calculated results from the MD simulation [386] are presented in **Table 6.9**. The calculated values though are found to be smaller than that predicted from QM calculation; it follows the same trend as by QM. The detailed simulation methodology is presented in Chapter 2, Section 2.7.5. Solvent of lower dielectric constant was found to be suitable for better extraction of Zn isotopes in chromatographic mode as it needs lesser energy for desolvation.

Table 6.9 Solvent phase free energy, ΔG (kcal/mole) for Zn^{2+} *-* $(H_2O)_6$ *cluster*

Free energy	Water	Ethanol	Acetone	DME
ΔG_{gp}	-313.2	-332.4	-339.3	-293.2
ΔG_{sol}	-461.2	-445.3	-435.4	-399.8
ΔG_{MD}	-415.03 (-458.1)	-397.8	-384.0	-303.2

*Value in parenthesis refers to experimental value[382]

6.2.5 Bonding analysis

6.2.5.1 Population analysis

It is interesting to explain the interaction of Zn^{2+} ion with crown ether in terms of highest occupied molecular orbital (HOMO) and lowest unoccupied molecular orbital LUMO[387] of crown ether and the charge transfer on the metal ion in the respective complexes using natural population analysis (NPA)[220]. The calculated values of NPA charges and orbital occupancies are given in **Table 6.10**. From the table it is seen that there is negligible charge populations in the f orbital indicating its non-participation in the complex formation but significant charge populations are observed for s and d orbital for all complexes suggesting covalency in cation-ligand bonding. The NPA charge is found to be highest in B12C4 and lowest in B18C6 and DB18C6 which is found to be correlated with the gas phase binding energy which follows the order B12C4<B15C5<B18C6<DB18C6.

Table 6.10 Average Second Order Stabilization Energy (kcal/mol) and Mulliken Population parameters of Zn-crown ether systems from ADF calculations

System	$E^{(2)}_{(i,j)}$ **(kcal/mol)**	**Charge (esu)**	**s**	**p**	**d**	**f**
B12C4	27.05	1.09	6.38	12.41	10.07	0.02
B15C5	26.54	1.02	6.37	12.48	10.08	0.02
B18C6	19.62	0.96	6.37	12.53	10.09	0.02
DB18C6	19.95	0.96	6.38	12.53	10.09	0.02

6.2.5.2 **Quantum chemical descriptors for crown ethers**

DFT has an extra-ordinary potential for calculating global and local indices that describe the inherent reactivity of chemical species quantitatively and is thus very useful to describe the host (crown ether) guest (metal ion) type interaction. Chemical systems are generally characterized by its electronic chemical potential, μ and absolute hardness, η and are defined as [388]

$$-\mu = (I+A)/2 = \chi \eta = (I-A)/2 \qquad (6.2)$$

where I is the ionization potential and A is the electron affinity. Here, χ is called the absolute electronegativity. According to Koopmans' theorem[163], I and A can be obtained as

$$I = -E_{HOMO} \qquad A = -E_{LUMO} \qquad (6.3)$$

If donor acceptor system is brought together, electrons will flow from that of lower χ to that of higherχ, until the chemical potentials become equal. The amount of charge transfer, ΔN can be calculated by applying the following formula [249]

$$\Delta N = (\chi_M - \chi_L) / \{2(\eta_M + \eta_L)\}. \qquad (6.4)$$

Here, M stands for metal ion, which acts as Lewis acid i.e. acceptor and L stands for crown ether, which acts as Lewis base i.e. donor.

A higher value of E_{HOMO} indicates a tendency of the molecule to donate electrons to appropriate acceptor molecule of low empty molecular orbital energy. On the other hand, the energy of the lowest unoccupied molecular orbital indicates the ability of the molecule to accept electrons. Larger values of the energy difference, $\Delta E = E_{LUMO} - E_{HOMO}$, provide low reactivity to a chemical species and lower values of the energy difference indicates higher reactivity.

The calculated values of HOMO and LUMO energies, energy gaps, absolute hardness (η), absolute electro negativity (χ) and charge transfer, ΔN of the optimized crown ligand –metal ion systems are given in **Table 6.11**. The calculated HOMO and LUMO of free crown ethers and

Table 6.11 Energies of HOMO, LUMO, HOMO-LUMO gap and quantum chemical descriptors for different ligand systems

System	**E_{HOMO} (eV)**	**E_{LUMO} (eV)**	**ΔE (eV)**	**η**	**χ**	**ΔN**
B12C4	-5.97	-0.38	5.59	2.795	3.175	1.402
B15C5	-5.41	0.05	5.46	2.729	2.680	1.441
B18C6	-5.47	0.07	5.55	2.77	2.70	1.433
DB18C6	-5.81	-0.24	5.56	2.785	2.785	1.412

Zn^{2+} complexes are depicted in **Figure 6.7** and **6.8** respectively. The HOMO-LUMO energy gap is found to be highest with B12C4 and lowest with B15C5 and B18C6 and DB18C6 stands in between them. The higher the gap lower is the reactivity and hence lower will be binding energy and is shown from the lowest binding energy of Zn^{2+} ion with B12C4. But, though, B15C5 has the lowest energy gap it is shown to be less reactive than B18C6 and DB18C with higher energy gap. In order to calculate the fractions of electron transferred from the donor crown ether to the metal ion, theoretical values for absolute electronegativity and absolute hardness for Zn^{2+} ion was calculated. The theoretical value of absolute electronegativity of Zn^{2+} ion is 27.51eV and absolute hardness is 5.88eV. This indicates that Zn^{2+} metal ion is hard acid. According to Pearson's HSAB principle, hard acids prefer to bind to hard bases and soft acids prefer to bind to soft bases. Crown ether ligand with oxygen as donor atom acts as a hard base as evident from high energy HOMO and high values of hardness (η) and electro negativity (χ). Hence in accordance with the HSAB principle crown ether forms strong complex with Zn^{2+} metal ion. A large value of ΔN is favourable for a donor-acceptor reaction. The fraction of electron transferred is largest for B15C5 followed by B18C6, DB18C6 and B12C4. As stated earlier the binding energy can be correlated with NPA charge transfer but no such correlation is obtained with the fraction of electron transfer, ΔN.

System	HOMO	LUMO
B12C4	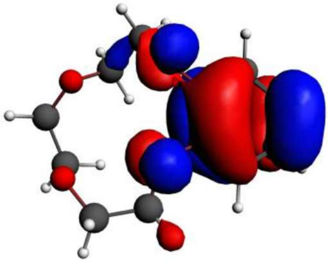	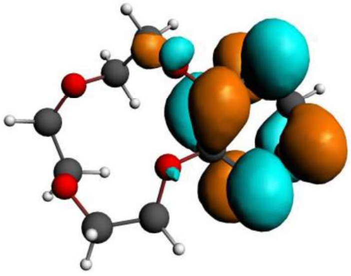
B15C5	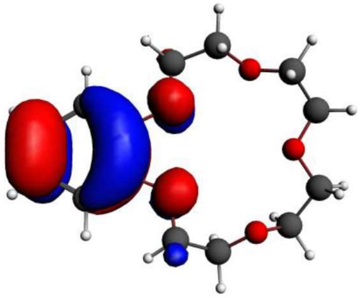	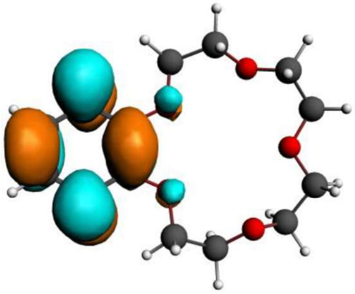
B18C6	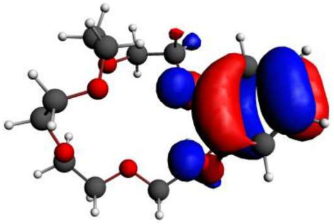	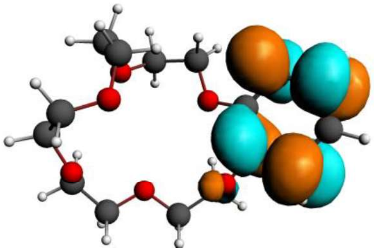
DB18C6	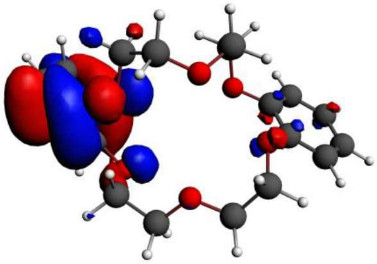	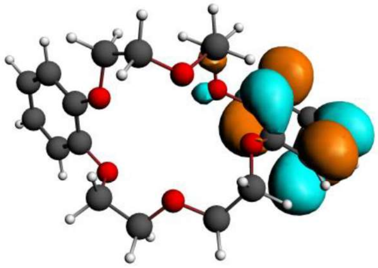

Figure 6.7 Calculated HOMO and LUMO of different crown ethers.

System	HOMO	LUMO
B12C4	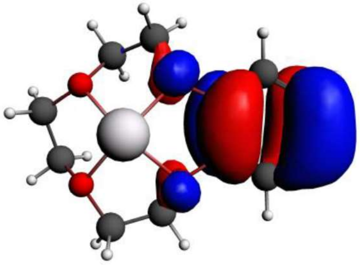	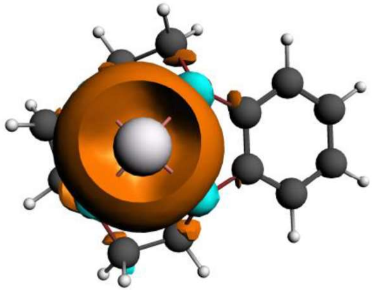
B15C5	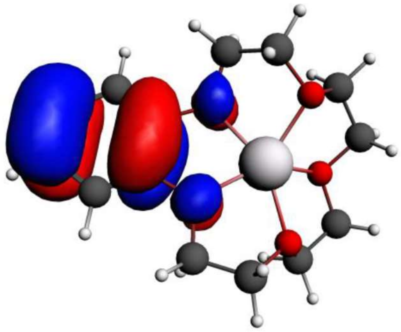	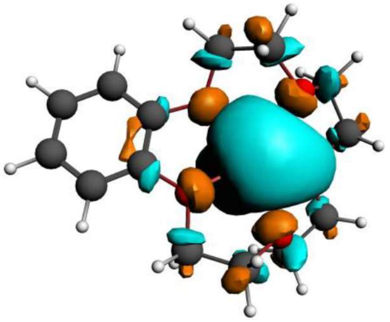
B18C6	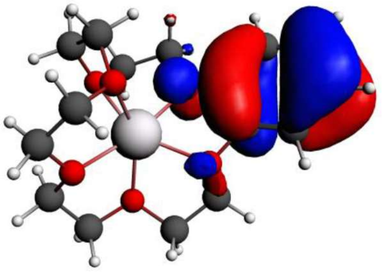	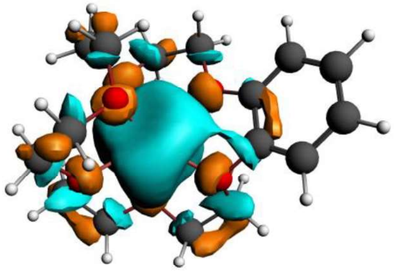
DB18C6	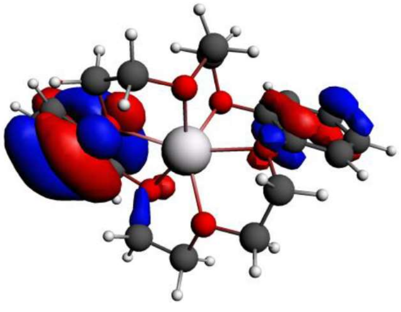	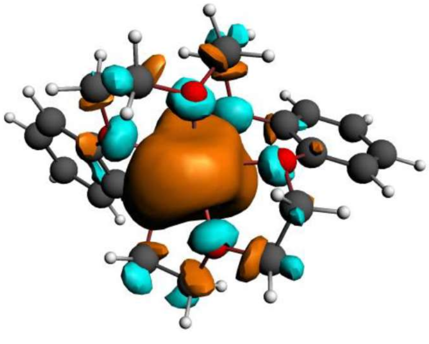

Figure 6.8 Calculated HOMO and LUMO of Zn-crown ether systems.

6.2.5.3 **Second order interaction energy**

The selectivity of metal ion with various ligands can be further investigated using natural bond order (NBO) analysis program NBO 5.0[389]as implemented in ADF package [390]. We have performed NBO analysis to understand the nature of coordinated interaction between metal ions and the ligands. In this analysis the values of second order interaction energies, $E_{ij}^{(2)}$ are used as measure of the strength of the coordinated interactions. The stability of a complex is related to the stabilization energy, $E_{ij}^{(2)}$. The larger the stabilization energy higher is the stability which in turn enhances the selectivity of the metal ion by the ligand. The stabilization energy, $E_{(i,j)}^{(2)}$ is nothing→ but the intermolecular delocalization (2e-stabilization) i j for each donor NBO (i) and acceptor NBO (j) orbital and is expressed as

$$E_{(i,j)}^{(2)} = \frac{q_i \times F_{(i,j)}^2}{(\varepsilon_i - \varepsilon_j)} \tag{6.5}$$

where, q_i is the donor orbital occupancy, and ε_i are diagonal elements (orbital energies), and $F_{(i,j)}$ is the off-diagonal NBO Fock matrix element. The $E_{(i,j)}^{(2)}$ is related to the strength of charge transfer interaction between Lewis type NBOs (donor) and non-Lewis NBOs (acceptor). The stronger the donor-acceptor interaction, larger the value of $E_{ij}^{(2)}$. The calculated values of $E_{(i,j)}^{(2)}$ is presented in **Table 6.10**. Lone pair of crown ligand, LP(O) acts as the NBO donor and the anti bonding vacant orbital of Zn2+ ion is the NBO acceptor, LP*(Zn). The stabilization energy from the lone pair of O atoms in case of B12C4 is highest and is lowest for B18C6. Though the binding energy is highest with

DB18C6 compared to B12C4, the $E^{(2)}_{(i,j)}$ is found to be higher in B12C4 compared to DB18C6.

6.3 Zinc adsorption and isotope separation using PMA, PMA-DB18C6 and PMA-B15C5 Resins

6.3.1 Batch Studies

6.3.1.1 Effect of pH

The adsorption of Zinc (II) solution was carefully studied over a pH range of 2.0 – 9.0. In order to investigate this effect of pH, experiments were initially performed to optimize the value of pH for our study. The adsorption of Zn (II) from the $ZnSO_4.7H_2O$ solution by PMA & DB18C6PMA resin was performed, and it was found that for PMA resin the optimum value of pH was found to be at pH 6, where maximum adsorption capacity was found to be as 0.56 mg/g. Similarly, the optimum value for Zn (II) uptake for DB18C6PMA was found as 0.74 mg/g at pH 7. The following plot (**Figure 6.9**) for effect of pH on adsorption of Zn (II) provides a clear picture.

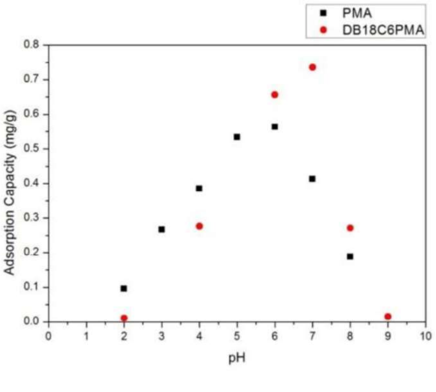

Figure 6.9 pH dependence on Zn adsorption by PMA ands PMA-DB18C6

The plot can be explained by the fact that, there is a tough competition between Zinc (II) and H^+ ions for the available and active adsorption sites on the PMA & DB18C6PMA resin surface at low pH levels; when the pH increases, the covered H^+ leaves the resin surface, making more adsorption sites available for Zinc (II). Adsorption is affected mainly by the protonation/deprotonation of the adsorbate and the change in the surface charge of the adsorbent which alters the pH value significantly. In general, the pH-dependent protonation/deprotonation brings about a change in the polarity of the adsorbate and consequently also in its absorbability. Moreover, the pH may disturb the surface charge of the adsorbent. Hence, the optimal pH value for Zn (II) extraction is 6.0 for PMA and 7.0 for DB18C6PMA.

6.3.1.2 **Kinetic studies**

To study the potential rate-controlling steps of adsorption, pseudo-first-order and pseudo-second-order kinetic models are used to simulate the experimental time dependent zinc adsorption data. The observed kinetic data and the fitted lines of first and second order kinetic equation are shown

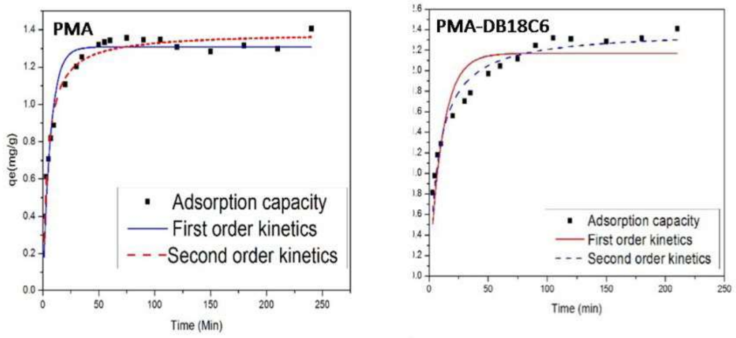

Figure 6.10 Effect of contact time and non-liner data fitting with first and second order model

in **Figure 6.10**. The adsorption of Zinc (II) by PMA and PMA – DB18C6 is greatly influenced by the contact time between the adsorbent and adsorbate. In the case of PMA resin adsorbent, the maximum adsorption capacity was attained in 75 minutes whereas for PMA – DB18C6 resin adsorbent it was achieved in 90 minutes. Thereafter the adsorption capacity didn't show any significant rise as the contact time was increased. This activity can be explained by the fact that, Zinc (II) ions in the solution were first adsorbed on the unsaturated functional sites found on the adsorbent surface. Then these adsorbent sites were saturated as zinc diffused into the adsorbent microspores, eventually saturating all the available adsorbent pores and refusing further adsorption. The first and second order kinetic models were utilized to obtain the non-linear fittings. The constant values of two adsorption kinetic models were tabulated in **Table 6.12**. The acquired R^2 values indicated that adsorption of Zn followed second order kinetics in both the adsorbents. For that reason, we conclude that chemisorption should be the rate controlling step of the adsorption of Zinc on PMA and PMA – DB18C6.

Table 6.12 Constant values of two adsorption kinetic models

Modelling	**Parameter**	**PMA**	**PMA - DB18C6**
First Order	R^2	0.91459	0.84789
	K_1 (min^{-1})	0.14834	0.08877
	q_e(mg/g)	1.30746	2.1685
Second Order	R^2	0.96476	0.95996
	K_2 (min^{-1})	0.16938	0.05003
	q_e (mg/g)	1.38442	2.39074

6.3.1.3 **Isotherm studies**

The equilibrium data for the Zn(II) sorption by PMA and PMA-DB18C6 were simulated with four known isotherm model as Section 4.6.1.2. The fitted parameters generated after non-linear fitting of the respective model are depicted in **Table 6.13**. The Langmuir model was fitted most suitably as the R^2 value for PMA and PMA – DB18C6 is maximum in Langmuir isotherm model i.e. $R^2 = 0.90996$ and 0.95193, respectively. The maximum monolayer sorption capacity (qm) of PMA and PMA-DB18C6 for Zn^{2+} ions evaluated using Langmuir isotherm model was found to be 1.11 and 3.67 mg/g, respectively. The enhancement in adsorption in PMA-DB18C6 compared to PMA may be linked to presence of DB18C6 crown ether on the surface of the former resin. The higher adsorption capabilities of PMA-DB18C6 are also evident from the higher n, C and ε values in Freundlich, Tempkin and D-R isotherms.

Table 6.13 Constant values of two adsorption isotherm models

Modelling	Parameters	PMA	M-PMA
Langmuir	q_e(mg/g)	1.11	3.67
	b(1/mg)	0.134	0.0141
	R^2	0.90996	0.9513
Freundlich	K	0.528	0.3387
	n	0.129	0.38
	R^2	0.8466	0.862
Tempkin	$A_T(g^{-1})$	27.787	0.1708
	C(j/mol)	0.1225	0.7508
	R^2	0.8841	0.9336

6.3.1.4 **Effect of temperature**

The change in adsorption capacity with change in temperature 30 to 80 ◦C of the feed Zn(II) aqueous is shown in Figure **6.11**. The adsorption capacity of PMA and M-PMA increased as the temperature increased from 30 to 80 ◦C. The adsorption capacity of PMA increased with increasing temperature from 30°C to 80°C, which suggests that high temperature accelerates the adsorption of Zinc (II) on the surface of PMA. This mainly happens due to the loosening effect produced by the high temperature condition. The loosening effect causes the structure of the PMA to open up, this result in increased porosity and more binding sites made available for adsorption. The adsorption capacity of PMA – DB18C6 decreased with increasing temperature due to the fact that Zn^{2+} metal ions adsorption was not in favor of temperature shows that the attractive forces and movement of the adsorbate Zn^{2+} metal ions in the direction of PMA – DB18C6 adsorbent declined with increasing temperature hence resulting in reduced adsorption capacity.

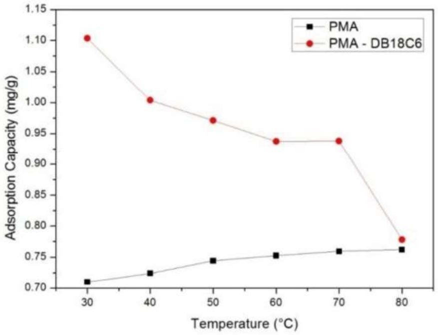

Figure 6.11 Temperature dependence plot

6.3.1.5 **Effect of Ionic strength**

The dependence ionic strength of the feed solution on the Zn(II) adsorption by PMA and PMA–DB18C6 is shown in **Figure 6.12**. The increasing ionic strength of the solution decreases the adsorption capacity of the resin. In this study, it was found that the adsorption of Zinc declined more steeply when the ionic strength was increased from its initial level to its transitional level compared to the transitional level to the peak level. The adsorption capacity for PMA and PMA – DB18C6 reduced drastically when the ionic strength was increased from 0.0 M to 0.01 M. The reason for such huge change can be attributed to the charge characteristics of the ions, which interferes in adsorption and thereby reducing the adsorption capacity.

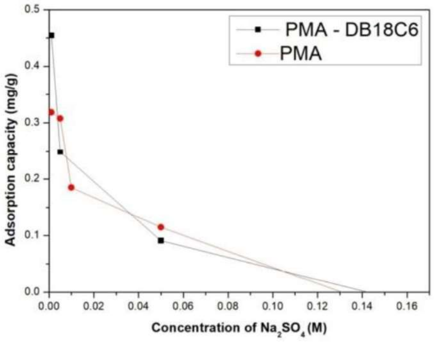

Figure 6.12 Dependence of ionic strength on adsorption

6.3.1.6 **Selectivity**

The preferential adsorption of Zn(II) in presence of another metal ions determines the use of an adsorbent for practical water treatment processes. This selectivity was studied by performing separation of Zn with one another metal ion forming a binary mixture. **Figure 6.13** shown below describes the competitive behaviour during adsorption of binary pair of Zinc (II) and other metal ions. PMA and PMA–DB18C6 showed maximum adsorption for Iron, Copper and Cadmium metal ions over Zinc. The transition elements follow a reactivity series of Fe > Cd > Cu where Fe being the highly reactive metal of all three. Thus these adsorbents may not be a good candidate for water treatment process to remove zinc ion, but can be used in zinc isotope separation process where high sorption capacity is not a essential requirement.

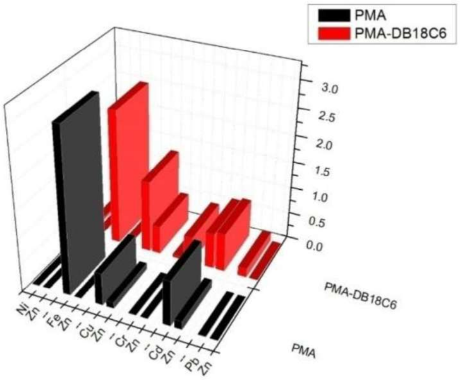

Figure 6.13 Binary selectivity of PMA and PMA-DB18C6 for Zn

6.3.1.7 **Regeneration**

Regeneration of used adsorbents can be advantageous as it proves to be economical by reducing the various costs associated with the process. Regenerating the adsorbent helps in recovering Zinc (II) and also curbs the secondary environmental pollution. 0.1M H_2SO_4 solution was used as desorbing agent. As it was seen in pH effect studies (Section 6.3.1.1) at low pH the adsorption is almost nil, because the –COOH and crown ether of PMA and PMA-DB18C6 would be protonated by H^+ ions which facilitates desorption of positively charged Zn (II). The regeneration cycles showed that desorption capacity decreases with increasing cycles and after 5 regeneration cycles it is halved (**Figure 6.14**).

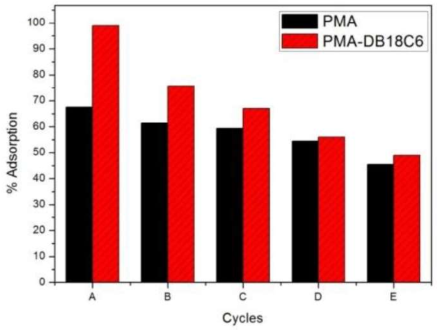

Figure 6.14 Five adsorption-desorption cycles

6.3.2 Fixed-bed Column Chromatographic Studies

6.3.2.1 **Breakthrough and Elution Curves**

The breakthrough and elution curves obtained from the column studies are shown below. In this study, flow rate of 4.5 mL/min was maintained by using a peristaltic pump. 1 L of Zn solution was passed through the column having 9.25 g of PMA-DB18C6 adsorbent. Effluent solution samples were collected for plotting the breakthrough curve. From the breakthrough plot shown in **Figure 6.15(i)**, we determined that the breakthrough (C_t/C_o = 0.05) was achieved at 3.76 mL, or t_b was found to be at approximately 4.44 minutes. The bed exhausted (C_t/C_o = 0.95) after 244.51 ml of Zn solution was passed through it, $t_e$was found to be approximately at 104.44 minutes. The area under the curve was calculated to evaluate the adsorption capacity using the formulas. The adsorption capacity determined was 3.71 mg/g which was close to the maximum capacity calculated by the Langmuir model which was 3.67 mg/g. Mass transfer zone was calculated from t_b and t_e and found to to be 0.9574 cm.

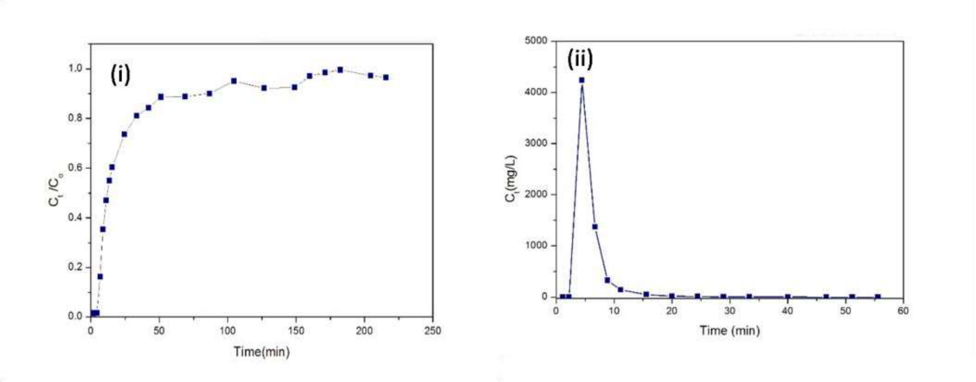

Figure 6.15 (i) Breakthrough and (ii) Elution curve for Zn^{2+} adsorption on PMA-DB18C6 column

The desorption of the loaded Zn on the PMA-DB18C6 bed was carried out using 1M H_2SO_4. The desorption or elution curve is shown in **Figure 6.15(ii)**. The complete desorption was achieved within 15 minutes of the elution. Thus the whole adsorbed zinc from can be calculated in ~45 mL of elution medium. The results of this column studies suggest that zinc isotope separation in column chromatographic operation can be carried out for higher depleted ^{64}Zn preparation, which is explored in the proceeding section

6.3.2.2 Evaluation of fixed bed adsorption parameters

The adsorption studies are very important to evaluate the data which can be used for scale up the adsorber system for its best performance. These studies can be carried out by developing different conditions like variation of flow rates, bed heights and influent concentrations. These different conditions can be helpful for prediction of changes in adsorber characteristics and the various adsorption performances.

6.3.2.2.1 Effect of influent Zn (II) concentration (C_0)

The mass transfer between the adsorbate and the adsorbent plays a vital role in the adsorbent column system. The mass transfer flux is the rate of mass transfer per unit area perpendicular to the adsorbate flow. Mass transfer flux generally depends on the mass transfer coefficient and the concentration gradient. Now, as the concentration gradient is responsible for the mass-transfer driving force the feed solution will surely affect the driving force of mass-transfer phenomenon. So, to determine this mass transfer driving force, the initial feed solution Zn (II) was varied from 70 to 500 mg/L with constant PMA-DB18C6 bed height (H_b) and flow rate (F_V) of 10 cm and 4.5 mL/min respectively, using fixed-bed column chromatographic set up as described in Figure 2.23 of Chapter 2. The effect of the various inlet Zn (II) concentrations with the adsorption breakthrough curves are shown in **Figure 6.16**. It is apparent from the Figure that the breakthrough time [391] was decreased as the initial Zn (II) feed concentration increased because of the increasing concentration gradient leading to the increased Zn (II) ions resulting more availability for binding sites. So, we can conclude that with higher concentrations we get higher adsorption. Conversely, a low feed concentration has lower concentration gradient

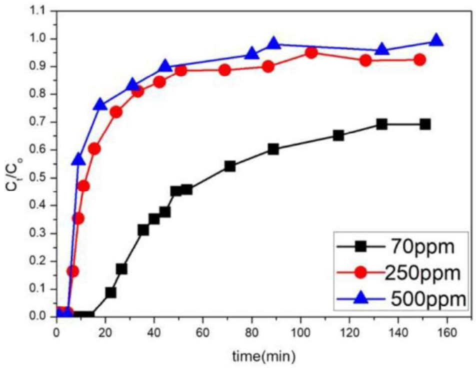

Figure 6.16 Breakthrough curves of Hg(II) adsorption at different initial inlet concentrations

which decreases Zn (II) adsorption on the adsorbent. At different initial Hg(II) feed concentrations of 70, 250 and 500 mg/L, the maximum bed capacities were increased with inlet concentration and thus adsorbent usage rate was increased with the Hg(II) feed concentration (**Table 6.14**).

6.3.2.2.2 Effect of influent volumetric flow rate (F_v)

The influent volumetric flow rates affect the rate of change in bed capacity significantly with respect to the service time. A higher solution volumetric flow rate decreases the residence time for the adsorbate to adsorb on adsorbent. As the adsorbates have then less time to react with the adsorbent, the bed capacity eventually will decrease. Therefore, a high flow rate usually decreases the bed adsorption capacities. **Figure 6.17** shows the effect of adsorbate solution feed volumetric flow rates on Zn (II) adsorption using experimental breakthrough curves. For that flow rate was varied from 0.5 to 4.5 mL/min with a constant bed height of 10 cm.

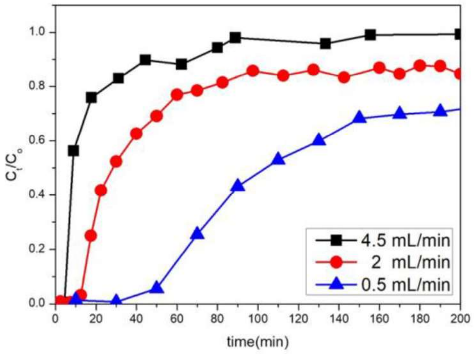

Figure 6.17 Breakthrough curves of Hg(II) adsorption at different flow rates

The values evaluated in the **Table 6.14** indicate that the breakthrough time [391] generally occurred lowered as the flow rate was decreased to 0.5mL/min. At high adsorbate flow rate, the Zn (II) had less time to contact with the adsorbent bed before reaching the adsorption equilibrium, leading to a steeper breakthrough curve and a reduction in removal efficiency. At lower flow rates with higher contact time the active sites of the adsorbent were occupied rapidly by the Zn (II) ions because of the increased mass transfer rate, and thus the adsorbent bed became saturated quicker. Conversely, at higher flow rates because of lower contact time the mass transfer decreased leading to the lower adsorption capacities.

6.3.2.2.3 Effect of adsorbent bed height (H_b)

In any fixed bed, the amount of adsorbent inside the adsorbent bed makes a huge impact on the bed capacity. To investigate the difference such between the removal capacities different bed heights were used. 2.45 to 9.62 g of PMA-DB18C6 were filled to an approximately 3 –10 cm of desired bed height. The effect of adsorbent bed height (H_b) was studied at an initial Zn (II) feed concentration of 250 mg/L and a flow rate of 4.5 mL/min, respectively. The breakthrough curves at different bed heights are shown in **Figure6.18**. It can be observed that the steepness of all the breakthrough curves is strongly influenced by the adsorbent bed height. The slope of the breakthrough curve decreased with increasing bed height due to a longer contact time which resulted in a

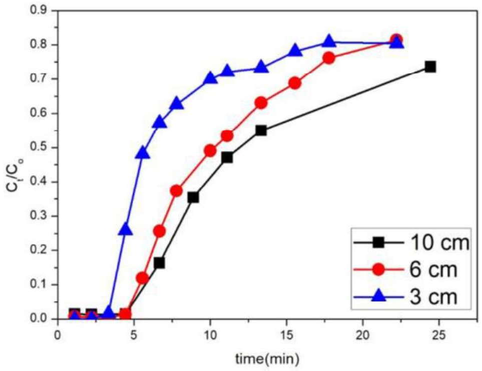

Figure 6.18 Breakthrough curves of Hg(II) adsorption at different flow rates

higher removal capacity and a lower solute concentration in the effluent. As the bed height was increased from 3 cm to 10 cm, the breakthrough point increased from 40 to 148 min **Table 6.14**.

Table 6.14 Experimental parameters of adsorptive removal of Hg(II) by PMA-DB18C6 in the

Parameter	**F_v(mL/min)**	**H_b(cm)**	**C_o(mg/L)**	**t_b(min)**	**t_s(min)**	**q_t(mg/g)**	**EBCT(min)**	**U_r(g/L)**
Flow rate	0.5	10	500	50	1130	13.38	35.34	0.46
	2.0	10	500	12.5	200	4.24	8.83	0.61
	4.5	10	500	4.44	133	2.04	3.92	0.92
Bed height	4.5	10	500	6.66	148	2.53	3.93	0.46
	4.5	6	250	3.33	56	1.94	2.35	0.55
	4.5	3	250	2.22	40	4.35	1.18	0.55
Inlet Concentration	4.5	10	500	4.44	133	2.04	3.93	0.92
	4.5	10	250	6.66	148	2.53	3.93	0.46
	4.5	10	70	22.22	257	8.81	3.93	0.15

This fact could be attributed to the increase in the effective surface area (larger bed) of adsorbent by increasing the mass of the adsorbent which supplies more fixation binding sites. The mass transfer zone becomes longer as the bed height increased which subsequently resulting in an extended break- through time leading to an increase in the volume of treated solution. However, high values of H_b are not advised because the longer bed tended to be more gradual indicating the adsorber will be difficult to completely exhaust.

6.3.2.3 **Washing of the unadsorbed Zn(II) from the bed**

After the adsorption of adsorbate on the adsorbent bed it should be washed with deionized water to remove the unadsorbed adsorbate on the column. The adsorbent bed was washed

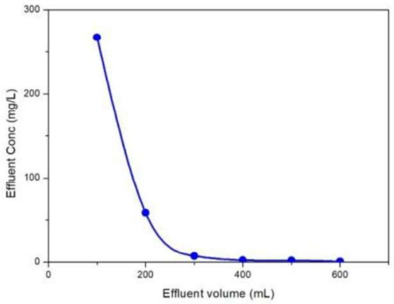

Figure 6.19 Washing of the unadsorbed Zn(II) in the PMA-DB18C6 bed

after the adsorption of every time with deionized water for before performing desorption. The washing is done for the removal of excess adsorbate that remained unadsorbed on the bed but still lingering in the column. The unadsorbed adsorbate is removed from the column by passing 500-600 mL of deionized water. The graphical presentation of effluent conc. vs effluent volume is shown in the **Figure 6.19**. This Figure shows the decrease in Zinc concentration after appropriate volume of deionized water is passed. The washing was done after desorption also to remove excess desorbing agent by passing deionised water.

6.3.2.4 **Estimation of Elution curves**

The adsorbed zinc ion onto the PMA-DB18C6 in all the above breakthrough experiments needed to be quantitatively desorbed for the reuse of the adsorbent and to get the pure or isotopically enriched/depleted analyte solution. **Figure 6.20** shows that all the used bed was quantitatively desorbed with 60 mL of elution volume.

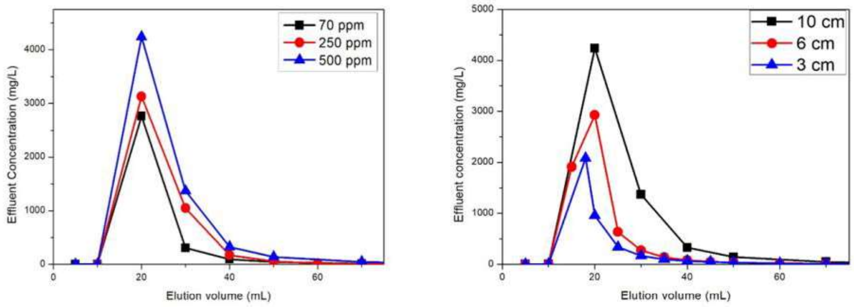

Figure 6.19 Elution of Zn(II) from the PMA-DB18C6 using 1M H2SO4

6.3.3 Separation performance of PMA-DB18C6 for zinc isotopes in Batch mode

The isotopic enrichment of ^{66}Zn and ^{64}Zn isotope pair was calculated from the isotopic ratio of these two isotope in the liquid phase of the batch adsorption studies using PMA and DB18C6-PMA. As seen from the **Table 6.15**, the heavier isotope ^{66}Zn is enriched in solution phase, whereas the lighter 64Zn enriched in the resin phase. This fractionation of two isotopes is more in case of DB18C6-PMA as indicated by the higher enrichment value. This means, ^{64}Zn depleted zinc can be made by collecting elution samples of a continuous adsorption run of natural zinc on DB18C6-PMA. Thus DB18C6 crown ether functionalization on the PMA resin has resulted in four time higher adsorption of zinc and ten order larger enrichment of ^{66}Zn/^{64}Zn isotope pair.

Table 6.15 Zinc isotope ratio and enrichment factor in batch study using PMA and PMA-DB18C6

	Isotope Ratio (^{66}Zn/^{64}Zn) Before adsorption	**Isotope Ratio (^{66}Zn/^{64}Zn) after adsorption**	**Enrichment (^{66}Zn/^{64}Zn)**
PMA	0.56395	0.56407	1.0002
DB18C6-PMA	0.56268	0.56398	1.0023

6.3.4 Zinc Isotope separation performance with PMA-DB18C6 in Column run

The isotopic analysis of fractional effluent solution collected at 0.5ml/min flow rate from 500 mg/L Zn(II) feed in a 10cm bed height (PMA and PMA-DB18C6) of a above column, were performed in MC-ICP-MS. The result of batch study in preceding section was reflected in the zinc isotopic ratio data of feed and fractional effluent samples. The separation coefficient (ε) for depletion of ^{64}Zn was calculated by using Equation 2.25 of Chapter 2 from the Zn adsorption and isotopic ratio (^{66}Zn/^{64}Zn, ^{68}Zn/^{64}Zn, ^{69}Zn/^{64}Zn, and ^{70}Zn/^{64}Zn) data. The evaluated ε values for PMA and PMA-DB18C6 were compared in **Figure 6.21**. The higher isotope separation efficiency of PMA-DB18C6 over PMA resin for all the isotope pair is noticeable. The role of crown ether cavity for isotope fractionation is evident from the graph. **Figure 6.22** represents a chromatographic breakthrough profile of Zn separation in the lower part and heavier to lighter Zn isotope

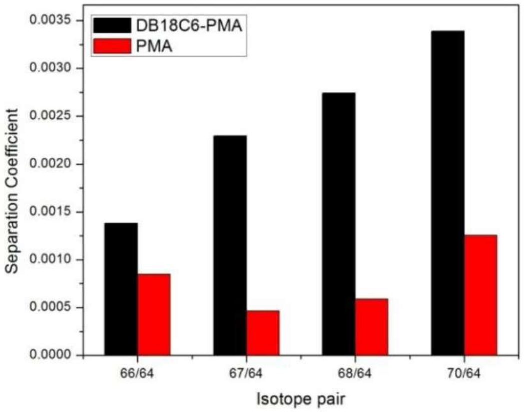

Figure 6.20 Zn isotope separation factor in column separation using PMA and DB18C6-PMA resin

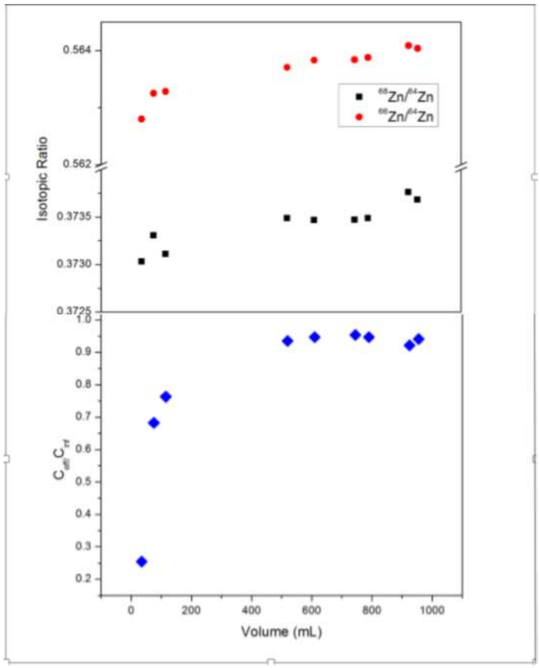

Figure 6.21 Zn isotope fractionation and effluent concentration profile separated using DB18C6-PMA resin

ratio (^{H}Zn/^{64}Zn) in the upper part in PMA-DB18C6 bed. In the mass transfer zone ^{H}Zn/^{64}Zn ratio increases steadily upto the saturation. i.e, the heavier Zn isotope is enriching in the effluent and depleting on the on the PMA-DB18C6 bed is. Thus elution effluent volume is of depleted ^{64}Zn which was tested in the desorbed sample.

6.3.5 Separation performance of PMA-B15C5 for zinc isotopes in Column run

Similar fixed-bed chromatographic run performed with synthesized PMA-B15C5 resin and the preliminary observed results, as shown in **Table 6.16**, reflects the increase in the ^{H}Zn/^{64}Zn in the mass transfer zone of the breakthrough effluent samples.

Table 6.16 Zn isotopic ration in chromatographic profile using PMA-B15C5 bed

Sample Name	$^{68}Zn/^{64}Zn$	$^{68}Zn/^{66}Zn$
Feed Zn (Natural)	0.423307	0.700346
PMA-B15C5-Effluent - I (after passing 140 ml of feed solution)	0.445854	0.745341
PMA-B15C5-Effluent - -II (after passing 185 ml of feed solution)	0.450641	0.753139
PMA-B15C5-Effluent -III (after passing 190 ml of feed solution)	0.453489	0.759003
PMA-B15C5-Effluent -IV (after passing 200 ml of feed solution)	0.447640	0.748611

6.4 Conclusion

Density functional theory is used to calculate the structure, bonding, energetic, thermodynamics and IR frequency of complexes of Zn^{2+} ion with crown ethers of different nano confinement and also with crown ether anchored on EDDP resin. The Zn^{2+} ion is found to be completely encapsulated in the cavity of B15C5 leading to five coordination. The gas phase binding energy was found to be increased from B12C4 to DB18C6 with increasing cavity size. The gas phase binding energy can be correlated with NPA charge transfer but no such correlation is obtained with the fraction of electron transfer, ΔN. The order of free energy of complexation was found to be: DB18C6>B18C6>B15C5>B12C4. The free energy of complexation was also reduced drastically in aqueous phase compared to gas phase but the trend remains same i.e DB18C6>B18C6>B15C5>B12C4. The reduced partition function ratio for complexes of Zn^{2+} ion with different solvents and crown ethers and crown ether resins is calculated which is further used to calculate the separation factor of zinc. It is shown that confinement induces separation of isotopes that can be used in practical separation process like chromatographic process. In the present calculation B18C6 resin is found to be most suitable crown resin whereas experiment predicts B15C5 resin is the best one. Further, it is shown that smaller the solvation energy of the metal ion higher will be distribution constant of Zn^{2+} ion as confirmed by experiments indicating solvents with low dielectric constant should be used for chromatographic separation process.

Adsorptive removal of Zn^{2+} ions was performed from aqueous solution by grafting crown ether on PMA resin. Adsorption batch studies were carried out for both PMA and crown ether grafted PMA for comparison purpose. Adsorption isotherms followed as Langmuir isotherm in both the adsorbents. Also, in the case of kinetics both the adsorbents shadowed second order kinetics. The maximum adsorption capacity for PMA resin was 1.2 mg/g and for PMA-DB18C6 was determined as 3.6 mg/g at room temperature which clearly represents the increased adsorption capacity because of the grafted crown ether. Five adsorption-desorption cycles were carried out without significant loss of adsorption capacity using 1M H_2SO_4 as desorbing agent.This fractionation of two isotopes is more in case of DB18C6-PMA as indicated by the higher enrichment value. This means, ^{64}Zn depleted zinc can be made by collecting elution samples of a continuous adsorption run of natural zinc on DB18C6-PMA. Thus DB18C6 crown ether functionalization on the PMA resin has resulted in four times higher adsorption of zinc and ten order larger enrichment of $^{66}Zn/^{64}Zn$ isotope pair. Isotopic profile was created in column chromatographic system using PMA and PMA-DB18C6. Solid phase was found to enriched with lighter isotope. Higher isotope separation coefficient was observed for PMA-DB18C6 that that of PMA.

7 Chapter 7: Summary and Future Scope

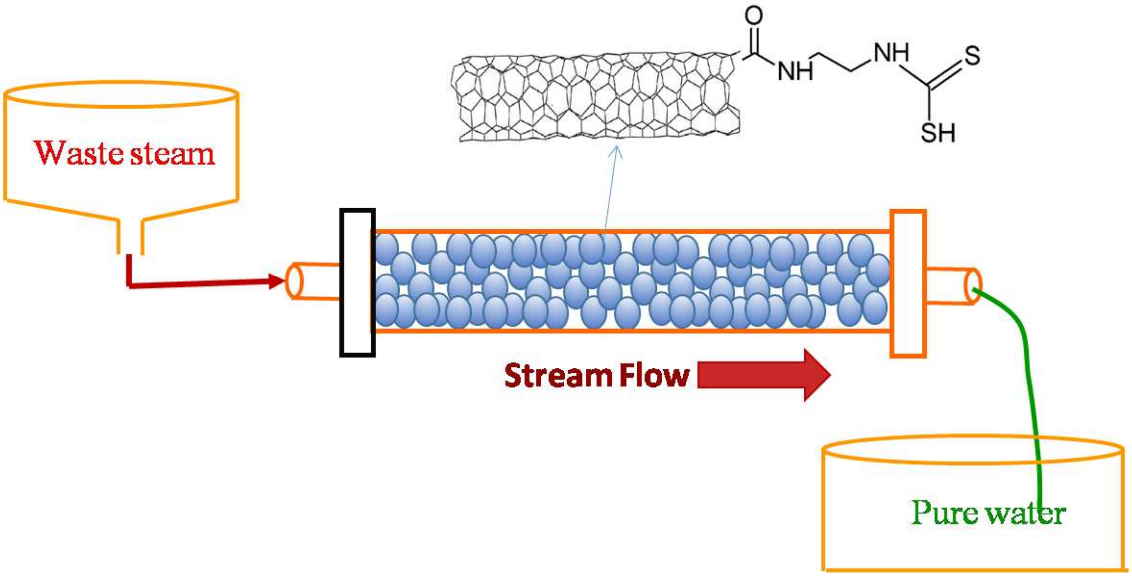

Summary

The waste treatment of either nuclear or on-nuclear has always drawn a widespread attention for safe and livable environment for the living creatures. This waste processing starts majorly with the removal of the toxic metals from the used up solution. There is a continuing endeavor to remove/recover the toxic metals by means of complexation with a complexing agent generally known as ligand/extractant/adsorbents etc. Among many, Th, U, Np, Pu, Am, Cm, and Hg are of major concerns due to their immediate removal/recovery before final disposal of the used up solution. Another important separation process by means of complexing is the isotope separation. Research are being pursued to develop a process for isotope separation of Zn because ^{64}Zn-depleted zinc is used in the primary coolant of nuclear power plant to reduce the formation of radioactive cobalt isotope, presence of which leads to radiation threat to the working personal. Therefore, a systematic and sincere effort lead to suitable ligand functionalized CNTs and polymeric solid support for metal ion (Th, U, Np, Pu, Am, Cm, and Hg) and isotope (Zn) separation after selecting proper ligand and solid support from literature using DFT calculations, preparation of the adsorbents and experimental adsorption studies.

In the liquid-liquid/solid extraction, several factors affect the adsorption of a particular metal ion and thus affect the efficiency of the adsorption process. Some of them are i) metal ion hydration environment, ii) distribution of the metal ion, iii) nature of ligand to be functionalized, iv) type of solid matrix. By alteration the molecular properties of the adsorbents, the overall efficacy of the separation process can be improved. From chapter 2-6, several important problems related to reprocessing of the nuclear/non-nuclear waste

as well isotope separation process have been addressed using computational and experiments and these studies will definitely provide the fundamental insights for the separation of metal ions and isotope separation. The conducted studies in this thesis will be useful for the future design of adsorbents which are summarized and concluded as follows:

In chapter 2, detailed experimental and theoretical methodologies adopted for the thesis have been presented. The structures, interaction, bonding and thermodynamic parameters for the complexation of Th^{4+} ion with p-CNT, CNT-COOH CNT-DGA using DFT were reported in chapter-3. The free energy of adsorption for Th^{4+} ion by the three CNTs was computed. Gas phase results though provide qualitative idea about the complexation reaction, does not represent the real system that occurs in solution phase. Results of aqueous phase calculation are comparable with the experimentally obtained trend of adsorption capacity of Th^{4+} with p-CNT, CNT-COOH and CNT-DGA. The p-CNT has positive free energy of adsorption implying zero interaction with Th^{4+} in aqueous phase. DGA being tridentate ligand compared to bidentate –COOH, CNT-DGA was expected to be shown higher interaction/complexation with Th^{4+} ion. But, CNT-COOH has higher free energy of adsorption than that of CNT-DGA; same is reflected from the experimental values of adsorption capacity. C60-COOH has quite high value of binding energy with Th^{4+} indicating enhancement of adsorption by CNT-COOH in presence of C60-COOH. The present study was a modest attempt to model the complex chemical problem like the complexation reaction of Th^{4+} ion with pristine, COOH and DGA functionalized CNT and can be used further for the future design of functionalized CNT for the removal of

Th^{4+} and other radionuclide ion from nuclear waste. Additionally, the structures, interaction, bonding and thermodynamic parameters for the complexation of Eu^{3+} and Am^{3+} ion with CNT-DGA using DFT were also computed. The free energy of transfer for Eu and Am ion with CNT-DGA was successfully captured. From the estimated distribution constant, it was indisputably established that the Eu^{3+} ion is preferentially extracted over Am^{3+} ion and hence confirm the acceptance of the explicit cluster model for ion solvation free energy and thermodynamic cycle for the evaluation of free energy of extraction in solution phase. Finally, this was the first study where the CNT-DGA was tested both theoretically and experimentally for the extraction of Eu^{3+}/Am ions. CNT-DGA was also demonstrated as a highly efficient sorbent for Am^{3+}, Pu^{4+} and PuO_2^{2+} with the trend in the K_d values: $Am^{3+} > Pu^{4+} > PuO_2^{2+}$. Based on the linear regression coefficients, the Langmuir isotherm was found to be predominating. The sorption energy calculated from the D-R isotherm revealed that there was chemical interaction between DGA-CNT and the actinide ions i.e. chemi-sorption. The sorption was found to proceed via pseudo 2nd order kinetics. Suitable stripping agents were also identified for the back extraction of the actinides of different oxidation states from CNT-DGA. The sorbent was also found to have good radiolytic stability. The photoluminescence investigation revealed that the Eu^{3+} in complex with CNT-DGA exists as single species. The complexation also led to the increase in covalency between Eu^{3+} and O bond from ligand functionality. DFT revealed the tridentate coordination mode of the DGA moiety towards Pu^{4+} and Am^{3+} and bidentate coordination mode towards PuO_2^{2+}. The binding energy of sorption with CNT-DGA of Pu^{4+} was higher than that of PuO_2^{2+} both in gaseous and aqueous phase, whereas for Am^{3+} it was higher than PuO_2^{2+} but less than Pu^{4+}. The free energy of sorption was also highest for Pu^{4+} uptake and lowest for PuO_2^{2+} both in gaseous and aqueous phase. The theoretical observation inferred that CNT-DGA binds Pu^{4+} and Am^{3+} strongly than PuO_2^{2+} and the same is corroborated from the sorption experiment. Amido-amine (AA) was shown to be good complexing ligand, hence novel AA functionalized MWCNT was synthesized and studied for adsorption of radionuclide in chapter-4. The MWCNT-AA showed high sorption capacity for ^{233}U and ^{241}Am. DFT studies proved the experimental observation of higher sorption capacity of ^{233}U compared to ^{241}Am due to stronger complexation strength of U-MWCNT-AA over Am-MWCNT-AA and higher negative solvation energy of U(VI) compared to Am(III). MWCNT-AA was demonstrated as highly selective and efficient sorbent for tetra and hexavalent plutonium also. Different isotherm analysis revealed that, Langmuir isotherm is predominantly operative through mono layer without mutual interaction of the neighboring complexation sites. The sorption was also found to be chemisorption. Based on linear regression analysis the sorption process was found to proceed via pseudo second order reaction. The sorbent was also found to show high radiolytic stability even up to a gamma exposure of 1500 kGy. DFT revealed that MWCNT-AA and all the nitrate anions were coordinated to Pu metal centre in bidentate mode for both Pu^{4+} and PuO_2^{2+} complexes. The present calculated free energy of complexation from DFT was shown to be almost three times higher for Pu^{4+} than PuO_2^{2+} both in gas and aqueous phase. The theoretical results confirmed that MWCNT-AA bind Pu^{4+} strongly than PuO_2^{2+}which was also corroborated from the sorption experiment. MWCNT-AA was found to be highly efficient sorbent for penta and hexavalent Np and also having high radiolytic stability. The sorption process was found to be chemisorption following Langmuir isotherm. The sorption capacities for NpO_2^+ and NpO_2^{2+} was evaluated as 58.1 and 83.9 mg g^{-1}, respectively. The pseudo second order reaction was found to be operative. The quantitative back extraction of penta and hexavalent neptunium was found to be achieved by EDTA and Na_2CO_3, respectively.

Adsorptive removal behavior of Hg^{2+} ions from aqueous solution by indigenously prepared functionalized CNTs, MWCNT-AA, were also performed. Adsorption process was found to follow pseudo second order kinetic equation and Redlich-Peterson isotherm model, revealing chemical nature of the sorption of mercury ions on the MWCNT-AA surface. The maximum sorption capacity of 101.35 mg/g at pH 6 and room temperature was observed which is higher than conventional absorbents (activated carbon/resin) and p-CNT. Adsorption was found to be an endothermic and spontaneous process. The adsorbent showed superior selectivity towards Hg(II) ions, as compared with other metal ions generally present in mercury containing industrial waste water. Six adsorption-desorption cycles were successfully carried out without significant loss of uptake using 0.05M EDTA as stripping agent. DFT showed that sidewall CNT-AA and its bi-dentate complexation with mercury was more favorable. Binding energy calculation for the selectivity of Hg^{2+} ions with other metal ions fall in congruence with the experimentally observed data. Results demonstrated the possibility of using CNT-AA as a material for removal of mercury ions through continuous flow separation in a fixed bed column.

A comparative study was carried out to understand the sorption of Pu^{4+} on MWCNT-PAMAM$_{G1}$ and MWCNT-PAMAM$_{G2}$. The sorption efficiency was found to increase with increase in aqueous feed acidity followed by plateau for both the sorbent, but the efficiency for 2nd generation dendrimer was found to be more. Based on the linear regression analyses of Langmuir, D-R, Fruendlich and Tempkin isotherms, the Pu^{4+} was found to follow Langmuir isotherm by interaction of the amidoamine functionality with the Pu^{4+} ion. To attain optimum K_d values, 180 min was found to be sufficient. The sorption of Pu^{4+} proceeded via pseudo 2ndorder kinetics with the rate constants, 0.00016 and 0.00020 mg g^{-1} min^{-1}, respectively. Both the sorbent showed high radiolytic stability upto 500 kGy while the 2nd generation dendrimer showed better stability compared to the other. More than 95 % Pu^{4+} was found to be back extracted from the sorbent by using 0.01 M oxalic acid. The overall evaluation indicated the potential application of these dendrimer functionalized carbon nano tubes for efficient separation of Pu^{4+} from aqueous acidic waste stream. This 1st and 2nd generation dendrimer was found have more sorption efficiency for Pu^{4+} compared to other carbon nanotube based sorbents. The present investigation revealed that in 1st generation of dendrimer, the K_d value enhanced to 1.5 E+04 which was found to increase further to 1.9 E+04 for the 2nd generation with retaining better radiolytic stability, selectivity and stripping behavior.

CNT-PAMAM$_{G1}$ and CNT-PAMAM$_{G2}$ were found to be highly efficient and selective for Am^{3+} and the efficiency enhances with higher generation. The sorption process followed Langmuir isotherm and pseudo second order rate kinetics. The sorption process was found to follow through chemical interaction of amidoamine group with the Am^{3+} ion.

The luminescence investigation revealed that the metal ion complex of 1st generation dendrimer was more asymmetric compared to the higher generation. In both the case there was no water molecule in the primary coordination sphere of the metal ion. EDTA was found to be successful for the effective stripping of the Am^{3+} from the loaded sorbent materials.

CNT–$PAMAM_{Gn}$ were also tested for the sorption of pentavalent neptunium from aqueous acidic solution. An increase in the feed acidity favored the sorption of Np(V) ions onto CNT–$PAMAM_{Gn}$ which was primarily due to the participation of nitrate ion in the complexation process. A thorough investigation of sorption kinetic data revealed that the sorption process followed pseudo second order kinetics with $1.4x10^{-4}$ and $6.84x10^{-4}$ g mg^{-1} min^{-1} as rate constants for CNT–$PAMAM_{G1}$ and CNT–$PAMAM_{G2}$, respectively. The energy values calculated through D–R isotherm showed that the sorption process proceeded via chemical interaction between Np(V) ions and the functionality on the surface of nanotubes. The experimental data fitted well to Langmuir isotherm model showing that the sorption is monolayer on a homogeneous sorbent surface. A small decrease in the sorption performance (~2%) was recorded for irradiated MWCNT–$PAMAM^{G2}$ whereas for MWCNT–$PAMAM_{G1}$, it was more than 17%, making these two sorbents viable for nuclear waste management. Among the two strippant solutions used, 0.5M oxalic acid was found most suitable for the back-extraction of the sorbed Np(V) ion. It can be concluded that poly(amidoamine) dendrimer functionalized CNTs can be used for the preconcentration of neptunium ions from nuclear waste solutions.

Mercury (Hg) has been categorized as a “priority hazard substance” by the Agency for Toxic Substances and Disease Registry because of its toxicity, mobility and a long residence time in the atmosphere. Mercury, a soft B-group metal, exhibits relatively weak interactions with oxygen containing ligands, moderate strength interactions with nitrogen-containing ligands, and strong interactions with sulfur-containing ligands. Therefore, two sulphur ligand functionalized CNTs, CNT-SH and CNT-DTC were synthesized, characterized and tested for adsorption of mercury(II) ions from aqueous solution in chapter-5. From the batch studies it was found that CNT-DTC has higher sorption capacity than that of CNT-SH due to the presence of more number of S binding sites. The equilibrium and kinetic adsorption data of both of the adsorbent fits properly with Langmuir and pseudo-second-order model suggesting surface complexation of Hg^{2+} ions on the sulphur binding sites on the surface of CNTs. The negative free energy of sorption supports the spontaneous nature of the process. The higher capacity of CNT-DTC was reflected from the more negative free energy of adsorption. Both the materials have good selectivity for Hg(II) with respect to other metal ions tested. Feasibility of continuous fixed bed separation using CNT-DTC was successfully carried out. The desorption, regeneration and reusability of the adsorbents were performed using thiourea solution. In all the experiments, CNT-DTC were proved to be superior adsorbent than CNT-SH for removal of Hg^{2+} ions from aqueous solution. The same trend has been established from the DFT calculation performed for the interaction of mercury(II) ion and mercuric chloride with CNT-SH and CNT-DTC. DFT results also inferred that the presence of chloride ions in the aqueous phase should be taken into account to arrive at the correct interaction insight.

In chapter-6, DFT is used to calculate the structure, bonding, energetic, thermodynamics and IR frequency of complexes of Zn^{2+} ion with crown ethers of different nano confinement and also with crown ether anchored on eddp resin. The Zn^{2+} ion is found to be completely encapsulated in the cavity of B15C5 leading to five coordination. The gas phase binding energy was found to be increased from B12C4 to DB18C6 with increasing cavity size. The gas phase binding energy can be correlated with NPA charge transfer but no such correlation is obtained with the fraction of electron transfer, ΔN. The order of free energy of complexation was found to be: DB18C6>B18C6>B15C5>B12C4. The free energy of complexation was also reduced drastically in aqueous phase compared to gas phase but the trend remains same i.e DB18C6>B18C6>B15C5>B12C4. The reduced partition function ratio for complexes of Zn^{2+} ion with different solvents and crown ethers and crown ether resins was calculated which is further used to calculate the separation factor of zinc. It was shown that confinement induces separation of isotopes that can be used in practical separation process like chromatographic process. B18C6 resin was found to be most suitable crown resin from DFT, whereas experiment predicted B15C5 resin as the best one. Further, it was shown that smaller the solvation energy of the metal ion higher will be distribution constant of Zn^{2+} ion as confirmed by experiments indicating solvents with low dielectric constant should be used for chromatographic separation process.

Comparative batch studies were carried out for both PMA and crown ether grafted PMA for Zn^{2+} ion adsorption. Adsorption isotherms followed as Langmuir isotherm in both the adsorbents. Also, in the case of kinetics both the adsorbents shadowed second order kinetics. The maximum adsorption capacity for PMA resin was 1.2 mg/g and for PMA-DB18C6 was determined as 3.6 mg/g which clearly represents the increased adsorption capacity because of the grafted crown ether. Five adsorption-desorption cycles were carried out without significant loss of adsorption capacity using 1M H_2SO_4 as desorbing agent. This fractionation of two isotopes was found to be more with DB18C6-PMA as indicated by the higher enrichment value indicating ^{64}Zn depleted zinc can be made by collecting elution samples of a continuous adsorption run of natural zinc on DB18C6-PMA. Thus DB18C6 crown ether functionalization on the PMA resin has resulted in four times higher adsorption of zinc and ten order larger enrichment of $^{66}Zn/^{64}Zn$ isotope pair.

Future Scope

In the present research scenario, computational chemistry based modeling is necessary for designing the state of the art molecules/adsorbent for the metal ion and isotope separations to compliment the experimental results or in planning the new experiments.

Most of the studies, reported here have been carried out using standard DFT functional without non-covalent interactions, but for large molecular systems the contribution of non-covalent interactions would be significant. Hence, dispersion corrected DFT functional would be of immense useful for these large molecular systems. Also, the heavy Ln/An metal ions were handled using ECP without spin-orbit coupling. It will be of fundamental interest to study the spin-orbit coupling effect on the stability of the complexes.

The present studies mostly include dielectric continuum based salvation model such as COSMO which does not take care of the structure of solvent. Hence, future studies should include structure of the solvent such as COSMO-RS for making the predicted data more realistic environment.

The isotope separation factor has been calculated in the gas phase. It has to be extended to solvent phase. The practical ligand functionalized adsorbents for isotopic separation of zinc was arrived by evaluating the for separation for development of isotope separation process of zinc. So DFT based modelling can be used to guide the complex experiments like isotope separation of Zn using screened ligand functionalized adsorbents. Further, classical or ab-inito molecular dynamics simulations will be of very useful for the prediction of adsorption capacity, type of isotherms, diffusion dyanmics and kinetics.

It has also been observed that most reported literature describe adsorption with these new generation nanoadsorbents in batch static process with quite good results, but very few deals at laboratory, pilot, and industrial scale columns, which are required urgently. Some workers combined nanoadsorbents with other separation technologies for complete water treatment. This needs further research for water treatment on a large scale. Much work has been carried out on this issue, and still there is huge surge in the field to develop better nano-sized adsorbents with increased affinity, capacity, selectivity, and capability, now it is a need for benchmarking of novel nanomaterials for ultimate application to work at column operations. The batch mode adsorption process conditions should be transferred to column operations with urgency so that nanoadsorption technology may be utilized for the welfare of human beings. Besides, the fate of the recovered pollutants and the exhausted nanoadsorbents has not been much addressed in the literature. To avoid hazards of the recovered pollutants and nanotoxicology of the used nanoadorbents, the scientists and technologists should develop a definite eco-friendly cost effective waste management methods.

References

1. S. Banerjee and H. P. Gupta, *Progress in Nuclear Energy*, 2017, **101**, 4-18.
2. IAEA, *Spent Fuel Reprocessing Options*, IAEA, Vienna, 2008.
3. P. K. Vijayan, V. Shivakumar, S. Basu and R. K. Sinha, *Progress in Nuclear Energy*, 2017, **101**, 43-52.
4. IAEA, *Nuclear Fuel Cycle Information System*, IAEA, Vienna, 2009.
5. H. A. C. McKay, *The PUREX process*, CRC Press, Inc, United States, 1990.
6. IAEA, *Thorium Fuel Cycle - Potential Benefits and Challenges*, IAEA, Vienna, 2005.
7. D. Magnusson, B. Christiansen, J. P. Glatz, R. Malmbeck, G. Modolo, D. Serrano-Purroy and C. Sorel, *Solvent Extraction and Ion Exchange*, 2009, **27**, 26-35.
8. P. D. Piotr Mazgaj, *Journal of Power Technologies*, 2014, **94**, 27-34.
9. IAEA, *Implications of Partitioning and Transmutation in Radioactive Waste Management*, IAEA, Vienna, 2004.
10. W. L. Lennemann, *IAEA Bulletin*, 1976, **18**, 40-47.
11. IAEA, *Classification of Radioactive Waste*, IAEA, Vienna, 2009.
12. *Status and Trends in Spent Fuel and Radioactive Waste Management*, INTERNATIONAL ATOMIC ENERGY AGENCY, Vienna, 2018.
13. K. Raj, K. K. Prasad and N. K. Bansal, *Nuclear Engineering and Design*, 2006, **236**, 914-930.
14. P. B. Tchounwou, C. G. Yedjou, A. K. Patlolla and D. J. Sutton, in *Molecular, Clinical and Environmental Toxicology: Volume 3: Environmental Toxicology*, ed. A. Luch, Springer Basel, Basel, Editon edn., 2012, pp. 133-164.
15. Euro Chlor, *The mercury cell process*, http://www.eurochlor.org/the-chlorine-universe/how-is-chlorine-produced/the-mercury-cell-process, Accessed 17 Sept, 2018.
16. in *Mercury Handbook: Chemistry, Applications and Environmental Impact*, The Royal Society of Chemistry, Editon edn., 2013, pp. 180-192.
17. T. Mihaiescu, R. Mihaiescu and A. Odagiu, *Bulletin of University of Agricultural Sciences and Veterinary Medicine Cluj-Napoca. Agriculture; Vol 69, No 2 (2012): Bulletin of University of Agricultural Sciences and Veterinary Medicine Cluj-Napoca Agriculture*, 2012.
18. A. B. Mukherjee, P. Bhattacharya, A. Sarkar and R. Zevenhoven, in *Mercury Fate and Transport in the Global Atmosphere: Emissions, Measurements and Models*, eds. R. Mason and N. Pirrone, Springer US, Boston, MA, Editon edn., 2009, pp. 81-112.
19. Toxics Link, *Mercury in India, Toxic Pathways*, New Delhi, 2013.
20. M. Ragheb, in *Nuclear, Plasma and Radiation Science: Inventing the Future* University of Illinois at Urbana-Champaign, Department of Nuclear, Plasma, and Radiological Engineering, Editon edn., 2012.
21. D. Karunasagar, M. V. Balarama Krishna, Y. Anjaneyulu and J. Arunachalam, *Environmental Pollution*, 2006, **143**, 153-158.

22. G. O. I. Directorate of Plant Protection Quarantine & Storage, *Pesticidewise consumption of indigenous pesticides during 2010-11 to 2015-16*, http://ppqs.gov.in/statistical-database/pesticidewise-consumption-indigenous-pesticides-during-2010-11-2015-16, Accessed 17 September, 2018.
23. G. O. I. Central Pollution Control Board, 2011.
24. N. Pirrone, S. Cinnirella, X. Feng, R. B. Finkelman, H. R. Friedli, J. Leaner, R. Mason, A. B. Mukherjee, G. Stracher, D. G. Streets and K. Telmer, in *Mercury Fate and Transport in the Global Atmosphere: Emissions, Measurements and Models*, eds. R. Mason and N. Pirrone, Springer US, Boston, MA, Editon edn., 2009, pp. 1-47.
25. C. T. Driscoll, R. P. Mason, H. M. Chan, D. J. Jacob and N. Pirrone, *Environmental Science & Technology*, 2013, **47**, 4967-4983.
26. K. R. Rao, *Current Science*, 2001, **81**, 1534-1546.
27. U. G. M. Assessment, *Sources, Emissions, Releases and Environmental Transport*, 2013.
28. IPCS, *Concise International Chemical Assessment Document 50: Elemental mercury and inorganic mercury compounds: human health aspects*, World Health Organization WHO,, Geneva, 2003.
29. P. H. a. Environment, *Exposure to Mercury: A major public health concern*, World Health Organization, Geneva, 2017.
30. Sustainability Program@BU, *Minamata Disease*, . http://www.bu.edu/sustainability/minamata-disease/.
31. IAEA, *Combined Methods for Liquid Radioactive Waste Treatment*, IAEA, Vienna, 2003.
32. B. M. Thomson, C. L. Smith, R. D. Busch, M. D. Siegel and C. Baldwin, *Journal of Environmental Engineering*, 2003, **129**, 492-499.
33. Q. Wang, L. Chen and Y. Sun, *Journal of Radioanalytical and Nuclear Chemistry*, 2012, **291**, 787-795.
34. S. E. Kentish and G. W. Stevens, *Chemical Engineering Journal*, 2001, **84**, 149-159.
35. A. Bonilla-Petriciolet, D. I. Mendoza-Castillo and H. E. Reynel-Ávila, in *Adsorption Processes for Water Treatment and Purification*, eds. A. Bonilla-Petriciolet, D. I. Mendoza-Castillo and H. E. Reynel-Ávila, Springer International Publishing, Cham, Editon edn., 2017, pp. 1-18.
36. E. Worch, *Adsorption Technology in Water Treatment, Fundamentals, Processes, and Modeling*, 2012.
37. R. C. Bansal and M. Goyal, *Activated carbon adsorption*, Dekker/CRC Press, Boca Raton, FL, 2005.
38. A. Mellah, S. Chegrouche and M. Barkat, *Journal of Colloid and Interface Science*, 2006, **296**, 434-441.
39. E. Taskaev and D. Apostolov, *Journal of Radioanalytical Chemistry*, 1978, **45**, 65-71.
40. M. Barkat, D. Nibou, S. Chegrouche and A. Mellah, *Chemical Engineering and Processing: Process Intensification*, 2009, **48**, 38-47.

41. M. Saleem, M. Afzal, R. Qadeer and J. Hanif, *Separation Science and Technology*, 1992, **27**, 239-253.
42. Z.-j. Yi, J. Yao, F. Wang, H.-l. Chen, H.-j. Liu and C. Yu, *Journal of Radioanalytical and Nuclear Chemistry*, 2013, **295**, 2029-2034.
43. A. Belgacem, R. Rebiai, H. Hadoun, S. Khemaissia and M. Belmedani, *Environmental Science and Pollution Research*, 2014, **21**, 684-694.
44. S. M. Yakout, S. S. Metwally and T. El-Zakla, *Applied Surface Science*, 2013, **280**, 745-750.
45. C. Kütahyalı and M. Eral, *Separation and Purification Technology*, 2004, **40**, 109-114.
46. C. Kütahyalı and M. Eral, *Journal of Nuclear Materials*, 2010, **396**, 251-256.
47. M. Caccin, F. Giacobbo, M. Da Ros, L. Besozzi and M. Mariani, *Journal of Radioanalytical and Nuclear Chemistry*, 2013, **297**, 9-18.
48. C. W. Christenson, M. B. Ettinger, G. G. Robeck, E. R. Hermann, K. C. Kohr and J. F. Newell, *Industrial & Engineering Chemistry*, 1951, **43**, 1509-1515.
49. K. Kadirvelu, M. Kavipriya, C. Karthika, N. Vennilamani and S. Pattabhi, *Carbon*, 2004, **42**, 745-752.
50. J.-G. Yu, B.-Y. Yue, X.-W. Wu, Q. Liu, F.-P. Jiao, X.-Y. Jiang and X.-Q. Chen, *Environmental Science and Pollution Research*, 2016, **23**, 5056-5076.
51. R. Munter, *Proceedings of the Estonian Academy of Sciences*, 2013, **62**, 122-132.
52. J. L. Means, D. A. Crerar, M. P. Borcsik and J. O. Duguid, *Nature*, 1978, **274**, 44.
53. K. A. Hunter, D. J. Hawke and C. Lee Kwee, *Geochimica et Cosmochimica Acta*, 1988, **52**, 627-636.
54. X. Shuibo, Z. Chun, Z. Xinghuo, Y. Jing, Z. Xiaojian and W. Jingsong, *Journal of Environmental Radioactivity*, 2009, **100**, 162-166.
55. S. Yusan and S. Erenturk, *Desalination*, 2011, **269**, 58-66.
56. B. A. Powell, R. A. Fjeld, D. I. Kaplan, J. T. Coates and S. M. Serkiz, *Environmental Science & Technology*, 2004, **38**, 6016-6024.
57. B. A. Powell, R. A. Fjeld, D. I. Kaplan, J. T. Coates and S. M. Serkiz, *Environmental Science & Technology*, 2005, **39**, 2107-2114.
58. M. T. Crespo, J. L. Gascón and M. L. Aceña, *Science of The Total Environment*, 1993, **130-131**, 383-391.
59. J. L. Gascon, M. T. Crespo and M. L. Aceña, *Journal of Radioanalytical and Nuclear Chemistry*, 1990, **146**, 67-73.
60. C. Alliot, L. Bion, F. Mercier, P. Vitorge and P. Toulhoat, in *Radiochimica Acta*, Editon edn., 2005, vol. 93, p. 435.
61. M. S. Rao, A. M. Gaikwad, V. K. Rao and P. R. Natarajan, *Separation Science and Technology*, 1985, **20**, 205-212.
62. B. Allard, V. Moulin, L. Basso, M. T. Tran and D. Stammose, *Geoderma*, 1989, **44**, 181-187.
63. C. Tiffreau, J. Lützenkirchen and P. Behra, *Journal of Colloid and Interface Science*, 1995, **172**, 82-93.
64. V. Antochshuk, O. Olkhovyk, M. Jaroniec, I.-S. Park and R. Ryoo, *Langmuir*, 2003, **19**, 3031-3034.

65. P. Figueira, C. B. Lopes, A. L. Daniel-da-Silva, E. Pereira, A. C. Duarte and T. Trindade, *Water Research*, 2011, **45**, 5773-5784.
66. M. Monier and D. A. Abdel-Latif, *Journal of Hazardous Materials*, 2012, **209-210**, 240-249.
67. D. M. Manohar, K. Anoop Krishnan and T. S. Anirudhan, *Water Research*, 2002, **36**, 1609-1619.
68. H. Parham, B. Zargar and R. Shiralipour, *Journal of Hazardous Materials*, 2012, **205-206**, 94-100.
69. D. Pérez-Quintanilla, I. d. Hierro, M. Fajardo and I. Sierra, *Journal of Hazardous Materials*, 2006, **134**, 245-256.
70. R. T. Yang, *Adsorbents: fundamentals and applications*, Wiley-Interscience, Hoboken, N.J., 2003.
71. H. Mimura and T. Kanno, *Journal of Nuclear Science and Technology*, 1985, **22**, 284-291.
72. M. W. Munthali, E. Johan, H. Aono and N. Matsue, *Journal of Asian Ceramic Societies*, 2015, **3**, 245-250.
73. A. Dyer and D. Keir, *Zeolites*, 1984, **4**, 215-217.
74. A. Kilincarslan and S. Akyil, *Journal of Radioanalytical and Nuclear Chemistry*, 2005, **264**, 541-548.
75. S. O. Aytas, S. Akyil and M. Eral, *Journal of Radioanalytical and Nuclear Chemistry*, 2004, **260**, 119-125.
76. A. Dyer and L. C. Jozefowicz, *Journal of Radioanalytical and Nuclear Chemistry*, 1992, **159**, 47-62.
77. P. Misaelides, A. Godelitsas, A. Filippidis, D. Charistos and I. Anousis, *Science of The Total Environment*, 1995, **173-174**, 237-246.
78. H. Mimura, Y. Ishihara and K. Akiba, *Journal of Nuclear Science and Technology*, 1991, **28**, 144-151.
79. R. O. A. Rahman, H. A. Ibrahium and Y.-T. Hung, *Water*, 2011, **3**, 551.
80. Z. V. P. Murthy, P. A. Parikh and N. B. Patel, *Journal of Dispersion Science and Technology*, 2013, **34**, 747-755.
81. M. Yin, Z. Li, Z. Liu, X. Yang and J. Ren, *ACS Applied Materials & Interfaces*, 2012, **4**, 431-437.
82. IAEA, *Application of Ion Exchange Processes for Treatment of Radioactive Waste and Management of Spent Ion Exchangers*, IAEA, Vienna, 2002.
83. J. L. Ryan and E. J. Wheelwright, *Industrial & Engineering Chemistry*, 1959, **51**, 60-65.
84. Y. W. James D. Navratil, *Nukleonika*, 2001, **46**, 75–80.
85. F. El-Sweify and S. A. Ali, *Journal of Radioanalytical Chemistry*, 1980, **60**, 353-363.
86. M. S. C. Karthika, *International Research Journal of Environmental Sciences*, 2012, **1**, 34-41.
87. L. Pennington and M. Williams, *Industrial & Engineering Chemistry*, 1959, **51**, 759-762.
88. S. Chiarle, M. Ratto and M. Rovatti, *Water Research*, 2000, **34**, 2971-2978.

89. J. De Clercq, *International Journal of Industrial Chemistry*, 2012, **3**, 1.
90. J. Patterson, *Capsule report: Aqueous mercury treatment.EPA/625/R-97/004 (NTIS PB98115330),* , 1997.
91. A. A. Atia, A. M. Donia and H. H. El-Nomany, *Journal of Dispersion Science and Technology*, 2009, **30**, 451-458.
92. C. Ji, S. Song, C. Wang, C. Sun, R. Qu, C. Wang and H. Chen, *Chemical Engineering Journal*, 2010, **165**, 573-580.
93. M. Fomina and G. M. Gadd, *Bioresource Technology*, 2014, **160**, 3-14.
94. B. Volesky, *Hydrometallurgy*, 2001, **59**, 203-216.
95. M. Tsezos and B. Volesky, *Biotechnology and Bioengineering*, 1981, **23**, 583-604.
96. S.-I. Ishikawa, K. Suyama and I. Satoh, in *Twentieth Symposium on Biotechnology for Fuels and Chemicals Held May 3–7, 1998, Gatlinburg, Tennessee*, eds. B. H. Davison and M. Finkelstein, Humana Press, Totowa, NJ, Editon edn., 1999, pp. 521-533.
97. S. K. Kazy, S. F. D'Souza and P. Sar, *Journal of Hazardous Materials*, 2009, **163**, 65-72.
98. M. Tsezos and B. Volesky, *Biotechnology and Bioengineering*, 1982, **24**, 955-969.
99. M. Tsezos and B. Volesky, *Biotechnology and Bioengineering*, 1982, **24**, 385-401.
100. N. Siddiqui, J. Don, K. Mondal and A. Mahajan, *Environmental Technology*, 2011, **32**, 383-394.
101. Z. Tan, J. Qiu, H. Zeng, H. Liu and J. Xiang, *Fuel*, 2011, **90**, 1471-1475.
102. L. Huang, C. Xiao and B. Chen, *Journal of Hazardous Materials*, 2011, **192**, 832-836.
103. Y. Zhou, X. Hu, M. Zhang, X. Zhuo and J. Niu, *Industrial & Engineering Chemistry Research*, 2013, **52**, 876-884.
104. J. Lv, L. Luo, J. Zhang, P. Christie and S. Zhang, *Environmental Pollution*, 2012, **162**, 255-261.
105. S.-X. Li, Z. Feng-Ying, H. Yang and N. Jian-Cong, *Journal of Hazardous Materials*, 2011, **186**, 423-429.
106. A. Macías-García, E. M. Cuerda-Correa, M. Olivares-Marín, M. Alexandre-Franco and V. Gómez-Serrano, *Journal of Natural Fibers*, 2012, **9**, 98-116.
107. C. B. Lopes, J. R. Oliveira, L. S. Rocha, D. S. Tavares, C. M. Silva, S. P. Silva, N. Hartog, A. C. Duarte and E. Pereira, *Environmental Science and Pollution Research*, 2014, **21**, 2108-2121.
108. L. S. Rocha, C. B. Lopes, J. A. Borges, A. C. Duarte and E. Pereira, *Water, Air, & Soil Pollution*, 2013, **224**, 1599.
109. L. S. Rocha, I. Lopes, C. B. Lopes, B. Henriques, A. M. V. M. Soares, A. C. Duarte and E. Pereira, *Environmental Science and Pollution Research*, 2014, **21**, 8146-8156.
110. S.-T. Song, N. Saman, K. Johari and H. Mat, *Industrial & Engineering Chemistry Research*, 2013, **52**, 13092-13101.

111. M. Zhang, R. Wang, W. Guo, T. Xue and J. Dai, *Soil and Sediment Contamination: An International Journal*, 2014, **23**, 49-62.
112. M. D. Mullassery, N. B. Fernandez and T. S. Anirudhan, *Separation Science and Technology*, 2014, **49**, 1259-1269.
113. A. Taha, A. Moustafa, H. Abdel-Rahman and M. Abd El-Hameed, *Adsorption Science & Technology*, 2018, **36**, 521-548.
114. Z. Wang, P. Yin, R. Qu, H. Chen, C. Wang and S. Ren, *Food Chemistry*, 2013, **136**, 1508-1514.
115. S. N. Azizi, A. R. Dehnavi and A. Joorabdoozha, *Materials Research Bulletin*, 2013, **48**, 1753-1759.
116. D. Z. Husein, *Desalination and Water Treatment*, 2013, **51**, 6761-6769.
117. T. Shu, P. Lu and N. He, *Bioresource Technology*, 2013, **136**, 182-187.
118. M. Aslam, S. Rais, M. Alam and A. Pugazhendi, *Journal of Chemistry*, 2013, **2013**, 11.
119. G. Z. Kyzas and K. A. Matis, *Journal of Molecular Liquids*, 2015, **203**, 159-168.
120. I. Ali, *Chemical Reviews*, 2012, **112**, 5073-5091.
121. P. Xu, G. M. Zeng, D. L. Huang, C. L. Feng, S. Hu, M. H. Zhao, C. Lai, Z. Wei, C. Huang, G. X. Xie and Z. F. Liu, *Science of The Total Environment*, 2012, **424**, 1-10.
122. C. Santhosh, V. Velmurugan, G. Jacob, S. K. Jeong, A. N. Grace and A. Bhatnagar, *Chemical Engineering Journal*, 2016, **306**, 1116-1137.
123. M. Anjum, R. Miandad, M. Waqas, F. Gehany and M. A. Barakat, *Arabian Journal of Chemistry*, 2016.
124. R. C. Olvera, S. L. Silva, E. Robles-Belmont and E. Z. Lau, *Resource-Efficient Technologies*, 2017, **3**, 1-11.
125. R. Narayan, *Materials Today*, 2010, **13**, 44-46.
126. R. K. Thines, N. M. Mubarak, S. Nizamuddin, J. N. Sahu, E. C. Abdullah and P. Ganesan, *Journal of the Taiwan Institute of Chemical Engineers*, 2017, **72**, 116-133.
127. S. C. Smith and D. F. Rodrigues, *Carbon*, 2015, **91**, 122-143.
128. E. W. Wong, P. E. Sheehan and C. M. Lieber, *Science*, 1997, **277**, 1971.
129. N. Yao and V. Lordi, *Journal of Applied Physics*, 1998, **84**, 1939-1943.
130. S. Iijima, C. Brabec, A. Maiti and J. Bernholc, *The Journal of Chemical Physics*, 1996, **104**, 2089-2092.
131. R. Saito, M. Fujita, G. Dresselhaus and M. S. Dresselhaus, *Applied Physics Letters*, 1992, **60**, 2204-2206.
132. B. Frank, A. Rinaldi, R. Blume, R. Schlögl and D. S. Su, *Chemistry of Materials*, 2010, **22**, 4462-4470.
133. A. Mahajan, A. Kingon, Á. Kukovecz, Z. Konya and P. M. Vilarinho, *Materials Letters*, 2013, **90**, 165-168.
134. E. B. Silberstein, A. Kornblut, D. A. Shumrick and E. L. Saenger, *Radiology*, 1974, **110**, 605-608.
135. D. W. Hwang, H. Y. Ko, J. H. Lee, H. Kang, S. H. Ryu, I. C. Song, D. S. Lee and S. Kim, *Journal of Nuclear Medicine*, 2010, **51**, 98-105.

136. R. T. O'Donnell, G. L. DeNardo, D. L. Kukis, K. R. Lamborn, S. Shen, A. Yuan, D. S. Goldstein, C. E. Carr, G. R. Mirick and S. J. DeNardo, *Journal of Nuclear Medicine*, 1999, **40**, 2014-2020.
137. C. Raynaud, D. Comar, M. Dutheil, P. Blanchon, O. Monod, R. Parrot and M. Rymer, *Journal of Nuclear Medicine*, 1973, **14**, 947-950.
138. M. Eiblmaier, R. Andrews, R. Laforest, B. E. Rogers and C. J. Anderson, *Journal of Nuclear Medicine*, 2007, **48**, 1390-1396.
139. C. C. Lin, *Progress in Nuclear Energy*, 2009, **51**, 207-224.
140. S. Ono, M. Haginuma, M. Kumagai, M. Kitamura, K. Tachibana and K. Ishigure, *Journal of Nuclear Science and Technology*, 1995, **32**, 125-132.
141. H. Hosokawa and M. Nagase, *Journal of Nuclear Science and Technology*, 2004, **41**, 682-689.
142. C. J. Pedersen, *Journal of the American Chemical Society*, 1967, **89**, 7017-7036.
143. K. Nishizawa, K. Nakamura, T. Yamamoto and T. Masuda, *Solvent Extraction and Ion Exchange*, 1993, **11**, 389-394.
144. K. Nishizawa, T. Satoyama, T. Miki, T. Yamamoto and M. Nomura, *Separation Science and Technology*, 1996, **31**, 2831-2841.
145. Y. Lin, J. Espinas, S. Pellet-Rostaing, A. Favre-Réguillon and M. Lemaire, *New Journal of Chemistry*, 2010, **34**, 388-390.
146. X. Cao, J. Zhang, D. Weissmann, M. Dolg and X. Chen, *Physical Chemistry Chemical Physics*, 2015, **17**, 20605-20616.
147. J. M. Keith and E. R. Batista, *Inorganic chemistry*, 2011, **51**, 13-15.
148. A. Bhattacharyya, T. K. Ghanty, P. K. Mohapatra and V. K. Manchanda, *Inorganic Chemistry*, 2011, **50**, 3913-3921.
149. C.-Z. Wang, W.-Q. Shi, J.-H. Lan, Y.-L. Zhao, Y.-Z. Wei and Z.-F. Chai, *Inorganic chemistry*, 2013, **52**, 10904-10911.
150. C.-Z. Wang, J.-H. Lan, Q.-Y. Wu, Y.-L. Zhao, X.-K. Wang, Z.-F. Chai and W.-Q. Shi, *Dalton Transactions*, 2014, **43**, 8713-8720.
151. T. Bala, B. Prasad, M. Sastry, M. U. Kahaly and U. V. Waghmare, *The Journal of Physical Chemistry A*, 2007, **111**, 6183-6190.
152. M. Sundararajan and S. K. Ghosh, *The Journal of Physical Chemistry A*, 2011, **115**, 6732-6737.
153. S. Sun, D. Zhang, C. Li, Y. Wang and Q. Yang, *Chemical Engineering Journal*, 2014, **258**, 128-135.
154. T. Liu, L. Xue, X. Guo and C.-G. Zheng, *Fuel*, 2014, **115**, 179-185.
155. J. R. Black, A. Kavner and E. A. Schauble, *Geochimica et Cosmochimica Acta*, 2011, **75**, 769-783.
156. T. Fujii, F. Moynier, P. Telouk and M. Abe, *Journal of Physical Chemistry A*, 2010, **114**, 2543-2552.
157. T. Fujii, F. Moynier, A. Uehara, M. Abe, Q. Z. Yin, T. Nagai and H. Yamana, *Journal of Physical Chemistry A*, 2009, **113**, 12225-12232.
158. F. Jensen, *Introduction to computational chemistry*, John Wiley & Sons, 2013.
159. J. J. P. Stewart, *Journal of molecular modeling*, 2013, **19**, 1-32.

160. I. N. Levine and P. H. I. Learning, *Quantum chemistry*, Pearson Prentice Hall Upper Saddle River, NJ, 2009.
161. R. Krishnan and J. A. Pople, *International Journal of Quantum Chemistry*, 1978, **14**, 91-100.
162. I. Shavitt and R. J. Bartlett, *Many-body methods in chemistry and physics: MBPT and coupled-cluster theory*, Cambridge university press, 2009.
163. R. G. Parr and W. Yang, *Density-functional theory of atoms and molecules*, Oxford university press, 1989.
164. M. Dolg and X. Cao, *Chemical reviews*, 2011, **112**, 403-480.
165. A. Klamt and G. SchÃ¼Ã¼rmann, *Journal of the Chemical Society, Perkin Transactions 2*, 1993, 799-805.
166. J. Wei, M. M. Denn, J. H. Seinfeld, A. Chakraborty, J. Ying, N. Peppas and G. Stephanopoulos, *Molecular modeling and theory in chemical engineering*, Academic Press, 2001.
167. A. K. S. Deb, S. M. Ali and K. T. Shenoy, *RSC Advances*, 2015, **5**, 80076-80088.
168. A. K. Singha Deb, S. M. Ali, K. T. Shenoy and S. K. Ghosh, *Molecular Simulation*, 2015, **41**, 490-503.
169. A. Sengupta, A. Kumar Singha Deb, K. Dasgupta, V. C. Adya and S. M. Ali, *New Journal of Chemistry*, 2017, **41**, 4531-4545.
170. A. K. S. Deb, S. Pahan, K. Dasgupta, S. Panja, A. K. Debnath, P. S. Dhami, S. M. Ali, C. P. Kaushik and J. S. Yadav, *Journal of Hazardous Materials*, 2018, **345**, 63-75.
171. P. Kumar, A. Sengupta, A. K. Singha Deb, K. Dasgupta and S. M. Ali, *RSC Advances*, 2016, **6**, 107011-107020.
172. A. Sengupta, A. K. Singha Deb, P. Kumar, K. Dasgupta and S. M. Ali, *Journal of Environmental Chemical Engineering*, 2017, **5**, 3058-3064.
173. A. K. Singha Deb, V. Dwivedi, K. Dasgupta, S. Musharaf Ali and K. T. Shenoy, *Chemical Engineering Journal*, 2017, **313**, 899-911.
174. P. Kumar, A. Sengupta, A. K. Singha Deb, K. Dasgupta and S. M. Ali, *Radiochimica Acta*, 2017, **105**, 677-688.
175. P. Kumar, A. Sengupta, A. K. S. Deb and S. M. Ali, *ChemistrySelect*, 2017, **2**, 975-985.
176. A. Sengupta, A. K. S. Deb, N. K. Gupta, P. Kumar, K. Dasgupta and S. M. Ali, *Journal of Radioanalytical and Nuclear Chemistry*, 2018, **315**, 331-340.
177. A. K. Singha Deb, N. Dhume, K. Dasgupta, S. M. Ali, K. T. Shenoy and S. Mohan, *Separation Science and Technology (Philadelphia)*, 2018.
178. A. K. Singha Deb, S. M. Ali, K. T. Shenoy and S. K. Ghosh, *Journal of Chemical and Engineering Data*, 2014, **59**, 2472-2484.
179. P. H. Toy and Y. Lam, *Solid-phase organic synthesis : concepts, strategies, and applications*, Wiley, Hoboken, N.J., 2012.
180. A. R. Vaino and K. D. Janda, *Journal of Combinatorial Chemistry*, 2000, **2**, 579-596.
181. R. Ahlrichs, M. Bär, M. Häser, H. Horn and C. Kölmel, *Chemical Physics Letters*, 1989, **162**, 165-169.

182. K. Dasgupta, J. B. Joshi, H. Singh and S. Banerjee, *AIChE Journal*, 2014, **60**, 2882-2892.
183. E. Shchori, J. Jagur-Grodzinski, Z. Luz and M. Shporer, *Journal of the American Chemical Society*, 1971, **93**, 7133-7138.
184. R. Ungaro, B. El Haj and J. Smid, *Journal of the American Chemical Society*, 1976, **98**, 5198-5202.
185. E. Valeur and M. Bradley, *Chemical Society Reviews*, 2009, **38**, 606-631.
186. T. Ramanathan, F. T. Fisher, R. S. Ruoff and L. C. Brinson, *Chemistry of Materials*, 2005, **17**, 1290-1295.
187. P. Nockemann, B. Thijs, K. Lunstroot, T. N. Parac-Voet, C. Görller-Walrand, K. Binnemans, K. Van Hecke, L. Van Meervelt, S. Nikitenko, J. Daniels, C. Hennig and R. Van Deun, *Chemistry - A European Journal*, 2009, **15**, 1449-1461.
188. P. Mahanandia, P. N. Vishwakarma, K. K. Nanda, V. Prasad, S. V. Subramanyam, S. K. Dev and P. V. Satyam, *Materials Research Bulletin*, 2006, **41**, 2311-2317.
189. J. Shen, W. Huang, L. Wu, Y. Hu and M. Ye, *Materials Science and Engineering: A*, 2007, **464**, 151-156.
190. H.-B. Zhang, G.-D. Lin, Z.-H. Zhou, X. Dong and T. Chen, *Carbon*, 2002, **40**, 2429-2436.
191. K. V. Kumar, *Journal of Hazardous Materials*, 2006, **137**, 1538-1544.
192. D. B. Singh, G. Prasad, D. C. Rupainwar and V. N. Singh, *Water, Air, and Soil Pollution*, 1988, **42**, 373-386.
193. Y. S. Ho and G. McKay, *Process Safety and Environmental Protection*, 1998, **76**, 332-340.
194. Y. S. Ho and G. McKay, *Process Biochemistry*, 1999, **34**, 451-465.
195. G. Sheng, Y. Li, X. Yang, X. Ren, S. Yang, J. Hu and X. Wang, *RSC Advances*, 2012, **2**, 12400-12407.
196. K. Y. Foo and B. H. Hameed, *Chemical Engineering Journal*, 2010, **156**, 2-10.
197. M. Ghiaci, A. Abbaspur, R. Kia and F. Seyedeyn-Azad, *Separation and Purification Technology*, 2004, **40**, 217-229.
198. K. Vasanth Kumar and S. Sivanesan, *Dyes and Pigments*, 2007, **72**, 130-133.
199. M. C. Ncibi, *Journal of Hazardous Materials*, 2008, **153**, 207-212.
200. D. Kalderis, D. Koutoulakis, P. Paraskeva, E. Diamadopoulos, E. Otal, J. O. d. Valle and C. Fernández-Pereira, *Chemical Engineering Journal*, 2008, **144**, 42-50.
201. E A Gomaa and R. Tarek Rashad, *Chem Sci J Chemical Sciences Journal*, 2018, **09**.
202. V. P. V. K.A. Krishnan, T.S. Anirudhan, International Conference on Water and Environment, New Delhi, 2003.
203. W. W. Eckenfelder, *Tata McGraw-Hill Ser. Pollut.*, 2000, **138**, 358-367.
204. W. L. McCabe, J. C. Smith and P. Harriott, *Unit operations of chemical engineering = Hua xue gong cheng dan yuan cao zuo*, 2008.
205. Y. S. Al-Degs, M. A. M. Khraisheh, S. J. Allen and M. N. Ahmad, *Journal of Hazardous Materials*, 2009, **165**, 944-949.
206. F. H. Spedding, J. E. Powell and H. J. Svec, *Journal of the American Chemical Society*, 1955, **77**, 6125-6132.

207. K. Kawada, T. Ol, M. Hosoe and H. Kakihana, *Journal of Chromatography A*, 1991, **538**, 355-364.
208. P. Hohenberg and W. Kohn, *Phys. Rev.* , 1964, **136**, B864.
209. W. Kohn and L. J. Sham, *Phys. Rev.* , 1965, **140**, A1133.
210. A. Klamt, *The Journal of Physical Chemistry*, 1995, **99**, 2224-2235.
211. S. De, A. Boda and S. M. Ali, *Journal of Molecular Structure: THEOCHEM*, 2010, **941**, 90-101.
212. C. J. Cramer, *Essentials of computational chemistry : theories and models*, Wiley, Chichester; Hoboken, NJ, 2006.
213. G. A. Shamov, G. Schreckenbach and T. N. Vo, *Chemistry – A European Journal*, 2007, **13**, 4932-4947.
214. G. Schreckenbach and G. A. Shamov, *Accounts of Chemical Research*, 2010, **43**, 19-29.
215. G. A. Shamov and G. Schreckenbach, *Journal of Physical Chemistry A*, 2005, **109**, 10961-10974.
216. S. M. Ali, J. M. Joshi, A. K. Singha Deb, A. Boda, K. T. Shenoy and S. K. Ghosh, *RSC Advances*, 2014, **4**, 22911-22925.
217. S. M. Ali, *Computational and Theoretical Chemistry*, 2014, **1034**, 38-52.
218. S. M. Ali, *European Journal of Inorganic Chemistry*, 2014, 1533-1545.
219. G. Schaftenaar and J. H. Noordik, *Journal of Computer-Aided Molecular Design*, 2000, **14**, 123-134.
220. A. E. Reed, R. B. Weinstock and F. Weinhold, *The Journal of Chemical Physics*, 1985, **83**, 735-746.
221. J. Bigeleisen, *Journal of the American Chemical Society*, 1996, **118**, 3676-3680.
222. M. G. Salinas-Pedroza and M. T. Olguín, *Journal of Radioanalytical and Nuclear Chemistry*, 2004, **260**, 115-118.
223. G. R. Choppin, *Radiochimica Acta*, 1999, **85**, 89-95.
224. C. Chen, X. Li, D. Zhao, X. Tan and X. Wang, *Colloids and Surfaces A: Physicochemical and Engineering Aspects*, 2007, **302**, 449-454.
225. C. L. Chen, X. L. Li and X. K. Wang, *Radiochimica Acta*, 2007, **95**, 261-266.
226. J. Wang, P. Liu, Z. Li, W. Qi, Y. Lu and W. Wu, *Materials*, 2013, **6**, 4168-4185.
227. M. Wang, X. Tao and X. Song, *Journal of Radioanalytical and Nuclear Chemistry*, 2011, **288**, 859-865.
228. A. K. S. Deb, B. N. Mohanty, P. Ilaiyaraja, K. Sivasubramanian and B. Venkatraman, *Journal of Radioanalytical and Nuclear Chemistry*, 2013, **295**, 1161-1169.
229. A. Schäfer, H. Horn and R. Ahlrichs, *The Journal of Chemical Physics*, 1992, **97**, 2571-2577.
230. A. Schäfer, C. Huber and R. Ahlrichs, *The Journal of Chemical Physics*, 1994, **100**, 5829-5835.
231. A. D. Becke, *The Journal of Chemical Physics*, 1993, **98**, 5648-5652.
232. C. Lee, W. Yang and R. G. Parr, *Physical Review B*, 1988, **37**, 785-789.
233. A. D. Becke, *Physical Review A*, 1988, **38**, 3098-3100.
234. J. P. Perdew, *Physical Review B*, 1986, **33**, 8822-8824.

235. J. P. Austin, M. Sundararajan, M. A. Vincent and I. H. Hillier, *Dalton Transactions*, 2009, 5902-5909.
236. N. K. Jena, M. Sundararajan and S. K. Ghosh, *RSC Advances*, 2012, **2**, 2994-2999.
237. M. Sundararajan, V. Sinha, T. Bandyopadhyay and S. K. Ghosh, *Journal of Physical Chemistry A*, 2012, **116**, 4388-4395.
238. D. Manna and T. K. Ghanty, *Physical Chemistry Chemical Physics*, 2012, **14**, 11060-11069.
239. G. Johansson, M. Magini and H. Ohtaki, *Journal of Solution Chemistry*, 1991, **20**, 775-792.
240. C. Hennig, K. Schmeide, V. Brendler, H. Moll, S. Tsushima and A. C. Scheinost, *Inorganic Chemistry*, 2007, **46**, 5882-5892.
241. H. Moll, M. A. Denecke, F. Jalilehvand, M. Sandström and I. Grenthe, *Inorganic Chemistry*, 1999, **38**, 1795-1799.
242. N. Torapava, I. Persson, L. Eriksson and D. Lundberg, *Inorganic Chemistry*, 2009, **48**, 11712-11723.
243. V. S. Bryantsev, M. S. Diallo and W. A. Goddard Iii, *Journal of Physical Chemistry B*, 2008, **112**, 9709-9719.
244. M. Dolg, X. Cao and J. Ciupka, *Journal of Electron Spectroscopy and Related Phenomena*, 2014, **194**, 8-13.
245. J. Ciupka, X. Cao-Dolg, J. Wiebke and M. Dolg, *Physical Chemistry Chemical Physics*, 2010, **12**, 13215-13223.
246. J. Wiebke, A. Moritz, X. Cao and M. Dolg, *Physical Chemistry Chemical Physics*, 2007, **9**, 459-465.
247. F. David, V. Vokhmin and G. Ionova, *Journal of Molecular Liquids*, 2001, **90**, 45-62.
248. F. H. David and V. Vokhmin, *New Journal of Chemistry*, 2003, **27**, 1627-1632.
249. R. G. Parr and R. G. Pearson, *Journal of the American Chemical Society*, 1983, **105**, 7512-7516.
250. A. Boda and M. A. Sheikh, *Journal of Physical Chemistry A*, 2012, **116**, 8615-8623.
251. Y. Marcus, *Journal of the Chemical Society, Faraday Transactions*, 1991, **87**, 2995-2999.
252. A. K. S. Deb, P. Ilaiyaraja, D. Ponraju and B. Venkatraman, *Journal of Radioanalytical and Nuclear Chemistry*, 2012, **291**, 877-883.
253. A. Sengupta, S. Jayabun, A. Boda and S. M. Ali, *RSC Advances*, 2016, **6**, 39553-39562.
254. N. K. Gupta, A. Sengupta, A. Boda, V. C. Adya and S. M. Ali, *RSC Advances*, 2016, **6**, 78692-78701.
255. Y. Buchatskaya, A. Romanchuk, R. Yakovlev, A. Shiryaev, I. Kulakova and S. Kalmykov, *Radiochimica Acta*, 2015, **103**, 205-211.
256. I. I. Fasfous and J. N. Dawoud, *Applied Surface Science*, 2012, **259**, 433-440.
257. S. Lu, L. Chen, Y. Dong and Y. Chen, *Journal of Radioanalytical and Nuclear Chemistry*, 2011, **288**, 587-593.

258. S. A. Perevalov and N. P. Molochnikova, *Journal of Radioanalytical and Nuclear Chemistry*, 2009, **281**, 603-608.
259. M. Wang, J. Qiu, X. Tao, C. Wu, W. Cui, Q. Liu and S. Lu, *Journal of Radioanalytical and Nuclear Chemistry*, 2011, **288**, 895-901.
260. V. K. Singh and P. N. Tiwari, *Journal of Chemical Technology and Biotechnology*, 1997, **69**, 376-382.
261. K. K. H. Choy, J. F. Porter and G. McKay, *Journal of Chemical and Engineering Data*, 2000, **45**, 575-584.
262. I. Billard, S. Mekki, C. Gaillard, P. Hesemann, G. Moutiers, C. Mariet, A. Labet and J. C. G. Bünzli, *European Journal of Inorganic Chemistry*, 2004, 1190-1197.
263. S. Arenz, A. Babai, K. Binnemans, K. Driesen, R. Giernoth, A. V. Mudring and P. Nockemann, *Chemical Physics Letters*, 2005, **402**, 75-79.
264. R. Schurhammer and G. Wipff, *Journal of Physical Chemistry B*, 2007, **111**, 4659-4668.
265. A. Sengupta and M. S. Murali, *Separation Science and Technology (Philadelphia)*, 2016, **51**, 2153-2163.
266. P. Zhang and T. Kimura, *Solvent Extraction and Ion Exchange*, 2006, **24**, 149-163.
267. R. Nagaishi, M. Arisaka, T. Kimura and Y. Kitatsuji, *Journal of Alloys and Compounds*, 2007, **431**, 221-225.
268. A. Sengupta, S. V. Godbole, P. K. Mohapatra, M. Iqbal, J. Huskens and W. Verboom, *Journal of Luminescence*, 2014, **148**, 174-180.
269. A. Sengupta, P. K. Mohapatra, M. Iqbal, J. Huskens and W. Verboom, *Journal of Luminescence*, 2014, **154**, 392-401.
270. A. Sengupta, L. Wu, W. Feng, L. Yuan and V. Natarajan, *Journal of Luminescence*, 2015, **158**, 356-364.
271. W. DeW Horrocks, Jr. and D. R. Sudnick, *Accounts of Chemical Research*, 1981, **14**, 384-392.
272. P. P. Barthelemy and G. R. Choppin, *Inorganic Chemistry*, 1989, **28**, 3354-3357.
273. T. Kimura and Y. Kato, *Journal of Alloys and Compounds*, 1998, **278**, 92-97.
274. P. K. Mohapatra, A. Sengupta, M. Iqbal, J. Huskens and W. Verboom, *Inorganic Chemistry*, 2013, **52**, 2533-2541.
275. B. R. Judd, *Physical Review*, 1962, **127**, 750-761.
276. O. L. Malta, H. F. Brito, J. F. S. Menezes, F. R. Gonçalves E Silva, S. Alves Jr, F. S. Farias Jr and A. V. M. De Andrade, *Journal of Luminescence*, 1997, **75**, 255-268.
277. G. F. De Sá, O. L. Malta, C. De Mello Donegá, A. M. Simas, R. L. Longo, P. A. Santa-Cruz and E. F. Da Silva Jr, *Coordination Chemistry Reviews*, 2000, **196**, 165-195.
278. D. Zhao, X. Qiao, X. Fan and M. Wang, *Physica B: Condensed Matter*, 2007, **395**, 10-15.
279. S. Wen, X. Zhang, S. Hu, L. Zhang and L. Liu, *Journal of Rare Earths*, 2008, **26**, 787-791.

280. M. Kumar, T. K. Seshagiri and S. V. Godbole, *Physica B: Condensed Matter*, 2013, **410**, 141-146.
281. A. Sengupta, Y. Fang, X. Yuan and L. Yuan, *Journal of Luminescence*, 2015, **166**, 187-194.
282. T. Lin, V. Bajpai, T. Ji and L. Dai, *Australian Journal of Chemistry*, 2003, **56**, 635-651.
283. W. Küchle, M. Dolg, H. Stoll and H. Preuss, *The Journal of Chemical Physics*, 1994, **100**, 7535-7542.
284. A. G. Rinzler, J. Liu, H. Dai, P. Nikolaev, C. B. Huffman, F. J. Rodriguez-Macías, P. J. Boul, A. H. Lu, D. Heymann, D. T. Colbert, R. S. Lee, J. E. Fischer, A. M. Rao, P. C. Eklund and R. E. Smalley, *Applied Physics A: Materials Science and Processing*, 1998, **67**, 29-37.
285. Y. H. Li, S. Wang, J. Wei, X. Zhang, C. Xu, Z. Luan, D. Wu and B. Wei, *Chemical Physics Letters*, 2002, **357**, 263-266.
286. Y. H. Li, J. Ding, Z. Luan, Z. Di, Y. Zhu, C. Xu, D. Wu and B. Wei, *Carbon*, 2003, **41**, 2787-2792.
287. X. Wang, C. Chen, W. Hu, A. Ding, D. Xu and X. Zhou, *Environmental Science and Technology*, 2005, **39**, 2856-2860.
288. N. Thamavaranukup, H. A. Hoppe, L. Ruiz-Gonzalez, C. P.M.F.J, J. Sloan and M. L. H. Kirkland, *Green Chem. Commun*, 2004, 1686.
289. A. Schierz and H. Zänker, *Environmental Pollution*, 2009, **157**, 1088-1094.
290. X. L. Tan, D. Xu, C. L. Chen, X. K. Wang and W. P. Hu, *Radiochimica Acta*, 2008, **96**, 23-29.
291. R. Kumar and S. K. Jain, *International Journal of Nanoscience*, 2012, **11**.
292. C. K. Aslani, F. Belloni, B. Çetinkaya and V. V. Rondinella, *Radiochimica Acta*, 2014, **102**, 931-940.
293. A. K. Singha Deb, A. Bhattacharyya, S. M. Ali, K. T. Shenoy and S. K. Ghosh, *Separation Science and Technology (Philadelphia)*, 2015, **50**, 395-403.
294. W. Chen, L. Duan and D. Zhu, *Environmental Science and Technology*, 2007, **41**, 8295-8300.
295. P. Zong and J. Gou, *Journal of Molecular Liquids*, 2014, **195**, 92-98.
296. X. Wang, L. U. Jialong and B. Xing, *Environmental Science and Technology*, 2008, **42**, 3207-3212.
297. R. Guillaumont, F. J. Mompen, T. Fanghanel, J. Fuger, I. Grenthe, V. Neck, D. A. Palmer and N. L. Rand, *Chemical Thermodynamics of Uranium, Neptunium, Plutonium, Americium*, 2017, **5**.
298. X. Wang, J. Li, S. Dai, T. Hayat, A. Alsaedi and X. Wang, *Chemical Engineering Journal*, 2015, **273**, 588-594.
299. A. Dąbrowski, *Advances in Colloid and Interface Science*, 2001, **93**, 135-224.
300. K. L. Salipira, B. B. Mamba, R. W. Krause, T. J. Malefetse and S. H. Durbach, *Environmental Chemistry Letters*, 2007, **5**, 13-17.
301. K. Pyrzynska, *Separation and Purification Reviews*, 2008, **37**, 375-392.
302. L. Hanchao, F. Suping, D. Xiaolin, Z. Nannan and L. Yongli, *Energy Procedia*, 2011, **5**, 985.

303. C. Chen and X. Wang, *Industrial and Engineering Chemistry Research*, 2006, **45**, 9144-9149.
304. C. Lu, H. Chiu and C. Liu, *Industrial and Engineering Chemistry Research*, 2006, **45**, 2850-2855.
305. G. P. Rao, C. Lu and F. Su, *Separation and Purification Technology*, 2007, **58**, 224-231.
306. M. Tuzen, K. O. Saygi and M. Soylak, *Journal of Hazardous Materials*, 2008, **152**, 632-639.
307. C. L. Chen, X. K. Wang and M. Nagatsu, *Environmental Science and Technology*, 2009, **43**, 2362-2367.
308. M. I. Temkin and V. Pyzhev, *Acta Physicochim. USSR*, 1940, **12**, 327-356.
309. C. Aharoni and M. Ungarish, *Journal of the Chemical Society, Faraday Transactions 1: Physical Chemistry in Condensed Phases*, 1977, **73**, 456-464.
310. A. O. Dada, A. P. Olalekan, A. M. Olatunya and O. Dada, *J. Appl. Chem.*, 2012, **3**, 38-45.
311. R. Chiarizia, E. P. Horwitz and S. D. Alexandratos, *Solvent Extraction and Ion Exchange*, 1994, **12**, 211-237.
312. A. Szabo and N. S. Ostlund, *Modern Quantum Chemistry*, 1989.
313. T. Koopmans, *uber Die Zuordnung von Wellen Funktionenund Eigenwertenzu Den Einzelnen Elektroneneines*, 1933, 104.
314. J. I. Kim and T. Sekine, *Radiochimica Acta*, 1991, **55**, 187-192.
315. S. Pahan, A. Boda and S. M. Ali, *Theoretical Chemistry Accounts*, 2015, **134**.
316. A. Sengupta, S. Jayabun, I. C. Pius and S. K. Thulasidas, *Journal of Radioanalytical and Nuclear Chemistry*, 2016, **309**, 841-852.
317. A. Sengupta, M. Keskar and S. Jayabun, *Journal of Radioanalytical and Nuclear Chemistry*, 2016, **310**, 979-989.
318. *Global Mercury Assessment 2013: Sources, Emissions, Releases and Environmental Transport*, 2013.
319. M. Kumar and A. Puri, *Indian Journal of Occupational and Environmental Medicine*, 2012, **16**, 40-44.
320. S. Mallakpour and E. Khadem, *Chemical Engineering Journal*, 2016, **302**, 344-367.
321. X. Ren, C. Chen, M. Nagatsu and X. Wang, *Chemical Engineering Journal*, 2011, **170**, 395-410.
322. X. Qu, P. J. J. Alvarez and Q. Li, *Water Research*, 2013, **47**, 3931-3946.
323. S. W. Kim, T. Kim, Y. S. Kim, H. S. Choi, H. J. Lim, S. J. Yang and C. R. Park, *Carbon*, 2012, **50**, 3-33.
324. J. Hu, C. Chen, X. Zhu and X. Wang, *Journal of Hazardous Materials*, 2009, **162**, 1542-1550.
325. Z. Veličković, G. D. Vuković, A. D. Marinković, M. S. Moldovan, A. A. Perić-Grujić, P. S. Uskoković and M. T. Ristić, *Chemical Engineering Journal*, 2012, **181-182**, 174-181.
326. M. G. Afshar, M. Soleimani and M. Bazrpach, *World Academy of Science, Engineering and Technology*, 2011, **75**, 388-389.

327. Q. Li, J. Yu, F. Zhou and X. Jiang, *Colloids and Surfaces A: Physicochemical and Engineering Aspects*, 2015, **482**, 306-314.
328. M. Hadavifar, N. Bahramifar, H. Younesi and Q. Li, *Chemical Engineering Journal*, 2014, **237**, 217-228.
329. R. K. Misra, S. K. Jain, T. N. Abraham and P. K. Khatri, *International Journal of Nanoscience*, 2011, **10**, 205-208.
330. K. A. Krishnan, V. P. Vinod and T. S. Anirudhan, *Proceedings of the International Conference on Water and Environment*, 2003.
331. J. Narbutt, A. Wodyński and M. Pecul, *Dalton Transactions*, 2015, **44**, 2657-2666.
332. N. M. Mubarak, J. N. Sahu, J. R. Wong, N. S. Jayakumar, P. Ganesan and E. C. Abdullah, *Chemical functionalization of carbon nanomaterials*, 2015, 82-101.
333. F. Zhang, B. Wang, S. He and R. Man, *Journal of Chemical and Engineering Data*, 2014, **59**, 1719-1726.
334. M. Behbahani, T. Gorji, M. Mahyari, M. Salarian, A. Bagheri and A. Shaabani, *Food Analytical Methods*, 2014, **7**, 957-966.
335. Y. Xu and D. Zhao, *Environmental Science and Technology*, 2005, **39**, 2369-2375.
336. A. Shahbazi, H. Younesi and A. Badiei, *Chemical Engineering Journal*, 2011, **168**, 505-518.
337. A. Proctor and J. F. Toro-Vazquez, *JAOCS, Journal of the American Oil Chemists' Society*, 1996, **73**, 1627-1633.
338. N. D. Hutson and R. T. Yang, *Adsorption*, 1997, **3**, 189-195.
339. S. V. Mohan and J. Karthikeyan, *Environmental Pollution*, 1997, **97**, 183-187.
340. D. J. M. Meyer, S. Bourg, O. Conocar, J. C. Broudic, J. J. E. Moreau and M. W. Chi Man, *Comptes Rendus Chimie*, 2007, **10**, 1001-1009.
341. D. M. Taylor, *Science of the Total Environment, The*, 1989, **83**, 217-225.
342. A. Sengupta, N. K. Gupta and V. C. Adya, *Journal of Radioanalytical and Nuclear Chemistry*, 2017, **314**, 1393-1404.
343. M. S. Diallo, S. Christie, P. Swaminathan, L. Balogh, X. Shi, W. Um, C. Papelis, W. A. Goddard Iii and J. H. Johnson Jr, *Langmuir*, 2004, **20**, 2640-2651.
344. Y. Zou, Y. Liu, X. Wang, G. Sheng, S. Wang, Y. Ai, Y. Ji, Y. Liu, T. Hayat and X. Wang, *ACS Sustainable Chemistry and Engineering*, 2017, **5**, 3583-3595.
345. W. Cheng, C. Ding, Q. Wu, X. Wang, Y. Sun, W. Shi, T. Hayat, A. Alsaedi, Z. Chai and X. Wang, *Environmental Science: Nano*, 2017, **4**, 1124-1131.
346. Y. Sun, S. Yang, Y. Chen, C. Ding, W. Cheng and X. Wang, *Environmental Science and Technology*, 2015, **49**, 4255-4262.
347. A. Sengupta and N. K. Gupta, *Journal of Environmental Chemical Engineering*, 2017, **5**, 5099-5114.
348. E. Zakharchenko, O. Mokhodoeva, D. Malikov, N. Molochnikova, Y. Kulyako and G. Myasoedova, *Proc. Chem*, 2012, **7**, 268-274.
349. I. C. Pius, M. M. Charyulu, B. Venkataramani, C. K. Sivaramakrishnan and S. K. Patil, *Journal of Radioanalytical and Nuclear Chemistry Letters*, 1995, **199**, 1-7.

350. R. Qu, M. Wang, R. Song, C. Sun, Y. Zhang, X. Sun, C. Ji, C. Wang and P. Yin, *Journal of Chemical and Engineering Data*, 2011, **56**, 1982-1990.
351. *Priority List of Hazardous Substances*, 2014.
352. C. Namasivayam and K. Kadirvelu, *Carbon*, 1999, **37**, 79-84.
353. S. T. Song, N. Saman, K. Johari and H. Mat, *Industrial and Engineering Chemistry Research*, 2013, **52**, 13092-13101.
354. N. M. Bandaru, N. Reta, H. Dalal, A. V. Ellis, J. Shapter and N. H. Voelcker, *Journal of Hazardous Materials*, 2013, **261**, 534-541.
355. M. Soleimani, M. G. Afshar and A. Sedghi, *Nanotechnology*, 2013, **2013**, 1-8.
356. Y. Zhou, J. Zhang, X. Luo and X. Lin, *Journal of Applied Polymer Science*, 2014, **131**, 9128-9136.
357. T. Masciangioli and W. X. Zhang, *Environmental Science and Technology*, 2003, **37**, 102A-108A.
358. A. S. Adeleye, J. R. Conway, K. Garner, Y. Huang, Y. Su and A. A. Keller, *Chemical Engineering Journal*, 2016, **286**, 640-662.
359. J. Cheng, K. A. S. Fernando, L. M. Veca, Y. P. Sun, A. I. Lamond, Y. W. Lam and S. H. Cheng, *ACS Nano*, 2008, **2**, 2085-2094.
360. K. Balasubramanian and M. Burghard, *Small*, 2005, **1**, 180-192.
361. Ihsanullah, A. Abbas, A. M. Al-Amer, T. Laoui, M. J. Al-Marri, M. S. Nasser, M. Khraisheh and M. A. Atieh, *Separation and Purification Technology*, 2016, **157**, 141-161.
362. S. Zhang, Y. Zhang, J. Liu, Q. Xu, H. Xiao, X. Wang, H. Xu and J. Zhou, *Chemical Engineering Journal*, 2013, **226**, 30-38.
363. T. Gao, J. Yu, Y. Zhou and X. Jiang, *Journal of the Taiwan Institute of Chemical Engineers*, 2017, **71**, 426-432.
364. Q. J. McCubbin, F. J. Stoddart, T. Welton, A. J. P. White and D. J. Williams, *Inorganic Chemistry*, 1998, **37**, 3753-3758.
365. A. H. El-Sheikh, *Talanta*, 2008, **75**, 127-134.
366. E. Humeres, N. A. Debacher, J. D. Franco, B. S. Lee and A. Martendal, *Journal of Organic Chemistry*, 2002, **67**, 3662-3667.
367. F. Haghseresht and G. Q. Lu, *Energy and Fuels*, 1998, **12**, 1100-1107.
368. A. Ramesh, D. J. Lee and J. W. C. Wong, *Journal of Colloid and Interface Science*, 2005, **291**, 588-592.
369. G. Liu, Y. Cai and N. O'Driscoll, *Environmental Chemistry and Toxicology of Mercury*, 2012.
370. F. H. Spedding, J. E. Powell and H. J. Svec, *Journal of the American Chemical Society*, 1955, **77**, 6125-6132.
371. K. G. Heumann and H. P. Schiefer, *Angewandte Chemie International Edition in English*, 1980, **19**, 406-407.
372. K. Nishizawa, S. I. Ishino, H. Watanabe and M. Shinagawa, *Journal of Nuclear Science and Technology*, 1984, **21**, 694-701.
373. K. Nishizawa, K. Nakamura, T. Yamamoto and T. Masuda, *Solvent Extraction and Ion Exchange*, 1994, **12**, 1073-1084.

374. K. Nishizawa, T. Nishida, T. Miki, T. Yamamoto and M. Hosoe, *Separation Science and Technology*, 1996, **31**, 643-654.
375. K. Nishizawa, T. Miki, R. Ikeda, T. Fujii, T. Yamamoto and M. Nomura, *J. Mass Spectrom. Soc. Jpn.*, 1997, **45**, 521-527.
376. I. M. Ismail, A. Fukami, M. Nomura and Y. Fujii, *Analytical Chemistry*, 2000, **72**, 2841-2845.
377. Y. Ban, M. Nomura and Y. Fujii, *Separation Science and Technology*, 2001, **36**, 2165-2180.
378. Y. Ban, M. Nomura and Y. Fujii, *Journal of Nuclear Science and Technology*, 2002, **39**, 279-281.
379. M. D. Abdul Matin, I. M. Ismail, M. Nomura and Y. Fujii, *Separation Science and Technology*, 2002, **37**, 2129-2142.
380. X. Ding, M. Nomura, T. Suzuki, Y. Sugiyama, T. Kaneshiki and Y. Fujii, *Journal of Chromatography A*, 2006, **1113**, 182-185.
381. X. Ding, T. Suzuki, M. Nomura, Y. Sugiyama, T. Kaneshiki and Y. Fujii, *Bulletin of the Chemical Society of Japan*, 2006, **79**, 1389-1392.
382. X. Ding, T. Suzuki, M. Nomura, H. J. Kim, Y. Sgiyama and Y. Fujii, *Journal of Radioanalytical and Nuclear Chemistry*, 2007, **273**, 79-84.
383. X. Ding, M. Nomura, T. Suzuki and Y. Fujii, *Chromatographia*, 2010, **71**, 195-199.
384. K. Rajagopal, R. V. Krisnakumar, M. Subha Nandhini, S. Kannan and S. Natarajan, *Acta Crystallogr.*, 2002.
385. S. Plimpton, *Journal of Computational Physics*, 1995, **117**, 1-19.
386. K. Fukui, *Angewandte Chemie International Edition in English*, 1982, **21**, 801-809.
387. T. Fujii, F. Moynier, M. L. Pons and F. Albarède, *Geochimica et Cosmochimica Acta*, 2011, **75**, 7632-7643.
388. R. G. Pearson, *Inorganic Chemistry*, 1988, **27**, 734-740.
389. E. D. Glendening, O. K. Badenhoop, A. E. Reed, J. E. Carpenter, J. A. Bohmann, C. M. Morales and F. Weinhold, 2001.
390. G. te Velde, F. M. Bickelhaupt, E. J. Baerends, C. Fonseca Guerra, S. J. A. van Gisbergen, J. G. Snijders and T. Ziegler, *Journal of Computational Chemistry*, 2001, **22**, 931-967.
391. S. Wang, T. Terdkiatburana and M. O. Tadé, *Separation and Purification Technology*, 2008, **62**, 64-70.

Appendix

Glossary of Symbols

Symbol	Description	Unit
ΔH_{ads}	Enthalpy of adsorption	kcal mol^{-1}
$t_{1/2}$	Half-life of radioactive element	years or days
q_t	The amount of metal ion adsorbed at time‘t’	mg g^{-1}
q_e	The amount of metal ion adsorbed at equilibrium	mg g^{-1}
C_o	Analyte concentrations at initial	mg L^{-1}
C_t	Analyte concentrations at time‘t’	mg L^{-1}
C_e	Analyte concentrations at equilibrium	mg L^{-1}
V	Volume of the solution	L or mL
m	Mass of the adsorbent	g
K_d	Distribution coefficient	mL g^{-1}
k_1	Rate constant of pseudo-first-order adsorption kinetic model	min^{-1}
k_2	Rate constant of pseudo-second-order adsorption kinetic model	g mg^{-1} min^{-1}
k_i	Rate constant of the intraparticle diffusion kinetic model	mg g^{-1} $min^{-1/2}$
q_m	Maximum monolayer coverage capacities	mg g^{-1}
b	Langmuir isotherm constant	L mg^{-1}
K_F	Freundlich isotherm constant	(mg/g) $(L/g)^n$
n	Adsorption intensity	
B_t	Tempkin isotherm constant	
K_T	Tempkin isotherm equilibrium binding constant	L g^{-1}
q_o	Theoretical isotherm saturation capacity	mg g^{-1}
B_{DR}	Dubinin–Radushkevich isotherm constant	$mol^2 kJ^{-2}$
Ea	Energy of adsoption	kJ mol^{-1}
K_{RP}	Redlich–Peterson isotherm constant	L g^{-1}
a_{RP}	Redlich–Peterson isotherm constant	$(L\ mg^{-1})^g$
g	Redlich–Peterson isotherm exponent	
K_{th}	Toth isotherm constant	mg g^{-1}
a_{th}	Toth isotherm constant	L mg^{-1}
t	Toth isotherm constant	
K_s	Sips isotherm model constant	L g^{-1}
A_s	Sips isotherm model constant	L mg^{-1}
b_s	Sips isotherm model exponent	
ΔG^o	Standard free energy change	kcal mol^{-1}

ΔH^o	Standard enthalpy change	kcal mol^{-1}
ΔS^o	Standard entropy change	kcal mol^{-1}K^{-1}
Ko	Equilibrium constant	
C_{solid}	Solid phase concentration at equilibrium	mg L^{-1}
T	Temperature	Kelvin
R	Universal gas constant	kJ mol^{-1}K^{-1}
Co/Ci	Ratio of outlet and inlet concentration in column separation	
Q_{tot}	Total quantity of adsorbate adsorbed	mg
Q_e	Adsorbent bed adsorption capacity	mg/g
F_v	Feed solution volumetric flow rate	mL min^{-1} or m^3 h^{-1}
t_b	Breakthrough time	min
t_e	Exhaustion time	min
V_T	Volume of effluent collected at t_e	mL or L
M	Mass of the adsorbent present in the fixed bed column	gram
h_z	height of the mass transfer zone	cm
L	bed height	cm
EBCT	empty bed contact time or bed service time	min
V_b	Breakthrough volume	L or mL
Ur	adsorbent usage rate	g/L
β	Isotope enrichment factor	
α	Isotope separation factor	
ε	Isotope separation coefficient	
q_i	Amount of zinc in each fraction sample	
R_i	Isotopic percentage of ^{H}Zn in sample fraction	